

REPORT DOCUMENTATION PAGE

Form Approved
OMB NO. 0704-0188

Public Reporting burden for this collection of information is estimated to average 1 hour per response, including the time for reviewing instructions, searching existing data sources, gathering and maintaining the data needed, and completing and reviewing the collection of information. Send comment regarding this burden estimates or any other aspect of this collection of information, including suggestions for reducing this burden, to Washington Headquarters Services, Directorate for information Operations and Reports, 1215 Jefferson Davis Highway, Suite 1204, Arlington, VA 22202-4302, and to the Office of Management and Budget, Paperwork Reduction Project (0704-0188,) Washington, DC 20503.

1. AGENCY USE ONLY (Leave Blank)		2. REPORT DATE June 7, 2004		3. REPORT TYPE AND DATES COVERED Final , 01 June 1999 to 31 Dec., 2003	
4. TITLE AND SUBTITLE Compact Reconfigurable HF-UHF antennas				5. FUNDING NUMBERS DAAD19-99-1-0197	
6. AUTHOR(S) Kamal Sarabandi					
7. PERFORMING ORGANIZATION NAME(S) AND ADDRESS(ES) Radiation Laboratory, Department of Electrical Eng. and Computer Science The University of Michigan Ann Arbor, MI 48109-2122				8. PERFORMING ORGANIZATION REPORT NUMBER 991549	
9. SPONSORING / MONITORING AGENCY NAME(S) AND ADDRESS(ES) U. S. Army Research Office P.O. Box 12211 Research Triangle Park, NC 27709-2211				10. SPONSORING / MONITORING AGENCY REPORT NUMBER 3 9 8 7 9 . 2 - E L	
11. SUPPLEMENTARY NOTES The views, opinions and/or findings contained in this report are those of the author(s) and should not be construed as an official Department of the Army position, policy or decision, unless so designated by other documentation.					
12 a. DISTRIBUTION / AVAILABILITY STATEMENT Approved for public release; distribution unlimited.				12 b. DISTRIBUTION CODE	
13. ABSTRACT (Maximum 200 words) The development of a compact reconfigurable HF-UHF antenna is of great practical importance in mobile military communications where low visibility and high mobility are required. Variations of monopole and dipole antennas in use today are narrowband and are prohibitively large and bulky at these frequencies. Broadband antennas are not only large, but also suffer from jamming susceptibility and undesirable complex multiplexing requirements. Development of efficient, small geometry, planar, and reconfigurable antennas is investigated. Based on a resonating slot structure, small antennas that exhibit simultaneous bandselectivity and antijam characteristics. So far very small antennas using novel topologies have been developed that areas as small as $(0.05\lambda)^2$. Also efficient reconfigurability over a very wide range of frequency using electronic switches has been demonstrated. Design of DC contact efficient MEMS switches and wideband designs are also being considered.					
14. SUBJECT TERMS Small antennas, Planar reconfigurable				15. NUMBER OF PAGES	
				16. PRICE CODE	
17. SECURITY CLASSIFICATION OR REPORT UNCLASSIFIED		18. SECURITY CLASSIFICATION ON THIS PAGE UNCLASSIFIED		19. SECURITY CLASSIFICATION OF ABSTRACT UNCLASSIFIED	
				20. LIMITATION OF ABSTRACT UL	

GENERAL INSTRUCTIONS FOR COMPLETING SF 298

The Report Documentation Page (RDP) is used for announcing and cataloging reports. It is important that this information be consistent with the rest of the report, particularly the cover and title page. Instructions for filling in each block of the form follow. It is important to ***stay within the lines*** to meet ***optical scanning requirements***.

Block 1. Agency Use Only (Leave blank)

Block 2. Report Date. Full publication date including day, month, and year, if available (e.g. 1 Jan 88). Must cite at least year.

Block 3. Type of Report and Dates Covered. State whether report is interim, final, etc. If applicable enter inclusive report dates (e.g. 10 Jun 87 - 30 Jun 88).

Block 4. Title and Subtitle. A title is taken from the part of the report that provides the most meaningful and complete information. When a report is prepared in more than one volume, repeat the primary title, and volume number, and include subtitle for the specific volume. On classified documents enter the title classification in parentheses.

Block 5. Funding Numbers. To include contract and grant numbers; may include program element number(s) project number(s), task number(s), and work unit number(s). Use the following labels:

C - Contract	PR - Project
G - Grant	TA - Task
PE - Program Element	WU - Work Unit Accession No.

Block 6. Author(s). Name(s) of person(s) responsible for writing the report, performing the research, or credited with the content of the report. If editor or compiler, this should follow the name(s).

Block 7. Performing Organization Name(s) and Address(es). Self-explanatory.

Block 8. Performing Organization Report Number. Enter the unique alphanumeric report number(s) assigned by the organization performing the report.

Block 9. Sponsoring/Monitoring Agency Name(s) and Address(es) Self-explanatory.

Block 10. Sponsoring/Monitoring Agency Report Number. (if known)

Block 11. Supplementary Notes. Enter information not included elsewhere such as; prepared in cooperation with...; Trans. of...; To be published in.... When a report is revised, include a statement whether the new report supersedes or supplements the older report.

Block 12a. Distribution/Availability Statement.

Denotes public availability or limitations. Cite any availability to the public. Enter additional limitations or special markings in all capitals (e.g. NORFORN, REL, ITAR).

DOD - See DoDD 4230.25, "Distribution Statements on Technical Documents."

DOE - See authorities.

NASA - See Handbook NHB 2200.2.

NTIS - Leave blank.

Block 12b. Distribution Code.

DOD - Leave Blank

DOE - Enter DOE distribution categories from the Standard Distribution for unclassified Scientific and Technical Reports

NASA - Leave Blank.

NTIS - Leave Blank.

Block 13. Abstract. Include a brief (*Maximum 200 words*) factual summary of the most significant information contained in the report.

Block 14. Subject Terms. Keywords or phrases identifying major subject in the report.

Block 15. Number of Pages. Enter the total number of pages.

Block 16. Price Code. Enter appropriate price code (NTIS *only*).

Block 17. - 19. Security Classifications. Self-explanatory. Enter U.S. Security Regulations (i.e., UNCLASSIFIED). If form contains classified information, stamp classification on the top and bottom of the page.

Block 20. Limitation of Abstract. This block must be completed to assign a limitation to the abstract. Enter either UL (Unlimited) or SAR (same as report). An entry in this block is necessary if the abstract is to be limited. If blank, the abstract is assumed to be unlimited.

**REPORT DOCUMENTATION PAGE (SF298)
(Continuation Sheet)**

Compact Reconfigurable HF-UHF Antenna

In this interim report the details of our progress during the last fiscal year is presented by providing the papers submitted for publications in archival journals and conferences and symposia. We submitted four journal papers and 4 conference papers, which have been presented or will be presented in the next few months. Two students are working on this project which are partially supported by the funds provided by this grant.

Journal Papers Submitted for Publications

1. R. Azadegan, K. Sarabandi, "High-Q double spiral miniaturized slot-line resonator filters," *IEEE Trans. Microwave Theory and Tech.* May. 2004, pp 1548-1557.
2. N. Behdad, and K. Sarabandi, "A Multi resonant Single-Element Wideband Slot Antenna", *IEEE Antennas and Wireless Propagation Letters*, Vol. 3, 2004, pp. 5-8.
3. R. Azadegan, K. Sarabandi, "Bandwidth enhancement of miniaturized slot antennas using folded, complementary and self-complementary realizations," submitted to *IEEE Trans. Antennas Propagat.* (Jan 04).
4. R. Azadegan, and K. Sarabandi, "A novel approach for miniaturization of slot antennas" *IEEE Trans. Antennas Propagat.*, March. 2003, pp 421-429.
5. K. Sarabandi and R. Azadegan, "Design of an efficient miniaturized UHF planar antenna," *IEEE Trans. Antennas Propagat.*, June. 2003, pp 1270-1276.
6. Peroulis, D., Pacheco, S. P., K. Sarabandi, and L. Katehi, "Electromechanical Considerations in Developing Low-Voltage RF MEMS Switches" *IEEE Trans. Microwave Theory and Techniques.*, Jan. 2003, pp 259-270.
7. Behdad, N., and K. Sarabandi, "Bandwidth Enhancement and Further Size Reduction of a Class of Miniaturized Slot Antennas", *IEEE Transactions on Antennas and Propagation*, vol. 52, no. 8, pp. 1928-1935, August 2004.
8. Peroulis, D., K. Sarabandi, and L. Katehi, "Design of Reconfigurable Slot Antennas", *IEEE Transactions on Antennas and Propagation*, to appear in Feb. 2005 issue
9. Peroulis, D., S. P. Pacheco, K. Sarabandi, L.P. Katehi, "Electromechanical Considerations in Developing Low-Voltage RF MEMS Switches", *IEEE Transactions on Microwave Theory and Techniques*, Vol. 51, No. 1, pp. 259-270, January 2003.

Conference Papers

1. N. Behdad and K. Sarabandi, "Miniaturized Slot Antennas with Enhanced Bandwidth," *Proc. IEEE Antennas Propagation & URSI Symp.* Columbus, OH, June 22-27, 2003.
2. N. Behdad and K. Sarabandi, "Slot antenna miniaturization using distributed inductive loading," *Proc. IEEE Antennas Propagation & URSI Symp.* Columbus, OH, June 22-27, 2003.
3. R. Azadegan, and K. Sarabandi, "A compact printed folded dipole antenna for wireless applications," *IEEE Antennas Propagat. Symp.* Columbus, OH., June 2003, vol. 1, pp.
4. R. Azadegan, and K. Sarabandi, "Miniaturized Slot-line and Folded-Slot Band-pass Filters", *IEEE International Microwave Symposium*, Philadelphia, PA, June 2003, vol. pp. 1595-1598.

5. Peroulis, D., K. Sarabandi, and L.P.B. Katehi, "Low Contact-resistance Series MEMS Switches", Proceeding: IEEE International Microwave Symposium, Seattle, WA, June 2-7, 2002.
6. Peroulis, S. P. Pacheco, K. Sarabandi, and L.P.B. Katehi, "Alleviating the Adverse Effects of Residual Stress in RF MEMS Switches", Proceeding: 31st European Microwave Conference 2001, London, U.K. September 24-28, 2001.
7. Peroulis, D., K. Sarabandi, and L.P.B. Katehi, "A Planar VHF Reconfigurable Slot Antenna", Proceeding: IEEE International Antennas and Propagation & URSI Symposium, Boston, MA, July 14-18, 2001.
8. Peroulis, D., S. Pacheco, K. Sarabandi, and L.P.B. Katehi, "Tunable Lumped Components with Applications to Reconfigurable MEMS Filters", Proceeding: IEEE Microwave Theory and Technical Symposium, Phoenix, Arizona, May 2001.
9. Peroulis, D., K. Sarabandi, L.P.B. Katehi, and B. Perlman, "Planar Reconfigurable Slot Antenna for Communications", SPIE's 8th Annual International Symposium on Smart Structures and Materials, Newport Beach, CA, March 2001.
10. Peroulis, D., S. Pacheco, K. Sarabandi, L.P.B. Katehi, "MEMS Devices for High Isolation Switching and Tunable Filtering", Proceeding: IEEE Microwave Theory and Technology Symposium(MMT-S), June 11-16, 2000, Boston, MA (Digest Vol. 2, pp. 1217-1220).
11. Peroulis, D., S. Pacheco, K. Sarabandi, L.P.B. Katehi, "MEMS Devices for High Isolation Switching and Tunable Filtering", Proceeding: IEEE Microwave Theory and Technology Symposium(MMT-S), June 11-16, 2000, Boston, MA (Digest Vol. 2, pp. 1217-1220).

Scientific Personal

R. Azadegan, N. Behdad, D. Peroulis.

Report of Invention

N.A

Scientific Progress and accomplishments

See attached papers

Technology Transfer

R. Azadegan and K. Sarabandi "Efficient Miniaturized Resonant Slot antennas" (patent pending)

D. Peroulis and K. Sarabandi, "Reconfigurable Slot Antennas for VHF/UHF Applications", Disclosure submitted to University of Michigan Intellectual Property Office, February 2002. File no. UM2269.

MASTER COPY: PLEASE KEEP THIS "MEMORANDUM OF TRANSMITTAL" BLANK FOR REPRODUCTION PURPOSES. WHEN REPORTS ARE GENERATED UNDER THE ARO SPONSORSHIP, FORWARD A COMPLETED COPY OF THIS FORM WITH EACH REPORT SHIPMENT TO THE ARO. THIS WILL ASSURE PROPER IDENTIFICATION. NOT TO BE USED FOR INTERIM PROGRESS REPORTS; SEE PAGE 2 FOR INTERIM PROGRESS REPORT INSTRUCTIONS.

MEMORANDUM OF TRANSMITTAL

U.S. Army Research Office
ATTN: AMSRL-RO-BI (TR)

P.O. Box 12211
Research Triangle Park, NC 27709-2211

- | | |
|--|--|
| <input type="checkbox"/> Reprint (Orig + 2 copies) | <input type="checkbox"/> Technical Report (Orig + 2 copies) |
| <input type="checkbox"/> Manuscript (1 copy) | <input type="checkbox"/> Final Progress Report (Orig + 2 copies) |
| | <input type="checkbox"/> Related Materials, Abstracts, Theses (1 copy) |

CONTRACT/GRANT NUMBER: DAAD19-99-1-0197

REPORT TITLE: Compact Reconfigurable HF-UHF Antenna

is forwarded for your information.

SUBMITTED FOR PUBLICATION TO (applicable only if report is manuscript):

Sincerely,
Kamal Sarabandi

Miniature High- Q Double-Spiral Slot-Line Resonator Filters

Reza Azadegan, *Student Member, IEEE*, and Kamal Sarabandi, *Fellow, IEEE*

Abstract—A new class of low insertion-loss miniaturized filters using slot-line resonators is proposed. Miniaturization is achieved by terminating the slot line with a double-spiral inductive termination at both ends. Using this miniaturized resonator, both positive and negative couplings may be realized, and therefore, both standard coupled-line and cross-coupled quasi-elliptic filters are realizable. The unloaded Q of these slot-line filters is considerably higher than that of miniaturized microstrip filters of comparable dimensions due to the inherent higher Q of the slot line. To demonstrate the validity of the design procedures and the performance characteristics, two different types of filters were fabricated and tested. One is a four-pole Chebyshev filter and the other is a quasi-elliptic filter where, in each case, the full-wave simulations show very good agreement with measurements.

Index Terms—Microstrip filters, microwave filters, miniaturized filters, quasi-elliptic filters, slot-line filters.

I. INTRODUCTION

MOBILE wireless systems of various kinds have been the driving force behind substantial research efforts toward miniaturizing RF front ends. High- Q low insertion-loss miniaturized filters are important requirements. A few approaches in the literature address filter miniaturization, among which are the use of lumped-element filters, high temperature superconducting (HTS) filters, bulk acoustic-wave (BAW) filters, and slow-wave distributed resonator filters [1]–[4].

Lumped-element filters can be made very small at lower frequencies. At higher frequencies, however, their extremely small size may result in high insertion loss and possibly low power-handling capacity. To cope with the insertion-loss problem, HTS filters have been proposed. BAW filters also have exceptionally small size and quite good performance, but may be extremely expensive to develop for any new application. These two classes of filters are not further considered in this paper, the subject of which is to introduce a new type of high- Q coiled slot-line resonator with comparison to the microstrip. On the other hand, conventional distributed element filters using coupled transmission-line resonators exhibit superior performance, but are frequently too large.

In order to reach a compromise between size and performance, some compact architectures have been proposed. The size reduction of ordinary microstrip line resonators, for

example, was made possible first by employing microstrip stepped-impedance resonators (SIRs) [5], [6] and then by using hairpin-line resonators [7]. A more compact hairpin filter using split-ring resonators with parallel coupled lines was later proposed [8]. This resonator is a capacitively end-loaded hairpin resonator where the loading is implemented by distributed coupled lines. The loaded hairpin resonator, together with the SIR, resulted in an improved hairpin resonator [9]. Incorporating dissimilar resonators in filter designs has also been reported [9].

Another form of resonator, which is similar to the above hairpin resonators, utilizes square open loops [10]. To further reduce size, the open-loop structure can be modified by introducing a narrow capacitive gap at the open end of the loop [11]. The same authors suggested an aperture coupled two-layer filter design using the same type of resonator [12]. Using the two sides of the substrate provides additional miniaturization. In both loaded open-loop and loaded hairpin resonators, electric and magnetic coupling can be implemented, which allows for the flexible design of many structures, such as quasi-elliptic filters.

Slot lines and coplanar waveguides (CPWs) are other important configurations for the realization of resonators and filters. In the early 1970s, slot transmission lines were shown to be a practical configuration for the realization of microwave filters and couplers [13], but more attention has been devoted to CPW filters [14]–[16]. Also known as uniplanar configurations, slot and CPWs are fundamental to many microwave and millimeter-wave integrated circuits [17], [18]. With regard to CPW filter miniaturization, the use of quarter-wave transmission-line resonators, e.g., a $\lambda/4$ CPW hairpin resonator [19], meandered superconducting CPW filters [20], double-surface CPW filters [21], and air-bridge capacitive loadings have been proposed. Additionally, the periodic loading of CPW lines has been suggested to construct a slow-wave transmission line and has been used in the fabrication of a miniature low-pass filter [22].

In contrast, the literature concerning the use of slot lines for filter design and filter miniaturization is rather sparse [23]. The Q of slot-line resonators is higher than that of microstrip resonators of similar dimensions due to the fact that the stored energy in the resonator is confined within a larger volume and that the electric current flows over a wider area, which translates into lower ohmic losses. Actually, slot lines are comparable to suspended substrate strip lines, which also have higher Q than microstrips due to the larger volume occupied by the stored energy.

In this paper, new filter architectures based on a miniaturized slot line with double-spiral inductive terminations are proposed.

Manuscript received December 1, 2003.

The authors are with the Radiation Laboratory, Department of Electrical Engineering and Computer Science, The University of Michigan at Ann Arbor, Ann Arbor, MI 48109-2122 USA (e-mail: azadegan@eecs.umich.edu; saraband@eecs.umich.edu).

Digital Object Identifier 10.1109/TMTT.2004.827044

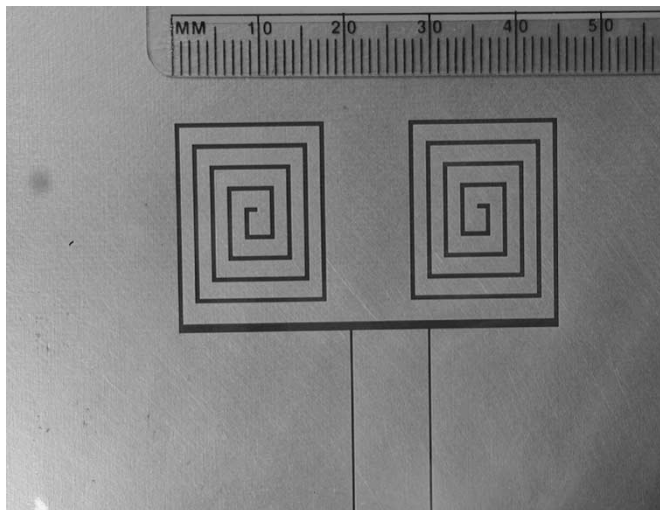


Fig. 1. Proposed miniaturized resonator capacitively coupled at 400 MHz with asymmetric end loadings.

Both electric and magnetic couplings are achievable by appropriate geometric layout of the miniaturized resonators, enabling quasi-elliptic filters to be designed.

II. MINIATURIZED SLOT-LINE RESONATOR TOPOLOGY

Recently, the authors proposed a highly efficient miniaturized slot antenna using a resonant slot-line geometry [24]. Comparing this slot antenna with its complementary printed strip counterpart shows a considerable increase in the antenna efficiency mainly due to lower ohmic losses [25]. Thus, miniaturized slot-line resonators may be expected to exhibit higher Q than their microstrip versions.

Fig. 1 shows the geometry of the miniaturized slot-line resonator with double-spiral inductive terminations. The very compact inductive end loading is realized by coiled shorted slot lines, each with a length smaller than a quarter-wavelength. This resonator exhibits a superior miniaturization factor and is capable of generating electric, magnetic, and mixed coupling mechanisms.

To assess the performance of the miniature slot-line resonators, a capacitively coupled miniaturized resonator, as shown in Fig. 1, was fabricated on a 0.787-mm-thick Duroid substrate with a dielectric constant of $\epsilon_r = 2.2$ and a loss tangent of $\tan \delta = 0.0009$.¹ The same substrate is used for the rest of the designs presented in this paper to give direct comparisons. A low-permittivity substrate was used to minimize the effects of dielectric loading on miniaturization. The resonator of Fig. 1 is designed to operate at 400 MHz and fits within a rectangular area with dimensions $0.06\lambda_0 \times 0.03\lambda_0$. The unloaded Q can be found using a single-port impedance/admittance measurement technique referred to as the critical-point method [26]. The unloaded Q of the miniaturized resonator at 400 MHz was measured to be $Q_0 \approx 210$, which compares favorably with the Q of miniaturized hairpin resonators [8], while being about an order of magnitude smaller in area.

TABLE I
EFFECT OF THE SLOT-TO-STRIP WIDTH (s/w) ON THE UNLOADED Q OF THE MINIATURIZED SLOT-LINE RESONATOR

s/w	0.2	0.33	0.5	1.0
f_0 [GHz]	2.29	2.37	2.45	2.605
Q_0	120	140	195	173

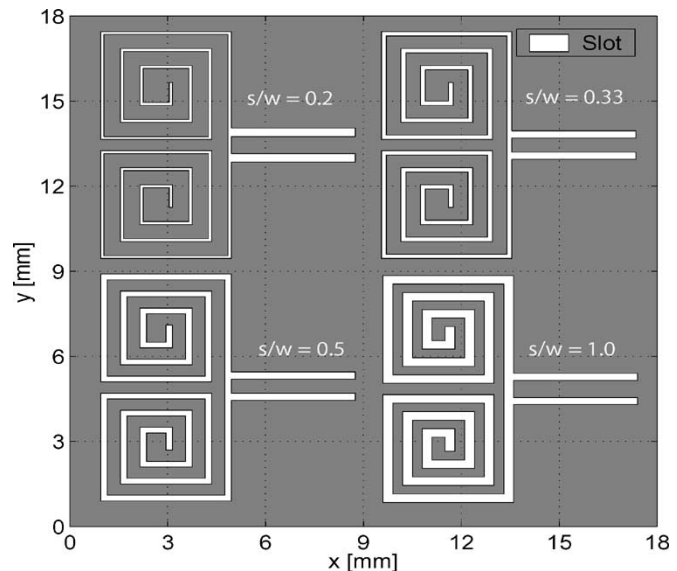


Fig. 2. Miniaturized slot-line resonator topology with different ratios of slot-to-strip width (s/w).

Using the relationship [1]

$$Q = Kb\sqrt{f} \quad (1)$$

where b is a linear dimension of the resonator, and K is a constant defined as a figure-of-merit, a better comparison can be made between miniature slot-line and microstrip resonators. For microstrip resonators, b is defined as the substrate thickness, while for the slot resonators, b represents the slot width. Invoking (1), the figure-of-merit constant K is found to be $K = 100$ for the miniaturized hairpin resonator [8], and $K = 330$ for the slot-line resonator of Fig. 1.

The ohmic loss of the CPW lines and slot lines is drastically affected by the width of the slot or, equivalently, the impedance of the line [13]. At resonance, the electric current distribution on the ground plane around the slot has a higher concentration near the edges. By making the slot wider, the peak of the current at the edges is reduced, and a smoother current distribution away from the slot edges is obtained. Lower current distribution at the edges translates into lower ohmic losses. In order to obtain the best Q_0 , for a given resonator, the width of the slot line may be optimized. Table I compares the unloaded Q of the proposed miniaturized resonator topology with a number of different slot-line widths (see Fig. 2). In this study, the overall size of the resonator is fixed while (s/w), i.e., the ratio of the slot width (s) to the adjacent metallic strip width (w), is varied as a parameter. For the proposed miniaturized double-spiral slot resonator, the width of the metallic strips should be approximately twice the width of the adjacent slots ($s/w = 0.5$). Fig. 3 shows an optimized miniaturized resonator at 2.45 GHz with approximately the same size as the previous resonator relative to the

¹RT/Duroid 5880, Adv. Circuit Mat. Div., Rogers Corporation, Chandler, AZ.

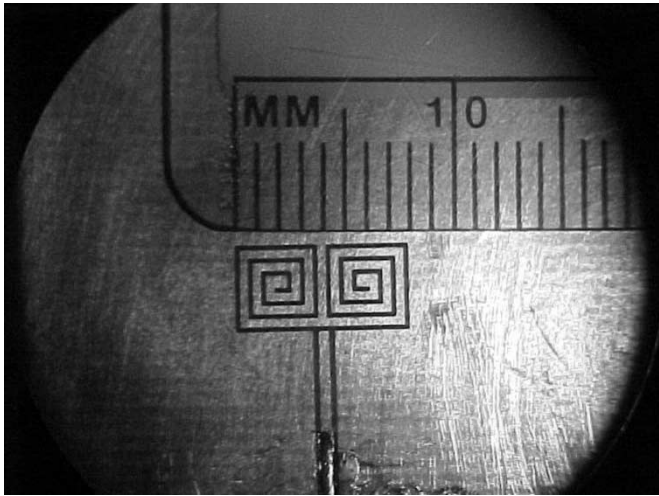


Fig. 3. Optimized miniature resonator at 2.45 GHz.

wavelength, namely, $0.03\lambda_0 \times 0.06\lambda_0$. The unloaded Q is found to be $Q_0 \approx 195$. A comparison of the Q_0 of this resonator with that of the scaled version of the resonator in Fig. 1 (shown in Table I with $s/w = 0.2$) exhibits a considerable improvement due to the effect of slot-line impedance on reducing the ohmic losses of the resonator. The figure-of-merit constant K for the optimized miniature resonator with ($s/w = 0.5$) at 2.4 GHz can be obtained from (1) as $K = 600$, which is four times higher than that of a half-wave microstrip resonator.

It is worth mentioning that (1) indicates that the Q of a given resonator increases as \sqrt{f} . However, there is a limitation on the maximum value of the linear dimension b , which is inversely proportional to frequency. Hence, if one compares resonators having the maximum possible values of b , one can define an available Q , which decreases by the square root of frequency.

To measure the radiation loss of the resonator, it was enclosed in a larger metallic cavity, and its Q was measured to be $Q'_0 = 265$. Therefore, the Q due to the radiation loss can be obtained from

$$\frac{1}{Q_{\text{rad}}} = \frac{1}{Q_0} - \frac{1}{Q'_0} \quad (2)$$

giving $Q_{\text{rad}} \approx 808$. This result indicates that the Q of the resonator is dominated by the ohmic and dielectric losses.

Here, only measurement has been used to identify the quality factor of the proposed resonators since a numerical estimate of Q for the miniaturized resonators does not provide very accurate results. For example, the finite-element method (FEM) would require enormous amounts of memory and extremely small cell sizes due to the very large ratio of fine and coarse features of the structure. On the other hand, full-wave methods based on integral equations [method of moments (MoM)] make use of the Green's function for multilayer structures of infinite extent. Hence, ground planes and substrates of finite size cannot be modeled efficiently. The equivalent magnetic-current method, however, provides a numerically efficient approach for the simulation of slotted structures. In this approach, the tangential electric field over the slot is replaced with an equivalent magnetic current, while the field is assumed to vanish over the ground plane. This assumption implies that the ground plane is a per-

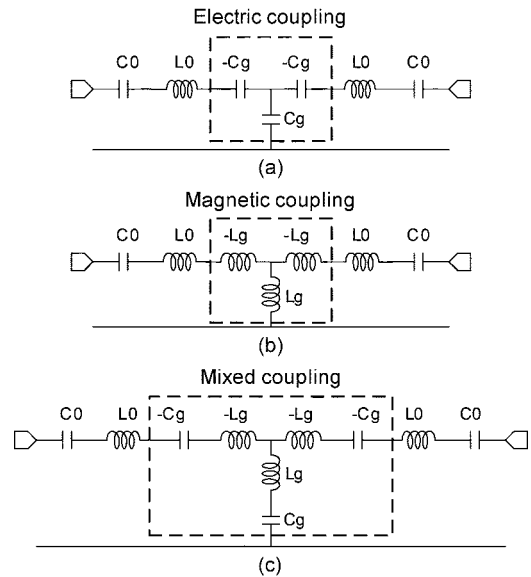


Fig. 4. Equivalent-circuit model of coupled miniaturized resonators exhibiting: (a) electric coupling, (b) magnetic coupling, and (c) mixed coupling.

fect conductor, and therefore, the ohmic loss cannot be modeled in this case. Obviously, the ground plane of the slot-line resonators under study is neither a perfect conductor, nor is it extended to infinity. Despite the aforementioned drawbacks of the integral-equation method, such as [27], it can predict the frequency response of the filters very accurately with the exception of the insertion loss.

III. DIRECT COUPLED FOUR-POLE FILTER

To demonstrate the versatility of the proposed miniaturized resonators to design different types of filters, we begin with the design of direct coupled bandpass filters.

A. Coupling Structures

For the case of capacitively coupled miniaturized slot resonators, the resonators have a series equivalent circuit model. Fig. 4 illustrates the equivalent circuit of two coupled miniaturized resonators exhibiting electric, magnetic, and mixed couplings, all realized by an impedance (K) inverter.

In order to realize the desired values for the coupling coefficients, there are differing coupling configurations. In each of these configurations, the coupling coefficients may be extracted using the pole-splitting method [10] in conjunction with full-wave simulations [27]. Given that f_u and f_l are the frequencies at which the S_{21} reaches its peak values, the coupling coefficients can be obtained from

$$k = \frac{f_u^2 - f_l^2}{f_u^2 + f_l^2}. \quad (3)$$

In the case of the pure electric or magnetic couplings whose appropriate circuit models are shown in Fig. 4(a) and (b)

$$k_e = \frac{C_0}{C_g} \quad (\text{electric coupling})$$

$$k_m = \frac{L_g}{L_0} \quad (\text{magnetic coupling}). \quad (4)$$

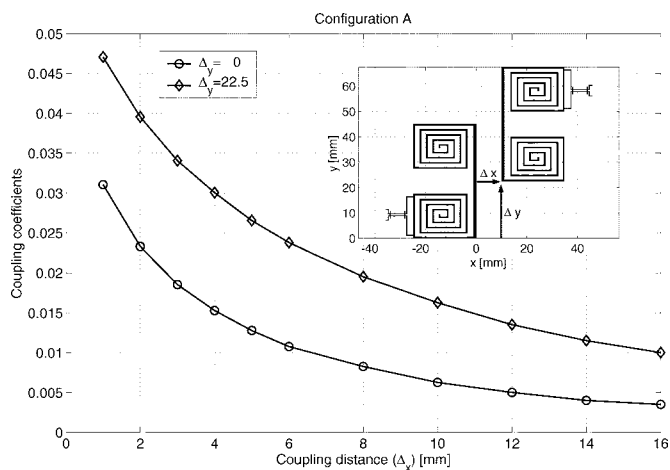


Fig. 5. Extracted coupling coefficients for a back-to-back coupling configuration A as a function of the horizontal separation Δx for two different values of vertical offsets Δy .

Note that, in the case of electric coupling, the capacitance to ground C_g of the impedance inverter is formed by the relatively wide ground-plane region of length Δx between the two resonators shown in Fig. 5. Since the inverter impedance is $K = 1/(\omega_0 C_g)$, a larger Δx gives a larger C_g , and the inverter impedance becomes smaller. Note that the coupling coefficient is proportional to K in the series representation [28], which is consistent with the looser coupling requirement as C_g and Δx increase. Also note that C_g relates only to the K inverter impedance and is unrelated to the mutual capacitance between the resonators.

Mixed coupling may also be represented by an impedance inverter, as shown in Fig. 4(c). Since usually $C_0 \ll C_g$ and $L_g \ll L_0$, the coupling coefficient for the mixed coupling can be simplified as

$$k_{em} = \frac{L_0 C_0 - L_g C_g}{L_g C_0 - L_0 C_g} \approx \frac{L_g}{L_0} - \frac{C_0}{C_g} = k_m - k_e. \quad (5)$$

Equation (5) indicates that, for mixed coupling, the electric and magnetic coupling are out-of-phase and tend to counteract each other. Examining the mixed coupling more closely, it becomes clear that, at the frequency of $\omega_n = 1/\sqrt{L_g C_g}$, the two resonators in Fig. 4(c) become decoupled, and a zero in the passband is introduced. For dominant electric coupling where $k_e > k_m$

$$\frac{1}{C_g \omega_0} > \omega_0 L_g \implies \omega_n > \omega_0 = \frac{1}{\sqrt{L_0 C_0}}. \quad (6)$$

Likewise, when the magnetic coupling is dominant, the zero appears below the passband, i.e., $\omega_n < \omega_0$.

In order to design the first Chebyshev sample design, two different coupling configurations are investigated. These configurations are identified according to the mutual orientation of the two resonators with respect to each other. The first coupling configuration, henceforth referred to as configuration A, is one in which the resonators are positioned back-to-back, as shown in Fig. 5. The coupling coefficient (k) is calculated from (3) and is plotted as a function of the horizontal distance between the resonators (Δx) for two different values of vertical

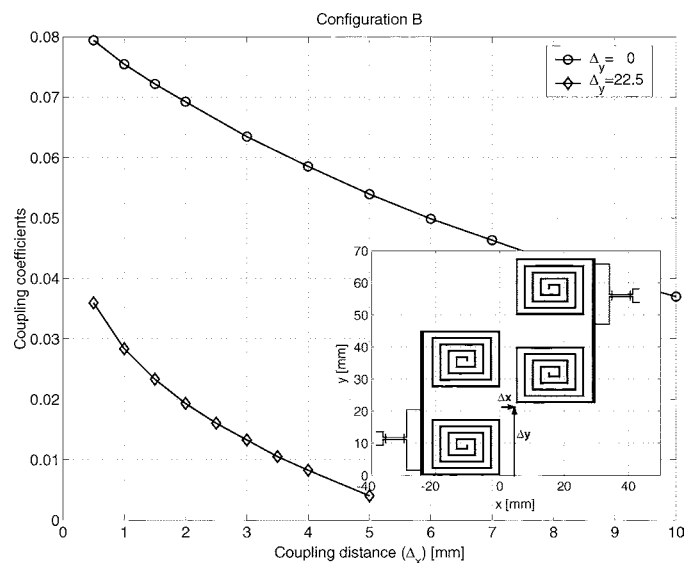


Fig. 6. Extracted coupling coefficients for configuration B (face-to-face arrangement) as a function of horizontal separation Δx for two different values of vertical offsets Δy .

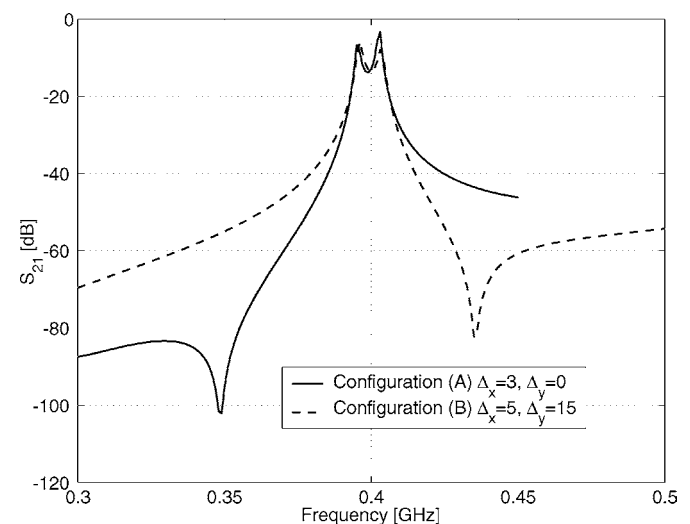


Fig. 7. Comparison between dominantly magnetic (configuration A) and dominantly electric (configuration B) for the same overall coupling coefficient. (Note the locations of zeros.)

offsets (Δy). Fig. 6 shows a face-to-face coupling arrangement and its calculated coupling coefficients, henceforth referred to as configuration B.

Since the proposed resonators are very compact and in close proximity to each other, the coupling mechanism is complex. The external coupling topology also has a significant effect on the nature of the couplings, and thus, each case should be studied separately. Fig. 7 shows the pole-splitting phenomenon in the S_{21} responses of the two coupling configurations. The coupling parameters for configuration A were set to $\Delta x = 3$ mm and $\Delta y = 0$, and for configuration B, to $\Delta x = 5$ mm and $\Delta y = 15$ mm so as to provide approximately the same coupling value. The S_{21} responses shown in Fig. 7 demonstrate that both structures are coupled through a mixed-coupling mechanism since there is a zero in the transmission. The locations of the zeros, however, are different. For configuration A, $\omega_n < \omega_0$, and thus,

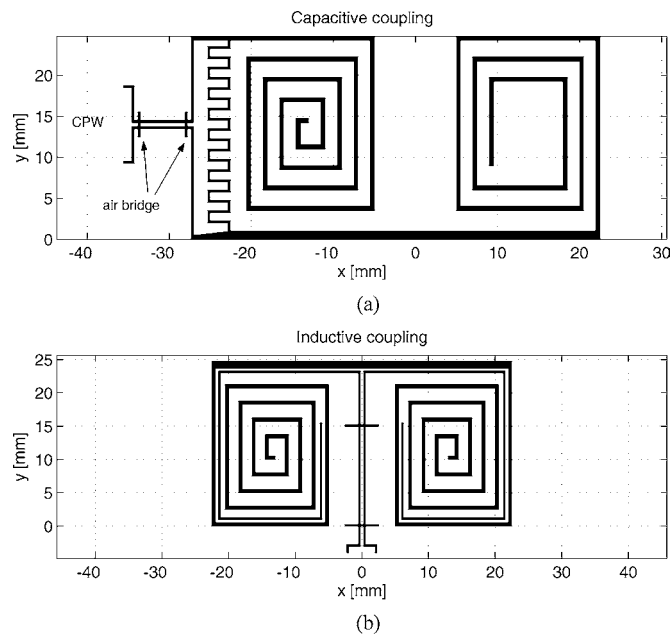


Fig. 8. Two different methods for external coupling. (a) Electric coupling. (b) Magnetic coupling.

magnetic coupling is dominant. For configuration B, $\omega_n > \omega_0$, indicating that the electric coupling is dominant.

Considering configuration A and recalling the fact that the electric-field distribution in a resonant slot line is maximum at the center, electric coupling is maximized when there is no vertical offset between the two resonators, namely, $\Delta y = 0$. However, it is interesting to note that although the electric coupling decreases as Δy increases, the overall coupling increases (see Fig. 5). This behavior indicates that magnetic coupling is dominant and electric coupling counteracts the effect of magnetic coupling in this configuration. This behavior is also consistent with the increasing trend of magnetic coupling as Δy is increased, noting that the electric current linkage (magnetic coupling) from the first resonator to the second one is increased by a factor proportional to Δy .

As for configuration B, shown in Fig. 6, two mechanisms give rise to electric coupling. One is the direct capacitance between the input and output, and the other arises from the electric coupling between the adjacent coiled slot arms. Both of these electric coupling components are inversely proportional to distance (Δx). Similarly, when Δy increases, these components are reduced. Conversely, the electric-current linkage (magnetic coupling) between the two resonators is increased. This argument confirms the fact that both types of couplings are present, and since the overall coupling decreases with an increase in Δy , the magnetic coupling is the one subtracted from the dominant electric coupling.

B. External Coupling

For the miniaturized slot-line resonator, both electric and magnetic external couplings can be realized. Fig. 8(a) and (b) illustrates input and output electric and magnetic couplings, respectively.

Electric coupling can be controlled by the value of the interdigital capacitor inserted between an input or output CPW

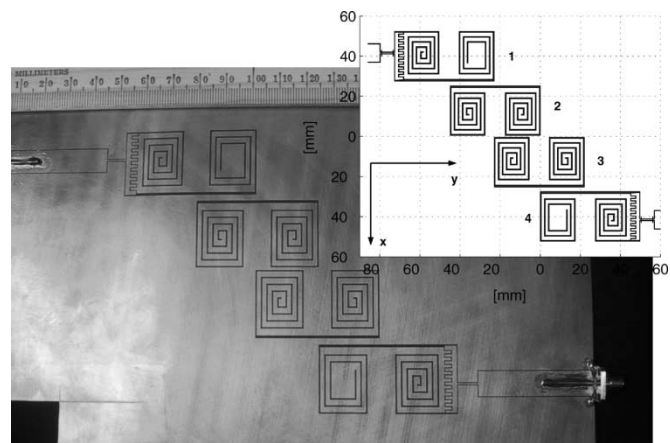


Fig. 9. Photograph and schematic of the miniaturized four-pole Chebyshev filter at 400 MHz.

line and the slot resonator. By changing the gap size and/or finger length of the interdigital capacitor, shown in Fig. 8(a), a wide range of electric external coupling values can be realized. However, note that when the finger length of the capacitor is increased, the resonant slot length is increased, and therefore, the resonant frequency of the structure shifts downward. To alleviate the frequency shift, the size of the resonator must be trimmed in a such a way as to maintain the resonance of the structure intact, which is why one of the inductive terminations in Fig. 8(a) is shorter. In the case of magnetic external coupling, depicted in Fig. 8(b), the length of the CPW coupled line extension controls the magnitude of the external coupling.

C. Examples

In order to demonstrate the performance of the proposed miniaturized filters, two examples are considered. In the first example, a four-pole Chebyshev filter with a fractional bandwidth of 5% and 0.25-dB ripple at 400 MHz is designed and shown in Fig. 9. The required coupling coefficients are $k_{12} = k_{34} = 0.0378$ and $k_{23} = 0.0310$, and the external coupling is $Q_{\text{ext}} = 27.565$ [28]. The prescribed coupling coefficients can be realized using the design curves of Figs. 5 and 6. For this design, a fixed vertical offset $\Delta y = 22.5$ mm was chosen in order to obtain a more realizable horizontal offset and also to ensure that nonadjacent resonators do not couple to each other. The horizontal offsets in the first example are found to be $\Delta x_{1,2} = \Delta x_{3,4} = 2.25$ mm and $\Delta x_{2,3} = 0.85$ mm. The area occupied by this filter is $0.22\lambda_0 \times 0.06\lambda_0 = 0.0132\lambda_0^2$. As illustrated in Fig. 10, the measured response of the filter accurately follows the numerical results obtained by a full wave MoM simulation [27].

A frequency shift of less than 0.5% occurs, which can be attributed to the finite size of the ground plane, noting that, in the MoM simulation, an infinite ground plane is assumed. The minimum measured insertion loss for this filter is approximately -1.7 dB, corresponding to a Q of 240. Note that the Q of a miniature microstrip filter of comparable dimensions is less than 70.

The next example considers an inductive mechanism for the external coupling of a four-pole Chebyshev bandpass filter with 3% bandwidth. For this example, an inline resonator design

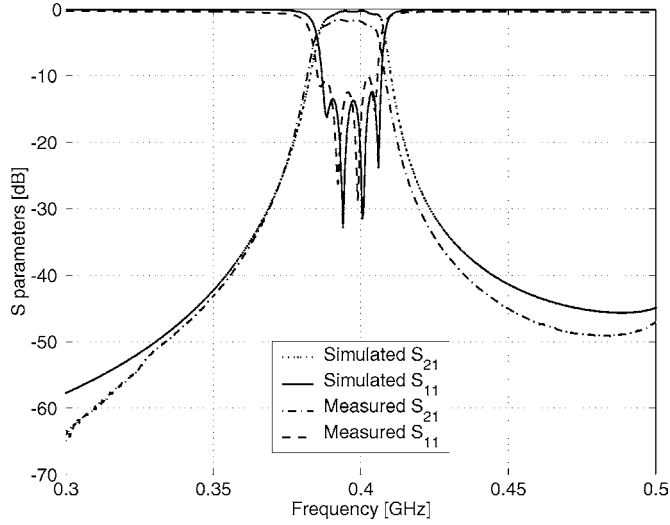


Fig. 10. Comparison between the simulated and measured S -parameters of the filter in Fig. 9.

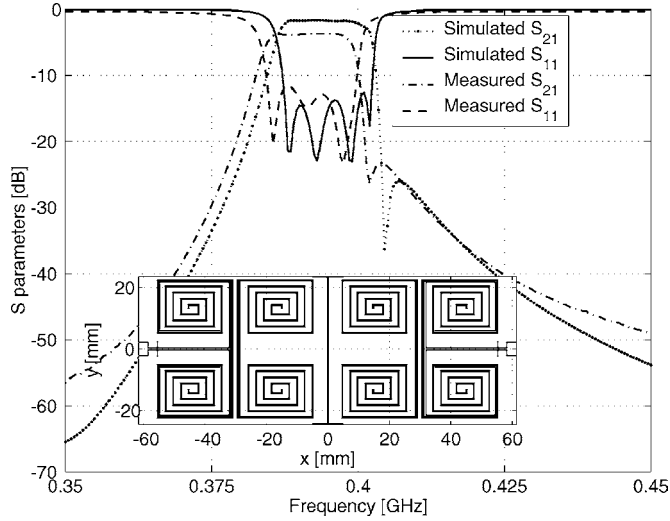


Fig. 11. Layout of a four-pole miniaturized filter with inline resonators at 400 MHz, as well as the comparison between its simulated and measured S -parameters.

($\Delta y = 0$) is used to further reduce the area occupied by the filter. In configuration B, electric coupling is dominant, which produces an excess coupling coefficient. If a short slot line is inserted between two face-to-face resonators, electric coupling can be reduced considerably, and therefore, a much smaller Δx is needed to achieve the prescribed coupling coefficient. Fig. 11 shows the designed filter in which configuration B is modified for further compactness.

The dimensions of this filter are $0.15\lambda_0 \times 0.06\lambda_0 = 0.009\lambda_0^2$. The comparison between the measured and simulated responses is illustrated in Fig. 11. In this example, an insertion loss of -3.7 dB is achieved, which corresponds to the Q of 220. Obviously, due to the modification to coupling configuration B, the zero associated with the mixed coupling now becomes closer to the passband ($\omega_n \rightarrow \omega_0$) and enhances the rejection in the upper band. This observed zero in the rejection band arises from a mechanism different from that of normal quasi-elliptical filters

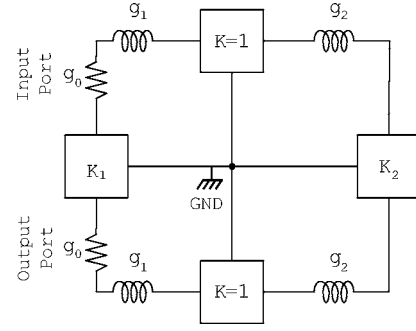


Fig. 12. Schematic of a low-pass prototype quasi-elliptic filter with series elements.

where the passband zeros are the results of the cancellation of multipath signals through different resonators.

IV. CROSS-COUPLED MINIATURE FILTERS

In the RF front end of many wireless devices, quasi-elliptic filters are commonly used because of their compactness and high selectivity. The enhanced out-of-band rejection of elliptic filters is due to the presence of zeros in the filter transfer function created by cross-couplings [29]–[31]. Here, the synthesis of a lumped-element low-pass prototype of a four-pole quasi-elliptic filter is demonstrated, and then, the required coupling coefficients and external couplings are extracted. Different coupling architectures appropriate for the proposed resonator and suitable for realizing the required coupling coefficients, including negative values, will be investigated. Following a procedure similar to the one used in Section III, a typical four-pole cross-coupled filter is designed, fabricated, and tested.

Fig. 12 shows a low-pass prototype for a four-pole cross-coupled filter with series elements. In the above, $g_0 = 1$ represents source and load normalized impedances, and the remaining four unknowns are found following a synthesis procedure outlined in [30].

For the following design example, a filter with a fractional bandwidth of $W = 5\%$ and passband ripple of 0.1 dB is considered. The transmission zero parameter is also set to $a = 2j$, which implies the occurrence of two transmission zeros at $\omega_n = \omega_0(1 \pm W)$. Thus, prototype elements in Fig. 12 are calculated to be $g_1 = 0.9526$, $g_2 = 1.3822$, $K_1 = -0.1629$, and $K_2 = 1.0615$. The corresponding coupling coefficients and external coupling can, therefore, be obtained as

$$\begin{aligned} k_{12} &= k_{34} = \frac{W}{\sqrt{g_1 g_2}} = 0.0436 \\ k_{23} &= K_2 \frac{W}{g_2} = 0.0384 \\ k_{14} &= K_1 \frac{W}{g_1} = -0.0085 \\ Q_{\text{ext}} &= \frac{g_1}{W} = 19.05. \end{aligned} \quad (7)$$

A few coupling configurations can be employed to realize the required coupling coefficients. Two such coupling structures, namely, configurations A and B, were discussed in Section III. Fig. 13 shows the coupling coefficients of configuration A, computed at 2.4 GHz, as a function of resonator separation Δx when

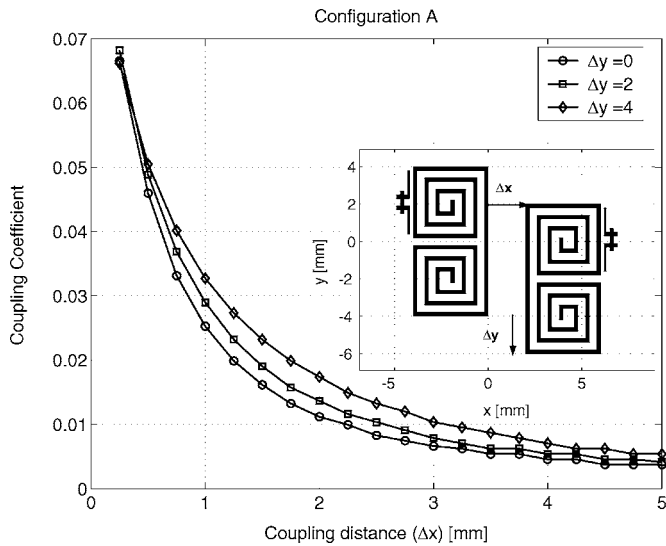


Fig. 13. Extracted coupling coefficients for configuration A as a function of resonator separation Δx for different values of vertical offsets Δy at 2.4 GHz.

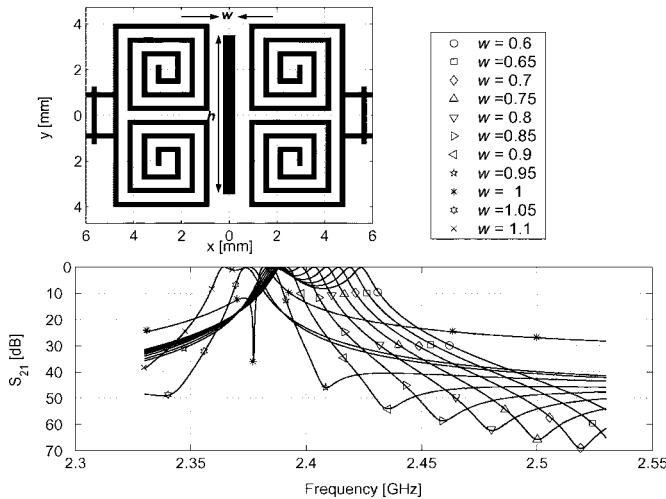


Fig. 14. Topology of the modified coupling configuration B and the effect of the width of slot incision (w) in the type and magnitude of coupling for the case of $h = 8$ mm.

the vertical offset denoted by Δy is varied as a parameter. The nature of this coupling is, again, a dominantly magnetic mixed coupling.

A variation of configuration B, in which a short slot line is incised between the two resonators, was used in the second example of Section III. In Fig. 7, it was shown that, in configuration B, electric coupling is dominant. To reduce the coupling coefficient without increasing the distance between the resonators, a slot incision is again introduced between the two resonators, as illustrated in Fig. 14. This figure also shows the pole splitting in the transfer function with the incision width w as a free parameter. In these simulations the length of the incision is $h = 8$ mm. As the width of the incision increases, the electric coupling between the resonators decreases, and therefore, the net coupling is reduced. In Fig. 14, when $w = 1$ mm, a null appears approximately at the center frequency $\omega_n \approx \omega_0$, which implies that the electric and magnetic coupling are equal and totally cancel each other. Also as the incision width is increased, the frequency at

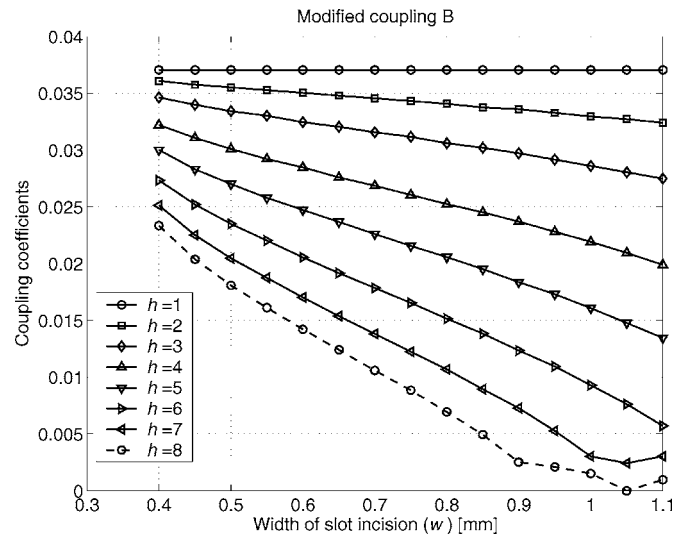


Fig. 15. Extracted coupling coefficients for the coupling configuration shown in Fig. 14 as a function of incision width and height (in millimeters) at 2.4 GHz.

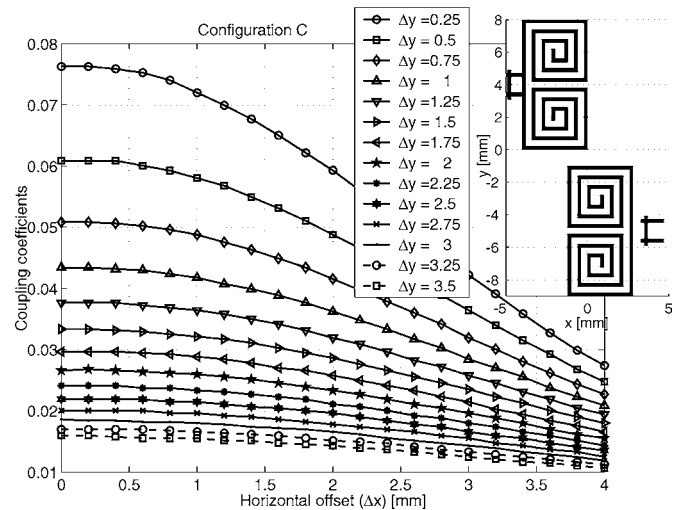


Fig. 16. Extracted coupling coefficients for coupling configuration C as a function of the horizontal offset between the resonators Δx for different values of vertical distances Δy at 2.4 GHz.

which the null occurs falls below the center frequency $\omega_n < \omega_0$. This indicates that the dominant coupling becomes magnetic for larger values of incision width. Fig. 15 illustrates the coupling coefficients of the structure shown in Fig. 14 versus the incision width (w) when the incision height is varied as a free parameter. This structure, which will be referred to as modified configuration B, provides rather small values for electric coupling (negative coupling) without sacrificing the compactness of the structure.

Finally, coupling coefficients for configuration C are shown in Fig. 16 as a function of the horizontal offset (Δx) with the vertical distance Δy used as a parameter. This configuration is similar to the two previous structures with the exception that the offset parameters are much larger. This structure exhibits a dominantly magnetic coupling. Defining dominantly magnetic coupling by convention as positive coupling, and electric coupling as negative coupling, all the coupling coefficients, as required by (7) to synthesize a quasi-elliptic filter, can be realized.

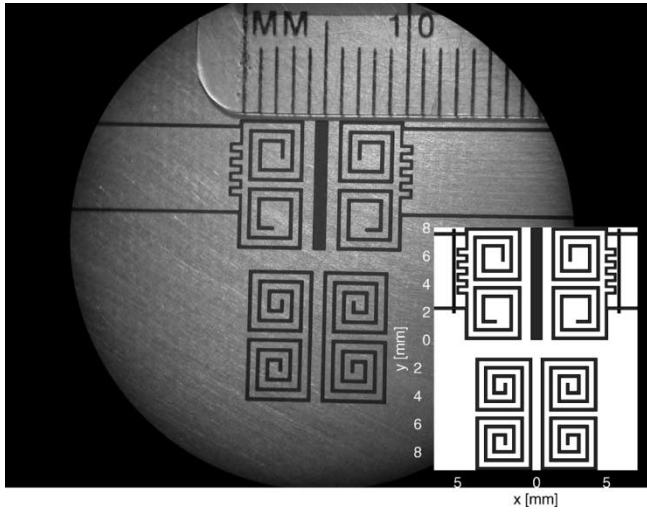


Fig. 17. Photograph and schematic layout of a miniaturized quasi-elliptic filter at 2.4 GHz with dimensions of $0.09\lambda_0 \times 0.14\lambda_0$.

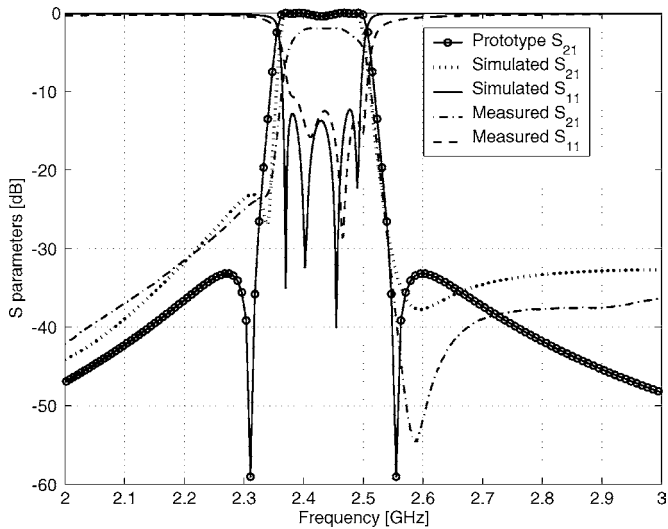


Fig. 18. Comparison between the lumped-element prototype, full-wave simulated, and measured S -parameters of the quasi-elliptic filter of Fig. 17.

Fig. 17 shows the layout and photograph of this filter. This four-pole filter occupies an area as small as $0.09\lambda_0 \times 0.14\lambda_0$, while having an insertion loss of approximately 2.0 dB corresponding to the Q of 180. The Q of a straight half-wave microstrip resonator is approximately 170, but becomes much smaller when coiled. The simulated and measured responses are illustrated in Fig. 18, where very good agreement between the measurement and full-wave simulation is observed.

The locations of transmission zeros in the measurement, however, are not as predicted using the lumped-element prototype of Fig. 12. The asymmetry observed in the location of the transmission zeros can be attributed to the frequency dependence of the coupling coefficients [12]. The impedance inverter models, used in the low-pass prototype, assume a frequency-independent coupling, whereas the electric and magnetic couplings are frequency dependent in nature. In quasi-elliptic filters where both types of electric and magnetic couplings with opposite frequency dependence are present, the location of transmission

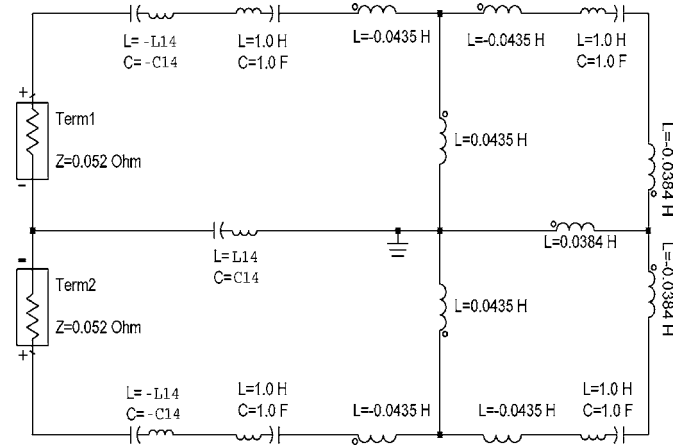


Fig. 19. Lumped-element prototype of a normalized quasi-elliptic bandpass filter in which the cross-coupling term k_{14} is realized by a mixed coupling where the difference between the two electric and magnetic coupling components is constant.

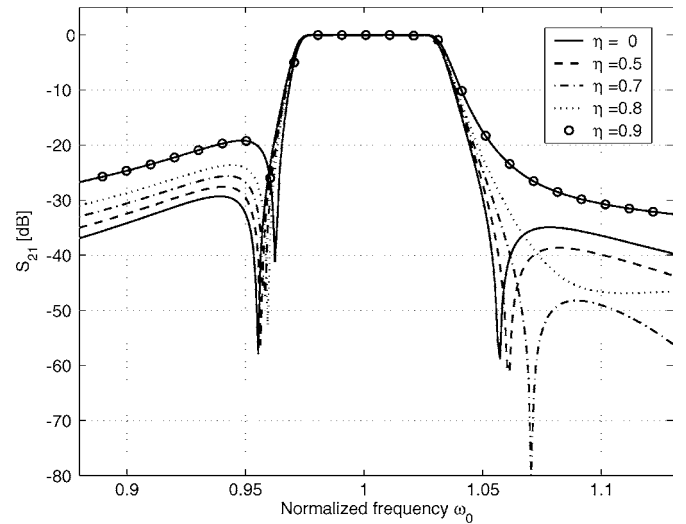


Fig. 20. Variation of the location of transmission zeroes of a normalized quasi-elliptic filter of Fig. 17 for different values of the ratio of the magnetic component to the electric component of the cross-coupling term $\eta = k_m/k_e$ given that $k_{14} = k_e - k_m$.

zeros can be shifted considerably. More importantly, in the proposed miniaturized design, the cross-coupling term, which controls the transmission zeros, is realized by subtracting two out-of-phase components of magnetic and electric couplings having different frequency dependence, resulting in an overall cross-coupling with a strong frequency dependence.

Fig. 19 shows the equivalent circuit of the normalized filter shown in Fig. 17, where the cross-coupling is realized by a dominantly electric mixed coupling. To ensure the proper value for the cross-coupling according to (7), the difference between the electric and magnetic has to be equal to k_{14} , i.e., $k_{14} = k_e - k_m = 1/C_{14}\omega_0 - L_{14}\omega_0$. Let $\eta = k_m/k_e < 1$ be the ratio of the magnetic component of the cross-coupling term to its electric component. Based on this definition, the value of the cross-coupling elements can be defined as $C_{14} = (1 - \eta)/k_{14}$ and $L_{14} = \eta k_{14}/(1 - \eta)$. Fig. 20 plots S_{21} of the equivalent circuit shown in Fig. 19 for different values of η , while keeping the net magnitude of the cross-coupling constant, namely, $k_{14} =$

0.0085. As seen in Fig. 20, the location of the transmission zero shifts when η is increased. The increase in η , while the overall cross-coupling term is fixed, indicates that a larger portion of the electric component of the cross-coupling is cancelled by an out-of-phase magnetic component. Obviously, the proper cancellation only takes place at the center frequency, but since the cross-coupling is frequency dependent, the coupling is more than required at frequencies above the passband and less below the passband. In order to alleviate the observed asymmetry in the location of transmission zeros and rejection band ripples, one might try to reduce η , which implies a smaller cancellation of the out-of-phase electric and magnetic couplings while maintaining the same value of k_{14} . As mentioned earlier, the required cross-coupling term needs to be rather small and can be realized by introducing a mixed electric–magnetic coupling in which the electric and magnetic couplings cancel each other out. To reduce the cancellation, and at the same time have the cross-coupling term remain intact, the absolute value of the electric coupling should be reduced using via-holes in the slot incision and/or increasing the vertical offset between the first and last resonators.

V. CONCLUSIONS

A new class of slot-line resonators for applications in miniaturized filter design have been demonstrated. The slot-line resonator offers flexibility of different coupling mechanisms, which facilitate various compact filter designs. It is shown that the resonators may be further miniaturized by increasing the value of inductive loading through increasing the number of turns in the coiled terminations with a moderate decrease in the resonator Q factor. The unloaded Q is higher than that of miniaturized microstrip filters of similar volume.

Both electric and magnetic couplings were demonstrated simply by positioning two such miniaturized resonators in different arrangements with respect to each other. A straightforward method was given to determine whether the coupling mechanism is magnetic or electric. A full-wave analysis was used to extract the coupling coefficients used in filter design.

To demonstrate the validity of the approach, three examples were studied including two four-pole Chebyshev filters, one of which used a mixed-coupling structure, and a four-pole quasi-elliptic filter. The agreement between the simulated and measured responses of these filters was shown to be excellent.

The prototype Chebyshev filters at 400 MHz with fractional bandwidths of 5% and 3% show insertion loss values of approximately 1.7 and 3.7 dB, while occupying a very small rectangular area $0.22\lambda_0 \times 0.06\lambda_0$ and $0.15\lambda_0 \times 0.06\lambda_0$, respectively. The unloaded Q of these filters is approximately three times greater than those of their microstrip counterparts.

A four-pole quasi-elliptic filter with $W = 5\%$ at 2.4 GHz was also fabricated, and its measured response was compared with numerical simulation. This filter with an improved out-of-band rejection gives 2-dB insertion loss while occupying a very small area of approximately $0.09\lambda_0 \times 0.14\lambda_0$. The effect of the frequency-dependent cross-coupling on the quasi-elliptic filter was also investigated.

ACKNOWLEDGMENT

The authors would like to thank Dr. R. Levy, R. Levy Associates, La Jolla, CA, for carefully reviewing this paper's manuscript and making very helpful suggestions.

REFERENCES

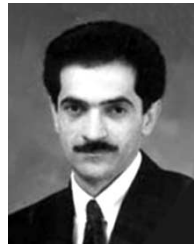
- [1] R. Levy, R. V. Snyder, and G. L. Matthaei, "Design of microwave filters," *IEEE Trans. Microwave Theory Tech.*, vol. 50, pp. 783–793, Mar. 2002.
- [2] R. R. Mansour, "Microwave superconductivity," *IEEE Trans. Microwave Theory Tech.*, vol. 50, pp. 750–759, Mar. 2002.
- [3] H. T. Su, F. Huang, and M. J. Lancaster, "Highly miniature HTS microwave filters," *IEEE Trans. Appl. Superconduct.*, vol. 11, pp. 349–352, Mar. 2001.
- [4] P. Bradley, R. Ruby, J. D. Larson, Y. Oshmyansky, and D. Figueredo, "A film bulk acoustic resonator (FBAR) duplexer for USPCS handset applications," in *Proc. IEEE MTT-S Int. Microwave Symp. Dig.*, vol. 1, May 2001, pp. 367–370.
- [5] A. Gopinath, A. F. Thomson, and I. M. Stephenson, "Equivalent circuit parameters of microstrip step change in width and cross junction," *IEEE Trans. Microwave Theory Tech.*, vol. MTT-24, pp. 142–144, Mar. 1976.
- [6] M. Makimoto and S. Yamashita, "Compact bandpass filters using stepped impedance resonators," *Proc. IEEE*, vol. 67, pp. 16–19, Jan. 1979.
- [7] E. G. Cristal and S. Frankel, "Hairpin-line and hybrid hairpin-line/half-wave parallel coupled-line filters," *IEEE Trans. Microwave Theory Tech.*, vol. MTT-20, pp. 719–728, Nov. 1972.
- [8] M. Sagawa, K. Takahashi, and M. Makimoto, "Miniaturized hairpin resonator filters and their application to receiver front-end MIC's," *IEEE Trans. Microwave Theory Tech.*, vol. 37, pp. 1991–1997, Dec. 1989.
- [9] S. Y. Lee and C. M. Tsai, "New cross-coupled filter design using improved hairpin resonators," *IEEE Trans. Microwave Theory Tech.*, vol. 48, pp. 2482–2490, Dec. 2000.
- [10] J.-S. Hong and M. J. Lancaster, "Couplings of microstrip square open-loop resonators for cross-coupled planar microwave filters," *IEEE Trans. Microwave Theory Tech.*, vol. 44, pp. 2099–2109, Dec. 1996.
- [11] —, "Theory and experiment of novel microstrip slow-wave open-loop resonator filters," *IEEE Trans. Microwave Theory Tech.*, vol. 45, pp. 2358–2365, Dec. 1997.
- [12] —, "Aperture-coupled microstrip open-loop resonators and their applications to the design of novel microstrip bandpass filters," *IEEE Trans. Microwave Theory Tech.*, vol. 47, pp. 1848–1855, Sept. 1999.
- [13] E. L. Mariani and J. P. Agrios, "Slot-line filters and couplers," *IEEE Trans. Microwave Theory Tech.*, vol. MTT-18, pp. 1089–1095, Dec. 1970.
- [14] K. C. Gupta, P. Garg, I. Bahl, and P. Bhartia, *Microstrip Lines and Slot-lines*, 2nd ed. Norwood, MA: Artech House, 1996.
- [15] D. F. Williams and S. E. Schwarz, "Design and performance of coplanar waveguide bandpass filters," *IEEE Trans. Microwave Theory Tech.*, vol. MTT-31, pp. 558–566, July 1983.
- [16] J. K. A. Everard and K. K. M. Cheng, "High-performance direct coupled bandpass filter on coplanar waveguide," *IEEE Trans. Microwave Theory Tech.*, vol. 41, pp. 1568–1573, Sept. 1993.
- [17] M. Muraguchi, T. Hirota, A. Minakawa, K. Ohwada, and T. Sugeta, "Uniplanar MMIC's and their applications," *IEEE Trans. Microwave Theory Tech.*, vol. 36, pp. 1896–1901, Dec. 1988.
- [18] T. Hirota, Y. Tarusawa, and H. Ogawa, "Uniplanar MMIC hybrids: A proposed new MMIC structure," *IEEE Trans. Microwave Theory Tech.*, vol. MTT-35, pp. 576–581, June 1987.
- [19] T. Tsujiguchi, H. Matsumoto, and T. Nishikawa, "A miniaturized end-coupled bandpass filter using $\lambda/4$ hair-pin coplanar resonators," in *IEEE MTT-S Int. Microwave Symp. Dig.*, Baltimore, MD, June 1998, pp. 829–832.
- [20] K. Yoshida, K. Sashiyama, S. Nishioka, H. Shimakage, and Z. Wang, "Design and performance of miniaturized superconducting coplanar waveguide filters," *IEEE Trans. Appl. Superconduct.*, vol. 9, pp. 3905–3908, June 1999.
- [21] T. Tsujiguchi, H. Matsumoto, and T. Nishikawa, "A miniaturized double-surface CPW bandpass filter improved spurious response," *IEEE Trans. Microwave Theory Tech.*, vol. 49, pp. 879–885, May 2001.
- [22] J. Sor, Y. Qian, and T. Itoh, "Miniature low-loss CPW periodic structures for filter applications," *IEEE Trans. Microwave Theory Tech.*, vol. 49, pp. 2336–2341, Dec. 2001.

- [23] R. Azadegan and K. Sarabandi, "Miniaturized slot-line and folded-slot bandpass filters," in *IEEE MTT-S Int. Microwave Symp. Dig.*, Philadelphia, PA, June 2003, pp. 1595–1598.
- [24] —, "A novel approach for miniaturization of slot antennas," *IEEE Trans. Antennas Propagat.*, vol. 51, pp. 421–429, Mar. 2003.
- [25] —, "A compact planar folded-dipole antenna for wireless applications," in *Proc. IEEE AP-S Int. Symp.*, vol. 1, Columbus, OH, June 2003, pp. 439–442.
- [26] E. Yuan and S. H. Chao, "Unloaded Q measurement: The critical-point method," *IEEE Trans. Microwave Theory Tech.*, vol. 43, pp. 1983–1986, Aug. 1995.
- [27] *IE3D Electromagnetic Simulation and Optimization Package*, 9.0 ed., Zeland Software Inc., Fremont, CA, 2-2.
- [28] G. L. Matthaei, L. Young, and E. M. T. Jones, *Microwave Filters, Impedance-Matching Networks and Coupling Structures*. New York: McGraw-Hill, 1964.
- [29] A. E. Atia and A. E. Williams, "Narrow-bandpass waveguide filters," *IEEE Trans. Microwave Theory Tech.*, vol. MTT-20, pp. 258–265, Apr. 1972.
- [30] R. Levy, "Filters with single transmission zeroes at real or imaginary frequencies," *IEEE Trans. Microwave Theory Tech.*, vol. MTT-24, pp. 172–181, Apr. 1976.
- [31] K. T. Jokella, "Narrow-band stripline or microstrip filters with transmission zeroes at real and imaginary frequencies," *IEEE Trans. Microwave Theory Tech.*, vol. MTT-28, pp. 542–547, June 1980.



Reza Azadegan (S'98) was born in Tehran, Iran, in 1974. He received the B.S. degree from the Sharif University of Technology, Tehran, Iran, in 1996, the M.S. degree from the K. N. Toosi University of Technology, Tehran, Iran, in 1996, both in electrical engineering, and is currently working toward the Ph.D. degree in electrical engineering from The University of Michigan at Ann Arbor.

From 1997 to 1999, he was a Research Engineer with The Computational Electromagnetic Laboratory, Sharif University of Technology, where he was involved with the optimal design of reflector antennas using high-frequency techniques and genetic algorithms. He was also involved with the numerical modeling of the electromagnetic-wave propagation in optical waveguides. In Fall 1999, he joined The Radiation Laboratory, The University of Michigan at Ann Arbor. His research interests include design and miniaturization of planar antennas and microwave filters for wireless communication systems and microsensors.



Kamal Sarabandi (S'87–M'90–SM'92–F'00) received the B.S. degree in electrical engineering from the Sharif University of Technology, Tehran, Iran, in 1980, and the M.S.E. and Ph.D. degrees from The University of Michigan at Ann Arbor, in 1986 and 1989, respectively, both in electrical engineering.

He is currently the Director of the Radiation Laboratory and a Professor with the Department of Electrical Engineering and Computer Science, The University of Michigan at Ann Arbor. His research areas of interest include microwave and millimeter-wave radar remote sensing, electromagnetic-wave propagation, and antenna miniaturization. He possesses 20 years of experience with wave propagation in random media, communication channel modeling, microwave sensors, and radar systems and is leading a large research group including two research scientists, ten Ph.D. and two M.S. students. Over the past ten years, he has generated 14 Ph.D. students. He was the Principal Investigator of many projects sponsored by the National Aeronautics and Space Administration (NASA), Jet Propulsion Laboratory (JPL), Army Research Office (ARO), Office of Naval Research (ONR), Army Research Laboratory (ARL), National Science Foundation (NSF), Defense Advanced Research Projects Agency (DARPA), and numerous industries. He has authored numerous book chapters and over 95 papers appearing in refereed journals on electromagnetic scattering, random media modeling, wave propagation, antennas, microwave-measurement techniques, radar calibration, inverse-scattering problems, and microwave sensors. He has also authored or coauthored over 200 papers and invited presentations in many national and international conferences and symposia on similar subjects. He is listed in *Who's Who in American Men and Women of Science*, *Who's Who in America*, and *Who's Who in Electromagnetics*.

Dr. Sarabandi is a vice president of the IEEE Geoscience and Remote Sensing Society (GRSS), chairman of the Awards Committee of the IEEE GRSS, and a member of the IEEE Technical Activities Board Awards Committee. He is the associate editor of the IEEE TRANSACTIONS ON ANTENNAS AND PROPAGATION and the IEEE SENSORS JOURNAL. He is also a member of Commission F of URSI and The Electromagnetic Academy. He was the recipient of the Henry Russel Award from the Regent of The University of Michigan (the highest honor the University of Michigan bestows on a faculty member at the assistant or associate level), the 1999 GAAC Distinguished Lecturer Award presented by the German Federal Ministry for Education, Science, and Technology, which is given to approximately ten individuals worldwide in all areas of engineering, science, medicine, and law, and a 1996 Teaching Excellence Award presented by the Electrical Engineering and Computer Science Department, The University of Michigan at Ann Arbor. Over the past several years, joint papers presented by his students at a number of symposia [IEEE Antennas and Propagation Society (IEEE AP-S) Symposia (1995, 1997, 2000, and 2001); the IEEE International Geoscience and Remote Sensing Symposium (1999); and the IEEE Microwave Theory and Techniques Society (IEEE MTT-S) International Microwave Symposium (IMS) (2001)] have been the recipients of Student Prize Paper Awards.

A Multiresonant Single-Element Wideband Slot Antenna

Nader Behdad, *Student Member, IEEE* and Kamal Sarabandi, *Fellow, IEEE*

Abstract—A new technique for designing wideband slot antennas is proposed. In this technique, the aperture's electric field distribution is manipulated to create two fictitious short circuits along the slot, hence creating two additional resonances besides the main one. The frequencies of these fictitious resonances can be chosen such that the overall bandwidth of the antenna is drastically increased. By using this technique, a slot antenna with a 1.8 : 1 bandwidth ratio is designed and fabricated. The measured results of this antenna show similar radiation patterns at different frequencies in its band of operation. Furthermore, the antenna has a relatively constant gain and more importantly, it has an excellent polarization purity over the entire bandwidth.

Index Terms—Broadband antennas, printed antennas, slot antennas.

I. INTRODUCTION

CURRENT advancements in printed antenna technology have resulted in a variety of different techniques for designing low profile, cost effective, and highly efficient wideband antennas. Most of these techniques, deal with marginal bandwidth improvement of more traditional antennas such as patch or printed wire antennas [1]. Another class of antennas that are suitable for miniaturization and have great reconfigurability potentials without compromising efficiency are slot antennas. However, not much attention has been paid to improving the bandwidth of this class of printed antennas. In this letter, we present a new technique for increasing the number of resonances and, hence, the bandwidth of a slot antenna by creating multiple fictitious short circuits along the slot.

Microstrip-fed wide slot antennas have been theoretically studied in [2]. Also, experimental investigations on very wide slot antennas are reported by various authors [3]–[5]. The drawback of these antennas are twofold: 1) they require a large area for the slot and a much larger area for the conductor ground plane around the slot and 2) they usually generate high cross-polarization levels that change with frequency [3]–[5]. This is mainly because these antennas can support two orthogonal modes with close resonant frequencies. The undesirable excitation of the orthogonal mode can easily occur and result in the generation of strong cross-polarized radiation. Therefore, it is important to limit the maximum width of the slot antennas

under investigation. It has recently been shown that a relatively wide slot antenna, fed with a narrow microstrip line, can be designed to show dual-resonance behavior with similar electric field (magnetic current) distributions at both resonant frequencies [6]. This similarity is critical since it results in similar radiation patterns and preservation of the desired polarization at different frequencies over the entire bandwidth of the antenna. The frequencies of the two resonances can be controlled in the design process such that the antenna acts as either a dual band or a broadband radiator [6]. In this letter, we will use the same concept and modify the microstrip feed to create two fictitious short circuits along the slot with close enough frequencies to obtain a much wider bandwidth. By using this technique, a single-element slot antenna with a bandwidth as high as 1.8 : 1 is designed and fabricated. This antenna shows similar radiation patterns with very low levels of cross-polarized radiation over the entire bandwidth. In what follows, first the design procedure is studied and then the measured results are presented and discussed.

II. DESIGN PROCEDURE

A relatively wide slot antenna, fed with a narrow microstrip line near an edge, can be designed to show a dual-resonance behavior, which can be exploited to obtain a wideband response [6]. When a relatively wide slot antenna is fed with a narrow microstrip line, the electric field generated by that part of the microstrip line over the slot (which does not have a ground plane), cancels the slot electric field, generated by the return current of the microstrip-line in the ground plane, at a certain location near the feed. This creates a fictitious short circuit along the slot near the microstrip feed and, hence, generates a fictitious resonance with a frequency, which is slightly higher than that of the main resonance [6]. The next challenging step is to examine whether it is possible to create more than one fictitious short using a similar approach or not. If this is possible, the bandwidth of the antenna can drastically be increased by merging these fictitious resonances. In order to test the validity of this idea, we begin by attempting to place two fictitious short circuits along the slot, using a two-prong microstrip feed. It is expected that this structure could present three distinct resonances at frequencies proportional to the resonant lengths L_{r1} , L_{r2} , and L_{r3} as shown in Fig. 1. If the locations of the two feed lines are chosen properly, the three resonant frequencies will be close and the overall bandwidth of the antenna can be increased significantly by using an appropriate feeding network. The location of the microstrip feeds, L_{s1} and L_{s2} in Fig. 2, determines L_{r2} and L_{r3} and, hence, the resonant frequencies of the two fictitious resonances.

Manuscript received December 8, 2003; revised December 10, 2003. This work was supported in part by the Engineering Research Centers Program of the National Science Foundation under NSF Award EEC-9986866 and by the U.S. Army Research Office under Contract DAA-99-1-01971.

The authors are with the Radiation Laboratory, Department of Electrical Engineering and Computer Science, University of Michigan, Ann Arbor, MI 48109-2122 USA (e-mail: behdad@engin.umich.edu).

Digital Object Identifier 10.1109/LAWP.2004.825093

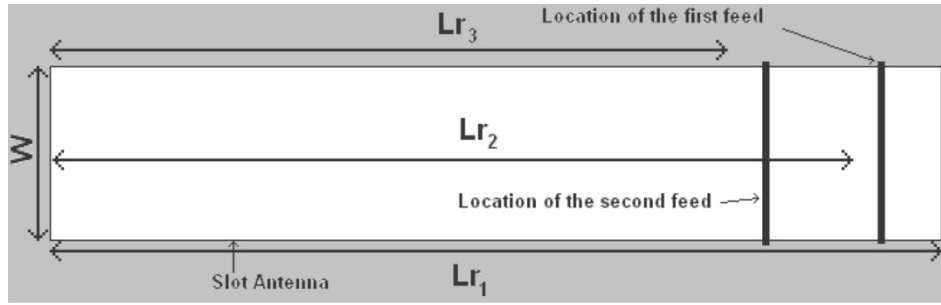


Fig. 1. Schematic of the relatively wide slot antenna and its equivalent resonant lengths.

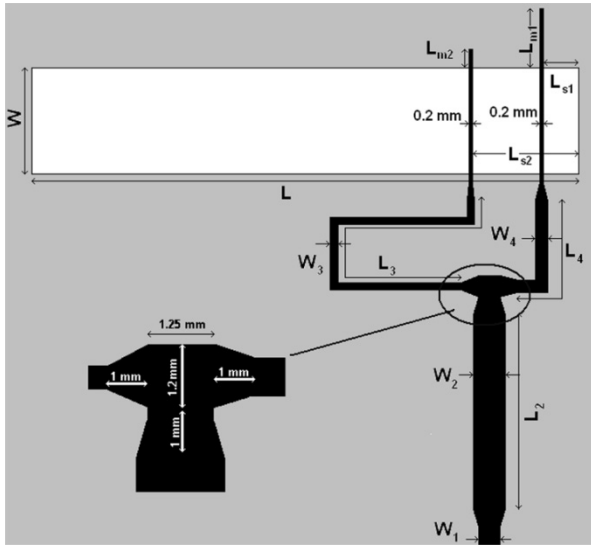


Fig. 2. Schematic of the broadband slot antenna and its microstrip feed network.

The feed topology chosen for this antenna (Fig. 2) can be viewed as a three-port microstrip network that achieves power division using a microstrip-Tee. In order to obtain a broadband response, matching is performed by choosing the feed network parameters, L_2 , W_2 , L_3 , W_3 , L_4 , W_4 , L_{s1} , L_{s2} , L_{m1} , and L_{m2} (shown in Fig. 2) appropriately. These parameters must be chosen such that the overall impedance bandwidth of the antenna is maximized. In order to obtain the optimum values of these parameters, a combined full-wave and network simulation technique is used. First, the antenna structure and its narrow microstrip feed lines (Fig. 1) are simulated as a four port network using a full-wave electromagnetic (EM) simulation tool [8]. Then the S-parameters of this four-port network are used in a network simulation and optimization software [9] from which the optimized values of the feed-network parameters are obtained. This technique allows for rapid optimization of the network parameters, but it ignores the coupling effects that exist between different components of the feed network. Therefore, a final full-wave simulation of the structure is performed and the different feed parameters are fine tuned to obtain a good response. The final schematic of the antenna is shown in Fig. 2, and the optimized dimensions of the antenna are given in Table I.

TABLE I
A SUMMARY OF THE PHYSICAL DIMENSIONS OF THE BROADBAND SINGLE-ELEMENT SLOT ANTENNA. ALL DIMENSIONS ARE IN MILLIMETERS

Parameter	L	W	L_2	W_2	L_3	W_3
Value	31	6	11	1.8	19.73	0.43
Parameter	l_4	W_4	l_{s1}	l_{s2}	L_{m1}	L_{m2}
Value	6.2	0.72	2	6	3.3	1

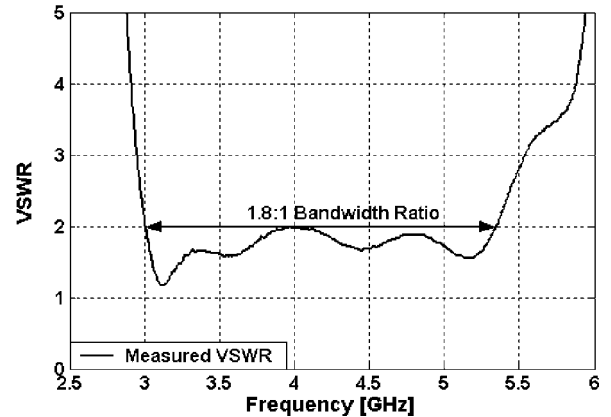


Fig. 3. Measured VSWR of the broadband slot antenna.

III. MEASUREMENT RESULTS AND DISCUSSION

The proposed antenna is fabricated on a 500- μm -thick RO4350B substrate with a dielectric constant of $\epsilon_r = 3.4$ and $\tan \delta$ of 0.003 with a ground plane size of 11.5 cm \times 10 cm. The voltage standing wave ratio (VSWR) of the antenna is measured using a calibrated vector network analyzer and is shown in Fig. 3. It is shown that the VSWR of the antenna remains below 2 over a bandwidth range of 3 to 5.4 GHz. This corresponds to a 1.8:1 impedance bandwidth ratio. However, in order to determine the overall bandwidth of the antenna, other radiation parameters such as radiation patterns, gain, and antenna polarization must also be carefully examined over the entire frequency band. The radiation patterns of the antenna are measured at five different frequencies in the anechoic chamber of the University of Michigan. For brevity, the patterns at only three frequencies are given in Fig. 4. It is observed that the radiation patterns at different frequencies are similar, which is expected from a wideband antenna. More importantly, the cross-polarization levels are very small for all the measured

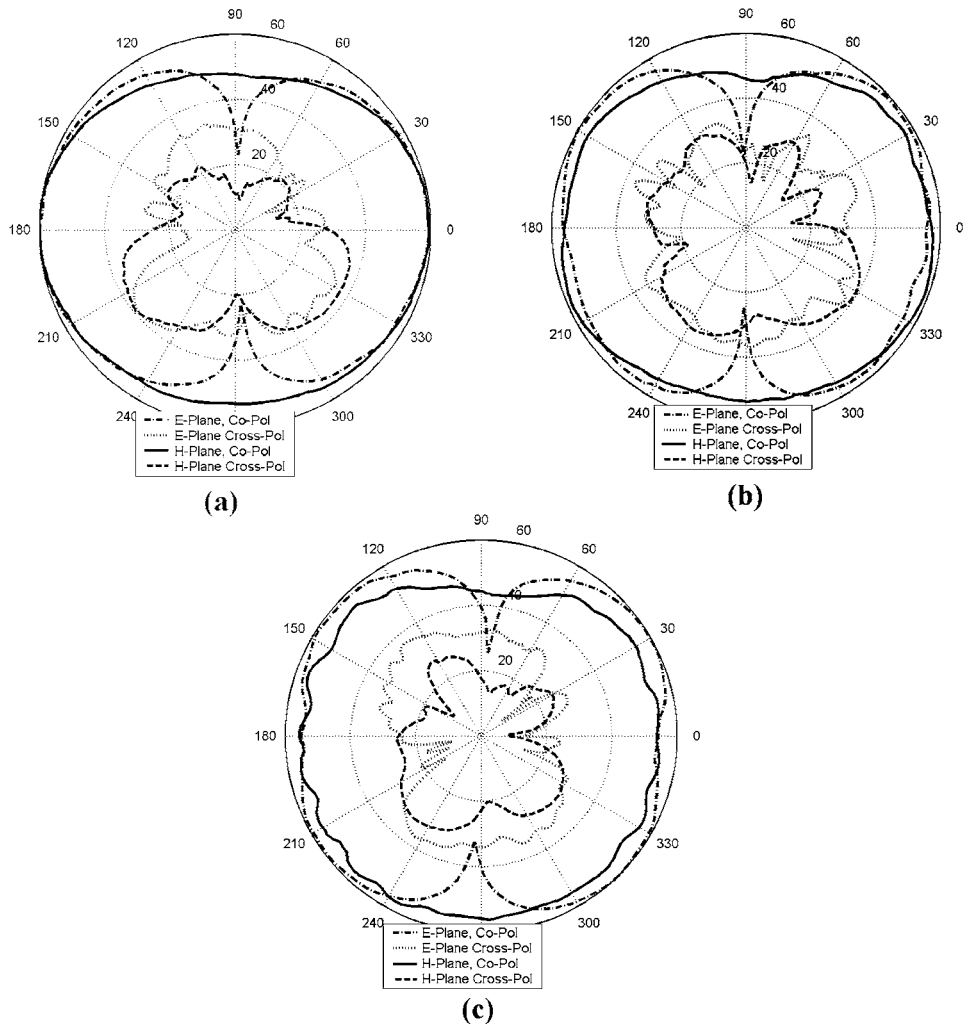


Fig. 4. Radiation patterns of the broadband slot antenna, measured at (a) $f = 3$ GHz, (b) $f = 4$ GHz, and (c) $f = 5$ GHz.

patterns. Specifically, a Co-Pol/Cross-Pol ratio of better than 30 dB is observed at boresight in all of the measured radiation patterns. The cross-polarization levels at other directions are also very small, indicating excellent polarization purity.

As can be observed from Fig. 4, the patterns of the antenna are not the dual of those of an electric dipole. The first difference is that the patterns in the E -plane (unlike the H -plane of an electric dipole) show two nulls at $\pm 90^\circ$, which are caused by two different mechanisms. The first mechanism is the cancellation that occurs at grazing angle as a result of the phase difference between E -fields on the top and bottom of the ground plane. This phase difference does not exist in the H -plane. Furthermore, the H -plane radiation pattern should inherently show two nulls at $\pm 90^\circ$ as a result of the boundary condition that forces the tangential component of the electric field to go to zero. The second reason for having these nulls is that the slot antenna is covered with a dielectric substrate at one side. This forces the normal component of the electric field at grazing angles to go to zero as described in [7]. Another difference is the minima (instead of nulls) in the H -plane which is a direct result of the radiation from the edges of the ground plane. The antenna gain is measured in the anechoic chamber using a standard double ridge horn and is presented

in Fig. 5. It is seen that the gain of the antenna remains relatively constant over the entire bandwidth. Based on the measured VSWR, radiation patterns, polarization purity, and gain of the antenna, the overall bandwidth is determined to be the same as its impedance bandwidth (1.8:1). Preserving the radiation patterns and excellent polarization purity are extremely important factors in designing wideband antennas. Since many of the existing wideband, single-element, printed antennas achieve wideband operation from different radiation mechanisms and field distributions at different frequencies, they cannot easily achieve these two important factors. This letter presents a very simple way of designing a wideband printed antenna with excellent radiation parameters over the entire bandwidth.

IV. CONCLUSION

A new and simple technique for designing wideband slot antennas is presented. This technique is based on creating a number of fictitious resonances along the slot with close frequencies and using them to obtain a wideband overall response with similar radiation patterns and polarization over the entire bandwidth of the antenna. This is accomplished

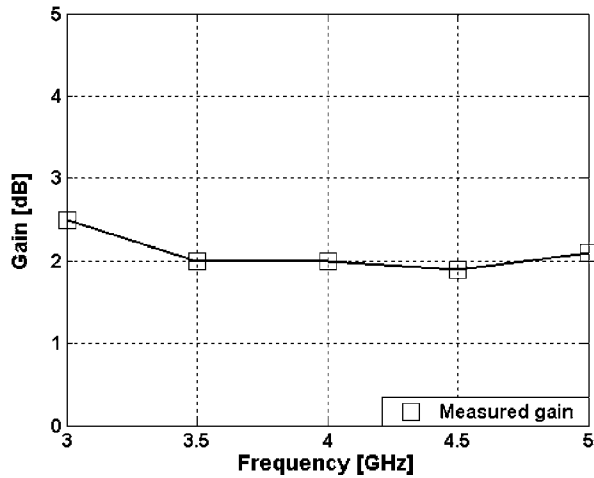


Fig. 5. Measured gain of the broadband slot antenna. Note that maximum measured gain in the azimuthal plane is reported.

using a two-prong microstrip feed on a single slot antenna and is shown to provide a 1.8:1 bandwidth as well as very low cross-polarization levels at different directions and frequencies.

Simplicity of the design process, consistent radiation parameters, and excellent polarization purity make this technique very attractive for designing wideband printed antennas.

REFERENCES

- [1] G. Kumar and K. P. Ray, *Broadband Microstrip Antennas*. Norwood, MA: Artech House, 2002.
- [2] M. Kahrizi, T. Sarkar, and Z. Maricevic, "Analysis of a wide radiating slot in the ground plane of a microstrip line," *IEEE Trans. Microwave Theory Tech.*, vol. 41, pp. 29–37, Jan. 1993.
- [3] J. Sze and K. Wong, "Bandwidth enhancement of a microstrip-line-fed printed wide slot antenna," *IEEE Trans. Antennas Propagat.*, vol. 49, pp. 1020–1024, July 2001.
- [4] H. L. Lee, H. J. Lee, J. G. Yook, and H. K. Park, "Broadband planar antenna having round corner rectangular wide slot," in *Proc. IEEE Antennas and Propagation Society Int. Symp.*, vol. 2, San Antonio, TX, June 2002, pp. 460–463.
- [5] P. H. Rao, V. Fusco, and R. Cahill, "A broadband antenna for PCN/UMTS applications," *High Freq. Postgrad. Student Colloq.*, pp. 2–5, Sept. 2000.
- [6] N. Behdad and K. Sarabandi, "A novel approach for bandwidth enhancement of slot antennas," in *Proc. Antenna Applications Symp.*, Monticello, IL, Sept. 17–19, 2003, pp. 176–189.
- [7] C. A. Balanis, *Antenna Theory: Analysis and Design*, 2nd ed. New York: Wiley, 1996, ch. 12.
- [8] *IE3D Electromagnetic Simulation and Optimization Software*.
- [9] *Advanced Design System*.

Bandwidth Enhancement of Miniaturized Slot Antennas Using Folded, Complementary, and Self-Complementary Realizations

Reza Azadegan, *Student Member, IEEE*, and Kamal Sarabandi, *Fellow, IEEE*

Abstract

Folded and self-complementary structures are considered as two effective approaches to increase the bandwidth of miniaturized antennas. Using miniaturized folded slot can result in more than 100% increase in the bandwidth as compared with that of the miniaturized slot antenna. The complimentary pair of the miniaturized folded slot, namely, the folded printed wire is also discussed in this paper. It will be shown that folded slots have a much higher radiation efficiency when compared with their complementary folded wire antennas. Another approach for bandwidth improvement is the implementation of self-complementary topologies to moderate the frequency dependence of the antenna input impedance. With regard to this approach, a folded self-complementary miniature antenna is studied, where a noticeable improvement over bandwidth is observed. A miniaturized folded slot, its complementary miniaturized folded printed wire, as well as their self-complementary realization, are fabricated and tested. These antennas do not need complicated external matching circuits and can fit into a very small rectangular area with dimensions as small as $0.065\lambda_0 \times 0.065\lambda_0$. Experimental and theoretical data shows that the folded structures exhibit bandwidths twice as wide as their ordinary miniaturized counterparts with similar sizes and gains. The self-complementary version of the folded antenna shows further increase in the bandwidth. In the efficiency/gain comparison, self-complementary structures fall between the slot and printed wires since they consist of equal proportions of the both slot and printed wire. A self-complementary H-shape antenna is also introduced whereby the required self-complementarity conditions are met at the expense of relaxing miniaturization, and consequently, a very wide bandwidth is achieved. With yet small dimensions of $0.13\lambda_0 \times 0.24\lambda_0$, a very wide bandwidth of (2.3:1) can be obtained. For the case of no dielectric substrate, even wider bandwidth of (3:1) is achieved.

Keywords

Slot antenna, folded slot, folded dipole, miniaturized antenna, self-complementary antenna.

I. INTRODUCTION

WITH recent advances in solid state devices and MEMS technology, realization of high performance miniaturized transmit and receive modules have become a reality. These modules, together with miniaturized sensors and transducers, have found numerous applications in industry, medicine, and the military. Nevertheless, an ongoing effort is underway to develop new methodologies for designing efficient miniaturized antennas that can easily be integrated to the rest of electronics and RF components in such wireless systems. Previous studies have shown that antenna miniaturization adversely impacts antenna efficiency, bandwidth, and impedance matching [1], [2], [3], [4], [5], [6]. The focus of these early investigations have mainly been restricted to the establishment of a relation between antenna size, bandwidth and efficiency. In these studies, a lower bound for the antenna quality factor (Q) in terms of the radius of the smallest fictitious sphere enclosing the antenna was derived. This analytical derivation is based on the spherical wave function expansion of the fields radiated from a small antenna, where the quality factor of the lowest order mode provides a lower bound for the antenna Q . Apart from introducing an upper bound on small antennas' bandwidths, the above literature does not deal with practical design considerations.

In recent years, practical aspects of antenna miniaturization have received significant attention. Most successful designs, however, rely on the use of high permittivity ceramics which are less desirable for their high costs and incompatibility with monolithic circuits. Recently, the authors proposed a

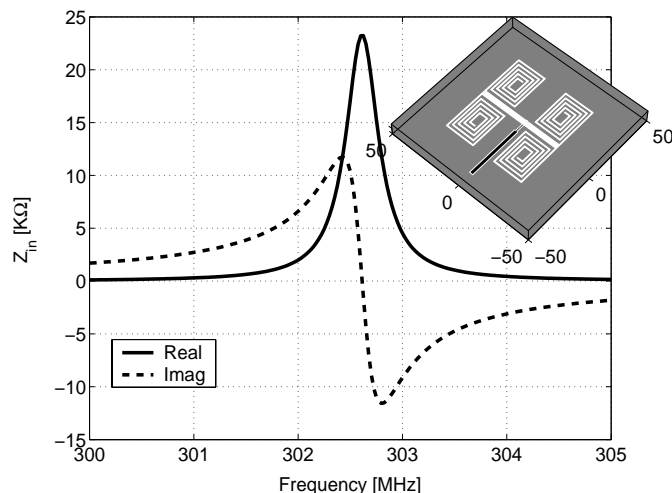


Fig. 1. The layout and the simulated input impedance of the miniaturized slot antenna around its resonance.

new class of efficient miniaturized slot antennas which can be easily matched without the need for external matching networks. The topology of a typical miniaturized slot antenna is shown in Fig. 1 [7]. The miniaturization is achieved by introducing symmetric inductive loading at both ends of a short radiating slot section to create a voltage discontinuity along a resonant slot-line. An important advantage of this topology is that the antenna size, depending on the application at hand, can be chosen almost arbitrarily small at the cost of reduction in bandwidth and efficiency. As an example, the design of a miniaturized antenna with dimensions as small as $0.05\lambda_0 \times 0.05\lambda_0$ showing a fairly high gain of -3 dBi was demonstrated [7]. Resonant antennas in general, and resonant slot antennas in particular, are inherently narrow band. Obviously, further bandwidth reduction is expected for miniature slotted structures. Another important issue regarding slot antennas is the ground plane size and its impact on antenna gain and efficiency. As demonstrated in [7], [8], the gain of the antenna decreases as the size of ground plane is reduced.

The objectives of this paper are two-fold, namely, enhancing the narrow bandwidth of small antennas, and mitigating the drawbacks related to the ground plane size. In order to improve the antenna bandwidth, a miniaturized folded topology is introduced, and its bandwidth is compared with that of a miniaturized slot antenna with a similar topology [7]. To alleviate ramifications related to the ground plane size, a complimentary topology is introduced, in which the slot is replaced by a metallic strip (printed wire), and the ground plane is eliminated. The duality principle between the two antennas, however, cannot be directly applied because of the presence of the dielectric substrate. To further improve the bandwidth of these antennas, a folded self-complementary topology comprised of two half structures of the miniaturized slot and wire antennas is also considered. Finally, we will proceed with an ultra wide band self-complementary antenna with a moderate miniaturization. Experimental and analytical analyses are carried out to compare the size, bandwidth, gain, and efficiency of these antennas.

II. MINIATURIZED FOLDED SLOT ANTENNA

The miniaturized slot antenna structure shown in Fig. 1 has a relatively narrow bandwidth. The radiating slot segment has a length of $\ell = 0.05\lambda_0$, which is 10 times smaller than a standard half-wave resonant slot. Since the physical aperture of this miniature antenna is much smaller than that of a standard slot antenna, its radiation conductance is much lower than a standard $\lambda/2$ slot. The input impedance of the miniature slot antenna, when fed by a short-circuited microstrip line, is shown to be about $25K\Omega$ at the resonance (see insert of Fig. 1). In order to match such a high impedance to a standard transmission line, impedance matching had to be done off resonance, where the reactance

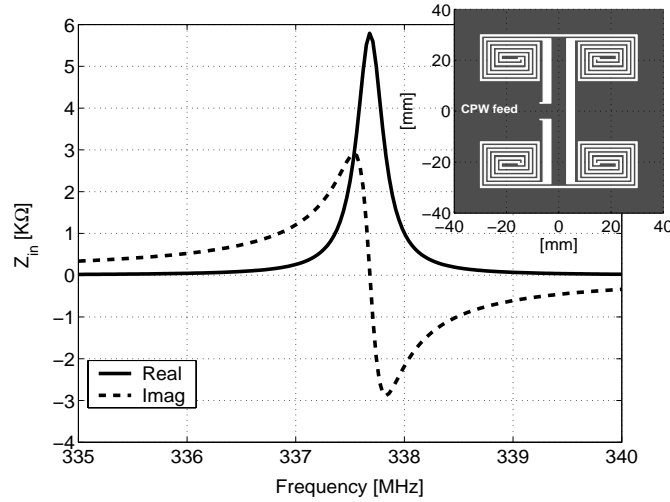


Fig. 2. The layout and the simulated input impedance of the miniaturized folded slot antenna around its resonance.

slope is very high. This high spectral variation of the antenna reactance limits the impedance matching to only a narrow band. If the radiation conductance of the miniaturized slot antenna can be increased without a significant increase in the antenna size, impedance matching over a wider bandwidth can be achieved. Increasing the physical aperture by means of introducing a suitable folded structure seems to be an appropriate approach, since the antenna aperture readily increases, while the antenna size can be kept almost the same.

The impedance of a folded dipole antenna is related to that of a dipole antenna by [9]

$$Z_{in}^{folded-dipole} = 4 Z_{in}^{dipole} \quad (1)$$

Using Bookers' relation [10], the input impedance of a resonant slot dipole can be obtained from its dual and vice versa as

$$Z_{in}^{folded-slot} = \frac{\eta^2}{4} \frac{1}{Z_{in}^{folded-dipole}} = \frac{Z_{in}^{slot}}{4} \quad (2)$$

Equation (2) shows that the input impedance of a folded slot is four times smaller than that of the standard slot dipole. Thus, the impedance of a miniaturized folded slot is expected to be much closer to the impedance of standard transmission lines, and thus easier to match.

Figure 2 shows the proposed miniaturized folded slot topology fed by a CPW line. The same figure shows the simulated input impedance as a function of frequency. Dimensions of the folded prototype are chosen to be the same as those of the miniaturized antenna in Fig 1. This antenna occupies an area of $6\text{cm} \times 6\text{cm}$. The resonant frequency of this folded antenna, however, is slightly higher than that of the original miniaturized slot. As illustrated, the miniature folded-slot impedance is reduced from about $25\text{K}\Omega$ for the original design to $6\text{K}\Omega$, which is easier to matched to a 50Ω line. Moreover, for the folded antenna, the reactance slope of the input impedance is much lower at the frequency where the real part of the antenna impedance is 50Ω , indicating the possibility of impedance matching over a wider frequency band.

Two solutions are available for matching the input impedance of the miniaturized slot antenna to a 50Ω . One solution is to tune the slot antenna below its resonance where the slot is inductive, using a capacitive coupling at the feed, and the other one is to inductively feed the slot and tune it slightly above its resonance. Since the objective is to minimize the antenna size, a capacitively coupled slot antenna is chosen. Figure 3 shows the proposed miniaturized folded slot antenna capacitively coupled to a 50Ω CPW line. An interdigital capacitor is placed in between the feed line and the antenna to control the amount of coupling between the line and the miniaturized folded slot, in order to achieve

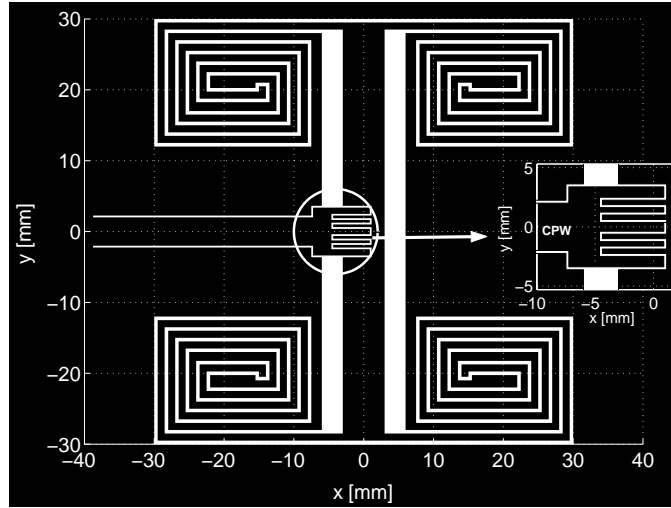


Fig. 3. Miniaturized folded-slot antenna fed by a capacitively coupled CPW line.

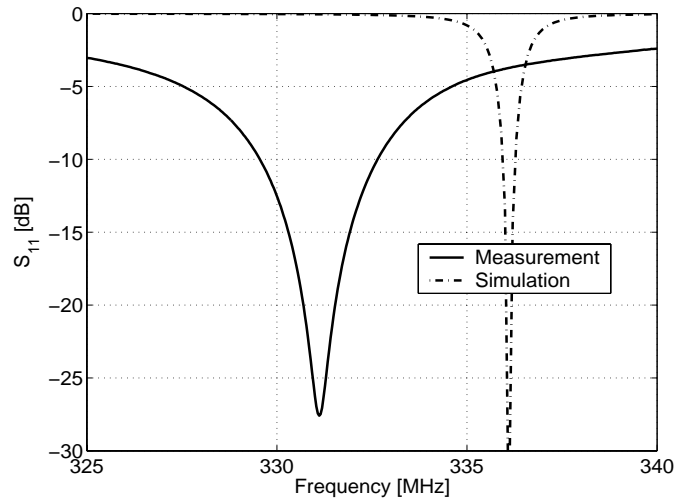


Fig. 4. Simulated and measured input return loss of the miniaturized folded slot antenna of Fig. 3.

the impedance match. The exact value of this capacitance is determined by modeling the miniaturized folded slot with an equivalent second-order resonant circuit model. The equivalent circuit parameters are extracted using a full-wave simulation of the antenna structure similar to what was done for the original miniaturized slot antenna [7].

A prototype of the miniaturized folded slot antenna shown in Fig. 3 was fabricated on a substrate with a dielectric constant of $\epsilon_r = 2.2$ and a loss tangent of $\tan \delta = 0.0009$, and a thickness of 0.787 mm [11]. Then, the input impedance and far-field co- and cross-polarized radiation patterns of this antenna were simulated and measured. The full-wave simulations were performed using a commercially available Moment Method package [12]. Figure 4 shows a comparison between the simulated and measured input return loss values of the antenna depicted in Fig. 3. As the simulation shows, the folded antenna occupies an area as small as $0.065\lambda_0 \times 0.065\lambda_0$ and is perfectly matched at 336.1 MHz. This frequency is lower than the resonant frequency of the folded slot structure (337.7 MHz) shown in Fig. 2 because of the insertion of the interdigitated matching capacitance. There is also a 1% shift in the measured resonant frequency of the antenna compared to the results obtained from the simulation. This discrepancy can be attributed to the finite size of the ground-plane, numerical errors, and the exclusion of the ohmic loss of the ground plane.

For slot-line structures, equivalent magnetic currents are usually used to facilitate efficient imple-

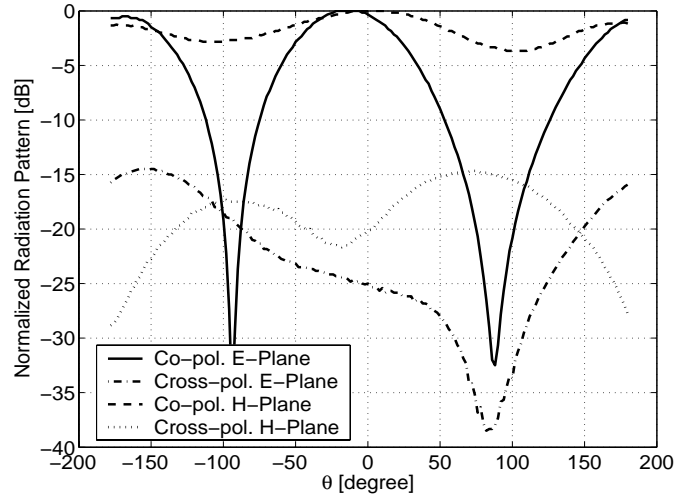


Fig. 5. Measured radiation pattern of the miniaturized folded slot antenna for E- and H- principle planes.

mentation of the Method of Moment solution. In this approach, the tangential electric field over the slot is replaced with an equivalent magnetic current, while the field is assumed to vanish over an infinite ground plane. This assumption implies that the ground plane is modeled by a perfect conductor, and therefore, the ohmic loss cannot be accounted for in this case. In reality, the ground plane of the slot-line structure has finite conductivity and finite size, which leads to the observed discrepancies between the simulation and the measured results. Whereas the finiteness of the ground plane is responsible for the observed disagreement between the measured and simulated antenna center frequency, exclusion of ohmic losses of the ground plane from simulation is responsible for the observed discrepancy in the -10 dB return loss bandwidth of the miniaturized folded slot (see Fig. 4).

To demonstrate the bandwidth enhancement of the miniaturized folded-slot compared to the original miniaturized antenna, both simulated and measured near-field and far-field characteristics of these antennas are summarized in Table I. Table I clearly shows an increase in the -10 dB return-loss bandwidth of the folded slot antenna over the original antenna from 0.34% to 0.93%. The gains of these antennas were measured against a standard half wavelength dipole antenna. The gain of the folded and original miniaturized slot antennas were, respectively, measured to be -2.7 dBi and -3.0 dBi. The measured values of the gains are lower than the simulated results. This again can be attributed to the the ohmic loss and finite size of the ground plane which have not been accounted for in the simulation.

Finally, the E-plane and H-plane radiation patterns of the miniaturized folded-slot antenna were measured in the anechoic chamber of the University of Michigan and are shown in Fig. 5. For the E-plane pattern, $E_{\theta}(\theta)$ was measured in the $\phi = 0^{\circ}$ plane. The measurement of $E_{\phi}(\theta)$ in the $\phi = 90^{\circ}$ plane provides the H-plane pattern of the antenna. In theory, a null should exist in the H-plane pattern of an infinitesimal folded-slot, since the ground plane forces the tangential electric field of $E_{\phi}(\theta = 90^{\circ}) = 0$ at $\phi = 90^{\circ}$ to vanish. This deep null, however, is not observed because of the finite dimensions of the ground plane. When the ground is not extended to infinity, the radiation by edges would fill the null. On the other hand, a null is created in the E-plane pattern, whereas the theory predicts a uniform pattern. This phenomenon is also caused by the finite dimensions of the ground plane. Based on the equivalence principle, the magnetic currents on the upper and lower half space flow in two opposite directions and create out of phase normal electric fields on the antenna plane ($\theta = 0^{\circ}$). When the ground plane is infinite, the lower and upper half spaces are decoupled, and no cancellation occurs. The cross-polarization component of the radiation pattern is small because of the symmetry of the structure in the principal E- and H-planes. The observed minor cross-polarized radiation is caused by the edges of the finite size ground plane and the re-radiation of the near field of

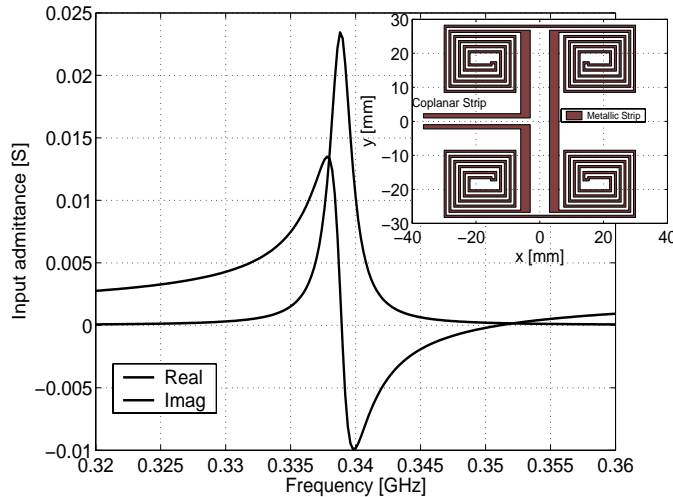


Fig. 6. Layout and real and imaginary parts of input impedance of the miniaturized folded printed wire antenna.

the antenna by the feeding cable.

III. MINIATURIZED FOLDED PRINTED WIRE ANTENNA

The size of the ground plane was found to be an important parameter in slot antenna gain, bandwidth, and depolarization. In general, the larger is the ground plane, the better antenna performance is expected. In many applications, such as automotive, aviation, and large arrays, metallic platforms of considerable size are already available. Therefore, ground plane size does not impose a major restriction on the antenna performance. When no large ground plane is available, an alternative miniaturized design may be considered. Basically, printed wire structures, unlike slotted structures, do not need a ground plane. In this section, a printed antenna topology which is the complementary pair of the miniaturized folded-slot of Fig. 2 is proposed and tested. This structure is shown in Figure 6, where the slot-lines are replaced by metallic strips and vice versa. Two vertical radiating elements at the center of the structure are terminated by distributed capacitive loadings. The electric current distribution attains its maximum on these vertical strips. Although the far-field radiation mainly emanates from the two vertical elements, the contribution of the distributed capacitive loads on the radiation resistance should not be overlooked.

The radiation resistance of an infinitesimal dipole with a constant current distribution can be calculated analytically [9]. This quantity is multiplied by a factor of four in the case of an infinitesimal folded dipole; that is;

$$R_a = 4 \times 80\pi^2 \left(\frac{\ell}{\lambda}\right)^2. \quad (3)$$

In the above equation, the antenna is assumed to be radiating in free space. For the miniature folded dipole considered in Fig. 6, $\ell = 0.065\lambda_0$ results in radiation resistance of $R_a = 13.34\Omega$. Equation (3) only accounts for the contribution of the main radiating arms, and the effects of capacitive loading and the dielectric substrate are not included in the calculation of the input resistance. In order to include all these parameters, the full-wave Moment Method code assuming infinite substrate is used, and the input admittance is calculated and shown in Fig. 6. The simulated input impedance of the printed folded dipole at the structure resonance is $R_a = 43\Omega$, which is considerably different from the value predicted by (3) for the reasons mentioned earlier.

Similar to its folded-slot counterpart, the folded printed-wire can be directly matched to a 50 Ω line, without a complicated matching network. The printed dipole antenna requires a balanced input to ensure a symmetric current distribution on the antenna. Both lumped element (RF transformer

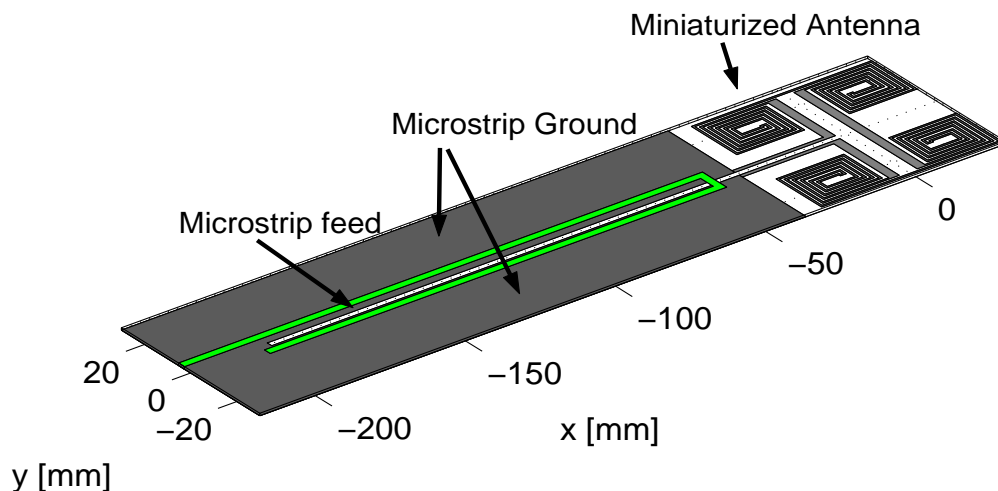


Fig. 7. The miniaturized folded printed wire antenna with balanced feed and fine tuning setup.

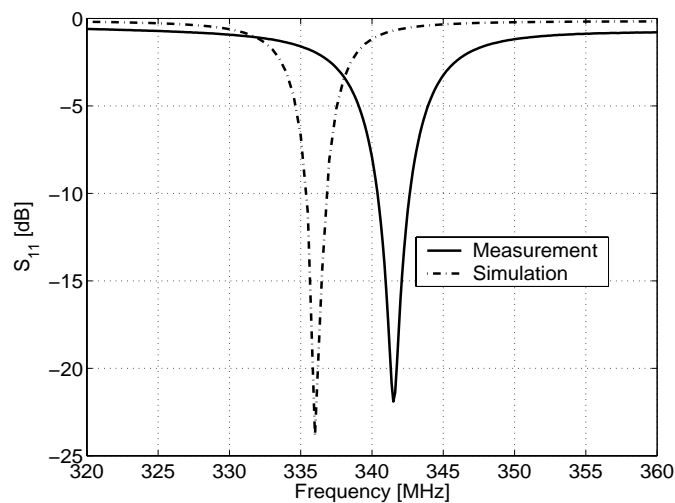


Fig. 8. Simulated and measured input return loss of the miniaturized antenna in Fig 7.

chips) and distributed baluns can be used to transform the unbalanced feed into balanced co-planar strips (CPS), which feed the miniaturized printed folded-dipole antenna of Fig. 6. Merchand balun is an example of distributed transformer which is used for a $50\ \Omega$ microstrip line to a CPS transition [13]. Figure 7 shows the layout of the printed wire antenna connected to a Merchand balun. Although the balun is considerably larger than the antenna itself, it should not be considered as a part of the antenna, and it has only been used here to characterize the antenna discretely. When the antenna is integrated with transceiver electronics, balanced circuitry can be utilized instead.

The design procedure for this antennas is similar to the one presented for the miniaturized slot antennas making use of the duality principle [7]. Figure 7, shows the miniature antenna fed by a $50\ \Omega$ microstrip line through a Merchand balun. Note that fine-tuning is accomplished by a small amount of inductive feed generated by having a microstrip line extension slightly less than $\lambda/4$. This antenna was fabricated on the same substrate used in the previous examples. Figure 8 shows a comparison between the simulated and measured input return loss values of the miniaturized printed folded antenna. This antenna can fit into a rectangular area of $0.06\lambda_0 \times 0.065\lambda_0$ at 336 MHz. However, there is about 1% shift in the measured operating frequency compared with the simulation, which again can be attributed to numerical errors and the finite dimensions of the dielectric substrate.

The measured radiation pattern of this printed antenna for E- and H-planes are plotted in Fig.

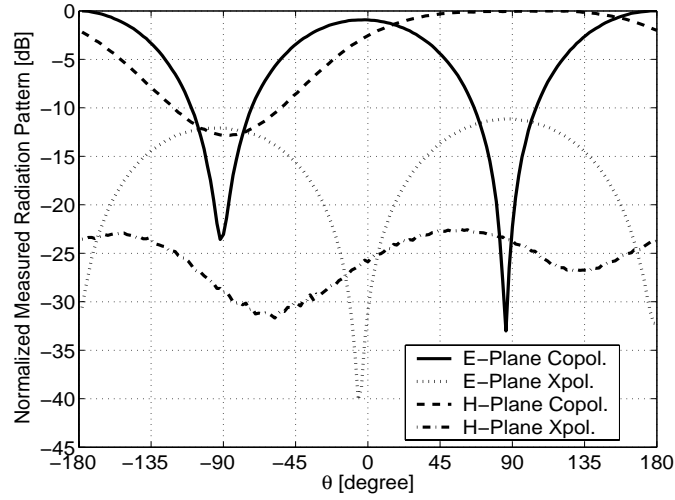


Fig. 9. E- and H-plane measured radiation patterns of the miniaturized folded printed wire of Fig 7.

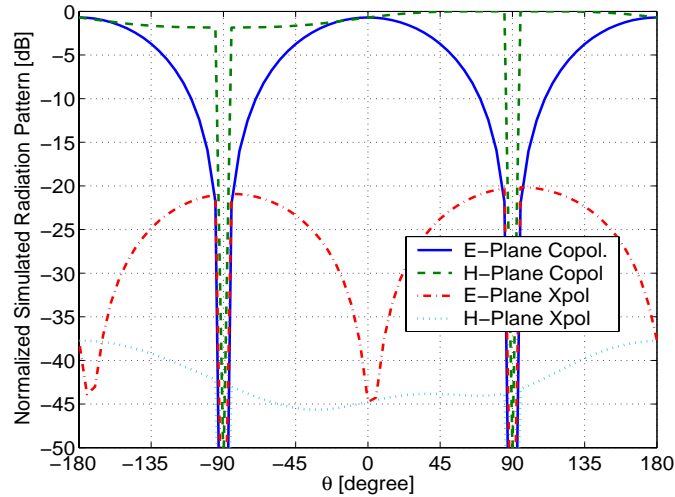


Fig. 10. The simulated radiation pattern of the miniaturized folded printed wire antenna without a balun.

9. Figure 10 illustrates the simulated radiation pattern of the antenna itself in the absence of the balun. The measured radiation pattern in the E-plane agrees with the numerical simulation and the theoretical radiation pattern of an infinitesimal folded dipole. In contrast, an asymmetric null appears in the H-plane pattern at $\theta = -90^\circ$, whereas a constant pattern in the H-plane is expected. This asymmetry emerges because of the presence of the balun. The major portion of the observed cross polarized radiation is believed to emanate from the feed cables rather than the antenna structure itself. The far-field gain of this antenna is measured to be -6.5 dBi, which is slightly higher than the value predicted by the simulation. Knowing that the balun creates a null in the H-plane pattern, one should expect the antenna to be more directive when the balun is present. That is why, the measured gain is slightly higher than the gain obtained from the simulation (see Table I). The observed difference between the gains of the miniaturized folded-slot and printed dipole is noteworthy. A 3.8 dB gain difference exists between the two antennas which is attributed to conductor ohmic losses. Slot antennas make use of more conductors, and therefore, ohmic losses are significantly less than the ohmic losses of their printed wire antennas counterpart.

TABLE I

COMPARISON AMONG CHARACTERISTICS OF MINIATURIZED SLOT, MINIATURIZED FOLDED SLOT, AND MINIATURIZED PRINTED FOLDED DIPOLE ANTENNAS.

Antenna Type	Size	Bandwidth [%]		Gain [dBi]		Directivity [dB]
		Sim.	Meas.	Sim.	Meas.	
Miniature slot [7]	$0.05\lambda_0 \times 0.05\lambda_0$	0.058	0.34	1.0	-3.0	1.9
Folded slot	$0.065\lambda_0 \times 0.065\lambda_0$	0.12	0.93	1.0	-2.7	1.9
Printed wire	$0.065\lambda_0 \times 0.065\lambda_0$	0.45	0.60	-7.0	-6.5	2.4
Self-comp. folded	$0.065\lambda_0 \times 0.065\lambda_0$	1.1	1.1	-5.5	-4.5	2.7

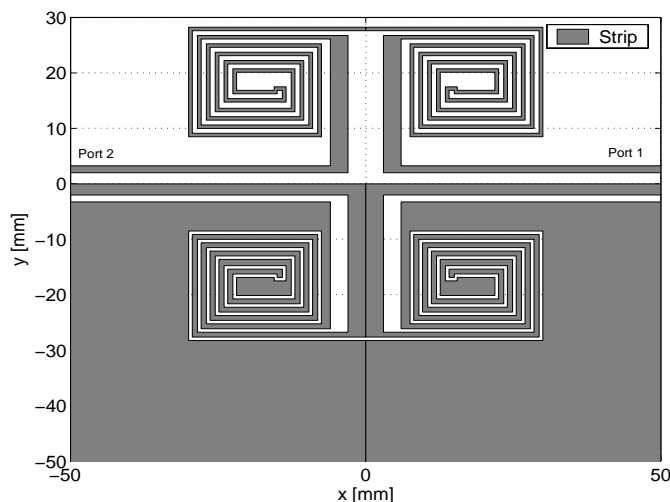


Fig. 11. The miniaturized self-complementary folded antenna fed by a tow-port self-complementary asymmetric CPW-line.

IV. MINIATURIZED SELF-COMPLEMENTARY FOLDED ANTENNA

The use of self-complimentary antennas has been suggested to obtain antennas with frequency independent input impedances [14]. The basic idea stems from the fact that these structures consist of two sections that are dual of each other. Therefore, the reactive parts of these two subsections tend to cancel each other, which leads to a purely real input impedance over the frequency band. In reality, however, a self-complementary radiating structure needs to be truncated, and this truncation by itself deteriorates the performance of a self-complementary design. The extent of this deterioration depends on the geometry as well as the truncation extent. Truncation becomes even more important when miniaturized antennas are considered. Apparently, miniaturized self-complementary antennas are subject to a very tight truncation whose effect should be closely examined.

Another important assumption in self-complimentary structures is that the antenna should radiate in free space or homogeneous media. Consequently, the introduction of a dielectric medium would provoke the required condition for self-complementarity, and thus, the prescribed theoretical results may not be achieved.

Figure 11 shows a self-complementary pair of the two previously introduced folded antennas, where the top half of the structure is similar to that of the folded printed wire in Fig. 6, and the lower half resembles the folded slot of Fig. 2. This structure is excited through self-complementary transmission line which resembles an asymmetric CPW waveguide. The characteristic impedance of this self-complementary transmission line is $Z_c \approx 60\pi/\sqrt{\epsilon_r}$, given that a dielectric substrate is present. This antenna has the same dimensions as the two previously introduced structures and is fabricated on the same dielectric substrate. In order to analyze the structure, the two-port antenna structure

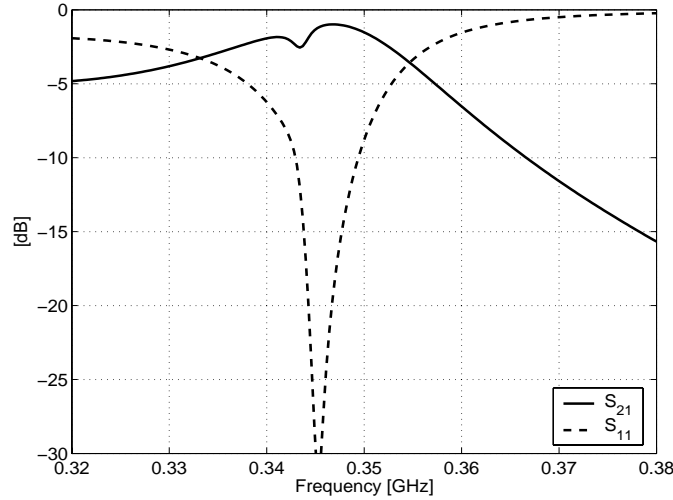


Fig. 12. The two-port simulated S-parameters of the miniaturized self-complementary folded antenna of Fig. 11 to be used for obtaining a proper lossless matching network.

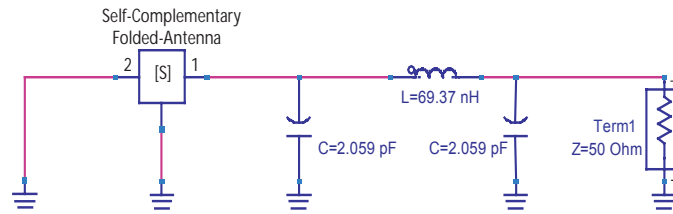


Fig. 13. The equivalent circuit of the required matching network to a 50Ω line.

shown in Fig. 11 is simulated using the Method of Moment [12], and its S-parameters are presented in Fig. 12. Based on the simulated S-parameters, the resonant frequency of the antenna can be determined. Furthermore, the knowledge of the S-parameters provides the information required for designing a matching network for the antenna.

A. Impedance Matching

In order to match the impedance of the antenna, two parameters should be determined. One is the terminating impedance of the second port, and the other parameter is an appropriate reactive circuit to be placed in series with the antenna at the first port. A trivial choice for the terminating impedance of the second port is the intrinsic impedance of the self-complementary CPW line, which is $Z_c \approx 60\pi/\sqrt{\epsilon_r} = 125\Omega$. This termination ensures no reflection from the line at the second port, but at the same time, the resistive termination reduces the radiation efficiency of the antenna drastically. That is why reactive (lossless) termination for the second port is preferred. In order to minimize ohmic losses, the second port is short circuited, and the matching circuit of Fig. 13 is proposed. The matching parameters of this circuit can be found using an optimization algorithm so that a wide band impedance matching may be obtained around the resonant frequency of the structure. The lossless matching circuit can either be realized by distributed elements or by lumped elements. Figure 14 illustrates the antenna with a distributed element realization of the matching network. Obviously, this distributed matching network is not a part of the antenna, and may be replaced with high Q lumped elements when the antenna is integrated with a transceiver.

The antenna of Fig. 14 is fabricated on the same substrate as the previous antennas, and its input return loss is measured and compared with those obtained from the full-wave simulation and the equivalent circuit model. This comparison is shown in Fig. 15 where a good agreement is observed. Both simulated and measured fractional bandwidths for this structure are found to be 1.1% which is

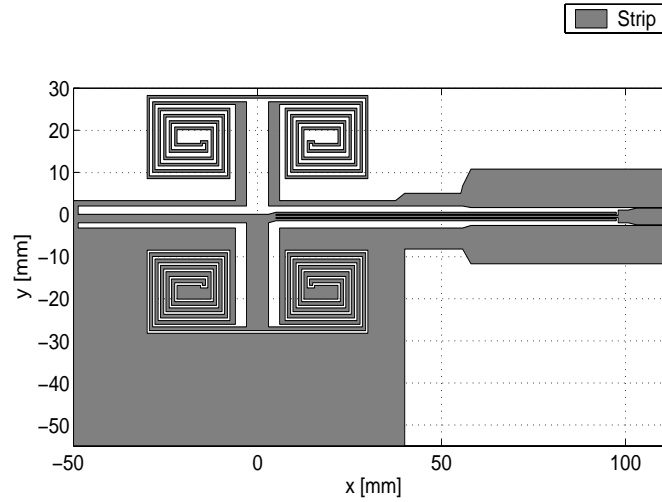


Fig. 14. The geometry of the miniaturized self-complementary folded antenna along with the distributed-element realization of the matching network of Fig. 13.

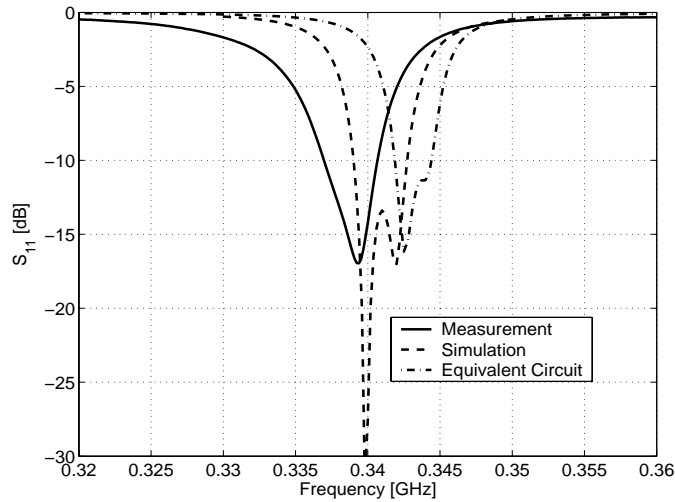


Fig. 15. The measured, simulated, input return losses of the antenna of Fig. 14, as well as that of the equivalent circuit model of Fig. 13.

at least 25% improved over the measured bandwidth of the miniaturized folded slot antenna in Table I. Unlike miniaturized slot and folded slot, the simulated and measured bandwidth and gain of this antenna agree favorably, since in the simulation of the self-complementary antenna notion of magnetic current was not used, and thus, the ohmic losses are accounted for.

The radiation pattern of this antenna might seem to be complicated at the first glance. However, the radiated fields can be considered as the superimposition of the field of a small folded dipole and that of a folded slot. Therefore, $\phi = \pm 45^\circ$ specifies the principle plane of the antenna given that both dipole and slot modes are excited in phase. The radiation pattern of the self-complementary folded antenna is measured in three cuts of $\phi = 0^\circ$, $\phi = 45^\circ$, and $\phi = 90^\circ$. Fig. 16 compares the measured and simulated radiation pattern of this antenna for these three cuts. Pattern measurement of self-complementary antennas with tight truncation is a rather involved procedure mainly due to the coexistence of the both electric and magnetic radiating elements, which have dual patterns. Therefore, the resultant radiation is neither symmetric with respect to the symmetry planes of the truncated structure nor with respect to the edges. This asymmetry also increases the chance that the near field of the antenna could excite currents on the feeding cable, and that those excited currents re-radiate,

and thus, interfere with the far fields of the antenna. In order to inhibit the unwanted radiation, a portion of the feeding cable at the immediate vicinity of the antenna was shielded and grounded.

The gain of this antenna was measured against a calibrated antenna. Under polarization matched condition a gain of -4.5 dBi was measured, which is slightly higher than the simulated gain for this antenna. The difference between the simulated and measured gain may be attributed to the perturbation of the radiation pattern of the antenna owing to the presence of the additional ground plane used in the measurement setup.

Comparing the self-complementary folded antenna with two previously discussed antennas, one can recognize that the self-complementary design has the widest bandwidth among the three though it is still far from being a wide-band antenna. This frequency dependence is caused by the tight truncation of the structure so as not to negate the miniaturization. Furthermore, the presence of the dielectric substrate and feeding network are two factors that tend to break the self-complementary conditions of the topology. The efficiency/gain of this antenna falls in between the gain of the two previous designs, which is inline with our expectation. Slot antennas are superior with respect to ohmic loss and printed wires have the highest ohmic loss. This self-complementary antenna is half slot and half strip. Thus, the self-complementary design is expected to be better than printed wire, and worse than slot, which is consistent with the observations summarized in Table I.

V. SELF-COMPLIMENTARY H-SHAPED ANTENNA

In the self-complementary antenna design of the previous section, the main objective was to maintain a very small size, regardless of how adversely the required conditions for self-complementary structures were affected. In this section, a more compatible design with the self-complementary conditions is introduced. In this design, the miniaturization criteria is relaxed by reducing the end-loading. By removing all of the loading spiral arms except for one, an H-antenna is obtained. Figure 17 shows the geometry of this structure fed by a short-circuited microstrip line. Again a substrate with $\epsilon_r = 2.2$ and thickness of 0.787 mm was used to fabricate this antenna. An impedance step in the microstrip line, as well as two short stubs, were introduced to enhance the impedance matching to a 50Ω line. The simulated and measured input return losses of this antenna are illustrated in Fig. 18. As shown in this figure, a very wide -10 dB bandwidth from 1.35 GHz to 3.2 GHz (2.3:1) is achieved. To demonstrate the effect of the substrate in perturbing the self-complementarity, the same structure is also simulated with no dielectric substrate ($\epsilon_r = 1.0$). The simulated return loss of this antenna without substrate is illustrated in Fig. 18, where it demonstrates a considerably wider bandwidth (1.3 GHz-3.9 GHz).

Another source of frequency dependance in the response of the antenna structure in Fig. 17 is the asymmetry created by the microstrip feed and the corresponding matching network. Comparing this feeding configuration with those of the perfectly self-complementary structures [15], [16], one can recognize that the symmetry can only be preserved when the antenna structure has two ports, and the second port is terminated by a resistance of $R_L = Z_0/2 = 60\pi\Omega$. Using this terminated configuration, the input impedance of the antenna becomes $60\pi = 188\Omega$ over a wide frequency band requiring an additional wide-band matching network, should the antenna be matched to a standard 50Ω line. Furthermore, introducing a resistive load reduces the antenna efficiency as mentioned earlier. The finite extent of the structure is another inevitable factor that deteriorates the frequency independent performance of the self-complementary antenna.

The far-field characteristics of this antenna is considered next. The bore-sight gain of this antenna was measured over the spectrum of the operation against that of a wide band calibrated ridged horn. The total measured gain of the antenna at the bore-sight ($\theta = 0^\circ$) is plotted in Fig. 19, where good agreement is observed between the simulated and measured values. The slight difference between the simulated and measured gains is mainly due to the response of the anechoic chamber as well as the potential multi-path and unwanted radiation by the feeding cable.

Finally, the radiation pattern of this antenna is measured at four frequency points within the antenna

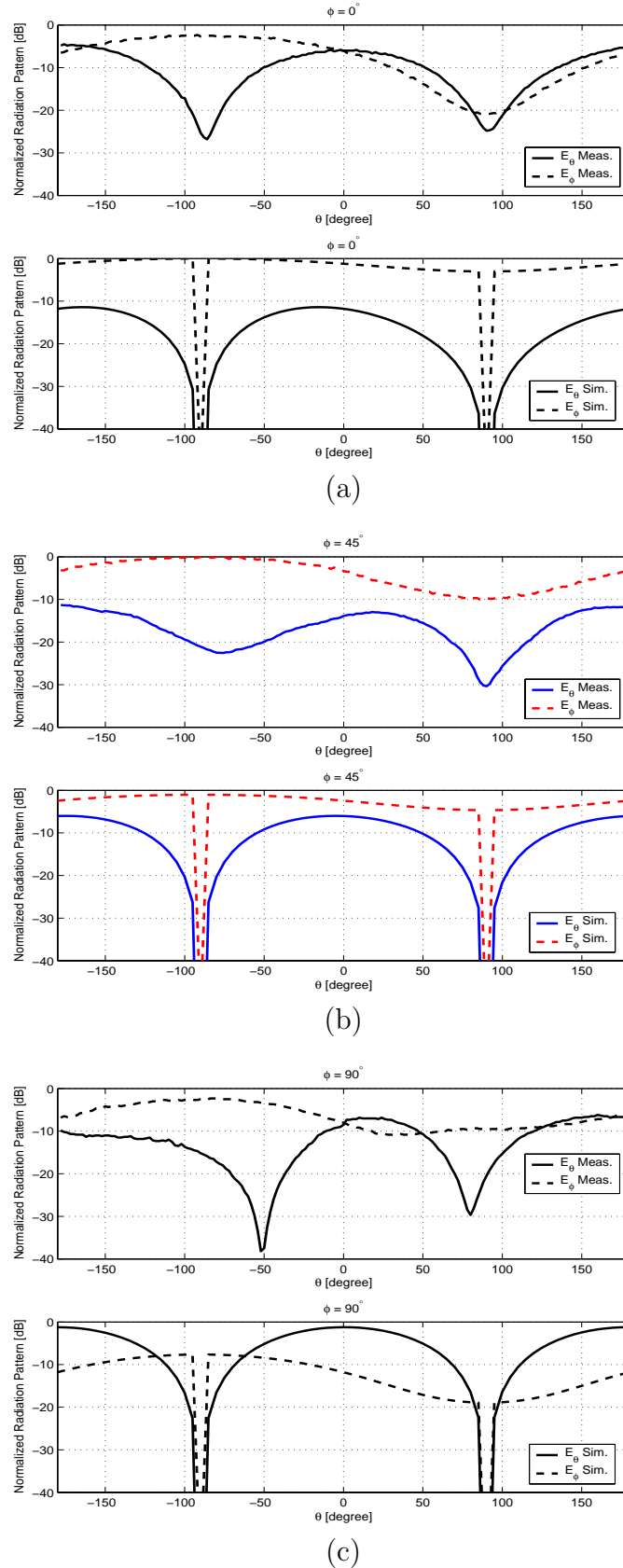


Fig. 16. Comparison between the measured and simulated radiation patterns of the miniaturized self-complementary antenna on three different planes of (a): $\phi = 0^\circ$, (b): $\phi = 45^\circ$, and (c): $\phi = 90^\circ$.

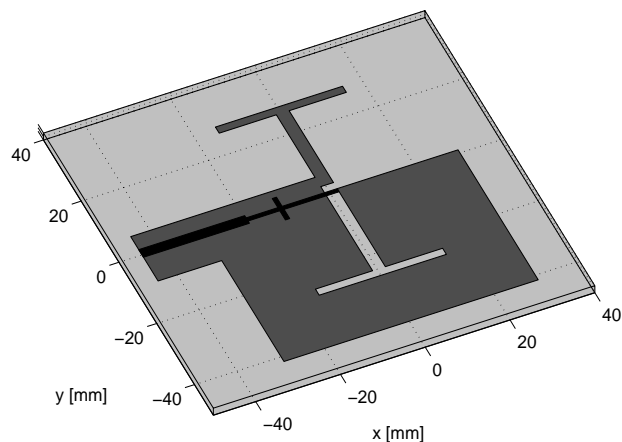


Fig. 17. The topology of a self-complementary H-antenna fed by a short-circuited microstrip line.

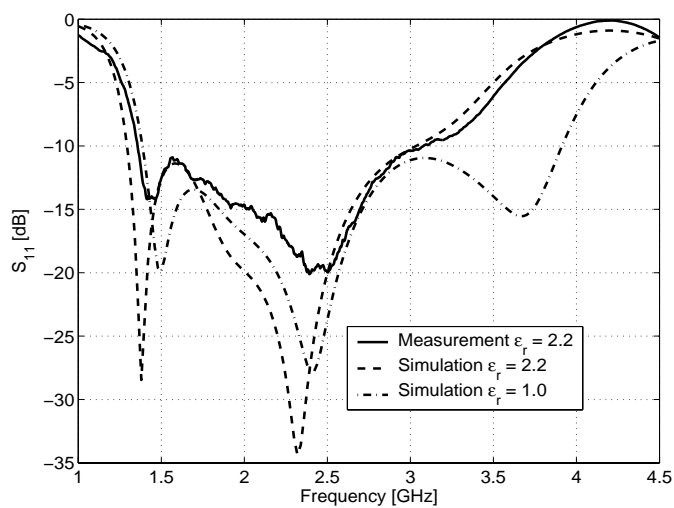


Fig. 18. Measured and simulated return loss of the H-antenna in Fig. 17, as well as that of the same structure without dielectric ($\epsilon_r = 1.0$).

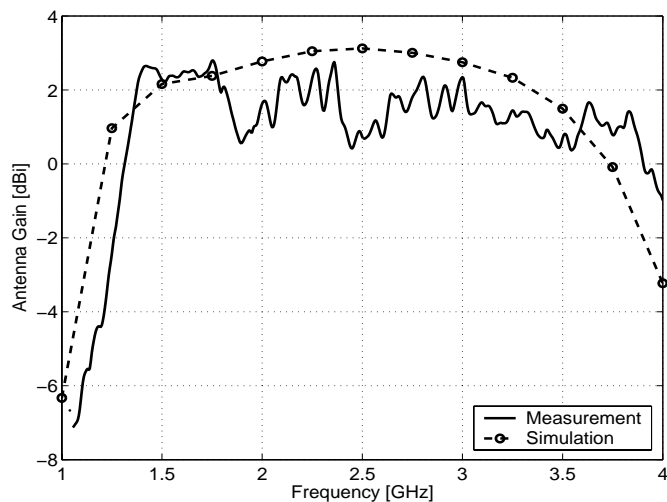


Fig. 19. Comparison between the measured and simulated gain of the self-complementary H-antenna as a function of frequency.

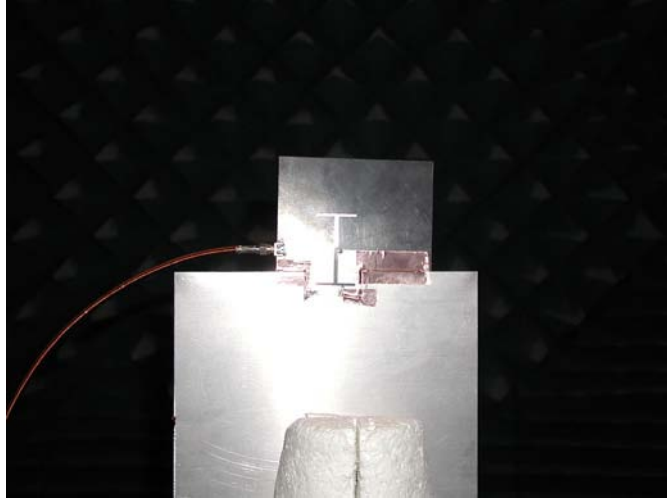


Fig. 20. Comparison between the measured and simulated gain of the self-complementary H-antenna as a function of frequency.

band namely, 1.5 GHz, 2.0 GHz, 2.5 GHz, and 3.0 GHz, at three different planes of $\phi = 0^\circ$, $\phi = 45^\circ$, and $\phi = 90^\circ$. Both horizontal ($E_\theta(\theta)$) and vertical ($E_\phi(\theta)$) polarizations were measured. Figure 20 shows the pattern measurement setup used in the experiment. Figures 21, 22, 23, 24 show the simulated and measured radiation patterns of the self-complementary H-antenna at 1.5 GHz, 2.0 GHz, 2.5 GHz and 3.0 GHz.

A few points should be explained before comparing the measured patterns with the simulated results. In the simulation, the dielectric substrate is assumed to be of an infinite extent, which explains the presence of a null in the simulated $E_\phi(\pm 90^\circ)$ patterns at all of the frequency points. Another factor that accounts for some of the discrepancies is the effect of the antenna mount fixture with a larger half-ground plane. As seen in Fig. 20, the effect of this fixture is minimal in the $\phi = 0^\circ$ plane. Therefore, very good agreement is observed between the simulated and measured patterns at all frequency points. On the other hand, the measurement fixture imposes a null on the $E_\phi(\theta = -90^\circ)$ pattern at $\phi = 45^\circ$ plane, which is why a weak null is observed in the E_ϕ at $\theta = -90^\circ$. The remaining patterns agree rather favorably with the simulation. By the same token, $E_\phi(\theta = 90^\circ)$ is perturbed due to a weak null at $\phi = 90^\circ$ plane. Radiation by the edges of the ground plane and the dielectric, as well as the radiation by feeding cable are among other reasons for the observed discrepancies.

VI. CONCLUSION

In this paper, two methodologies to increase the bandwidth of miniaturized antennas were investigated. The first approach was to introduce the folded miniature antenna which may increase the effective aperture of the miniature antenna without compromising the size drastically, and the second approach was to take advantage of the self-complementary structures to reduce the frequency dependence of the antenna characteristics. The first approach was demonstrated through introducing miniaturized folded slot antenna that occupies a region as small as $0.65\lambda_0 \times 0.65\lambda_0$ with the measured gain and fractional bandwidth of -2.7 dBi and 0.93%, respectively. When compared with the original miniaturized topology [7], the simulation shows a four-time decrease in the slot impedance, and over 100% increase in the simulated bandwidth, while its dimensions (relative to the wavelength) are increased by 13%. The complementary pair of this structure, that is, a miniaturized folded printed wire was also presented with a moderate bandwidth of 0.7% and measured gain of -6.5 dBi. This gain is substantially lower (about 3.8 dB) than its slotted counterpart. This reduction in gain indicates that slot structures are far more suitable for antenna miniaturization when a metallic platform of adequate size is available to be used as ground plane.

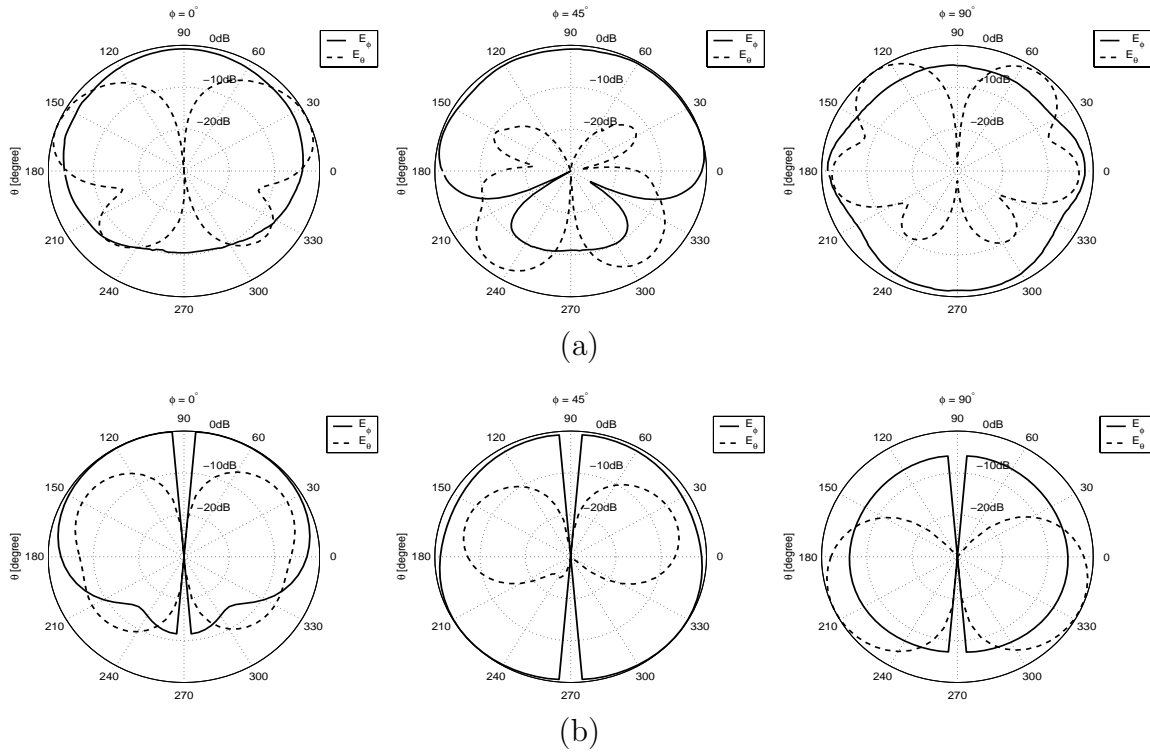


Fig. 21. Comparison between the measured and simulated radiation patterns of the self-complementary H antenna at 1.5 GHz for three cuts of $\phi = 0^\circ$, $\phi = 45^\circ$, $\phi = 90^\circ$; (a): measurements, (b): simulations.

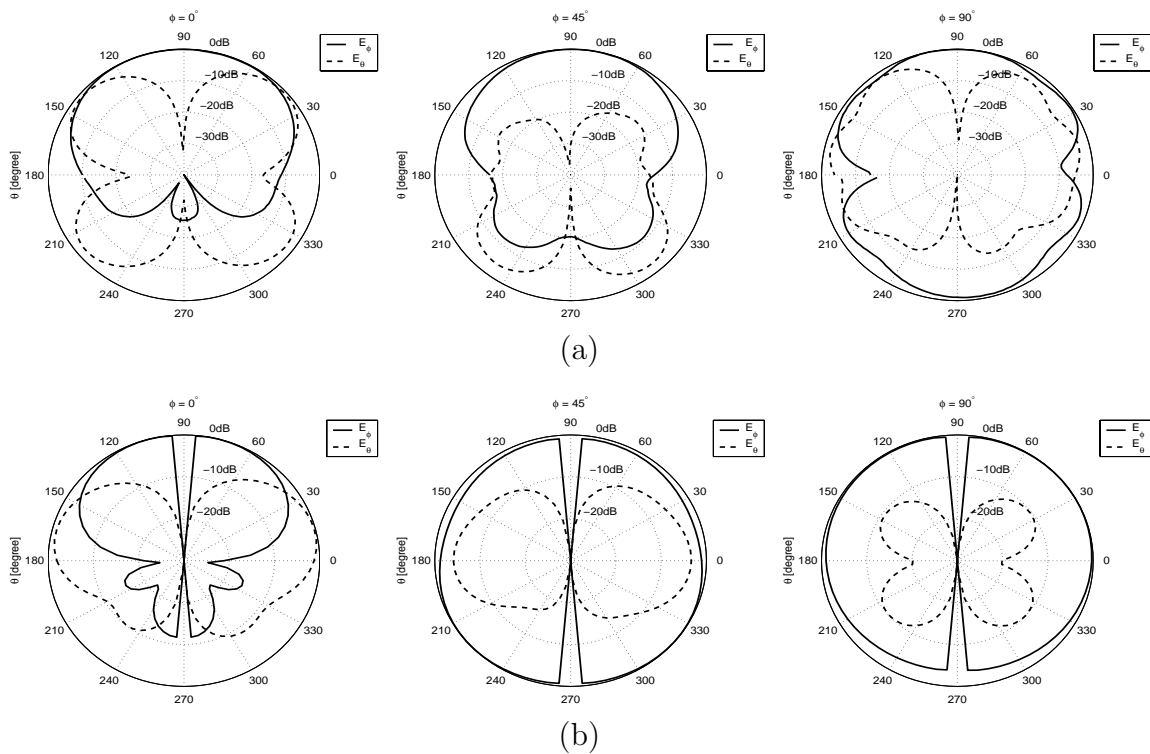


Fig. 22. Comparison between the measured and simulated radiation patterns of the self-complementary H antenna at 2.0 GHz for three cuts of $\phi = 0^\circ$, $\phi = 45^\circ$, $\phi = 90^\circ$; (a): measurements, (b): simulations.

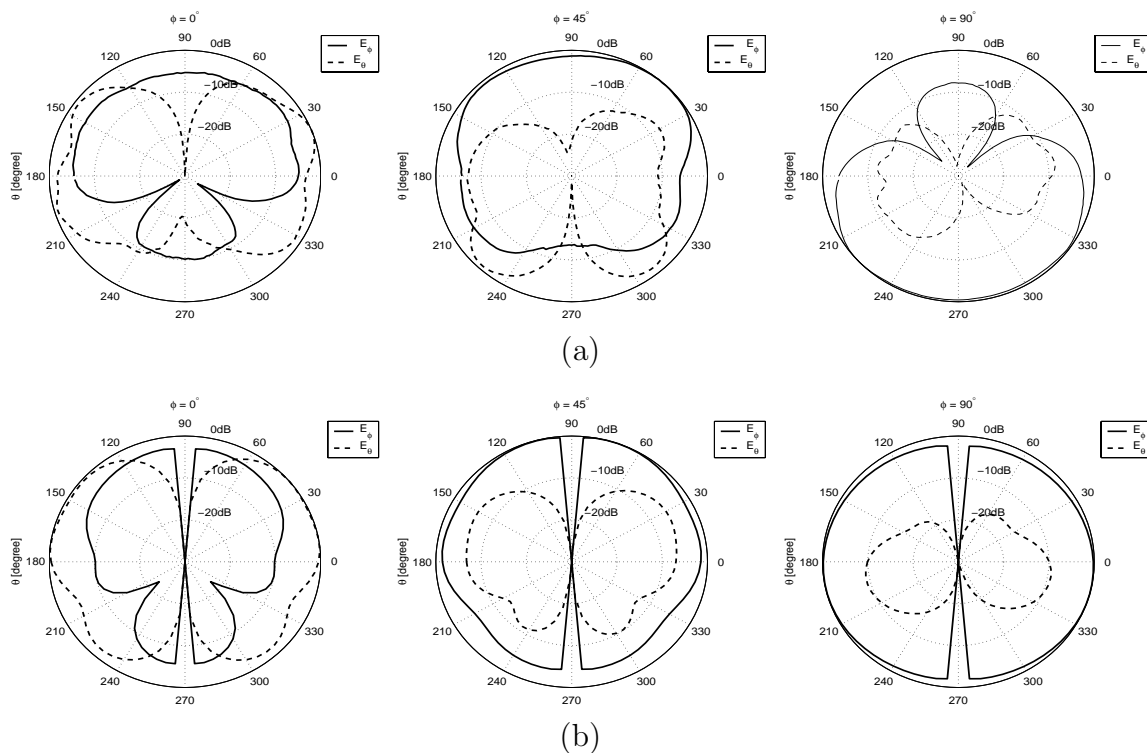


Fig. 23. Comparison between the measured and simulated radiation patterns of the self-complementary H antenna at 2.5 GHz for three cuts of $\phi = 0^\circ$, $\phi = 45^\circ$, $\phi = 90^\circ$; (a): measurements, (b): simulations.

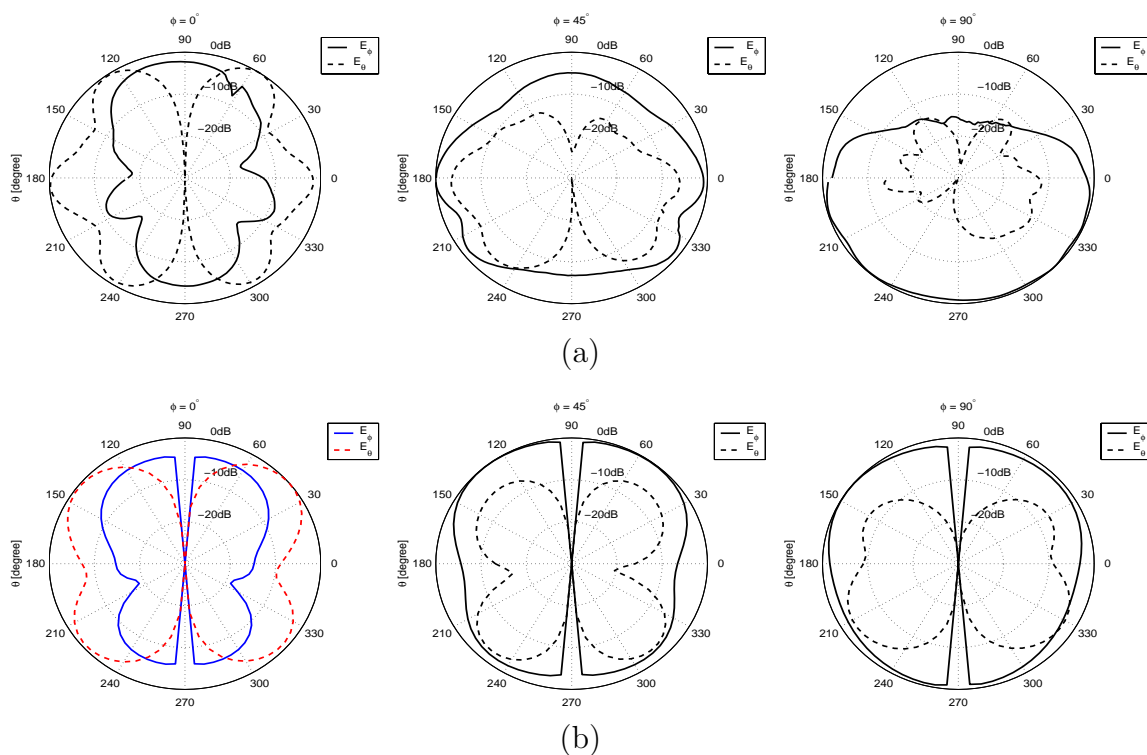


Fig. 24. Comparison between the measured and simulated radiation patterns of the self-complementary H antenna at 3.0 GHz for three cuts of $\phi = 0^\circ$, $\phi = 45^\circ$, $\phi = 90^\circ$; (a): measurements, (b): simulations.

The self-complementary pair of these two folded antennas is the third design presented in this paper to exploit the wide-band characteristics of self-complementary structures. Maintaining the same dimensions, the fractional bandwidth of the self-complementary antenna reaches to 1.1%, which exhibits at least 25% increase over its slotted and printed strip counterparts. The gain/efficiency of this antenna, as expected, falls between those of the folded slot and printed wire antennas. When miniaturization criteria is relaxed in exchange for satisfying more of the self-complementarity conditions, a much wider bandwidth can be obtained, an example of which is an H-antenna. This antenna demonstrates a very wide -10 dB return loss bandwidth of 2.3:1 and a fairly constant gain of slightly above 1 dBi over the entire frequency band of operation. The dimensions of this antenna are $0.13\lambda_0 \times 0.24\lambda_0$ at the lowest frequency of operation (1.3 GHz).

REFERENCES

- [1] H. A. Wheeler, "Fundamental limitations of small antennas," *Proc. IRE*, vol. 35, pp. 1479-1484, Dec. 1947.
- [2] L. J. Chu, "Physical limitations of omni-directional antennas," *J. Appl. Phys.*, vol. 19, pp. 1163-1175, Dec 1948.
- [3] R. F. Harrington, "Effect of antenna size on gain, bandwidth, and efficiency," *J. Res. Nat. Bur. Stand.*, vol. 64D, pp. 1-12, 1960.
- [4] H. A. Wheeler, "Small antennas," *IEEE Trans. Antennas Propagat.*, vol. 23, pp. 462-469, Jul. 1975.
- [5] R. E. Collin, "Small antennas," *IEEE Trans. Antennas Propagat.*, vol. 12, pp. 23-27, Jan. 1964.
- [6] R. C. Hansen, "Fundamental limitations in antennas," *Proc IEEE*, vol. 69, pp. 170-182, Feb. 1981.
- [7] R. Azadegan, K. Sarabandi, "A novel approach for miniaturization of slot antennas," *IEEE Trans. Antennas Propagat.*, vol. 51, pp. 421-429, Mar. 2003.
- [8] K. Sarabandi, R. Azadegan, "Design of an Efficient Miniaturized UHF Planar Antenna," *Antennas and Propagation Society International Symposium, AP-S. Digest*, vol. 4, pp. 446-449, 2001.
- [9] C. A. Balanis *Antennas Theory Analysis and Design*, 2nd edition John-Wiley, 1997.
- [10] R. S. Elliot *Antennas Theory and Design*, Prentice-Hall, 1981.
- [11] RT/duroid 5880, *Roger Corporation Microwave Material Division*.
- [12] IE3D, Electromagnetic Simulation and Design Package, *Zeland Software Inc.*, ver. 10.
- [13] K. V. Pugilia, "Application notes: Electromagnetic simulation of some common balun structures," *IEEE Microwave Mag.*, pp. 56-61, Sep. 2002.
- [14] Y. Mushiake *Self-Complementary Antennas*, Springer-Verlag, 1996.
- [15] T. Ishizone, Y. Mushiake, "A self-complementary antenna composed of unipole and notch antennas," *Antennas and Propagation Society International Symposium, AP-S. Digest*, vol. 15, pp. 215-218, 1977.
- [16] P. Xu, k. Fujimoto, L. Shiming, "Performance of quasi-self-complementary antenna using a monopole and a slot," *Antennas and Propagation Society International Symposium, AP-S. Digest*, vol. 2, pp. 464-467, 2002.

A Novel Approach for Miniaturization of Slot Antennas

Reza Azadegan, *Student Member, IEEE*, and Kamal Sarabandi, *Fellow, IEEE*

Abstract—With the virtual enforcement of the required boundary condition (BC) at the end of a slot antenna, the area occupied by the resonant antenna can be reduced. To achieve the required virtual BC, the two short circuits at the end of the resonant slot are replaced by some reactive BC, including inductive or capacitive loadings. The application of these loads is shown to reduce the size of the resonant slot antenna for a given resonant frequency without imposing any stringent condition on the impedance matching of the antenna. In this paper, a procedure for designing this class of slot antennas for any arbitrary size is presented. The procedure is based on an equivalent circuit model for the antenna and its feed structure. The corresponding equivalent circuit parameters are extracted using a full-wave forward model in conjunction with a genetic algorithm optimizer. These parameters are employed to find a proper matching network so that a perfect match to a $50\ \Omega$ line is obtained. For a prototype slot antenna with approximate dimensions of $0.05\lambda_0 \times 0.05\lambda_0$ the impedance match is obtained, with a fairly high gain of -3 dBi, for a very small ground plane ($\approx 0.20\lambda_0$). Since there are neither polarization nor mismatch losses, the antenna efficiency is limited only by the dielectric and Ohmic losses.

Index Terms—Miniaturized antenna, slot antenna.

I. INTRODUCTION

THE TOPIC of small antennas has been a subject of interest for more than half a century, but in recent years, it has attained significant attention because of an exorbitant demand for mobile wireless communication systems. The need for antenna miniaturization stems from the fact that most mobile platforms have a limited space for all of the required antennas in ever increasing wireless systems. Compact antennas are needed so that more antennas can be closely packed together without the risk of mutual and parasitic coupling between them. For local area networks, there is an emerging interest in making antennas small enough to ultimately fit on a single chip with the rest of the receiving front-end. As part of a general trend in monolithic circuit integration, using the area of substrate more efficiently is another strong motivation. At low frequencies (HF–VHF), miniature antennas are in high demand, since the antenna size often imposes a significant limitation on the overall size of a portable wireless system.

Earlier studies on small antennas focused on establishing a relation between the volume occupied by the antenna to radiation characteristics and the bandwidth of the antenna [1]–[4]. In these studies, a relation between the Quality Factor (Q) of the

antenna and the radius of the smallest fictitious spherical enclosure containing the antenna was derived. This derivation was based on the spherical wave function expansion of the fields radiated from the antenna. Each spherical mode was represented by an equivalent circuit for which a quality factor (Q_n) was calculated. Since the spherical eigenfunctions are orthogonal, no energy could be coupled among modes. Therefore, the Q of the antenna was expressed as a function of the Q of individual modes. Finally, it was shown that the quality factor of the lowest order mode is a lower bound for the Q of a single resonant antenna [2]. A similar approach was adopted by Collin [5] for cylindrical antennas using cylindrical wave functions to provide a tighter lower limit on the Q of thin antennas with large aspect ratios. Results of these studies have been summarized and referred to as the fundamental limitations of small antennas [6]. However, in the aforementioned papers there are no discussions about procedures to design miniaturized antennas.

In addition to high Q , a direct result of antenna miniaturization is reduction in the antenna efficiency owing to the relatively high conduction and/or polarization currents on the conductors or within the dielectric part of the antenna structure. Furthermore, the matching network of a miniaturized antenna is usually complex and lossy. An example of miniaturized antennas is a meandered antenna where a half wavelength dipole is made compact by meandering the wire [7]. A similar approach can be applied to design a meander type slot antenna [8]. In order to increase the efficiency of these antennas by reducing dissipation, the use of a high temperature superconductor (HTS) has been proposed [9], [10]. On the other hand, meandered antennas are very hard to match to a $50\text{-}\Omega$ line. This difficulty is due to the fact that the radiation of almost in-phase electric currents flowing in opposite directions on closely spaced wires tend to cancel each other in the far-field region. This cancellation renders a considerable portion of opposing currents ineffective as far as radiation efficiency is concerned and leads to a very low radiation resistance that might have been increased using a two-strip meandered line [11]. Consequently, these antennas are difficult to match, and yet require a very low temperature of operation to control material losses [12].

Another approach for antenna miniaturization, reported in the literature, is to use very high dielectric constant materials in dielectric loaded antennas [13], [14]. Obviously, dielectric loading provides a size reduction factor on the order of $\sqrt{\epsilon_r}$ for the leaky dielectric and cavity resonator type antennas (e.g., microstrip patch antennas), where ϵ_r is the relative permittivity of the dielectric material. This miniaturization method, however, is less effective for terminated transmission line antennas, such as slot or printed dipole antennas since these antennas see an effective permittivity (ϵ_{eff}), which is considerably less than ϵ_r .

Manuscript received August 24, 2001; revised February 18, 2002.

The authors are with the Radiation Laboratory, Department of Electrical Engineering and Computer Science, The University of Michigan, Ann Arbor, MI 48109 USA.

Digital Object Identifier 10.1109/TAP.2003.809853

Although this method of miniaturization is susceptible to surface wave excitation, it might be found beneficial, especially when the electrical thickness of the substrate is small compared to the wavelength. It is worth mentioning that this type of antenna miniaturization is not immune to the aforementioned adverse effects such as high Q , low efficiency, and complexity in the matching network.

Nevertheless, there is another important methodology in antenna miniaturization; that is, modifying the antenna geometry. Recently a new topology based on an S-shape quarter wavelength resonant slot antenna was reported by the authors [15]. A miniaturized quarter wavelength slot antenna was proposed using a short circuit at one end of the slot and an open circuit at the other end. The open circuit was realized by a coiled quarter wavelength slot-line. Using this design, a very efficient miniaturized antenna with dimensions of the order of $0.12\lambda_0 \times 0.12\lambda_0$ on a substrate having $\epsilon_r = 4.0$ was constructed using a microstrip feed.

In this paper, we propose a novel procedure to design a miniaturized slot antenna where its dimensions (relative to wavelength) can be arbitrarily chosen, depending on the application, without any adverse effects on the impedance matching. As will be shown, in order to fine-tune the resonant frequency of this structure, the antenna is first fed by a two-port microstrip line, and then the location of the null in the insertion loss (S_{21}) is found and adjusted. To specify the terminating impedance at the second port in such a way that a perfect match is achieved, an equivalent circuit for the antenna is proposed and its parameters are extracted using a genetic algorithm (GA) in conjunction with a full-wave simulation tool. Finally, a prototype antenna is designed, fabricated, and its performance is evaluated experimentally.

II. ANTENNA GEOMETRY

For a resonant slot antenna, one needs to apply two boundary conditions (BCs) at both ends of a slot line to form a resonant standing wave pattern. These two conditions are chosen so as to enforce zero electric current (open circuit) for a wire antenna or zero voltage (short circuit) for the slot antenna, and yield a half-wave resonant antenna. On the other hand, these alternative BCs result in a smaller resonant length than a half wavelength antenna [16]. One choice which is conducive to antenna miniaturization is the combination of a short circuit and an open circuit, which allows a shorter resonant length of $\lambda/4$ [15]. The choice of the two BCs, however, is not restricted to the above conditions, whereas the effect of reactive BCs in reducing the resonant length and antenna miniaturization is investigated in what follows.

A. Slot Radiator Topology

Starting from a $\lambda_s/2$ slot and in the view of the transmission line approximation for the slot dipole, the equivalent magnetic current distribution along a linear slot antenna can be expressed as

$$M(z) = M_0 \cos\left(\frac{\pi}{\lambda_s} z\right) \quad (1)$$

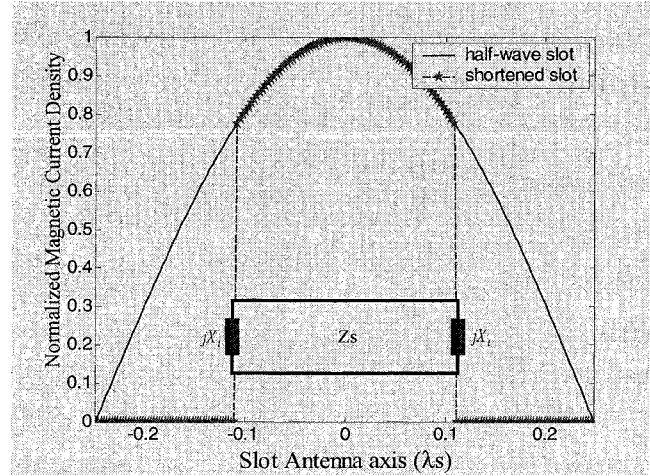


Fig. 1. Magnetic current distribution on a half wavelength and inductively terminated miniaturized slot antenna.

where λ_s is the guided wavelength in the slot-line. In (1), M_0 represents the amplitude of the magnetic current density (electric field across the slotline). This approximate form of the current distribution satisfies the short circuit BCs at the end of the slot antenna. If by using an appropriate boundary condition, the magnetic current density at any arbitrary point $|z'| < \lambda_s/4$ along the length of a modified slot antenna can be maintained the same as the $\lambda_s/2$ slot antenna, then it is possible to make a smaller slot antenna. Any size reduction of interest can be achieved so long as the appropriate BCs are in place at the proper location on the slot. Fig. 1 illustrates the idea where it is shown that by imposing a finite voltage at both ends of a slot, the desired magnetic current distribution on a short slot antenna can be established.

To create a voltage discontinuity, one can use a series inductive element at the end of the slot antenna. It should be pointed out that terminating the slot antenna with a lumped inductance or capacitance is not practical since the slot is embedded in a ground plane, which can in fact short-circuit any termination. To circumvent this problem, a lumped inductor could be physically realized by a compact short-circuited slotted spiral. To ensure inductive loading, the length of the spiral slot must be less than a quarter wavelength. Instead of a single inductive element at each end, it is preferred to use two inductive slotlines opposite of each other [see Figs. 2(c) and 3]. Since these two inductors in the slot configuration are in series, a shorter slotline provides the required inductive load at the end of the slot antenna. Another reason for choosing this configuration is that the magnetic currents flowing in opposite directions cancel each other's fields on the planes of symmetry, and thereby, minimize the near-field coupling effect of the inductive loads on the desired current distribution along the radiating slot.

It should be noted that the mutual coupling within the spiral slotline reduces the effective inductance, and therefore, a longer spiral length compared with a straight section [Fig. 2(c)] is needed to achieve the desired inductance. To alleviate this adverse effect, a narrower slot width must be chosen for the spiral slotline.

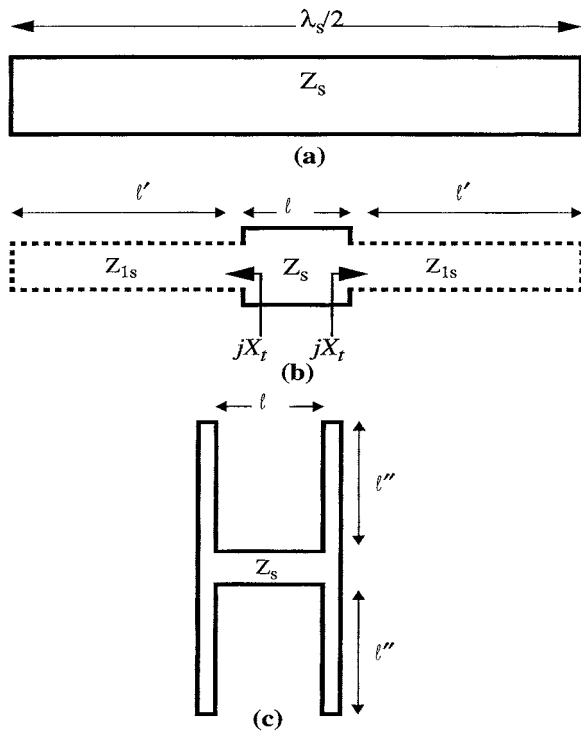


Fig. 2. Transmission line model of a slot antenna (a) half-wave slot antenna. (b) Inductively terminated slot antenna. (c) Two series inductive terminations.

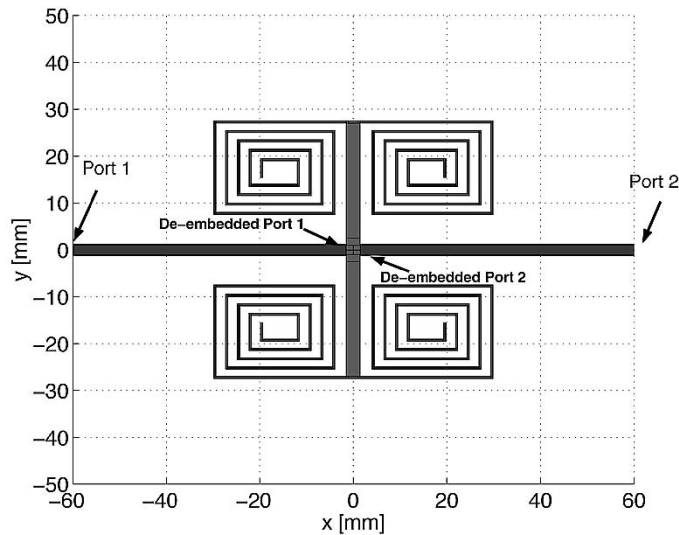


Fig. 3. Proposed antenna geometry fed by a two-port microstrip feed. This two-port geometry is used to find out the exact resonant frequency of the inductively loaded slot.

B. Antenna Feed

A microstrip transmission line is used to feed this antenna. The choice of the microstrip feed, as opposed to a coaxial line, is based on the ease of fabrication and stability. This feed structure is also more amenable to tuning by providing the designer with an additional parameter. Instead of short-circuiting the microstrip line over the slot, an open-ended microstrip line with an appropriate length extending beyond the microstrip-slot crossing point (additional parameter) can be used.

A coplanar waveguide (CPW) can also be used to feed the antenna providing the ease of fabrication, whereas it is more

TABLE I
SLOTLINE CHARACTERISTICS FOR TWO DIFFERENT VALUES OF SLOT WIDTH w , AND THE DIELECTRIC CONSTANT OF $\epsilon_r = 2.2$ AND THICKNESS OF $h = 0.787$ (mm) AND $f = 300$ MHz

w (mm)	λ_s (mm)	Z_{0s} (Ω)
0.5	918	81
3.0	960	107

difficult to tune. Usually, a metallic bridge is needed to suppress the odd mode in the CPW. The use of CPW lines also reduces the effective aperture of the slot antenna, especially when a very small antenna is to be matched to a 50- Ω line. Typically for a low dielectric constant substrate, the center conductor in the CPW lines at 50 Ω is rather wide and the gap between the center conductor and the ground planes is relatively narrow. Hence, feeding the slot antenna from the center blocks a considerable portion of the miniaturized slot antenna [17]. There are other methods to feed the slot antenna with CPW lines, including an inductively or capacitively fed slot [18].

III. DESIGN PROCEDURE

In this section, a procedure for designing a novel miniaturized antenna with the topology discussed in the previous section is presented. To illustrate this procedure, a miniaturized slot antenna at 300 MHz is designed. This frequency is the lowest frequency at which we could accurately perform antenna measurements in the anechoic chamber, and yet, the miniature antenna is large enough so that standard printed circuit technology can be used in the fabrication of the antenna. A microwave substrate with a dielectric constant of $\epsilon_r = 2.2$, a loss tangent of $\tan \delta \approx 10^{-3}$, and a thickness of 0.787 mm (31 mil) [19] is considered for the antenna prototype.

As the first step, the basic transmission line model is employed to design the antenna and then, a full-wave Moment Method analysis is used for fine tuning. Table I shows the finite ground plane slotline characteristic impedance Z_{0s} and guided wavelength λ_s for the above mentioned substrate and for two slot widths of $w = 0.5$ mm and $w = 3.0$ mm, all at 300 MHz. As mentioned before, the antenna size can be chosen as a design parameter, and in this example, we attempt to design a very small antenna with a length of $\ell = 55$ mm $\approx 0.05\lambda_0$. A slot width of $w = 3$ mm is chosen for the radiating section of the slot antenna. A slot antenna whose radiating slot segment is of a length ℓ , should be terminated by a reactance given by

$$X_t = Z_{0s} \tan \frac{2\pi}{\lambda_s} \ell \quad (2)$$

in order to maintain the magnetic current distribution of a $\lambda_s/2$ resonant slot antenna (see Fig. 2). In (2)

$$\ell = \frac{1}{2} \left(\frac{\lambda_s}{2} - \ell \right) \quad (3)$$

and Z_{0s} and λ_s are the characteristic impedance and the guided wavelength of the slotline, respectively. As mentioned before, the required terminating reactance of X_t can be constructed by two smaller series slotlines. Denoting the length of a terminating

slotline by ℓ'' , as shown in Fig. 2(c), the relationship between the required reactance and ℓ'' is given by

$$\frac{X_t}{2} = Z'_{0s} \tan \frac{2\pi}{\lambda'_{0s}} \ell'' \quad (4)$$

where Z'_s and λ'_s are the characteristic impedance and the guided wavelength of the terminating slotline. A narrower slot is used to construct the terminating slotlines so that a more compact configuration can be achieved. As shown in Table I, the narrower slotline has a smaller characteristic impedance and guided wavelength which results in a slightly shorter length of the termination (ℓ''). Although ℓ'' is smaller than ℓ' , the actual miniaturization is obtained by winding the terminating line into a compact spiral as seen in Fig. 3.

According to (2) and (4), and also the values for the guided wavelengths, ℓ'' is found to be $\ell'' = 193.7$ mm. Referring to Fig. 3, the vertical dimension (along the y axis) of the rectangular spiral should not exceed half of the length of the radiating slot segment (ℓ). This constraint on the inductive rectangular spiral is imposed so that the entire antenna structure can fit into a square area of $55 \text{ mm} \times 55 \text{ mm}$, which is about $0.05\lambda_0 \times 0.05\lambda_0$. Since the dielectric constant and the thickness of the substrate chosen for this design are very low ($\epsilon_r = 2.2$), the guided wavelength ($\lambda_s = 96 \text{ cm}$) is not very much different from that of free space ($\lambda_0 = 100 \text{ cm}$). Thus, the miniaturization is mainly achieved by the proper choice of the antenna topology. It is worth mentioning that further size reduction can be obtained once a substrate with higher permittivity is used.

IV. FULL-WAVE SIMULATION AND TUNING

In Section III, the transmission line model was employed for designing the proposed miniature antenna. Although this model is not very accurate, it provides the intuition necessary for designing the novel topology. The transmission line model ignores the coupling between the adjacent slot lines and the microstrip to slot transition. For calculation of the input impedance and exact determination of the length of different slotline segments, a full-wave simulation tool is required. IE3D, a commercially available Moment Method code is used for required numerical simulations [20].

Fig. 3 shows the proposed antenna geometry fed by a two-port 50Ω microstrip line. The two-port structure is constructed to study the resonant frequency of the antenna as well as the transition between microstrip and the slot antenna. The microstrip line is extended well beyond the slot transition point so that the port terminals do not couple to the slot antenna. The radiating slot length is chosen to be $\ell = 55 \text{ mm}$, and the length of the rectangular spirals are tuned such that the antenna resonates at 300 MHz. The resonance at the desired frequency is indicated by a deep null in the frequency response of S_{21} . The simulated S-parameters of this two-port structure are shown in Fig. 4. This figure indicates that the antenna resonates at around 304 MHz, which is close to the desired frequency of 300 MHz. In fact, the resonant frequency of the radiating structure must be chosen at a slightly higher or lower frequency. The reason is that small slot antennas have a low radiation conductance at the first resonance and therefore, it should be tuned slightly off-resonance if it is to be matched to a $50\text{-}\Omega$ transmission line. Fig. 5 shows an

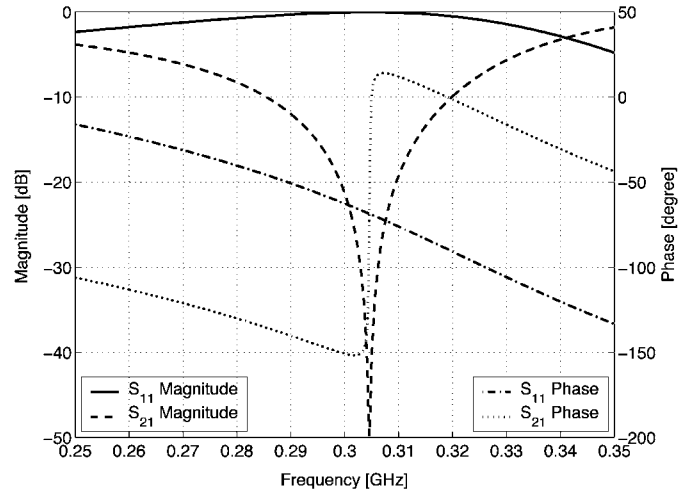


Fig. 4. S-parameters of the two-port antenna shown in Fig. 3.

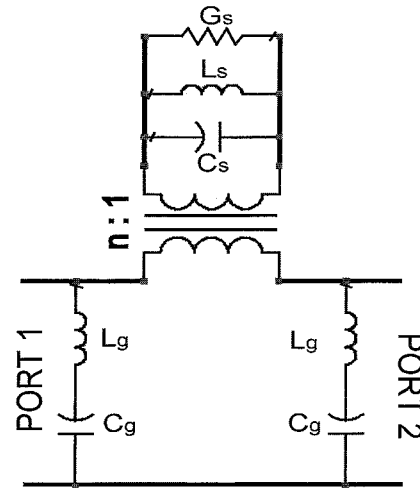


Fig. 5. Topology of the equivalent circuit for the two-port antenna.

equivalent circuit model for the two-port device when the transition between microstrip and slot line is represented by an ideal transformer with a frequency dependent turn ratio (n^2) [21], and the slot is modeled by a second order shunt resonant circuit near its resonance [22]. The radiation conductance G_s , which is also referred to as the slot conductance, attains a low value that corresponds to a very high input impedance at the resonant frequency. However, this impedance would decrease considerably, when the frequency moves off the resonance. The 4 MHz offset in the resonant frequency of the antenna is maintained for this purpose.

Having tuned the resonant frequency of the antenna, coupled to the two-port microstrip feed (Fig. 3), we need to design a lossless impedance matching network. This can be accomplished by providing a proper impedance to terminate the second port of the microstrip feed line. To fulfill these tasks systematically, we need to extract the equivalent circuit parameters shown in Fig. 5. It should be pointed out that for the proposed miniaturized slot antenna, a simplistic model for standard size slots, which treats the slot antenna as an impedance in series with the microstrip line is not sufficient. Essentially, the parasitic effects caused by the coupling between the microstrip feed and rectangular spirals

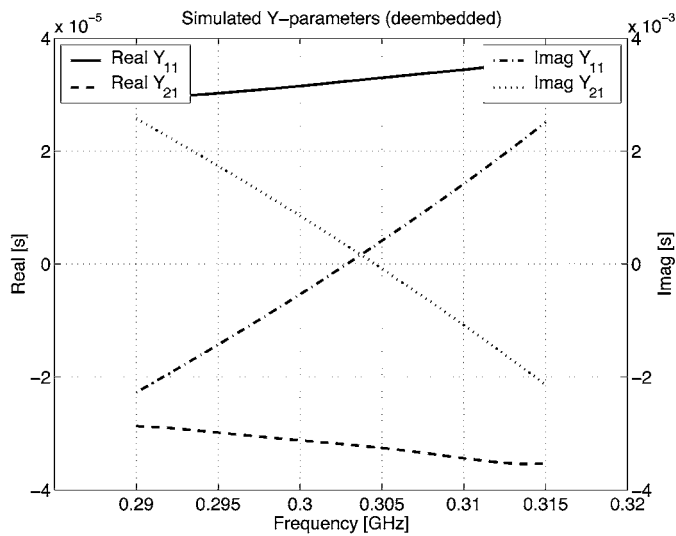


Fig. 6. Y -parameters of the two-port antenna after deembedding the microstrip feed lines.

as well as the mutual coupling between the radiator section and the rectangular spirals should also be included in the equivalent circuit.

A. Equivalent-Circuit Model

In this section, an equivalent circuit model for the proposed antenna is developed. This model is capable of predicting the slot radiation conductance and the antenna input impedance near resonance. This approach provides very helpful insight as to how this antenna and its feed network operate. As mentioned before, this model is also needed to find a proper matching network for the antenna.

Near resonant frequencies, the slot antenna can be modeled by a simple second order RLC circuit. Since the voltage across the slot excites the slot antenna at the feed point, it is appropriate to use the shunt resonant model for the radiating slot as shown in Fig. 5. The coupling between the microstrip and the slot is modeled by a series ideal transformer with a turn ratio n .

To model the feeding mechanism right at the cross junction of the microstrip and slot, it is necessary to deembed the effect of the microstrip lines between the terminals and the crossing points. There are different deembedding schemes reported in [24] and [25]. The advantage of proper deembedding, as opposed to the mere shifting of the reference planes by the corresponding phase factor is to exclude the effect of radiation and other parasitic effects of the line.

To model the parasitic coupling of the microstrip line and the slot (coupling of radiated field from the microstrip line and slot), two additional parasitic parameters, namely, L_g and C_g are included in the model. The use of shunt parasitic parameters has previously been suggested to model the effects of fields as perturbed by a wide slot [23]. Fig. 6 shows the deembedded Y -parameters of the two-port microstrip-fed slot antenna where the location of deembedded ports are shown in Fig. 3. Note that these two ports are now defined at the microstrip-slot junction.

TABLE II
THE PARAMETERS OF THE GENETIC ALGORITHM OPTIMIZER

Population Size	300
Number of Iteration	50,000
Chromosome Length	128
$P_{Crossover}$	0.55
$P_{Mutation}$	0.005

TABLE III
THE EQUIVALENT CIRCUIT PARAMETERS OF THE MICROSTRIP FED SLOT ANTENNA

Turn Ratio (n)	0.948007
$R_s(\Omega)$	33979
$L_s(\mu H)$	0.0207
$C_s(pF)$	13.1744
$L_g(\mu H)$	0.49997
$C_g(pF)$	0.125

According to the lumped element model of Fig. 5, the Y -parameters are given by

$$Y_{11} = \frac{-j}{L_g\omega - \frac{1}{C_g\omega}} + \frac{1}{n^2} \left[G_s + j \left(C_s\omega - \frac{1}{L_s\omega} \right) \right] \quad (5)$$

$$Y_{21} = -\frac{1}{n^2} \left[G_s + j \left(C_s\omega - \frac{1}{L_s\omega} \right) \right]. \quad (6)$$

Using reciprocity and noting the symmetry of the equivalent circuit, it can easily be shown that $Y_{11} = Y_{22}$ and $Y_{21} = Y_{12}$.

In order to extract the equivalent circuit parameters, a GA optimization code has been developed and implemented [26]. The sum of the squares of relative error for real and imaginary parts of Y -parameters over 40 frequency points around the resonance is used as the objective (fitness) function of the optimization problem. We ran the program with different random number seeds to ensure the best result over the entire domain of the parameters space. Also, the parameters were constrained only to physical values in the region of interest. The parameters of the GA optimizer are shown in Table II. Table III shows the extracted equivalent circuit parameters after 50,000 iterations.

The S -parameters of the equivalent circuit as well as the S -parameters extracted from the full-wave analysis are shown in Fig. 7. Excellent agreement is observed between the full-wave results and those of the equivalent circuit.

B. Antenna Matching

Having found the equivalent circuit parameters, the antenna's matching network can readily be designed. For matching networks, especially when efficiency is the main concern, lossless terminations are usually desired. Therefore, we seek a purely reactive admittance to terminate the feed line, which in fact is the load for the second port of the two-port equivalent circuit model. The explicit expression for a termination admittance (Y_t) to be placed at the second terminal of the two-port model in order to match the impedance of the antenna is given by

$$Y_t = -Y_{11} + \frac{Y_{12}^2}{Y_{11} - Y_0}. \quad (7)$$

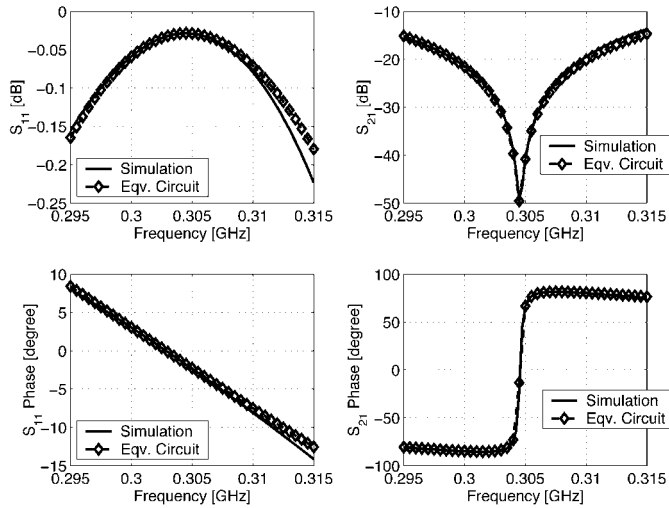


Fig. 7. Comparison between the full-wave simulated S -parameters of the antenna and that of the equivalent circuit.

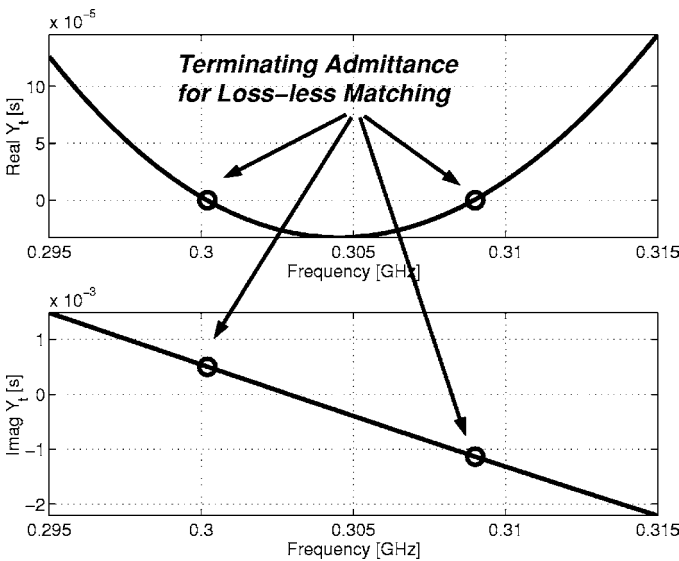


Fig. 8. The required terminating admittance for the second port of the two-port model in order to match the antenna to a $50\text{-}\Omega$ line.

Fig. 8 shows the spectral behavior of Y_t for a standard $50\text{-}\Omega$ line ($Y_0 = 0.02 \text{ U}$). Interesting to note are the two distinct frequency points at which the real part of Y_t vanishes. This implies that we can match this antenna at these two frequency points, namely, 300 and 309 MHz. As mentioned earlier, a small slot antenna has a very low radiation conductance. The value of this low conductance, shown in Table III, suggests a very high input impedance of the order of $30 \text{ K}\Omega$ at resonance, considering the transformer turn ratio. Thus, in order to match the antenna to a lower impedance transmission line, the matching should be done at a frequency slightly off the resonance. At an off-resonance frequency, the input impedance does not remain a pure real quantity, however, the imaginary part can easily be compensated for by an additional reactive component created by an open-ended microstrip. At each resonance, there are two possibilities. One possibility is to match the antenna slightly below the slot resonance, that is 304 MHz (Fig. 4), and terminate the second

TABLE IV
THE PHYSICAL LENGTH OF THE $50\text{-}\Omega$ MICROSTRIP LINE NEEDED FOR REALIZING THE TERMINATION SUSCEPTANCE, WHERE THE DIELECTRIC MATERIAL PROPERTIES ARE AS SPECIFIED IN TABLE I

f (MHz)	300	309
$Y_t(s)$	$j5.4 \times 10^{-4}$	$-j1.14 \times 10^{-3}$
λ_g (mm)	725.57	704.52
$Z_0(\Omega)$	50	50
Line extension (mm)	3.1514	345.80

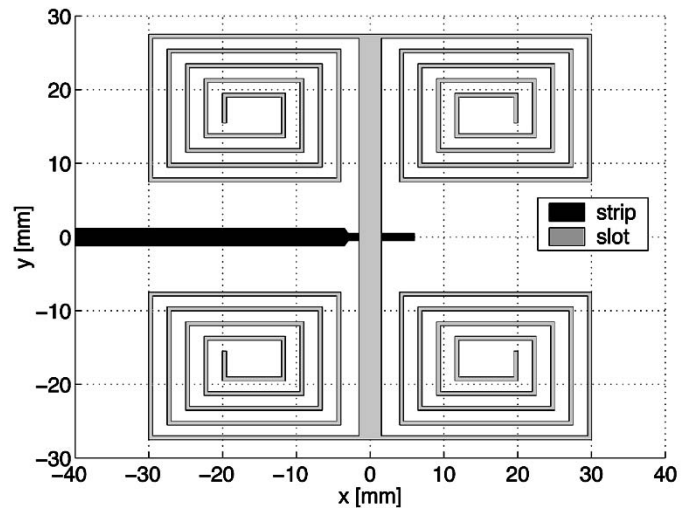


Fig. 9. The geometry of the antenna and its feed designed to operate at 300 MHz.

port capacitively. The second possibility is to tune the antenna slightly above the slot resonance and terminate the second port inductively.

Based on what is shown in Table IV, a very short open-ended-microstrip line extension is required at the second port, in contrast with a quarter wavelength extension for an ordinary half wavelength slot antenna. This short extension introduces a small capacitance, which compensates the additional inductance introduced as a result of operating below resonance. After tuning the antenna, the original slot resonant frequency at 304 MHz, shifts down to the desired frequency of 300 MHz, as shown in Fig. 8 and Table IV.

V. ANTENNA SIMULATION AND MEASUREMENTS

In this section, simulation results for the proposed antenna are illustrated. Fig. 9 shows the antenna geometry matched to a $50\text{-}\Omega$ line. As seen in this figure and suggested by Table IV, the feed line has been extended a short distance beyond the slot line. The width of the microstrip, where it crosses the slot, is reduced so that it may block a smaller portion of the radiating slot. It is worth mentioning that the effect of the feed linewidth on its coupling to the slot was investigated, and it was found that as long as the linewidth is much smaller than the radiating slot length, the equivalent circuit parameters do not change considerably.

As mentioned, the antenna has been simulated using a commercial software (IE3D) [20]. Using this software, the return loss (S_{11}) of the antenna is calculated and shown in Fig. 10. In

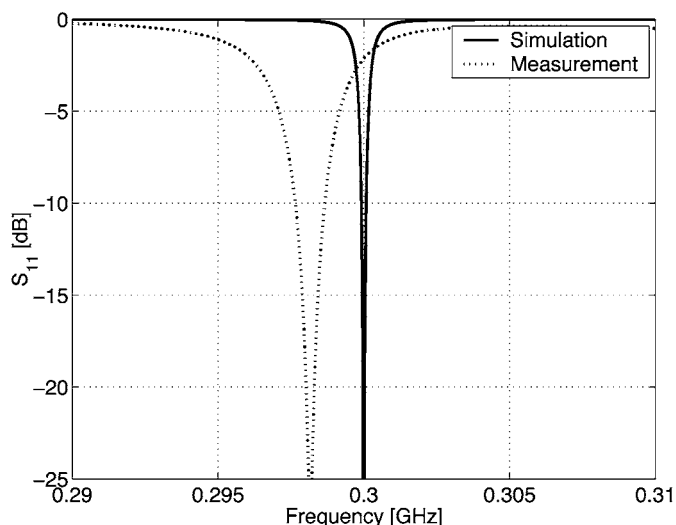


Fig. 10. Measured and simulated return loss of the miniaturized antenna.

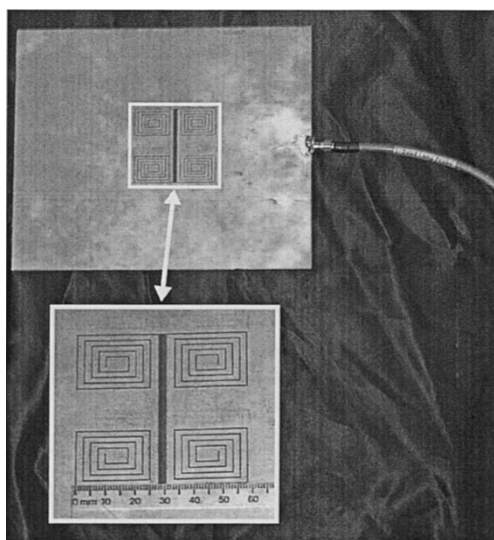


Fig. 11. A photograph of the fabricated antenna.

order to experimentally validate the design procedure, equivalent circuit model, and simulation results, the antenna was fabricated on a 0.787-mm-thick substrate with $\epsilon_r = 2.2$ and $\tan \delta = 0.001$.

Fig. 11 shows a photograph of the fabricated antenna. The return loss (S_{11}) of the antenna was measured using a calibrated vector network analyzer and the result is shown in Fig. 10. The measured results show a slight shift in the resonant frequency of the antenna ($\approx 1\%$) from what is predicted by the numerical code. The errors associated with the numerical code could contribute to this frequency shift. This deviation can also be attributed to the finite size of the ground plane, $0.21\lambda_0 \times 0.18\lambda_0$ for this prototype, knowing that an infinite ground plane is assumed in the numerical simulation. The shift in the resonant frequency resulted from the finite size of the ground plane for slot antennas is discussed in [15].

The far-field radiation patterns of the antenna were measured in the anechoic chamber of The University of Michigan. The gain of the antenna was measured at the bore-sight direction

TABLE V
ANTENNA CHARACTERISTICS AS A FUNCTION OF TWO DIFFERENT SIZE GROUND PLANES COMPARED WITH THE SIMULATED RESULTS FOR THE SAME ANTENNA ON AN INFINITE GROUND PLANE

Ground-Plane size [cm]	Resonant frequency [MHz]	Return Loss [dB]	Antenna Gain [dBi]
21×18	298.1	-27	-3.0
58×43	298.8	-30	0.6
$simulation(\infty)$	300	< -30	0.75

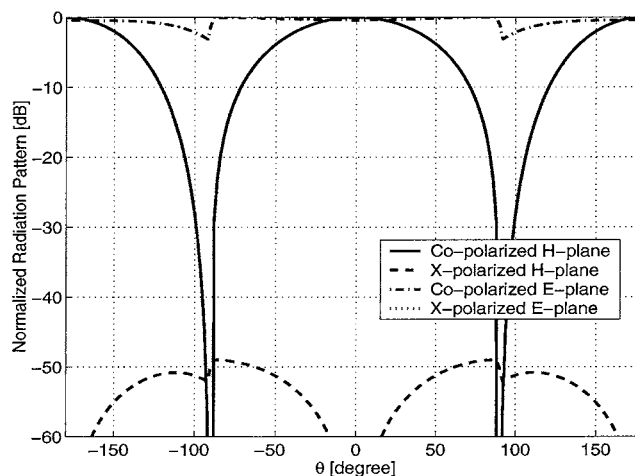


Fig. 12. Simulated radiation pattern of the miniaturized antenna.

under polarization-matched condition using a standard antenna whose gain is known as a function of frequency. The gain of -3 dBi (relative to an isotropic radiator) was measured. Having perfectly matched the impedance of the antenna, the simulated efficiency of this antenna is found to be $\eta = 87\%$ (-0.6 dB), which can exclusively be attributed to dielectric loss. Obviously, the contribution of the conductor loss, which is the main source of dissipation in slot antennas, is not accounted for in the simulated antenna efficiency. The simulated radiation efficiency is the ratio of the total radiated power to the input power of the antenna. The directivity of this antenna (with infinite ground plane) was computed to be $D = 2.0$ dB. This value of directivity is very close to that of a dipole antenna. Based on the definition of the antenna gain [16], under the impedance matched condition, one might expect to measure the maximum gain of

$$G = \eta \cdot D = -0.6 \text{ dB} + 2.0 \text{ dB} = 1.4 \text{ dB} \quad (8)$$

for this antenna. There is still a considerable difference between the measured and simulated gains (about 4.4 dB), which stems from two major factors, in addition to the ohmic loss of the ground plane. First, in the simulation, an infinite ground plane is assumed, whereas the actual ground plane size for the measured antenna is approximately $0.2\lambda_0 \times 0.2\lambda_0$. As the ground plane size decreases, the level of electric current around the edges increases considerably. This increase in the level of the electric current results in an additional ohmic loss compared to the infinite ground plane. Another reason is that as the ground plane size decreases, the directivity of the slot antenna is reduced. Basically, as the ground plane becomes smaller, the null in the pat-

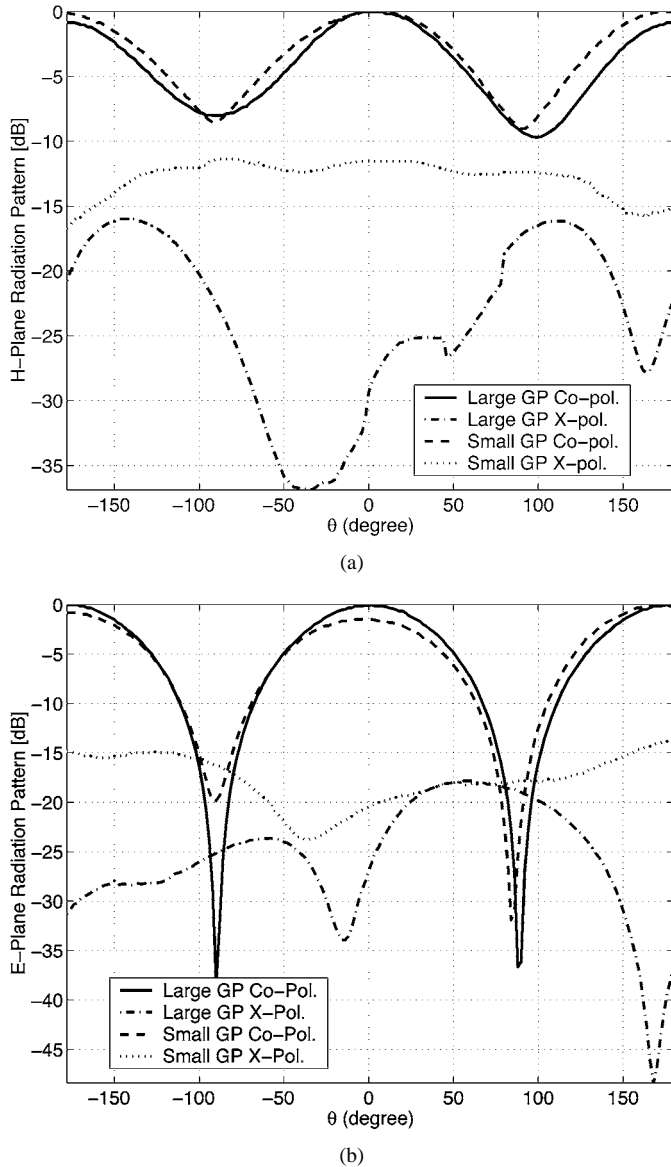


Fig. 13. Measured radiation patterns of the antenna with a small ($0.2\lambda_0 \times 0.2\lambda_0$) and a larger ($0.5\lambda_0 \times 0.5\lambda_0$) Ground Plane (GP): (a) H plane pattern. (b) E plane pattern.

tern diminishes and the pattern approaches that of an isotropic radiator. The reduction in the directivity of the slot antenna with a finite ground plane can also be attributed to the radiation from the edges and surface wave diffraction [27]. To further study the effect of the size of the ground plane, the same antenna with a slightly larger ground plane ($0.58\lambda_0 \times 0.43\lambda_0$) was fabricated and measured. Table V shows the comparison between the radiation characteristics of these two antennas and simulated results. As explained, when the size of the antenna ground plane increases, the gain of the antenna increases from -3.0 dBi to 0.6 dBi, which is almost equal to the gain of a half wavelength dipole and very close to the simulated value for the antenna gain.

Finally, the radiation patterns of the proposed antenna in the principal E and H plane were measured and compared with the theoretical ones. For H plane pattern, we measured $E_\phi(\theta)$ in the $\phi = 90^\circ$ plane, and for E plane pattern, $E_\theta(\theta)$ was measured in the $\phi = 0^\circ$. The simulated radiation patterns of this antenna are

shown in Fig. 12. It is seen that the simulated radiation pattern of the proposed antenna with an infinite ground plane is almost the same as that of an infinitesimal slot dipole. Fig. 13(a) and (b) show the normalized co- and cross-polarized radiation patterns of the H and E plane, respectively, for two different ground planes. As expected, the null in the H plane radiation pattern is filled considerably, owing to the finite ground plane size. The ground plane enforces the tangential E -field, $E_\phi(\theta)$, to vanish along the radiating slot at $\theta = 90^\circ$, which in fact creates the null in the H plane pattern. On the other hand, a deep null in the measured E plane pattern is observed, whereas in simulation this cut of the pattern is constant except at the dielectric-air interface where the normal E -field is discontinuous. This null in the E plane is the result of the cancellation of fields, which are radiated by the two opposing magnetic currents. The equivalent magnetic currents, flowing in the upper and lower side of the ground plane, are in opposite directions and consequently, their radiation in the point of symmetry at the E plane cancel each other. However, in the case of an infinite ground plane, the upper and lower half-spaces are isolated, and therefore, the E plane radiation pattern remains constant.

Moreover, an increase in the measured cross-polarized component is observed as compared with the simulation results. Although it may seem that there is a considerable cross-polarization radiation due to the presence of spiral slots at the terminations, there is no such component in the principal planes as well as the $\phi = \pm 45^\circ$ planes since the geometry is symmetric with respect to those planes. The cross polarization appeared in these measurements is mainly caused by radiation from the edges as well as the feed cable. The contribution of the anechoic chamber, giving rise to the cross-polarized component at the low frequency of 300 MHz, is also a factor. The radiated field of the antenna is always capable of inducing currents on the feeding cable, especially when the ground plane size is very small compared to the wavelength. Then, the induced currents re-radiate and give rise to the cross polarization. Nevertheless, both of the above mentioned sources for the cross polarization can be eliminated by increasing the ground plane size.

VI. CONCLUSION

In this paper, a procedure for designing a new class of miniaturized slot antennas was proposed. In this design the area occupied by the antenna can be chosen to be arbitrarily small, depending on the applications at hand and the tradeoff between the antenna size and the required bandwidth. As an example, an antenna with the dimensions $0.05\lambda_0 \times 0.05\lambda_0$ was designed at 300 MHz and perfectly matched to a 50Ω transmission line. In this prototype, a substrate with a low dielectric constant of $\epsilon_r = 2.2$ was used to ensure that the dielectric material would not contribute to the antenna miniaturization. An equivalent circuit for the antenna was developed, which provided the guidelines necessary for designing a compact lossless matching network for the antenna. To validate the design procedure, a prototype antenna was fabricated and measured at 300 MHz. A perfect match for this very small antenna was demonstrated with a moderate gain of -3.0 dBi when the antenna is fabricated on a very small ground plane with the approximate dimensions of

$0.2\lambda_0 \times 0.2\lambda_0$. The gain of this antenna can increase to that of a half-wave dipole when a slightly larger ground plane of about $0.5\lambda_0 \times 0.5\lambda_0$ is used. The fractional bandwidth for this antenna was measured to be 0.034%.

REFERENCES

- [1] H. A. Wheeler, "Fundamental limitations of small antennas," *Proc. IRE*, vol. 35, pp. 1479–1484, Dec. 1947.
- [2] L. J. Chu, "Physical limitations of omni-directional antennas," *J. Appl. Phys.*, vol. 19, pp. 1163–1175, Dec. 1948.
- [3] R. F. Harrington, "Effect of antenna size on gain, bandwidth, and efficiency," *J. Res. Natl. Bur. Stand.*, vol. 64D, pp. 1–12, 1960.
- [4] H. A. Wheeler, "Small antennas," *IEEE Trans. Antennas Propagat.*, vol. AP-23, pp. 462–469, July 1975.
- [5] R. E. Collin, "Small antennas," *IEEE Trans. Antennas Propagat.*, vol. AP-12, pp. 23–27, Jan. 1964.
- [6] R. C. Hansen, "Fundamental limitations in antennas," *Proc IEEE*, vol. 69, pp. 170–182, Feb. 1981.
- [7] J. Rashed and C. T. Tai, "A new class of Resonant antennas," *IEEE Trans. Antennas Propagat.*, vol. 39, pp. 1428–1430, Sept. 1991.
- [8] J. M. Kim, J. G. Yook, W. Y. Song, Y. J. Yoon, J. Y. Park, and H. K. Park, "Compact meander-type slot antennas," in *Proc. Antennas Propagat. Soc. Int. Symp., AP-S. Dig.*, vol. 2, Boston, MA, July 2001, pp. 724–727.
- [9] L. P. Ivrisimtzis, M. J. Lancaster, and M. Esa, "Miniature super conducting coplanar strip antennas for microwave and mm-wave applications," in *PROC. IEEE AP-S 9th Int. Conf. Antennas Propagat.*, vol. 1, Apr. 1995, pp. 391–395.
- [10] L. P. Ivrisimtzis, M. J. Lancaster, T. S. M. Maclean, and N. McN. Alford, "High-gain series fed printed dipole arrays made of high-T superconductors," *IEEE Trans. Antennas Propagat.*, vol. 42, pp. 1419–1429, Oct. 1994.
- [11] K. Noguchi, N. Yasui, M. Mizusawa, S. Betsudan, and T. Katagi, "Increasing the bandwidth of a two-strip meander-line antenna mounted on a conducting box," in *Proc. Antennas Propagat. Soc. Int. Symp., AP-S. Dig.*, vol. 4, 2001, pp. 112–115.
- [12] H. Chaloupka, N. Klein, M. Peiniger, H. Piel, A. Pischke, and G. Splitt, "Miniaturized high-temperature superconductor microstrip patch antenna," *IEEE Trans. Microwave Theory Tech.*, vol. 39, pp. 1513–1521, Sept. 1991.
- [13] Y.-P. Zhang, T. K.-C. Lo, and Y.-M. Hwang, "A dielectric-loaded miniature antenna for micro-cellular and personal communications," in *Antennas Propagat. Soc. Int. Symp., AP-S. Dig.*, vol. 2, 1995, pp. 1152–1155.
- [14] Y. Hwang, Y. P. Zhang, K. M. Luk, and E. K. N. Yung, "Gain-enhanced miniaturized rectangular dielectric resonator antenna," *Electron. Lett.*, vol. 33, pp. 350–352, Feb. 1997.
- [15] K. Sarabandi and R. Azadegan, "Design of an efficient miniaturized UHF planar antenna," in *Proc. Antennas Propagat. Soc. Int. Symp., AP-S. Dig.*, vol. 4, 2001, pp. 446–449.
- [16] R. E. Collin, *Antennas and Radiowave Propagation*. New York: McGraw-Hill, 1985.
- [17] B. K. Kormanyos, W. Harokopus, L. Katehi, and G. Rebeiz, "CPW-fed active slot antennas," *IEEE Trans. Microwave Theory Tech.*, vol. 42, pp. 541–545, Apr. 1994.
- [18] S. Sierra-Garcia and J. Laurin, "Study of a CPW inductively coupled slot antenna," *IEEE Trans. Antennas Propagat.*, vol. 47, pp. 58–64, Jan. 1999.
- [19] Roger Corporation Microwave Material Division, "RT/duroid 5880,"
- [20] IE3D, "Electromagnetic Simulation and Optimization Package," Zeland Software, Inc., Fremont, CA, ver. 8.2.
- [21] K. C. Gupta, P. Garg, I. Bahl, and P. Bhartia, *Microstrip Lines and Slot-lines*, 2nd ed. Norwood, MA: Artec House, 1996.
- [22] H. G. Akhavan and D. Mirshekar-Syahkal, "Approximate model for microstrip fed slot antennas," *Electron. Lett.*, vol. 30, pp. 1902–1903, Nov. 1994.
- [23] L. Zhu and K. Wu, "Complete circuit model of microstrip-fed slot radiator: Theory and experiments," *IEEE Microwave Guided Wave Lett.*, vol. 9, pp. 305–307, Aug. 1999.

- [24] M. Fariana and T. Rozzi, "A short-open deembedding technique for method-of-moments-based electromagnetic analyzes," *IEEE Trans. Microwave Theory Tech.*, vol. 49, pp. 624–628, Apr. 2001.
- [25] L. Zhu and K. Wu, "Unified equivalent-circuit model of planar discontinuities suitable for field theory-based CAD and optimization of M(H)MIC's," *IEEE Trans. Microwave Theory Tech.*, vol. 47, pp. 1589–1602, Sept. 1999.
- [26] J. M. Johnson and Y. Rahmat-Samii, "Genetic algorithms in engineering electromagnetics," *IEEE Antennas Propagat. Mag.*, vol. 39, pp. 7–21, Aug. 1997.
- [27] B. Stockbroeckx, I. Huynen, and A. Vander Vorst, "Effect of surface wave diffraction on radiation pattern of slot antenna etched in finite ground plane," *Electron. Lett.*, vol. 36, pp. 1444–1446, Aug. 2000.



Reza Azadegan (S'98) was born in Tehran, Iran, on October 20, 1974. He received the B.S. degree from Sarif University of Technology, Tehran, Iran, and the M.S. degree, in electrical engineering, from K. N. Toosi University of Technology, Tehran, in 1996 and 1998, respectively. He is currently working toward the Ph.D. degree in the Radiation Laboratory at the University of Michigan, Ann Arbor.

From 1997 to 1999, he was with the Computational Electromagnetic Laboratory, Sharif University of Technology, as a Graduate Researcher working on the optimal design of parabolic reflector antennas using high-frequency techniques and genetic algorithms, and electromagnetic wave propagation in optical waveguides. He is working on the miniaturization of planar antennas and microwave filters for wireless communication systems.

Kamal Sarabandi (S'87–M'90–SM'92–F'00) received the B.S. degree in electrical engineering from Sharif University of Technology, Tehran, Iran, in 1980, the M.S. degree in electrical engineering in 1986, the M.S. degree in mathematics, and the Ph.D. degree in electrical engineering, all from The University of Michigan, Ann Arbor, in 1989.

He is Director of the Radiation Laboratory and a Professor with the Department of Electrical Engineering and Computer Science, University of Michigan. His research interests include microwave and millimeter-wave radar remote sensing, electromagnetic wave propagation, and antenna miniaturization. He has 20 years of experience with wave propagation in random media, communication channel modeling, microwave sensors, and radar systems and is leading a large research group, including two research scientists, ten Ph.D. and two M.S. students. Over the past ten years, he has graduated 14 Ph.D. students. He has served as the Principal Investigator on many projects sponsored by NASA, JPL, ARO, ONR, ARL, NSF, DARPA, and numerous industries. He has published many book chapters and more than 95 papers in refereed journals on electromagnetic scattering, random media modeling, wave propagation, antennas, microwave measurement techniques, radar calibration, inverse scattering problems, and microwave sensors. He also had more than 200 papers and invited presentations in many national and international conferences and symposia on similar subjects.

Dr. Sarabandi is a Vice President of the IEEE Geoscience and Remote Sensing Society (GRSS), Chairman of the Awards Committee of the IEEE GRSS, and a member of the IEEE Technical Activities Board Awards Committee. He is serving as the Associate Editor of the IEEE TRANSACTIONS ON ANTENNAS AND PROPAGATION (AP) and the *IEEE Sensors Journal*. He is a Member of Commission F of URSI and of The Electromagnetic Academy. He is listed in *American Men & Women of Science Who's Who in America* and *Who's Who in Electromagnetics*. He was the recipient of the prestigious Henry Russel Award from the Regent of The University of Michigan (the highest honor the University of Michigan bestows on a faculty member at the assistant or associate level). In 1999, he received a GAAC Distinguished Lecturer Award from the German Federal Ministry for Education, Science, and Technology given to about ten individuals worldwide in all areas of engineering, science, medicine, and law. In 1996, he received the Teaching Excellence Award from the EECSS Department, The University of Michigan.

Design of an Efficient Miniaturized UHF Planar Antenna

Kamal Sarabandi, *Fellow, IEEE*, and Reza Azadegan, *Student Member, IEEE*

Abstract—In this paper, the design aspects and the measured results of a novel miniaturized planar antenna are described. Such architectural antenna design is of great importance in mobile military communications where low visibility and high mobility are required. Slot radiating elements, having a planar geometry and capable of transmitting vertical polarization when placed nearly horizontal, are appropriate for the applications at hand. Slot antennas also have another useful property, so far as impedance matching is concerned. Basically, slot dipoles can easily be excited by a microstrip line and can be matched to arbitrary line impedances simply by moving the feed point along the slot. Antenna miniaturization can be achieved by using a high permittivity or permeability substrate and superstrate materials and/or using an appropriate antenna topology. Here, we demonstrate miniaturization by designing an appropriate geometry for a resonant narrow slot antenna. A very efficient radiating element that occupies an area as small as $0.12\lambda_0 \times 0.12\lambda_0$ is designed and tested. Simulation results, as well as the measured input impedance and radiation patterns of this antenna, are presented. This structure shows a measured gain of 0.5 dBi on FR4 substrate, which has a loss-tangent of the order of 0.01. Also, the effect of finite ground plane size on gain and resonant frequency is investigated experimentally.

Index Terms—Miniaturized antennas, small antennas, slot antennas.

I. INTRODUCTION

WITH THE advent of wireless technology and ever increasing demand for high data rate mobile communications the number of radios on military mobile platforms has reached a point that the available real estate for these antennas has become a serious issue. Similar problems are also emerging in the commercial sector where the number of wireless services planned for future automobiles, such as FM and CD radios, analog and digital cell phones, GPS, keyless entry, etc., is on the rise.

To circumvent the aforementioned difficulties to some extent, antenna miniaturization and/or compact multifunctional antennas must be considered. The subject of antenna miniaturization is not new. Literature concerning this subject dates back to the early 1940s [1], [2]. To our knowledge, the fundamental limitations of small antennas were first addressed by Chu in 1948 [2]. Using a multipole expansion and a clever equivalent

circuit model, Chu was able to derive the Q factor of the equivalent circuit for each spherical mode in terms of the normalized radius (a/λ) of the smallest sphere enclosing the antenna. In [2] it is also shown that the Q of the lowest order mode is a lower bound for the Q of a single resonant antenna. This subject was revisited by Wheeler [3], Harrington [4], and Collins [5]. In [5], a similar procedure is used for characterization of a small dipole antenna using cylindrical wave functions. Then a cylindrical enclosing surface is used which produces a tighter lower bound for the Q of small antennas with large aspect ratios such as dipoles and helical antennas. Qualitatively, these studies show that for single resonant antennas, the smaller the maximum dimension of an antenna, the higher is its Q or, equivalently, the lower is its bandwidth [6]. However, in these papers no discussion is provided about miniaturization methods, antenna topology, or impedance matching.

Considering wave propagation where line-of-sight communication is an unlikely event, such as in an urban environment or over irregular terrain, carrier frequencies at the HF–UHF band are commonly used. At these frequencies, there is considerable penetration through vegetation and buildings, wave diffraction around obstacles, and wave propagation over curved surfaces. However, at these frequencies, the size of efficient antennas are relatively large, and therefore, a large number of such antennas may not fit in the available space without the risks of mutual coupling and co-site interference. Efficient antennas require dimensions of the order of half a wavelength for single frequency operation. To cover a wide frequency range, broadband antennas may be used. However, dimensions of these antennas are comparable to or larger than the wavelength at the lowest frequency. Besides, depending on the applications, the polarization and the direction of maximum directivity for different wireless systems operating at different frequencies may be different and hence a single broadband antenna may not be sufficient. It should also be noted that any type of broadband antenna is highly susceptible to electronic warfare jamming techniques. Variations of monopole and dipole antennas in use today are prohibitively large and bulky at HF through VHF.

In this paper, the topology of an efficient, miniaturized, resonant slot antenna is presented, and then its radiation, input impedance, and bandwidth characteristics are investigated. This class of antennas can simultaneously exhibit band selectivity and antijam characteristics in addition to possessing a planar structure and low profile, which is easily integrable with other RF and microwave circuits.

In what follows, we first investigate the design aspects of a miniaturized resonant slot spiral (coiled dipole) at low frequencies. It is shown that although a very good impedance match can be achieved, these antennas do not radiate efficiently. Then,

Manuscript received February 6, 2001; revised April 4, 2002. This work was supported in part by the US Army Research Office under contract DAA-99-1-0197 and by CACI Technologies, Inc.

The authors are with the Radiation Laboratory, Department of Electrical Engineering and Computer Science, The University of Michigan, Ann Arbor, MI 48109-2122 USA (saraband@eecs.umich.edu; azadegan@eecs.umich.edu).

Digital Object Identifier 10.1109/TAP.2003.812239

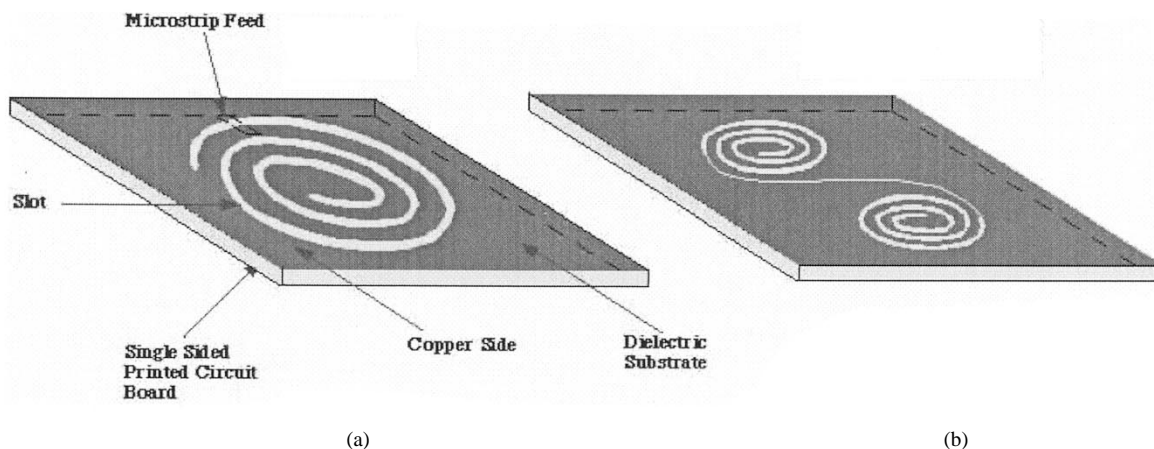


Fig. 1. The geometry of an (a) equiangular and (b) cornu resonant spiral antennas.

an alternate novel design for the construction of an efficient miniature antenna is considered, and the design aspects, in addition to the simulated results, are described. In Section III, the measured radiation characteristics of a prototype miniaturized antenna operating around 600 MHz is presented to validate the design procedures and simulations. Finally the effect of the finite size ground plane on this type of slot antenna is addressed.

II. DESIGN OF A MINIATURIZED UHF ANTENNA

Equiangular and Archimedean spiral antennas [7], [8] are commonly used as broadband antennas. These antennas usually have an arm length larger than a wavelength. Not much has been reported about the performance of spiral antennas when the arm length is half of the guided wavelength (a resonance condition). One obvious reason is that slot spiral antennas are usually center fed where at the first resonance the input impedance is very high and impedance matching becomes practically impossible. However, if we allow the feed point to be moved to one end of the arm, impedance matching to transmission lines with typical characteristic impedances seems possible.

First, an equiangular spiral slot, as shown in Fig.1 (a), is considered. Using electrostatic analysis, the guide wavelength of a slot line with finite ground plane was calculated. The calculated guide wavelength was used to design an arm length of $\lambda_g/2$. The spiral was fed from the outer end using a microstrip line. The location of feed point along the arm was found by trial and error until a good match was achieved. Also, a slot dipole ($\lambda/2$) coil around two center points (cornu spiral) as shown in Fig.1 (b) was considered. For this antenna, the microstrip feed was coiled around one arm on the other side of the substrate (over the ground plane) in order to feed the slot near an end point. Again by trial and error the location of feed point for best impedance match was found. A return loss of better than 20 dB for these antennas was obtained. However, gain measurement of these antennas showed poor radiation efficiencies (less than -10 dB.) The efficiency of the cornu spiral was higher than the simple spiral antenna, however, neither showed an acceptable level of antenna efficiency. Far-field pattern and gain measurements at 60 MHz were carried out in an outdoor slant range using a boom truck and two antenna positioners.

The main problem in these designs seems to stem from the fact that the far-field generated by opposing equivalent magnetic currents along a resonant spiral antenna tend to cancel. To investigate whether ohmic losses are responsible for the low antenna efficiency, a similar antenna having the same geometry and substrate dielectric constant were constructed using a different dielectric quality factor and copper thickness. It was found that ohmic losses were not responsible for the lack of antenna efficiency to the degree observed in our measurements. By putting absorbers around the feed cable and antenna positioner, it was found that these antennas produce a very strong near field which can excite current on the nearby objects, such as the cable feeding them and the antenna positioner. The current induced on these objects in turn radiated the input power, but not necessarily in the direction of the maximum antenna radiation pattern.

A different topology for a miniaturized resonant slot dipole is sought that does not have the drawbacks of the previously discussed spiral and cornu geometries. A major reduction in size is achieved by noting that a slot dipole can be considered as transmission line resonator where at the lowest resonant frequency the magnetic current (transverse electric field in the slot) goes to zero at each end of the dipole antenna. As mentioned before at this frequency the antenna length $l = \lambda_g/2$ where λ_g is the wavelength of the quasi-TEM mode supported by the slot line. λ_g is a function of substrate thickness, dielectric constant, and the slot width, which is shorter than the free-space wavelength. In view of transmission line resonators, one can also make a quarter-wave resonator by creating a short circuit at one end and an open circuit at the other end. However, creating a physical open circuit for slot lines is not practical. The new design borrows the idea of nonradiating tightly coiled slot spiral from the previous design. Basically, a spiral slot of a quarter wavelength and shorted at one end behaves as an open circuit at the resonant frequency. Therefore, a quarter-wave slot line short-circuited at one end and terminated by the nonradiating quarter-wave spiral should resonate and radiate electromagnetic waves very efficiently. With this topology the size of the slot dipole can be reduced by approximately 50%. Further reduction can be accomplished by bending the radiating section. This bending procedure should be done so that no section of the resulting line geometry carries a magnetic current

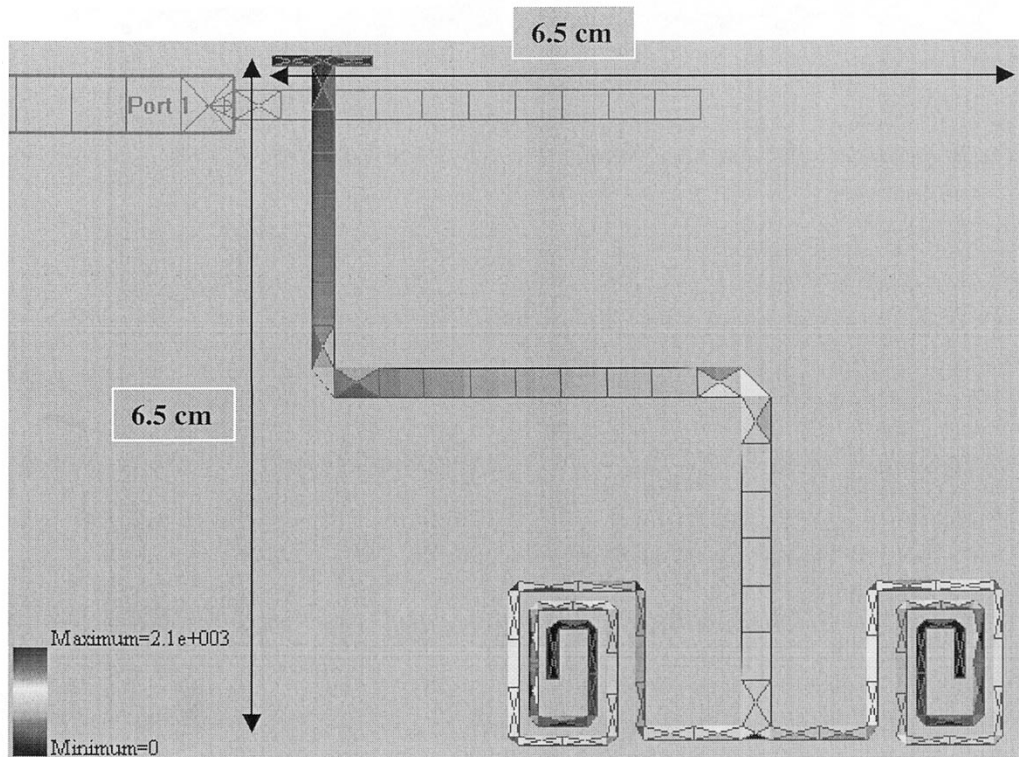


Fig. 2. Magnetic current distribution on the UHF miniaturized slot antenna at the resonance frequency (600 MHz). The figure shows the ground-plane side of the antenna and the meshing configuration used in the method of moments calculations. PiCASSO software was used in these calculations.

opposing the current on any other sections. Fig. 2 shows the geometry of a typical $\lambda_g/4$ compact resonating slot antenna. The radiating section is terminated with two identical quarter-wave nonradiating spiral slots to maintain the symmetry. It was found that by splitting the magnetic current at the end into equal and opposing magnetic currents the radiation efficiency is enhanced. Since the magnetic current distribution attains its maximum at the end of the quarter-wave line, the magnetic current in the beginning segments of a single (unbalanced) quarter-wave spiral reduces the radiation of the radiating section. But the opposite magnetic currents on two such spirals simply cancel the radiated field of each other, and as a result, the radiated field of the radiating section remains intact. Some additional size reduction can also be achieved, by noting that the strength of the magnetic current near the short-circuited end of the radiating section is insignificant. Hence, bending this section of the line does not significantly reduce the radiation efficiency despite allowing opposing currents. In Fig. 2 the T-top represents a small reduction in length of the line without affecting the radiation efficiency. This antenna is fed by an open ended microstrip line. A quarter wavelength line corresponds to a short-circuit line under the slot. However, using the length of the microstrip line as an adjustable parameter, the reactive part of the antenna input impedance can be compensated for.

Figs. 2 and 3, respectively, show the electric current distribution on the microstrip feed and the magnetic current distribution on the slot of the compact UHF antenna designed to operate at 600 MHz. For this design, we chose an ordinary FR4 substrate with thickness of 3 mm (120 mil) and dielectric constant $\epsilon_r = 4$. PiCASSO software was used for the simulations of this antenna

[9]. The microstrip feed is constructed from two sections: 1) a 50Ω line section and 2) an open-ended 80Ω line. The 80Ω line is thinner which allows for compact and localized feeding of the slot. The length of this line is adjusted to compensate for the reactive component of the slot input impedance. Noting that the slot appears as a series load in the microstrip transmission line, a line length of less than $\lambda_m/4$ compensates for an inductive reactance and a line length of longer than $\lambda_m/4$ compensates for a capacitive reactance. Here, λ_m is the guided wavelength on the microstrip line. First, a quarter wavelength section was chosen for the length of the microstrip line feeding the slot. In this case, the simulation predicts the impedance of the slot antenna alone. Through this simulation, it was found that the slot antenna fed near the edge is inductive. So, a length less than $\lambda_m/4$ is chosen for the open-ended microstrip line to compensate for the inductive load. The real part of input impedance of a slot dipole depends on the feed location along the slot and increases from zero at the short-circuited end to about 2000Ω at the center (quarter wavelength from the short circuit). This property of the slot dipole allows for matching to almost all practical transmission lines. The crossing of the microstrip line over the slot was determined using the full-wave analysis tool, (PiCASSO) and by trial-and-error. The uniform current distribution over the 50Ω line section indicates no standing wave pattern, which is a result of a very good input impedance match.

Apart from the T-top section, the quarter-wave radiating section of the slot dipole is composed of three slot line sections, two vertical and one horizontal. Significant radiation emanates from the middle and lower sections. Polarization of the antenna can be chosen by changing the relative size of these two sections.

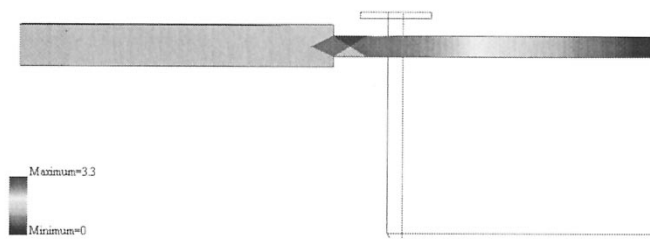
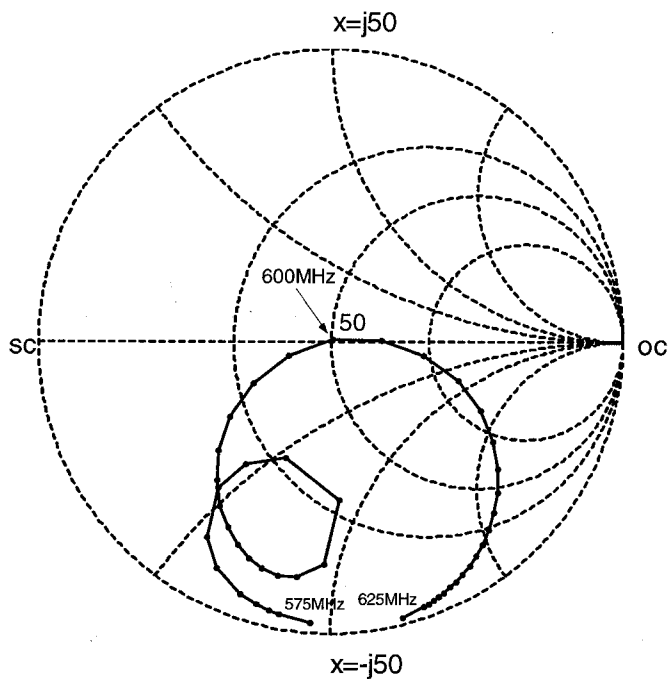
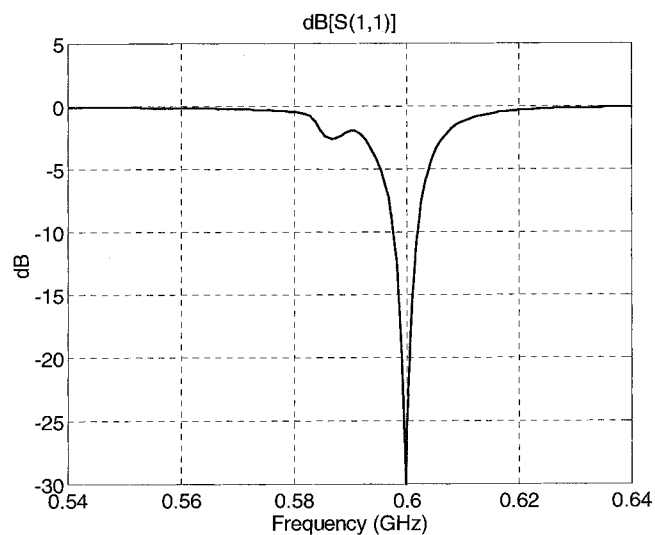


Fig. 3. Electric current distribution on the microstrip feed of the slot antenna at the resonant frequency.



(a)



(b)

Fig. 4. Simulated reflection coefficient of the miniaturized UHF antenna on an infinite ground plane. (a) Smith chart representation. (b) Magnitude of $|S_{11}|$ in logarithmic scale.

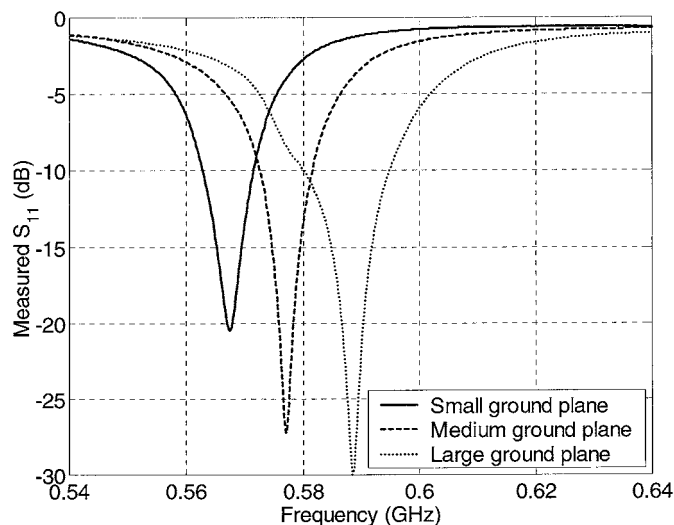


Fig. 5. Measured magnitude of reflection coefficient of three miniaturized UHF slot antennas, described in Table I and shown Fig. 7, all having the same size and geometry, but with a different ground plane sizes.

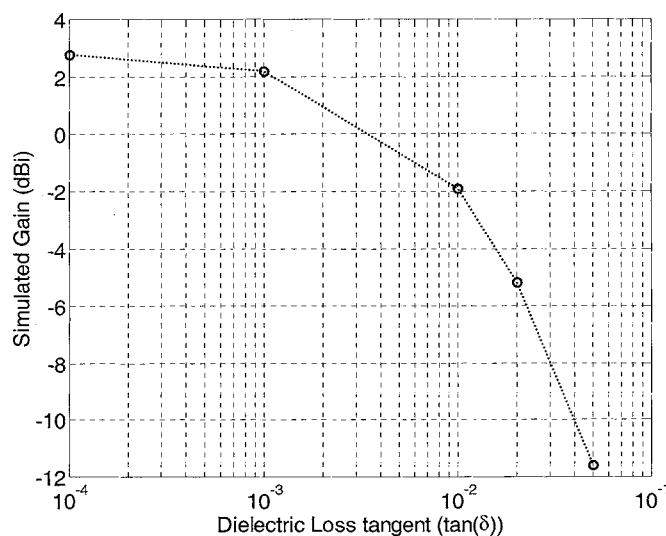


Fig. 6. Simulated gain of the UHF miniaturized antenna on an infinite substrate with $\epsilon_r = 4.0(1 - j \tan \delta)$.

In this design the relative lengths of the three line sections were chosen in order to minimize the area occupied by the slot structure. The slot width of the first section can be varied in order to obtain an impedance match as well. When there is a limitation in moving the microstrip and slot line crossing point, the slot width may be changed. At a given point from the short-circuited end, an impedance match to a lower line impedance can be achieved when the slot width is narrowed. This was used in this design, as the slot line width of the top vertical section is narrower than the other two sections. It should be pointed out that, by narrowing the slot line width, the magnetic current density increases but the total magnetic current in the line does not. In other words, there is no discontinuity in the magnetic current along the line at points where the slot width is changed, however, there are other consequences. One is the change in the char-

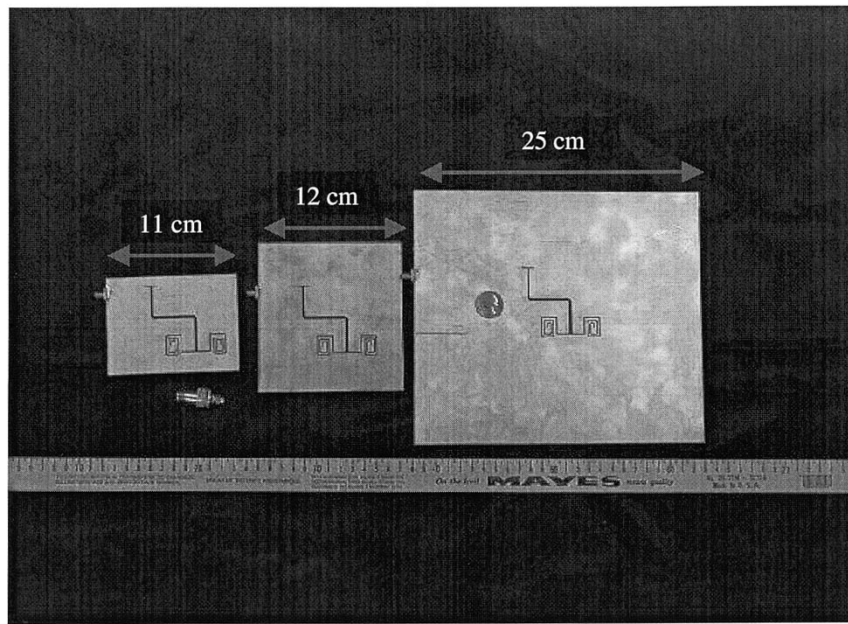


Fig. 7. A photograph of three miniaturized UHF antennas. As shown, all three slot antennas have the same geometry and dimensions. The only difference is the size of the ground.

acteristic impedance of the line, and the second is the change in the antenna efficiency, considering the finite conductivity of the ground plane. There are two components of electric current flowing on the ground plane, one component flows parallel to the edge and the other is perpendicular. For narrow slots, the current density of the parallel component near the edge goes up, and as a result, this current sees a higher ohmic resistance. The magnetic current over the T-top section is very low and does not contribute to the radiated field but its length affects the resonant frequency. Half the length of the T-top section originally was part of the first vertical section, which is removed and placed horizontally to lower the vertical extent of the antenna.

The slot line sections were chosen so that a resonant frequency of 600 MHz was achieved. At this frequency the slot antenna occupies an area of $(6.5 \text{ cm} \times 6.5 \text{ cm})$ or in terms of the free-space wavelength $0.12\lambda_0 \times 0.12\lambda_0$. Fig. 4 (a) and (b), respectively, show the simulated input impedance and return loss of the miniaturized UHF antenna as a function of frequency. It is shown that the 1.2 VSWR (-10 dB return loss) bandwidth of this antenna is around 6 MHz, which corresponds to a 1% fractional bandwidth. This low bandwidth is characteristic of miniaturized and resonant slot dipoles. The simulation also shows a weak resonance, which may be caused by the interaction between the radiating element and the nonradiating spirals. In fact, careful examination of the magnetic current distributions over the nonradiating spirals shows the asymmetry caused by the near field interaction of the radiating element with the nonradiating spirals.

The polarization of this antenna may appear to be rather unpredictable at a first glance due to its convoluted geometry. However, it can be conjectured that the polarization of any miniaturized antenna whose dimensions are much smaller than a wavelength cannot be anything other than linear. This is basically because of the fact that the small electrical size of the antenna does not allow for a phase shift between two orthogonal

TABLE I
RESONANT FREQUENCIES AND THE GROUND PLANE SIZES OF THREE IDENTICAL UHF MINIATURIZED SLOT ANTENNAS. HERE THE EFFECT OF GROUND PLANE SIZE ON THE RESONANT FREQUENCY AND ANTENNA GAIN IS DEMONSTRATED

	Ground Plane Size	Resonant Frequency	Gain (dBi)
Antenna 1	8.5 cm x 11 cm	568 MHz	-5.0
Antenna 2	12 cm x 13 cm	577 MHz	-2.0
Antenna 3	22.5 cm x 25 cm	592 MHz	0.5

components of the radiated field required for producing an elliptical polarization. Hence, by rotating the antenna a desired linear polarization along a given direction can be obtained.

III. REALIZATION AND MEASUREMENTS

An antenna based on the layout shown in Figs. 2 and 3 was made on a FR4 printed-circuit-board. In the first realization, the size of the ground plane was chosen to be $8.5 \text{ cm} \times 11 \text{ cm}$. The return loss of this antenna was measured with a network analyzer and the result is shown by the solid line in Fig. 5. It is noticed that the resonant frequency of this antenna is at 568 MHz, which is significantly lower than what was predicted by the simulation. Also, the measured return loss for the designed microstrip feed line (not shown here) was around -10 dB . To get a better return loss the length of the microstrip line had to be extended slightly. Fig. 5 shows the measured return loss after the modification. The gain of this antenna was also measured against a calibrated antenna. Under a polarization matched condition a gain of -5.0 dBi (gain in dB against an isotropic radiator) is measured. The simulated gain value of this antenna using an infinite ground plane and $\epsilon = 4.0 - j0.0$ is found to be 2.8 dBi. The difference in the simulation results and the measured ones can be attributed to the finiteness of the ground plane, finite conductivity of the ground plane, and

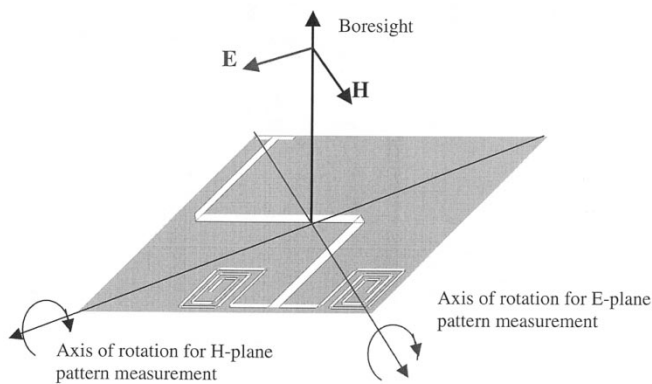
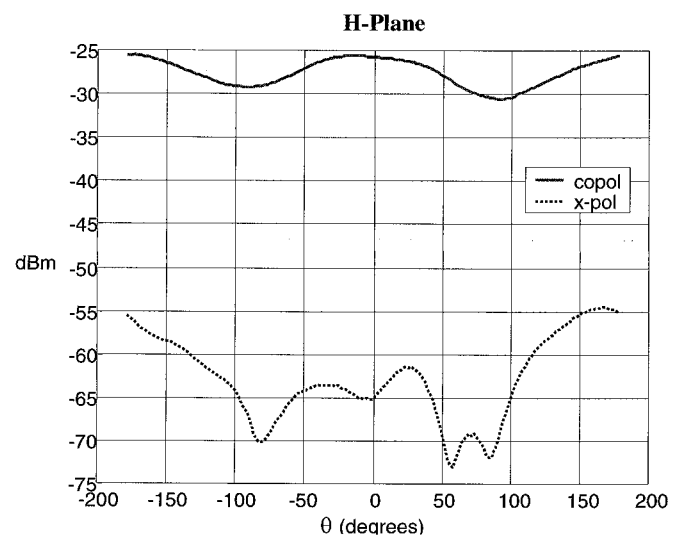


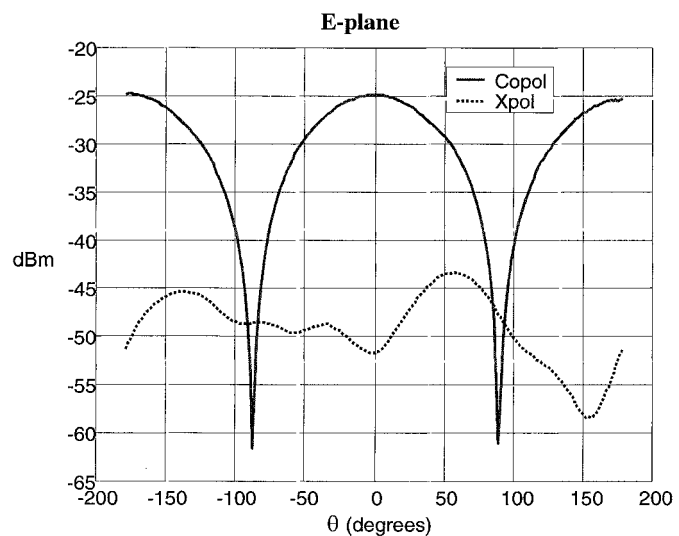
Fig. 8. E- and H-planes of the antenna under test characterized experimentally. Co- and cross-polarized pattern measurements are performed in these two principal planes.

the loss tangent of the substrate. The effect of the imaginary part of the substrate dielectric constant ($\epsilon = 4.0 - j\epsilon''$) can be quantified using a numerical simulation. Fig. 6 shows the simulated gain values of this antenna as a function of ϵ'' with an infinite ground plane. It is shown that, as expected, the gain is decreased when the loss tangent is increased. Hence, it is very important to use substrates with a very low loss tangent. The FR4 used for this antenna has a loss tangent ($\tan \delta \approx 0.01$) at UHF. To investigate the effect of ground plane size on the resonance frequency and radiation efficiency, two more antennas having the same geometry and dimensions but with different ground plane sizes were made. The measured resonant frequencies are also shown in Fig. 5. Fig. 7 shows the photograph of these antennas. The dimensions of the ground planes and the measured gain of these antennas are reported in Table I. As expected the resonant frequency and the gain of the antenna approaches predicted values as the size of the ground plane is increased. The gain of Antenna 3 is almost as high as the gain of an ideal dipole considering the loss tangent of the substrate used in these experiments.

The gain reduction as a function of ground plane size can be explained by noting that the equivalent magnetic currents that flow in the upper and lower side of the ground plane are in opposite directions. In the case of infinite ground plane, the upper and lower half spaces are electromagnetically decoupled. However, when the ground plane is finite and small compared to the wavelength the radiated field from the lower half space can reduce the radiated field from the magnetic current in the upper half space. The level of back radiation depends on the size of the ground plane; that is, the smaller the ground plane the higher the back radiation. Ignoring the substrate ($\epsilon_r = 1$), radiation from the upper and lower magnetic currents completely cancel each other in the plane of the perfect conductor (creates a null in the radiation pattern). However, because of the substrate and depending on its thickness and relative dielectric constant, a perfect cancellation does not occur. This explains the discrepancies observed between the measured and predicted radiation patterns (for infinite ground plane). Also, there are strong edge currents on the periphery of a finite ground which decrease as the size of the ground plane is increased. The confined currents around



(a)



(b)

Fig. 9. Co- and cross-polarized pattern of the miniaturized UHF antenna in (a) H-plane and (b) E-plane.

the edge experience an ohmic loss which is responsible for the decrease in the antenna gain.

The radiation patterns of these antennas were also measured at the University of Michigan anechoic chamber. A linearly polarized antenna was used as the reference. First, the polarization of the antenna was determined at the direction of maximum radiation (normal to the ground plane). Then by rotating the antenna under test about the direction of maximum radiation, it was found that indeed the polarization of the miniaturized antenna is linear. Fig. 8 shows the direction of maximum radiation, the direction of electric field (polarization), and magnetic field at the antenna boresight. Figs. 9 (a) and (b) show the co- and cross-polarized antenna patterns in the H- and E-planes, respectively. It is shown that the antenna polarization remains linear on these principal planes. As discussed before, the E-plane gain in the plane of the ground plane ($\theta = 90^\circ$) drops because of the finiteness of the ground plane. If the substrate were to be removed, the

E-plane gain in the plane of the conductor would drop to zero. Hence, having a thick substrate helps achieve a more uniform pattern. Thick and high permittivity substrate also increases front-to-back radiation ratio. Since our substrate thickness is only a small fraction of the wavelength, almost similar gain values are measured in the upper and lower half spaces.

It is worth mentioning that further miniaturization can easily be accomplished by increasing the dielectric constant of the substrate. In this case, the guide wavelength shortens which in turn allows for a smaller antenna. As mentioned in Section I, further antenna miniaturization is accompanied by a reduction of the antenna bandwidth. Also, confining the electric currents on the ground plane into a smaller area results in a higher ohmic loss or equivalently lower antenna efficiency.

IV. CONCLUSION

A novel topology for designing an electrically small resonant slot antenna is demonstrated. A major size reduction was achieved by constructing a $\lambda_g/4$ resonant slot rather than the traditional $\lambda_g/2$ antenna. This is accomplished by generating a virtual open circuit at one end of the slot. Further miniaturization was achieved by bending the slot into three pieces in order to use the area of the board more efficiently. The antenna geometry occupies a very small area ($0.014\lambda_0^2$) of a PC board with $\epsilon_r = 4.0$ and thickness 3 mm. The antenna is very efficient and shows a gain as high as a dipole antenna and a 1% bandwidth. It is also shown that if the antenna is made on a small ground plane its gain will be reduced and its radiation pattern changes slightly.

REFERENCES

- [1] H. A. Wheeler, "Fundamental limitations of small antennas," *Proc. IRE*, vol. 35, pp. 1479–1484, Dec. 1947.
- [2] L. J. Chu, "Physical limitations of omni-directional antennas," *J. Appl. Phys.*, vol. 19, pp. 1163–1175, Dec. 1948.
- [3] H. A. Wheeler, "Small antennas," *IEEE Trans. Antennas Propagat.*, vol. AP-23, pp. 462–469, July 1975.
- [4] R. F. Harrington, "Effect of antenna size on gain, bandwidth, and efficiency," *J. Res. Nat. Bur. Stand.*, vol. 64D, pp. 1–12, 1960.
- [5] R. E. Collin, "Small antennas," *IEEE Trans. Antennas Propagat.*, vol. AP-12, pp. 23–27, Jan. 1964.
- [6] R. C. Hansen, "Fundamental limitations in antennas," *Proc. IEEE*, vol. 69, pp. 170–182, Feb. 1981.
- [7] J. A. Kaiser, "The Archimedean two-wire spiral antenna," *IRE Trans. Antennas Propagat.*, vol. AP-8, pp. 312–323, May 1960.
- [8] P. E. Mayes, "Planar and other wide-angle logarithmic spiral over ground," *Electromagn.*, vol. 14, pp. 329–362, 1994.
- [9] em PiCASSO Pro., EMAG Technologies, Inc., Ann Arbor, MI.



Kamal Sarabandi (S'87–M'90–SM'92–F'00) received the B.S. degree in electrical engineering from Sharif University of Technology, Tehran, Iran, and the M.S. degrees in electrical engineering and mathematics and the Ph.D. degree in electrical engineering, all from The University of Michigan, Ann Arbor, in 1980, 1986, and 1989, respectively.

He is the Director of the Radiation Laboratory and a Professor in the Department of Electrical Engineering and Computer Science at the University of Michigan. His research areas of interest include microwave and millimeter-wave radar remote sensing, electromagnetic wave propagation, and antenna miniaturization. He has 20 years of experience with wave propagation in random media, communication channel modeling, microwave sensors, and radar systems, and is leading a large research group including two research scientists, ten Ph.D. degree students, and two M.S. degree students. Over the past ten years, he has graduated 14 Ph.D. degree students. He has served as the Principal Investigator on many projects sponsored by the National Aeronautics and Space Administration, ASA, JPL, the Army Research Office, the Office of Naval Research, ARL, the National Science Foundation, DARPA, and numerous industries. He has published many book chapters and more than 95 papers in refereed journals on electromagnetic scattering, random media modeling, wave propagation, antennas, microwave measurement techniques, radar calibration, inverse scattering problems, and microwave sensors. He has also had more than 200 papers and invited presentations in many national and international conferences and symposia on similar subjects.

Dr. Sarabandi is a Vice President of the IEEE Geoscience and Remote Sensing Society (GRSS), Chairman of the Awards Committee of the IEEE GRSS, and a Member of IEEE Technical Activities Board Awards Committee. He is currently serving as the Associate Editor of the IEEE TRANSACTIONS ON ANTENNAS AND PROPAGATION and the IEEE SENSORS JOURNAL. He is also a Member of Commission F of URSI and of The Electromagnetic Academy. He is listed in *American Men & Women of Science Who's Who in America* and *Who's Who in Electromagnetics*. He was the recipient of the prestigious Henry Russel Award from the Regent of The University of Michigan (the highest honor the University of Michigan bestows on a faculty member at the assistant or associate level). In 1999, he received a GAAC Distinguished Lecturer Award from the German Federal Ministry for Education, Science, and Technology given to about ten individuals worldwide in all areas of engineering, science, medicine, and law. He was also a recipient of a 1996 Teaching Excellence Award from the EECS Department of The University of Michigan. In the past several years, joint papers presented by his students at a number of symposia (IEEE AP'95,'97,'00,'01, IEEE IGARSS'99, IEEE MTTs'01) have received student paper prize awards.



Reza Azadegan (S'98) was born in Tehran, Iran, in 1974. He received the B.S. degree in electrical engineering from Sarif University of Technology, Tehran, Iran, and the M.S. degree in electrical engineering from K. N. Toosi University of Technology, Tehran, Iran, in 1996 and 1998, respectively. He is currently working toward the Ph.D. degree in the Radiation Laboratory at the University of Michigan, Ann Arbor, where he is working on the miniaturization of planar antennas and microwave filters for wireless communication systems.

From 1997 to 1999, he was with the Computational Electromagnetic Laboratory, Sharif University of Technology, as a Graduate Researcher working on the optimal design of parabolic reflector antennas using high frequency techniques and genetic algorithms and electromagnetic wave propagation in optical waveguides.

Electromechanical Considerations in Developing Low-Voltage RF MEMS Switches

Dimitrios Peroulis, *Member, IEEE*, Sergio P. Pacheco, *Member, IEEE*, Kamal Sarabandi, *Fellow, IEEE*, and Linda P. B. Katehi, *Fellow, IEEE*

Abstract—This paper reports on the design, fabrication, and testing of a low-actuation voltage Microelectromechanical systems (MEMS) switch for high-frequency applications. The mechanical design of low spring-constant folded-suspension beams is presented first, and switches using these beams are demonstrated with measured actuation voltages of as low as 6 V. Furthermore, common nonidealities such as residual in-plane and gradient stress, as well as down-state stiction problems are addressed, and possible solutions are discussed. Finally, both experimental and theoretical data for the dynamic behavior of these devices are presented. The results of this paper clearly underline the need of an integrated design approach for the development of ultra low-voltage RF MEMS switches.

Index Terms—Low actuation voltage, microelectromechanical systems (MEMS) switches, residual stress, spring constant, switching speed, top-electrode switches.

I. INTRODUCTION

MICROMACHINING and microelectromechanical systems (MEMS) are among the most promising enabling technologies for developing low-power low-cost miniaturized RF components for high-frequency applications. Several universities and companies have developed RF MEMS switches [1]–[8] in the last decade that can be primarily classified as: 1) series or shunt; 2) fixed–fixed membranes or cantilever beams; and 3) capacitive or metal-to-metal contact type [9]. The main driving force behind this major research effort is the outstanding demonstrated RF performance of the MEMS switches from dc to 100 GHz compared to p-i-n diodes or FET transistors. Furthermore, electrostatically driven switches require only a few microwatts of dc power compared to several milliwatts that their solid-state counterparts dissipate. It is for this reason, as well as for the simplicity of their biasing

networks, that most of the developed switches are electrostatic in nature.

These studies, however, have only limited their focus on the RF performance of MEMS switches and have provided little information on several important phenomena directly related to the inherent electromechanical characteristics of these structures. Their sheer interdisciplinary nature imposes a very tight coupling between the electrical and mechanical domains. For instance, thin-film residual stress and viscous damping may have a far greater influence on the performance of the device than intuitively anticipated. Moreover, the vast majority of the switches in the literature typically require a pull-in and hold-down voltage of 40–100 and 15–30 V, respectively. Whereas no difficulty exists in achieving these ranges in a typical laboratory environment, they may be quite challenging for handheld mobile phones, automotive vehicles, and similar wireless devices that rely on low-voltage power supplies. In addition, Goldsmith *et al.* [16] have shown that the lifetime of capacitive switches strongly depends on the applied actuation voltage. In particular, for capacitance switches, they experimentally observed a lifetime improvement of a decade for every 5–7-V drop on the switch pull-in voltage. Consequently, reducing the actuation voltage of MEMS switches may not only broaden the range of their possible applications, but also significantly enhance their performance. It would seem, therefore, that further investigations are needed in order to provide the MEMS engineer with complete and accurate information on the design and operation of these devices.

It is the purpose of this paper to present the results of our investigation on these issues. First, in Section II, we focus on the design of the low spring-constant beams that support the main switch structure. We also demonstrate a number of designs that resulted in switches with pull-in voltages of as low as 6 V. Section III discusses the effects of residual axial and gradient stress on the device performance and shows how minor design and fabrication details may have a significant impact on the final structure. Section IV concludes our study by presenting experimental and theoretical results on the dynamic behavior of the low-voltage MEMS switch.

II. SPRING CONSTANT AND ACTUATION VOLTAGE

A. Design

The mechanical design of most electrostatically based switches starts with considering the required dc actuation voltage. Equation (1) presents a widely cited formula (e.g., [8])

Manuscript received April 22, 2002. This work was supported by the System on a Chip/Jet Propulsion Laboratory under the Center for Integrated Space Microsystems Project and by the Department of Defense Research and Engineering under the Multidisciplinary University Research Initiative on “Low Power Electronics” and “Multifunctional Adaptive Radio, Radar and Sensors” programs.

D. Peroulis and K. Sarabandi are with the Radiation Laboratory, Electrical Engineering and Computer Science Department, The University of Michigan at Ann Arbor, Ann Arbor, MI 48109-2122 USA (e-mail: dperouli@engin.umich.edu).

S. P. Pacheco was with the Radiation Laboratory, Electrical Engineering and Computer Science Department, The University of Michigan at Ann Arbor, Ann Arbor, MI 48109-2122 USA. He is now with Digital DNA Laboratories, Motorola, Tempe, AZ 85284 USA.

L. P. B. Katehi was with the Radiation Laboratory, Electrical Engineering and Computer Science Department, The University of Michigan at Ann Arbor, Ann Arbor, MI 48109-2122 USA. She is now with the College of Engineering, Purdue University, West Lafayette, IN 47907 USA.

Digital Object Identifier 10.1109/TMTT.2002.806514

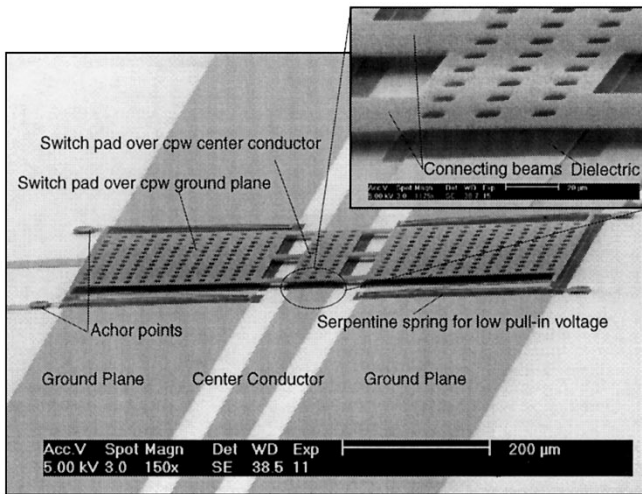


Fig. 1. SEM picture of the proposed low-voltage capacitive shunt switch over a CPW line.

for calculating the pull-in voltage of fixed-fixed beams or air bridges as follows:

$$V_p = \sqrt{\frac{8K_z g_0^3}{27\epsilon_0 A}}. \quad (1)$$

K_z is the equivalent spring constant of the moving structure in the direction of desired motion (typically the z -direction), g_0 is the gap between the switch and the actuation electrode, ϵ_0 is the free-space permittivity, and A is the switch area where the electrostatic force is applied. Equation (1) implies that there are several ways that may decrease the required actuation voltage. For instance, reducing g_0 can significantly lower the pull-in voltage. Although this solution can be partly applied to low-frequency applications (<10 GHz), it will adversely affect the high-frequency off-state switch performance by compromising the switch isolation (for a series switch) or insertion loss (for a shunt switch). A second approach in lowering the pull-in voltage would be to increase the actuation area A . This area, however, has to stay within reasonable limits, primarily imposed by our desire for miniaturized circuits. The third alternative, which offers the maximum design flexibility for a low-to-moderate actuation voltage, is to lower the switch spring constant, hence, designing a compliant switch.

Fig. 1 shows an SEM picture of our proposed switch in a coplanar waveguide (CPW) configuration. The switch consists of three movable metallic plates, one over each conductor of the CPW line. These plates are connected together with three short beams (connecting beams) and the whole structure is connected to the substrate at four points (anchors) through four beams. Due to their shape, we will call these beams serpentine springs or folded-suspension beams. The switch is typically suspended 3–4 μm above the CPW line and is electrostatically actuated when a dc voltage is applied between the switch and the CPW ground planes.

B. Fabrication

The fabrication process is fairly simple, requires only four masks, and is described in detail in [10]. The CPW line is typ-

ically made of Ti/Au (500/9000 \AA) and is defined first through a liftoff process. A plasma-enhanced chemical vapor deposition (PECVD) of approximately 1400–2000 \AA Si_3N_4 follows. Since the switch is made of metal (typically Ni), this dielectric layer is primarily needed during the actuation stage to prevent a direct dc contact between the switch and CPW line. Therefore, a positive photoresist intended to protect the Si_3N_4 underneath the switch is deposited with a normal lithography and the remaining dielectric layer is etched through a reactive ion etching (RIE) process. After the photoresist removal, the sacrificial layer (polyimide or photoresist) is deposited and the switch anchor points are photolithographically defined. Afterwards, a seed layer (typically Ti/Ni 2000/500 \AA), is deposited, patterned, and electroplated. The last step is the removal of the sacrificial layer and the supercritical CO_2 drying of the structure.

C. Spring Design

Since the mathematical details of the electrostatic actuation [including (1)] have been extensively analyzed in the past [17], [18], we will just briefly describe the basic principle here. When no dc bias is applied, the switch presents a very small shunt capacitance (typically in the order of 30–50 fF) between the center conductor and ground planes. This is called the up or off state and the RF signal can propagate with minimal loss (typically with -0.1 dB at X-band). On the other hand, if the applied bias exceeds the actuation voltage, the switch collapses on the dielectric layer underneath, resulting in a significant shunt capacitance, which is equivalent to an RF short circuit. This is called the down or on state and virtually all the incident RF power is reflected back to the source.

As was previously mentioned, the switch of Fig. 1 is connected to the substrate through four serpentine springs that are used to substantially lower the switch spring constant. If k_z is the z -directed spring constant for each one of the springs, the total switch spring constant K_z is given by

$$K_z = 4k_z. \quad (2)$$

Compared to simple cantilever beams of equal total length, these springs have the additional advantage of occupying considerable less space, but they also show higher spring constant. As will be shown, however, adding more meanders can significantly lower it without excessively increasing the required space. In the following, we calculate the spring constant of an N -section meander [see Fig. 2(a)] when a virtual force F_z is applied at its free end. An analytical solution for a similar folded meander has been obtained by Fedder [19] and our analysis is based on his study.

Each meander of the whole spring is defined as the set of four beams: two primary beams of length a and two secondary beams of length b . Therefore, an N -meander spring has $2N$ primary beams and $2N$ secondary beams. The switch shown in Fig. 1, for instance, has a single-section meander ($N = 1$) with $a = 20 \mu\text{m}$ and $b = 240 \mu\text{m}$. All the necessary dimensions and material constants for our switch are given in Table I. For the analytical calculation, it is assumed that all six degrees of freedom of the anchor point [point A in Fig. 2(a)] are fixed. Moreover, the guided-end boundary conditions are applied for the free-end

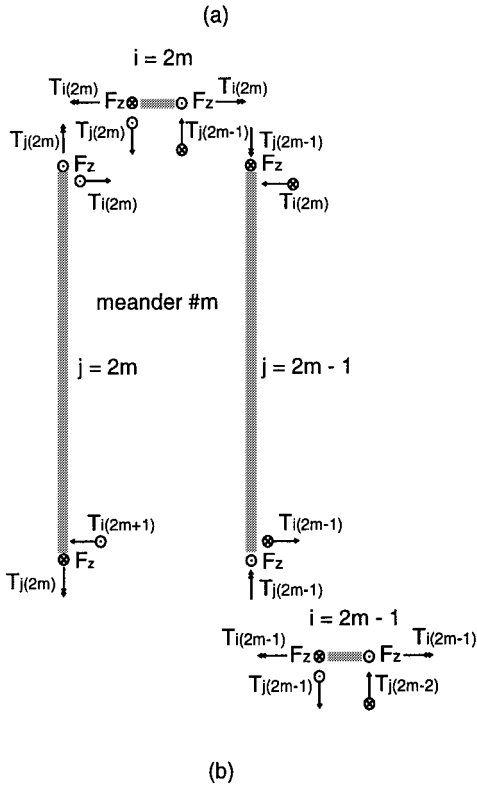
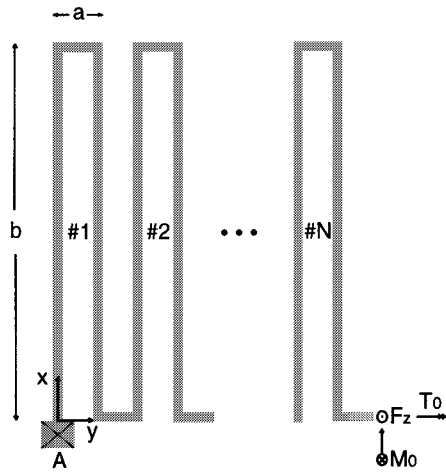


Fig. 2. (a) Schematic (drawn to scale) of an N -meander serpentine spring. (b) Forces, torques, and moments in the m th meander.

point of the spring since this point is attached to the main switch body. Consequently, a moment M_0 and a torsion T_0 are applied to this point to constrain the rotation angles around the x - and y -axes. The torsion and moment of each beam are then given by [19] [see Fig. 2(b)]

$$\begin{aligned} M_{a,i} &= M_0 - F_z [x + (i-1)] \\ T_{a,i} &= T_0 + \left[\frac{1 + (-1)^i}{2} \right] F_z b \\ M_{b,j} &= (-1)^j T_0 - F_z x + \left[\frac{1 + (-1)^j}{2} \right] F_z b \\ T_{b,j} &= (-1)^j (i F_z a - M_0) \end{aligned} \quad (3)$$

TABLE I
PHYSICAL DIMENSIONS AND MATERIAL CONSTANTS FOR THE
LOW-VOLTAGE SWITCH

Primary meander length (a)	20 μm
Secondary meander length (b)	240 μm
Switch thickness (t)	2 μm
Beam width (both beams) (w)	5 μm
Ni Young's modulus (E)	207 GPa
Ni Poisson's ratio (ν)	0.31
Shear modulus (G)	$E/(2(1+\nu))$
x-axis moment of inertia (I_x)	$wt^3/12$
z-axis moment of inertia (I_z)	$tw^3/12$
polar moment of inertia (I_p)	$I_x + I_z$
Torsion constant (J)	$0.413I_p$ (see [20])

where $M_{a,i}$ and $T_{a,i}$ ($M_{b,j}$ and $T_{b,j}$) are the moment and torsion of the i th primary beam (j th secondary beam) with $i = 1$ to $2N$ ($j = 1$ to $2N$). In these equations, x is the longitudinal dimension along each one of the beams.

Following the virtual work method, the total elastic strain energy of the meander is given by

$$U = \sum_{i=1}^{2N} \int_0^a \left(\frac{M_{a,i}^2}{2EI_x} + \frac{T_{a,i}^2}{2GJ} \right) dx + \sum_{j=1}^{2N} \int_0^b \left(\frac{M_{b,j}^2}{2EI_x} + \frac{T_{b,j}^2}{2GJ} \right) dx \quad (4)$$

where I_x , I_z , G , and J are defined in Table I. Finally, the spring constant is given by

$$k_z = F_z \delta_z = F_z \frac{\partial U}{\partial F_z} \quad (5)$$

along with the boundary conditions

$$\phi_0 \equiv \frac{\partial U}{\partial M_0} = 0 \text{ and } \psi_0 \equiv \frac{\partial U}{\partial T_0} = 0. \quad (6)$$

These equations lead to the following expressions for the reactions M_0 and T_0 :

$$M_0 = \frac{2Na}{EI_x} + \frac{(2N+1)b}{GJ} a F_z \quad (7)$$

$$T_0 = -\frac{F_z b}{2} \quad (8)$$

and for the spring constant k_z

$$k_z = \left[\frac{8N^3 a^3 + 2Nb^3}{3EI_x} + \frac{abN[3b + (2N+1)(4N+1)a]}{3GJ} - \frac{Na^2 \left[\frac{2Na}{EI_x} + \frac{(2N+1)b}{GJ} \right]^2}{2 \left(\frac{a}{EI_x} + \frac{b}{GJ} \right)} - \frac{Nb^2}{2} \left(\frac{a}{GJ} + \frac{b}{EI_x} \right) \right]^{-1}. \quad (9)$$

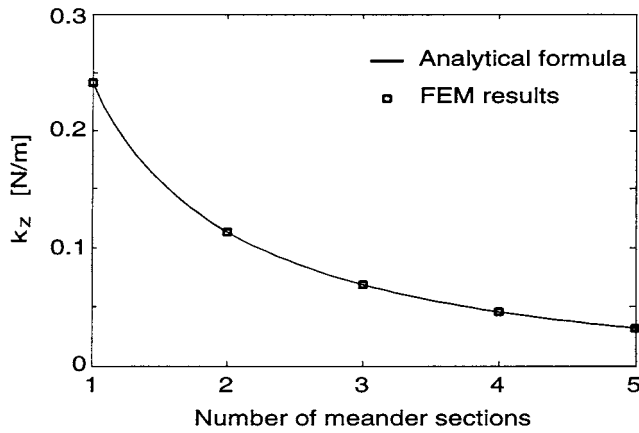


Fig. 3. Analytically computed and FEM simulated results of the z -directed spring constant of an N -section meander.

Although (9) is lengthy, it is written in an intuitive way that may facilitate the design of these meanders or similar beams. The first two terms of the denominator represent the percentage of the spring constant that is due to beam bending (first term) and twisting (second term). In other words, these terms depend solely on the meander geometry and the ability of the beam material to bend and twist. The last two terms of the denominator are due to the boundary conditions of the meander moving end and correspond to its inability to rotate around the x - and y -axes. These two terms may have comparable magnitude to the first two and considerably increase the switch spring constant.

Equation (9) was verified by a commercially available finite-element method (FEM) code [21]. The dimensions of Table I were input in the code and several linear simulations were performed for springs with 1–5 meanders. For each simulation, a concentrated z -directed force of $F_z^{\text{FEM}} = 1 \mu\text{N}$ was applied at the tip of the spring along with the necessary guided-end boundary conditions. The resulting deflection Δ_z was then computed and the FEM spring constant was extracted as $k_{mz}^{\text{FEM}} = F_z^{\text{FEM}}/\Delta_z$. Excellent agreement between the analytically and numerically computed spring constants is observed in Fig. 3, which graphically presents the two spring constants as a function of the number of the meanders. This graph also illustrates that the serpentine spring constant is not significantly reduced after including four or five meander sections. Hence, three or four meanders would be a good compromise between low spring-constant requirements and space limitations.

D. Actuation Voltage Measurements

Five switch designs with 1–5 meanders in their folded suspensions were fabricated and measured. Except for the serpentine springs, all designs were identical and were fabricated on the same wafer by the same fabrication process. For each design, we measured the pull-in voltage using an HP 4275A multifrequency LCR meter with an internal bias option. These measurements are presented in Table II, which also compares the extracted switch spring constant from the measured pull-in voltage [based on (1)] with the corresponding theoretical results. The theoretical values have been calculated for a switch thickness of $t = 2.5 \mu\text{m}$ (because of over-plating in the fabricated switches)

TABLE II
ACTUATION VOLTAGE MEASUREMENTS FOR SEVERAL MEMS SWITCHES

Meanders	Experimental		Theoretical	
	V_p [V]	K_z [N/m]	V_p [V]	K_z [N/m]
1	30	26.9	8.3	2.08
2	22	14.5	5.7	0.97
3	17	8.6	4.4	0.58
4	11	3.6	3.6	0.38
5	6	1.1	3.0	0.27

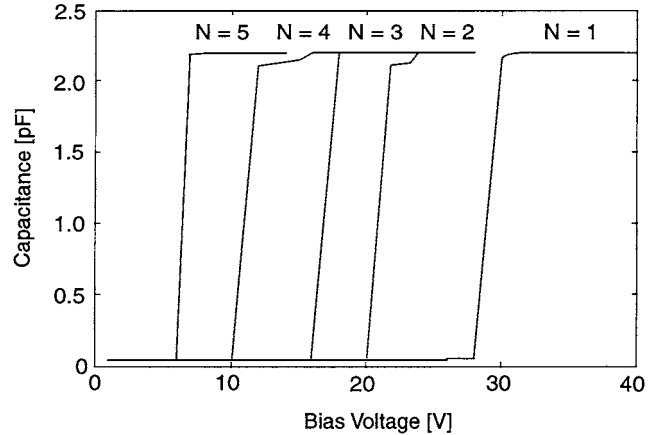


Fig. 4. Measured dc switch capacitance as a function of the applied bias voltage and number of meanders.

and an initial gap of $g_0 = 5 \mu\text{m}$. The reason for this higher gap is that, although the sacrificial layer thickness was $4 \mu\text{m}$, the induced residual stress across the structure caused a slight out-of-plane deflection, which, on average, increased the total distance from the substrate to $5 \mu\text{m}$. We will discuss stress issues in more detail in Section III. Fig. 4 also shows the measured dc capacitance of the switches as a function of the applied bias voltage and the number of meanders.

These data reveal several discrepancies between the simulated and measured results. The first dissimilarity is the fact that the measured pull-in voltages are 5–10 times higher than the theoretically calculated ones. The second and most interesting one is related to the percentage of the spring-constant reduction as the number of meanders is increased. For example, when the number of meanders was increased from one to two, the experimentally extracted spring constant was decreased by 46%, while the theoretical calculations predicted 53%. Although these results are in fair agreement, this is not the case for switches with more meanders. The switches with five meanders, for instance, had 70% lower spring constant than the ones with four. According to (9), however, this number should be close to 30%. Fig. 5 graphically illustrates these observations for all cases. All these issues are due to the high intrinsic axial stress built into the Ni layer during the fabrication and are studied in Section III.

E. Stiction and Top Electrode Design

Although low spring constant is essential in obtaining low-voltage switches, preventing down-state stiction is equally

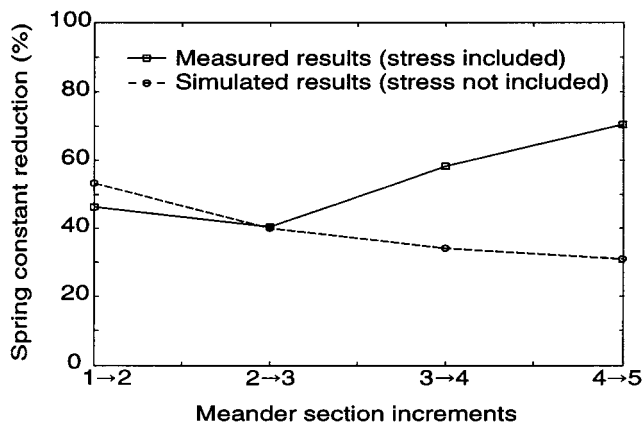


Fig. 5. Experimental and theoretical percentage change of the switch spring constant as the number of meanders is increased.

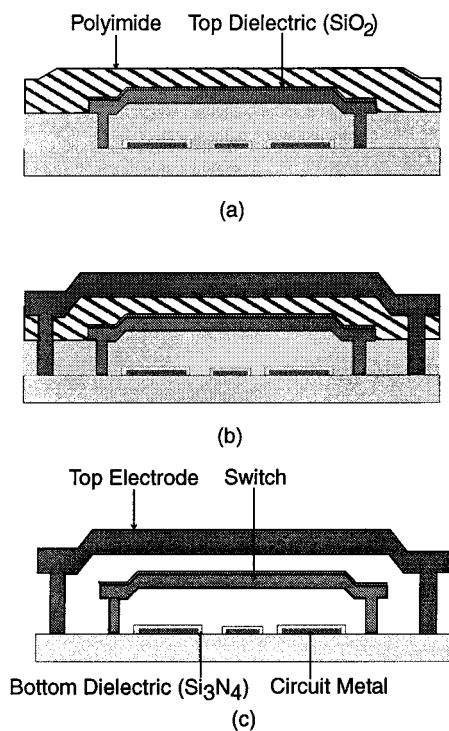


Fig. 6. Top electrode concept and fabrication process. (a) 2500 Å of SiO₂ are deposited on top of the switch followed by a second sacrificial layer. (b) The top electrode is electroplated in a low-stress Au solution. (c) The whole structure is released by etching the sacrificial layers followed by a standard supercritical drying process.

important. A low-voltage switch experiences a relatively weak restoring force while in the down state, which may not be sufficiently high to pull the switch up, particularly in humid or contaminated environments. This drawback of this family of switches can be overcome by including top electrodes. Fig. 6 illustrates the idea of fabricating a metallic plate (top electrode) above the switch. By applying a dc voltage between this top electrode and switch, the switch can be pulled up from the down state, even if the restoring force is not sufficiently high.

Fig. 7 shows an example of a four-meander switch with top electrodes over the dc switch pads. There is no electrode suspended above the center conductor pad because such an elec-

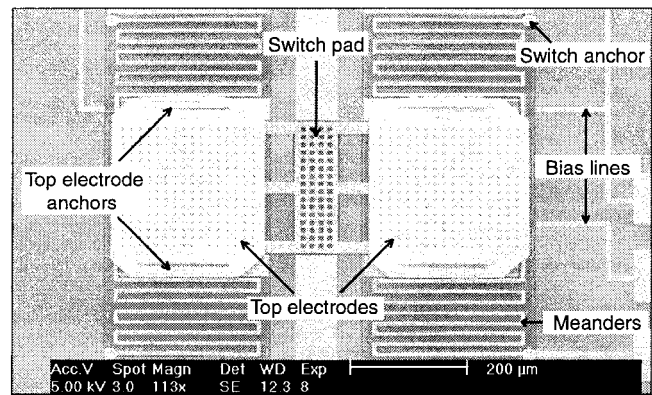


Fig. 7. Four-meander switch with top electrodes. Each top electrode is approximately 5–6-μm thick and is fabricated with a low-stress Au electroplated process.

trode would significantly deteriorate the up-state switch capacitance. These top electrodes are very stiff fixed-fixed plates (5–6-μm-thick low-stress electroplated Au) with a spring constant higher than 2300 N/m. Any movement of these electrodes would require voltages in excess of 250 V and, compared with the switch, they can be considered as static plates. Additionally, they provide stabilization to the overall switch structure against severe mechanical shocks. Measured and theoretical results of switches with top electrodes and power measurements of the same switches are reported in [22].

III. INTRINSIC RESIDUAL STRESS ISSUES

Although the previous analysis allows for a first estimate of the switch spring constant and pull-in voltage, it does not account for any intrinsic residual stress on the structure. Residual stress, however, is developed during the fabrication of most microstructures and typically presents most of the major challenges in developing these devices. Under this stress, thin-film structures can experience undesirable deformations, which may be significant, particularly for high-aspect ratio structures. Additionally, many MEMS switches must satisfy very stringent requirements for reliable performance, including being planar over the circuit underneath it. Any undesirable buckling or curling may easily deteriorate the performance of the switch, or lead to the complete failure of the device. A lot of attention, therefore, has to be paid to residual stress and its effects on compliant structures before any successful devices can be developed.

When a thin film is deposited on a sacrificial layer at a temperature lower than its flow temperature, then intrinsic stresses develop in the film-sacrificial layer system [23]. A number of studies have been already performed to theoretically explain the mechanisms of these stresses [24], [25] and to experimentally measure their effects [26], [27]. Nonetheless, in general, thin-film stress is complicated and heavily depends on the specifics of the fabrication process. There is also very little information for metallic microstructures built by thin-film depositions and effective ways that can control its stress and/or its effects. This section illuminates the most important stress-related challenges for developing low-voltage switches.

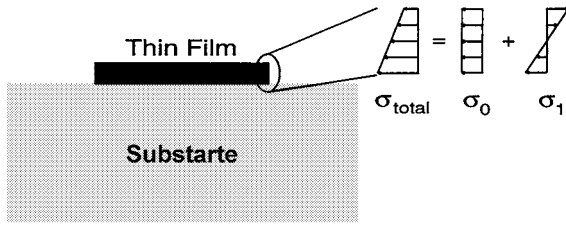


Fig. 8. Thin-film residual-stress approximation.

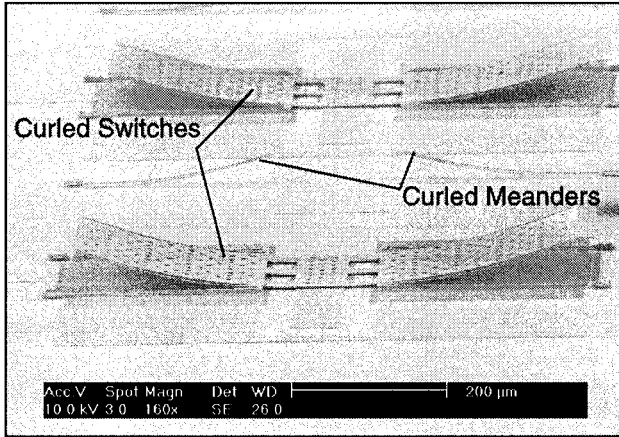


Fig. 9. Switches with considerable deflection as a result of a poorly designed fabrication process.

A. Gradient Residual Stress

A general uniaxial residual stress field in a thin film can be represented as [26]

$$\sigma_{\text{total}} = \sum_{k=0}^{\infty} \sigma_k \left(\frac{y}{h} \right)^k \quad (10)$$

where h is the film thickness and $y \in (-h/2, h/2)$ is the coordinate across the film thickness, with its origin at the mid-plane of the film. For a first-order approximation, the total stress can be calculated as

$$\sigma_{\text{total}} \simeq \sigma_0 + \sigma_1 \left(\frac{2y}{h} \right) \quad (11)$$

This equation implies that the total stress can be expressed as a superposition of the constant mean stress σ_0 (positive or negative depending on whether the film is in tension or compression) and a gradient stress σ_1 about the mid-plane (see Fig. 8). The effects of the gradient stress are analyzed in this subsection and those of the mean stress in the following one.

It is widely known that residual gradient stress causes undesirable out-of-plane deformation. Fig. 9 shows two examples of extremely warped switches. These switches were 4- μm thick and the maximum deformation, defined as the distance between the higher and lower switch points, was on average 30 μm . This deformation was recorded for switches 640- μm long (not counting the length of the meanders), but increased to 70–80 μm for switches close to 1-mm long. This substantial deformation renders both structures unusable because: 1) the required actuation voltage is much higher than the design value (>80 V) and 2) the up-state switch RF capacitance is considerably higher than

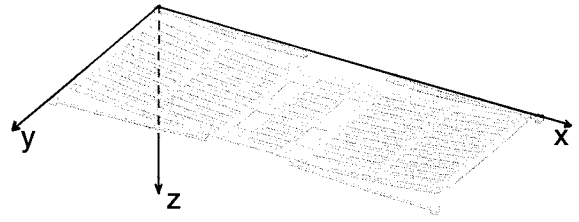


Fig. 10. Simulated warped switch structure (by SUGAR). The maximum switch deflection is approximately 23 μm .

anticipated ($C_{\text{up}} > 150$ fF, instead of 50 fF). The sacrificial and seed layers that resulted in such a stress were the polyimide DuPont PI2545 and an evaporated Ti/Ni (1500/500- \AA) layer, respectively. The switches were then electroplated in an Ni solution (Nickel Sulfamate, Barrett SN by Mac Dermid) with a steady current density of 4 mA/cm^2 for approximately 30 min. The induced stress with this fabrication process was repeatable over a period longer than six months.

This switch shape under residual gradient stress was also theoretically validated using SUGAR.¹ Fig. 10 shows the simulated switch shape, which agrees very well with the fabricated switches. The maximum gradient stress value in the software was varied until the measured maximum deflection was obtained.

One way to alleviate this problem without increasing the actuation voltage is to selectively increase the switch thickness [28]. In this technique, the main switch body thickness is increased to 6–8 μm , but the springs remain 2- μm thick [see Fig. 11(a)]. This process utilizes the following two electroplating steps:

Step 1) The switch and the springs are plated.

Step 2) The switch main body is subsequently plated again until it reaches a thickness of 6–8 μm .

Due to some adhesion difficulties between the two plated structures, the process was slightly changed by plating only a switch frame during the first step instead of the whole switch [see Fig. 11(b)]. This improvement resulted in a 98% yield.

The drawback of this technique, however, is that, although it limits the switch warping to 1–3 μm and may prove useful for other types of MEMS devices, it also results in less conformal switches with lower down-state capacitance than the original switches.

We experimentally found that a better solution is to sputter deposit the Ti layer (instead of evaporating) above the sacrificial layer. More specifically, the Ti sputtering process is performed with The University of Michigan at Ann Arbor sputtering tool with a dc source calibrated to deposit 90 $\text{\AA}/\text{min}$ under 7 mT of Ar pressure. The actual deposition is typically done for 25–26 min, resulting in a film of 2250–2350 \AA of Ti. After the sputtering process is completed, the sample is immediately (in order to minimize Ti oxidation) taken to the Ni e-beam evaporator where 500 \AA of Ni are deposited. It is also very important to point out that nothing else is changed in the process, including the Ni electroplating solution, current density, and sacrificial layer etching. Furthermore, this process can be followed with either polyimide or photoresist with negligible differences.

¹[Online]. Available: <http://www.bsac.eecs.berkeley.edu/cfm/>

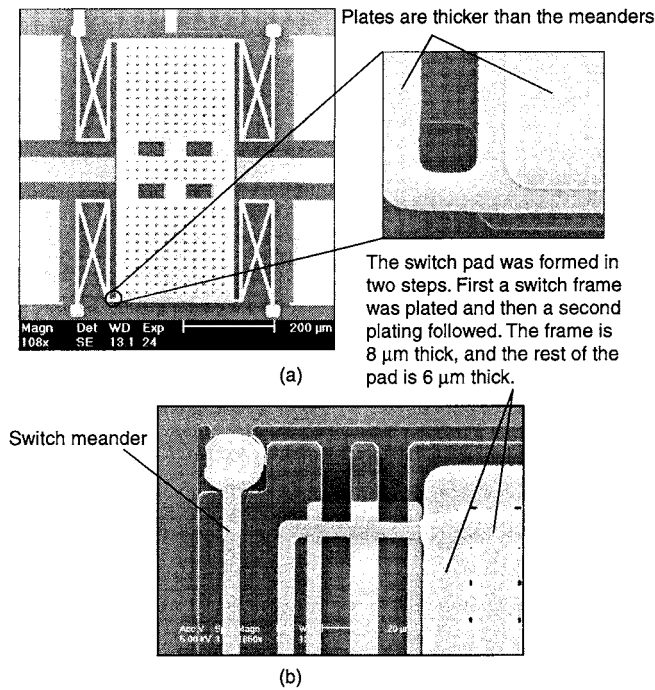
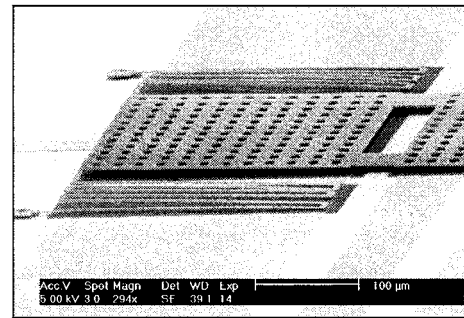


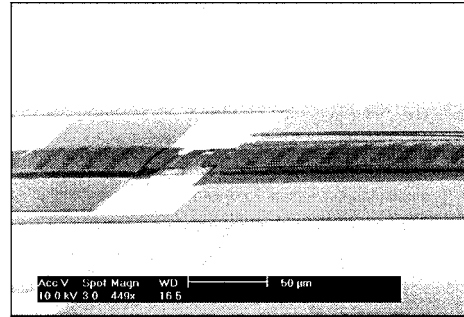
Fig. 11. Fabricated switches with the selective electroplating process. The adhesion problems of the first switch were solved by increasing the seed layer area that was exposed to the second plating.

Fig. 1 is one example of the plane switches fabricated with this process and Fig. 12 shows some details of three more examples. The switches shown in Figs. 1 and 12(a) are 2- μm thick and suspended over a 40/60/40- μm CPW line. Although the latter switch was fabricated with three meanders instead of one, no appreciable difference in the warping profile was observed. The maximum measured deflection (as defined in Fig. 9) for both of them is approximately 0.5 μm . This corresponds to less than 0.1% of the main switch length (640 μm) and does not affect the RF switch performance since it is strongly localized at the end of the dc actuation pad.

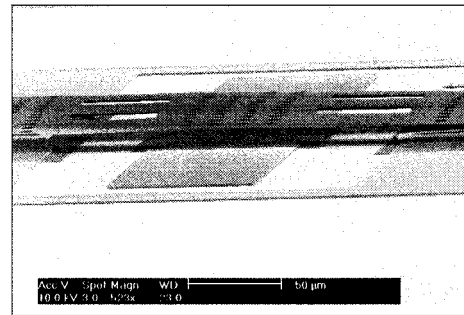
The improved fabrication process was also tested with switches only 1- μm thick, 680- μm long, and 240- μm wide. Two of these switches are shown in Fig. 12(b) and (c). Both switches include one meander, but in the first one, we have replaced the straight connecting beams with a second meandering beam. Evidently both structures are fairly plane and their residual gradient stress is nearly negligible. The first one, however, exhibits somewhat straighter profile, which is related to the axial residual stress, analyzed in the following section. This meandering connecting beam was originally employed to increase the shunt switch inductance [11], but it also proved useful in releasing the in-plane switch stress. As for the three short connecting beams, the slightly less plane switch may not appear very appealing at first, but it is very useful in limiting the high-frequency up-state insertion loss because it substantially reduces the up-state capacitance (by 50%–70%). Furthermore, the pull-in voltage increase is negligible (both structures actuate with 15–20 V) because most of the electrostatic force is concentrated on the ground-plane switch pads. Finally, both structures experienced some warping along their width, but this did not prove to be



(a)



(b)



(c)

Fig. 12. Very flat switches fabricated with sputtered Ti layer instead of evaporated. (a) This three-meander switch is 640- μm long, 2- μm thick, its maximum out-of-plane deformation is less approximately 0.5 μm , and the used sacrificial layer was polyimide. (b) and (c) These switches are 680- μm long, 1- μm thick, and photoresist was their sacrificial layer. Their warping level is approximately 3 μm and is mostly along their short dimension.

a problem. The switches were thin enough that were able to conform on the dielectric surface in the down state.

B. In-Plane Residual Stress

In-plane residual stress primarily increases the switch spring constant and is, therefore, essential to control it within reasonable limits. It was experimentally found [27] that the induced tensile stress during the fabrication process was in the order of 150 MPa. A first-order approximation that shows the impact of this stress on the spring constant is analyzed in [29] where the deflection of a guided-end cantilever is calculated under simultaneous axial tension and concentrated transverse loading. The maximum deflection at the tip of the beam is given by

$$z_{\max} = \frac{W}{\gamma P} \left[\frac{(\cosh(\gamma l) - 1)^2}{\sinh(\gamma l)} - (\sinh(\gamma l) - \gamma l) \right] \quad (12)$$

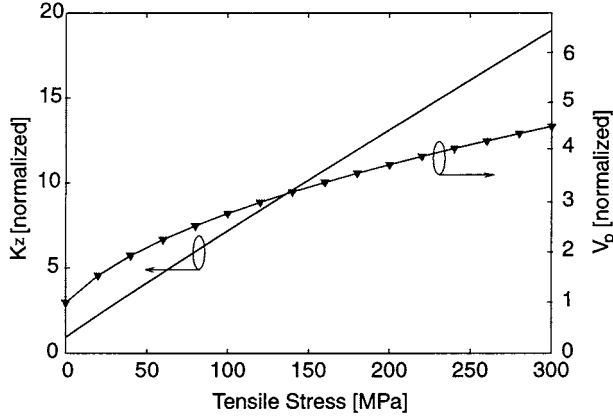


Fig. 13. Spring constant and pull-in voltage as a function of axial residual stress for a guided-end cantilever with simultaneous axial tension and concentrated transverse loading.

where P is the axial tensile load, W is the transverse concentrated load at the tip of the beam, l is the length of the beam, and γ is defined by

$$\gamma = \sqrt{\frac{P}{EI_x}}. \quad (13)$$

This leads to the following expression for the spring constant:

$$K_z^{\text{cant}} = \frac{\gamma P \sinh(\gamma l)}{2(1 - \cosh(\gamma l)) + \gamma l \sinh(\gamma l)}. \quad (14)$$

Fig. 13 shows the variation of the normalized spring constant and the associated actuation voltage (with respect to the spring constant and actuation voltage of zero axial stress) for an axial tensile stress of 0–300 MPa. This figure clearly demonstrates the considerable impact of the axial stress on the switch actuation voltage. For instance, a tensile stress of 150 MPa would increase the pull-in voltage of a switch suspended by four cantilever beams by over three times.

The serpentine beams shown in Fig. 2 exhibit higher flexibility in handling the in-plane mean stress than the simple cantilever beam. In other words, as the number of meanders is increased, not only is the z -directed spring constant reduced, but also the lateral ones. To show this effect, the x - and y -directed spring constants were calculated with a similar process to that of Section II. The y -directed spring constant can be expressed as

$$k_y = \frac{\frac{2S_{1y}}{Nb^2} EI_z}{2 \left(a + \frac{2b}{3} \right) S_{1y} - (a+b)S_{2y} - 3(2N+1)a(a+b)^2} \quad (15)$$

where S_{1y} and S_{2y} are calculated by

$$S_{1y} = 4N^2 a^2 + (4N^2 - 1) b^2 + 2(4N^2 + 1) ab \quad (16)$$

$$S_{2y} = 2N(2N-3)a^2 + (4N^2 - 1) b^2 + (8N^2 - 6N - 1) ab. \quad (17)$$

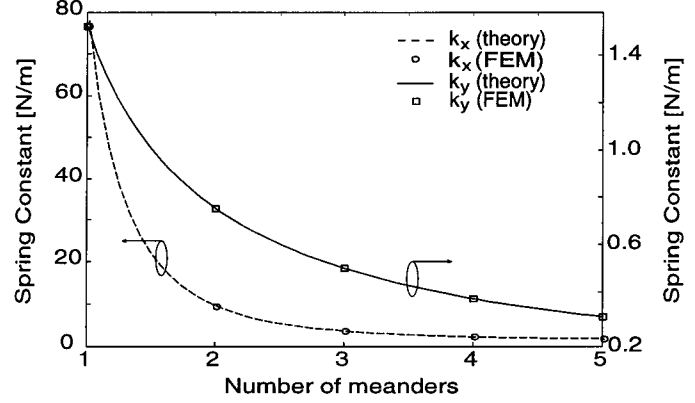


Fig. 14. In-plane spring constants of the serpentine spring for various number of meanders.

Similarly, the x -directed spring constant is given by

$$k_x = \frac{EI_z}{Na^2 \left[S_{1x} + S_{2x} + \frac{8N^2 a + (2N+1)(4N+1)b}{3} \right]} \quad (18)$$

where

$$S_{1x} = (2Na + (2N+1)b) \left[-\frac{2N+1}{2} + \frac{a \left(a + \frac{2b}{3} \right)}{(a+b) \left(a + \frac{b}{3} \right)} \right] \quad (19)$$

$$S_{2x} = -(2N+1)(a+b) \frac{a}{2 \left(a + \frac{b}{3} \right)}. \quad (20)$$

Linear FEM simulations verified the previous formulas and the results are given in Fig. 14. From this figure, we clearly observe that the spring constant of the serpentine spring is greatly reduced as the number of meanders is increased. For instance, a spring with three meanders is 177 times more flexible along the x -dimension than a spring with one meander. As a result, such a spring can help release the axial switch stress along its long dimension much more effectively than a spring with one meander. In other words, springs with many meanders are much more effective as stress buffers than springs with one only one meander. A similar tendency exists for k_y , which decreases by a factor of 5.2 when the meanders are increased from one to five. These results provide a qualitative explanation for the trends observed in Fig. 5.

IV. MEMS SWITCH DYNAMIC BEHAVIOR

Switching speed is one of the few disadvantages of MEMS components compared to p-i-n diodes and FET transistors. While their mass is typically very small (in the order of 10^{-11} to 10^{-9} kg), inertia due to mechanical movement still limits their speed typically in the order of a few microseconds. The fastest switch thus far has been developed by researchers at the Massachusetts Institute of Technology (MIT) Lincoln Laboratories [3]. It is a very compact cantilever switch (less than $50\text{-}\mu\text{m}$ long) with a speed of approximately $1\ \mu\text{s}$. This very low speed is primarily due to its very small dimensions, mass, and limited

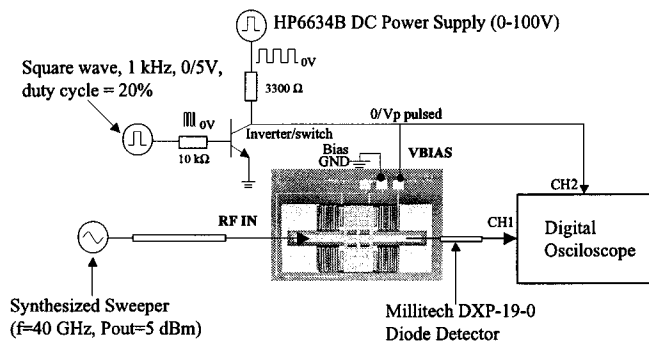


Fig. 15. Switching speed measurement setup (courtesy of Gabriel Rebeiz, The University of Michigan at Ann Arbor).

squeeze-film damping. It does require, however, a high pull-in voltage of 50–60 V, while it is typically actuated with 70–80 V. Low-voltage switches are generally expected to be slower since they typically have to move a relatively large actuation area. This is particularly true if the switch is expected to operate in air or another gas environment, such as N_2 for limiting the humidify level around the structure.

The switching speed is measured by recording the change in the power transmitted through the switch when a step voltage is applied at the bias of the device (Fig. 15) [30]. The RF input signal at 40 GHz is provided by an RF synthesizer, while the RF output signal is recorded by a high-frequency diode detector. The biasing signal is provided by a suitable combination of two dc power supplies and an inverter. Fig. 16 presents two typical measurements taken with this set-up for three-meander switches. The measured switches were suspended a mean distance of $5 \mu\text{m}$ above the CPW line and the applied bias voltage was only 20%–30% higher than their actuation voltage. Both pull-in and release times were measured for these switches. Pull-in time is the time it takes the switch to touch the dielectric underneath it. On the other hand, the time that is required for the switch to move from the down state to its original height (or within 5% from this value) is defined as the release time. Fig. 16 shows that the actuation and release times are approximately 52 and 213 μs , respectively. However, for the release time measurement, it takes the switch only 25 μs to reach its normal height, but another 190 μs are needed to settle within 5% of its original height. It is also interesting to note that, during the first 30 μs of the actuation stage, the switch does not move significantly. These effects will be discussed in the remainder of this section.

To explain the experimental results, we employed a simple one-dimensional (1-D) nonlinear model that has been adopted by several researchers [17], [31], [32]. This model treats the switch as a single lumped mass and applies classical Newtonian mechanics to predict its behavior under the applied electrostatic force. A model that would accurately predict the dynamic behavior of the MEMS structure should integrate a good understanding of several different phenomena including electrostatics, mechanics, residual stress, contact forces, compressible squeeze film damping, and impact effects on a microscale. Many of these areas are currently under investigation and there is not a complete model that would account for all of these effects. Furthermore, our switch is a relatively large structure that

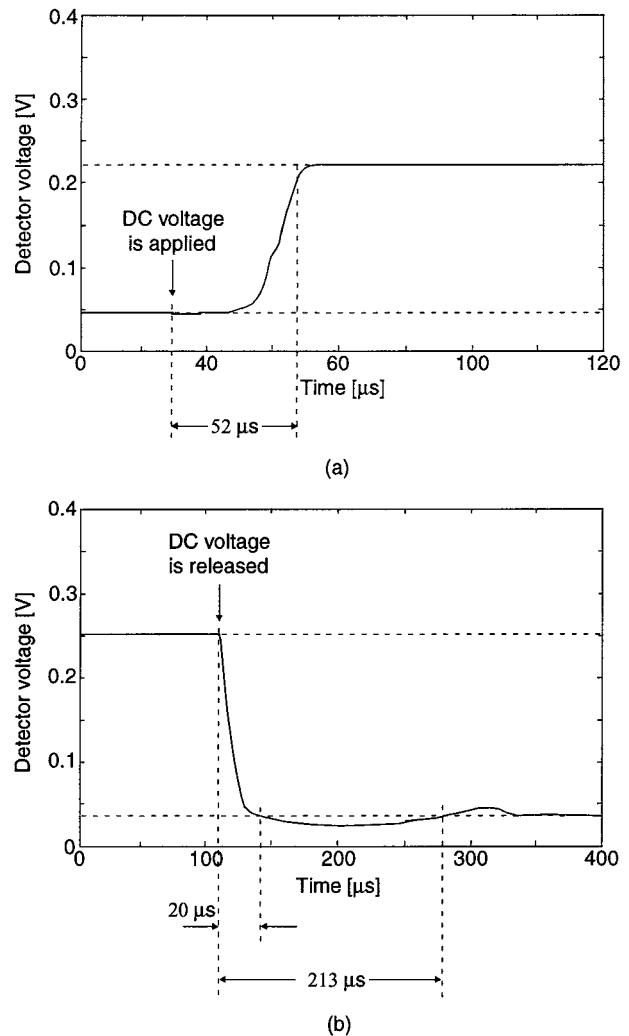


Fig. 16. Measurements of the switching time for the: (a) up-down and (b) down-up movements. Due to the diode detector, high-voltage level corresponds to low RF power and vice-versa.

cannot be perfectly approximated as a lumped mass. Nevertheless, the 1-D model can be used for an at least qualitative explanation of the measured switch behavior and provide reasonable approximations for the switching times.

The following equation of motion if the basic formula for the 1-D model:

$$mz'' + bz' + K_z z = F_e + F_c \quad (21)$$

where m is the switch mass, b is the damping coefficient, K_z is the switch spring constant in the direction of motion, A is the switch actuation area, g_0 is the initial gap, ϵ_r and t_d are the dielectric layer constant and thickness, respectively, V is the applied dc voltage, F_e is the electrostatic force, and F_c is the contact force when the switch touches the dielectric. Several approximations may be adopted for calculating the parameters in this model. For instance, although the viscous damping can be considered constant for small displacements, this is not the case when the switch is moving completely toward the substrate. Our

model for the switching speed calculations is based on the discussion presented in [31] and [33] where these effects are taken into account. These equations can be summarized as follows:

$$F_e = \frac{\epsilon_0 AV^2}{2 \left(g_0 + \frac{t_d}{\epsilon_r} - z \right)^2} \quad (22)$$

$$b = \frac{K_z}{\omega_0 Q}, \quad \text{where } \omega_0 = \sqrt{\frac{K_z}{m}} \quad (23)$$

$$Q = Q_0 \left(1 - \left(\frac{z}{g_0} \right)^2 \right)^{3/2} \left(1 + 9.638 \left(\frac{\lambda}{g_0 - z} \right)^{1.159} \right) \quad (24)$$

$$F_c = \frac{m_1 A}{(g_0 - z)^3} - \frac{m_2 A}{(g_0 - z)^{10}}. \quad (25)$$

Equation (24) calculates the switch quality factor and takes into account the damping dependence on the switch height. If this is ignored, the second term of the right-hand side should be replaced by one. Furthermore, the third term reduces the gas flow resistance underneath the switch because of the slip effect, where particles can have fewer interactions before escaping [34]. The variable λ of this term is called the mean free path and is approximately $0.1 \mu\text{m}$ at standard temperature pressure (STP). The damping coefficient, which is related to Q_0 by (23), has been derived in [35] for a square plate with area A as

$$b = \frac{3}{2\pi} \frac{\mu A^2}{g_0^3} \quad (26)$$

where μ is the air viscosity (at STP $\mu = 1.845 \cdot 10^{-5} \text{ Pa} \cdot \text{s}$). For the switch dimensions and for a gap of $5 \mu\text{m}$ $b \simeq 2.5 \cdot 10^{-4} \text{ Pa} \cdot \text{s}$ and $Q_0 = 0.64$ (for $K_z = 8.6 \text{ N/m}$). However, the holes included in the switch allow the air underneath to escape more easily, thus reducing the damping coefficient and increasing the Q of the structure. Therefore, this value can be considered as a low bound for the switch quality factor. In fact, our experimental results suggest a quality factor of about two. The final equation of the model (25) was used to provide a stable solution to the simulation when the switch contacts the dielectric layer.

Fig. 17(a) shows the simulated results for the pull-in and release time. A spring constant of 8.6 N/m (Table II) and an actuation voltage of 25% higher than the pull-in voltage have been used for these simulations. These simulations provide a valuable insight in the measured dynamic behavior of the switch. The pull-in time, for instance, is approximately $50 \mu\text{s}$, from which approximately $30 \mu\text{s}$ are needed for the switch to move from 5 to $3.5 \mu\text{m}$. The RF capacitance, however, does not change appreciably between this distance and this explains the relatively long period that is required to note any difference between the measured output power level (see Fig. 16). On the other hand, during the release stage, the switch reaches its original height within $35 \mu\text{s}$, but 140 additional microseconds are required for stabilization within 5% of its original height. We have also plotted in the same figure the simulated release time assuming a constant quality factor $Q = Q_0$. Evidently, taking into account the quality-factor variation versus height is of vital importance for meaningful simulations.

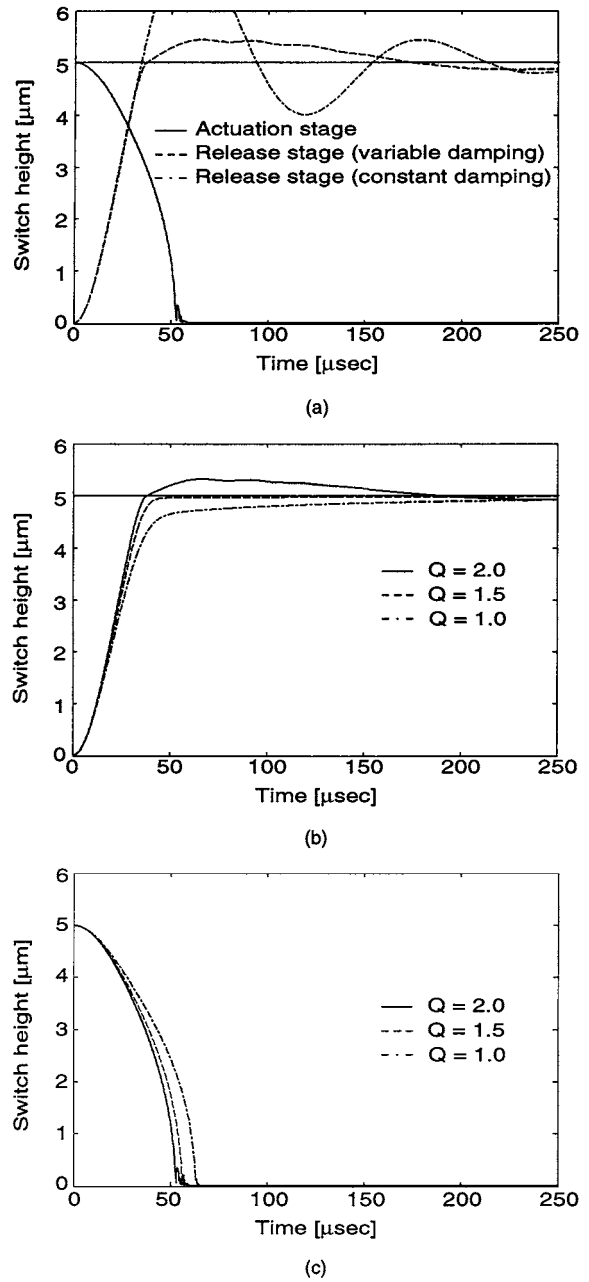


Fig. 17. (a) Simulated switch pull-in and release times. (b) Comparison of simulated release times for different values of the quality factor. (c) Comparison of simulated pull-in times for different values of the quality factor.

The problem of the long stabilization time can be easily corrected by decreasing the quality factor by approximately one. Fig. 17(b) shows the simulated release time for quality factors of 2, 1.5, and 1. This figure clearly demonstrates that the release time can be decreased by more than three times if a lower quality factor is achieved. This can be done by optimizing the hole orientation on the main switch structure and by reducing their number per unit area. This change will not appreciably increase the pull-in time, as shown in Fig. 17(c). For example, for $Q = 1.5$, the pull-in time will be increased by only 10%, yet the release time will be reduced by 300%. Consequently, an optimization of the switch holes can lead to a design with switching times in the order of $50\text{--}60 \mu\text{s}$.

V. CONCLUSIONS

Low-voltage RF MEMS switches have been studied in this paper. The design, fabrication, and testing of these structures has been thoroughly discussed and switch designs with as low as 6-V actuation voltages have been measured. Moreover, residual stress issues associated with this family of switches have been addressed and it has been experimentally demonstrated that sputtered seed layer films result in devices with superior performance when compared with evaporated films. Furthermore, the dynamic operation of low-voltage switches has been experimentally and theoretically characterized and adequate switching speeds in the order of 50 μ s have been achieved.

ACKNOWLEDGMENT

The authors are grateful to G. L. Tan, The University of Michigan at Ann Arbor, and G. M. Rebeiz, The University of Michigan at Ann Arbor, for designing and developing the measurement setup shown in Fig. 15.

REFERENCES

- [1] R. E. Mihailovich, M. Kim, J. B. Hacker, E. A. Sovero, J. Studer, J. A. Higgins, and J. F. DeNatale, "MEM relay for reconfigurable RF circuits," *IEEE Microwave Wireless Comp. Lett.*, vol. 11, pp. 53–55, Feb. 2001.
- [2] D. Hyman, A. Schmitz, B. Warneke, T. Y. Hsu, J. Lam, J. Brown, J. Schaffner, A. Walston, R. Y. Loo, M. Mehregany, and J. Lee, "Surface-micromachined RF MEMS switches on GaAs substrates," *Int. J. RF Microwave Computer-Aided Eng.*, vol. 9, pp. 348–361, Aug. 1999.
- [3] S. Duffy, C. Bozler, S. Rabe, J. Knecht, L. Travis, P. Wyatt, C. Keast, and M. Gouker, "MEMS microswitches for reconfigurable microwave circuitry," *IEEE Microwave Wireless Comp. Lett.*, vol. 11, pp. 106–108, Mar. 2001.
- [4] P. M. Zavracky, N. E. McGruer, R. H. Morrison, and D. Potter, "Microswitches and microrelays with a view toward microwave applications," *Int. J. RF Microwave Computer-Aided Eng.*, vol. 9, pp. 338–347, July 1999.
- [5] C. L. Goldsmith, Z. Yao, S. Eshelman, and D. Denniston, "Performance of low-loss RF MEMS capacitive switches," *IEEE Microwave Guided Wave Lett.*, vol. 8, pp. 269–271, Aug. 1998.
- [6] G. L. Tan and G. M. Rebeiz, "DC-26 GHz MEMS series-shunt absorptive switches," in *IEEE MTT-S Int. Microwave Symp. Dig.*, vol. 1, May 2001, pp. 325–328.
- [7] D. Peroulis, K. Sarabandi, and L. P. B. Katehi, "Low contact resistance series MEMS switches," in *IEEE MTT-S Int. Microwave Symp. Dig.*, vol. 1, June 2002, pp. 223–226.
- [8] J. B. Muldavin and G. M. Rebeiz, "High-isolation CPW MEMS shunt switches—Part 1: Modeling," *IEEE Trans. Microwave Theory Tech.*, vol. 48, pp. 1045–1052, June 2000.
- [9] G. M. Rebeiz and J. B. Muldavin, "RF MEMS switches and switch circuits," *IEEE Microwave Mag.*, vol. 2, pp. 59–71, Dec. 2001.
- [10] S. P. Pacheco, L. P. B. Katehi, and C. T. Nguyen, "Design of low actuation voltage RF MEMS switch," in *IEEE MTT-S Int. Microwave Symp. Dig.*, vol. 1, June 2000, pp. 165–168.
- [11] D. Peroulis, S. Pacheco, K. Sarabandi, and L. P. B. Katehi, "MEMS switches for high-isolation switching and tunable filtering," in *IEEE MTT-S Int. Microwave Symp. Dig.*, vol. 2, June 2000, pp. 1217–1220.
- [12] N. S. Barker and G. M. Rebeiz, "Optimization of distributed MEMS transmission-line phase shifters—U-band and W-band design," *IEEE Trans. Microwave Theory Tech.*, vol. 48, pp. 1957–1966, Nov. 2000.
- [13] J. S. Hayden and G. M. Rebeiz, "Low-loss cascaded MEMS distributed X-band phase shifters," *IEEE Microwave Guided Wave Lett.*, vol. 10, pp. 142–144, Apr. 2000.
- [14] D. Peroulis, S. Pacheco, K. Sarabandi, and L. P. B. Katehi, "Tunable lumped components with applications to reconfigurable MEMS filters," in *IEEE MTT-S Int. Microwave Symp. Dig.*, vol. 1, June 2001, pp. 341–344.
- [15] J. C. Chiao, Y. Fu, J. M. Chio, M. DeLisio, and L. Y. Lin, "MEMS reconfigurable antenna," in *IEEE MTT-S Int. Microwave Symp. Dig.*, vol. 2, June 1999, pp. 1515–1518.

- [16] C. Goldsmith, J. Ehmke, A. Malczewski, B. Pillans, S. Eshelman, Z. Yao, J. Brank, and M. Eberly, "Lifetime characterization of capacitive RF MEMS switches," in *IEEE MTT-S Int. Microwave Symp. Dig.*, vol. 1, June 2001, pp. 227–230.
- [17] E. K. Chan, E. C. Kan, and R. W. Dutton, "Non-linear dynamic modeling of micromachined microwave switches," in *IEEE MTT-S Int. Microwave Symp. Dig.*, vol. 3, June 1997, pp. 1511–1514.
- [18] R. K. Gupta and S. D. Senturia, "Pull-in time dynamics as a measure of absolute pressure," in *IEEE 10th Int. MEMS Workshop*, Jan. 1997, pp. 290–294.
- [19] G. K. Fedder, "Simulation of microelectromechanical systems," Ph.D. dissertation, Dept. Elect. Eng. Comput. Sci., Univ. California at Berkeley, Berkeley, CA, 1994.
- [20] S. P. Timoshenko and J. N. Goodier, *Theory of Elasticity*. New York: McGraw-Hill, 1970.
- [21] CADRE Analytic, "CADRE light, v. 1.3," in *Finite Element Structural Analysis Software* Samammish, WA, 1999.
- [22] D. Peroulis, S. P. Pacheco, K. Sarabandi, and L. P. B. Katehi, "RF MEMS switches with enhanced power handling capabilities," *IEEE Trans. Microwave Theory Tech.*, submitted for publication.
- [23] M. T. A. Saif and N. C. MacDonald, "Planarity of large MEMS," *J. Microelectromech. Syst.*, vol. 5, pp. 79–97, June 1996.
- [24] J. A. Thornton and D. W. Hoffman, "Stress related effects in thin films," *Thin Solid Films*, vol. 171, pp. 5–31, Apr. 1989.
- [25] S. M. Hu, "Stress related problems in silicon technology," *J. Appl. Phys.*, vol. 70, pp. 53–79, Sept. 1991.
- [26] W. Fang and J. A. Wickert, "Determining mean and gradient residual stresses in thin films using micromachined cantilevers," *J. Microelectromech. Syst.*, vol. 6, pp. 301–309, Sept. 1996.
- [27] L. Lin, A. P. Pisano, and R. T. Howe, "A micro strain gauge with mechanical amplifier," *J. Microelectromech. Syst.*, vol. 9, pp. 313–321, Dec. 1997.
- [28] D. Peroulis, S. Pacheco, K. Sarabandi, and L. P. B. Katehi, "Alleviating the adverse stress effects of residual stress in RF MEMS switches," in *Proc. Eur. Microwave Conf.*, vol. 1, Sept. 2001, pp. 173–176.
- [29] R. J. Roark and W. Young, *Formulas for Stress and Strain*, 6th ed. New York: McGraw-Hill, 1989.
- [30] G. L. Tan, "High-performance RF MEMS circuits and phase shifters," Ph.D. dissertation, Dept. Elect. Eng. Comput. Sci., Univ. Michigan at Ann Arbor, Ann Arbor, MI, 2002.
- [31] J. B. Muldavin and G. M. Rebeiz, "Nonlinear electro-mechanical modeling of MEMS switches," in *IEEE MTT-S Int. Microwave Symp. Dig.*, vol. 3, June 2001, pp. 2119–2122.
- [32] F. Shi, "Dynamic analysis of micro-electro-mechanical systems," *Int. J. Numer. Methods Eng.*, vol. 39, pp. 4119–4136, 1996.
- [33] J. B. Muldavin, "Design and analysis of series and shunt MEMS switches," Ph.D. dissertation, Dept. Elect. Eng. Comput. Sci., Univ. Michigan at Ann Arbor, Ann Arbor, MI, 2001.
- [34] T. Veijola, H. Kuisma, J. Lahdenpera, and T. Ryhanen, "Equivalent-circuit model of the squeezed gas film in a silicon accelerometer," *Sens. Actuators A, Phys.*, vol. 48, pp. 239–248, May 1995.
- [35] J. J. Blech, "On isothermal squeeze films," *J. Lubrication Tech.*, vol. 105, pp. 615–620, October 1983.



Dimitrios Peroulis (S'91–M'02) was born in Athens, Greece, in 1975. He received the Diploma degree in electrical and computer engineering from the National Technical University of Athens, Athens, Greece, in 1993, the M.S. degree in electrical engineering from The University of Michigan at Ann Arbor, in 1999, and is currently working toward the Ph.D. degree at The University of Michigan at Ann Arbor.

His current research is focused on MEMS and their applications to reconfigurable circuits and antennas for microwave and millimeter-wave frequencies.

Mr. Peroulis was the recipient of the 2002 Rackham Graduate School Pre-Doctoral Fellowship presented by The University of Michigan at Ann Arbor and the Third Place Award at the Student Paper Competition presented at the 2001 IEEE Microwave Theory and Techniques Society (IEEE MTT-S) International Microwave Symposium, Phoenix, AZ. He was also the recipient of two Student Paper Awards (honorable mentions) at the Student Paper Competitions presented at the 2002 IEEE MTT-S International Microwave Symposium, Seattle, WA, and the 2001 IEEE Antennas and Propagation Society (IEEE AP-S) International Symposium, Boston, MA, and two awards for academic excellence presented by the Technical Chamber of Greece and the Hellenic National Science Fellowship Foundation in 1997 and 1996, respectively.



Sergio P. Pacheco was born in Salvador, Bahia, Brazil, in 1969. He received the B.S.E.E. and M.S.E.E. degrees from Auburn University, Auburn, AL, in 1993 and 1995, respectively, and is currently working toward the Ph.D. in electrical engineering at The University of Michigan at Ann Arbor.

Since May 2001, he has been a Senior Staff Engineer with the Emerging Technologies Group, Digital DNA Laboratories, Motorola, Tempe, AZ. His research is focused on the application of MEMS to RF and wireless applications.

Mr. Pacheco is member of the IEEE Microwave Theory and Techniques Society (IEEE MTT-S) and the IEEE Electron Device Society (IEEE ED-S). He is also a member of the Omicron Delta Kappa, Eta Kappa Nu, and Tau Beta Pi Honor Societies. He was the recipient of the Judge's Best Paper Award presented at the IEEE MTT-S International Microwave Symposium in 1998.



Kamal Sarabandi (S'87-M'90-SM'92-F'00) received the B.S. degree in electrical engineering from the Sharif University of Technology, Tehran, Iran, in 1980, and the M.S.E. and Ph.D. degrees from The University of Michigan at Ann Arbor, in 1986 and 1989, respectively, both in electrical engineering.

From 1980 to 1984 he was a Microwave Engineer with the Telecommunication Research Center. He is currently the Director of the Radiation Laboratory and a Professor in the Department of Electrical

Engineering and Computer Science, The University of Michigan at Ann Arbor. He was the Principal Investigator of many projects sponsored by the National Aeronautics and Space Administration (NASA), Jet Propulsion Laboratory (JPL), Army Research Office (ARO), Office of Naval Research (ONR), Army Research Laboratory (ARL), National Science Foundation (NSF), Defense Advanced Research Projects Agency (DARPA), and numerous industries. He has authored or coauthored numerous book chapters and over 90 papers in refereed journals on electromagnetic scattering, random media modeling, wave propagation, antennas, microwave measurement techniques, radar calibration, inverse scattering problems, and microwave sensors. He has also had over 170 papers and invited presentations in national and international conferences and symposia on similar subjects. His research areas of interest include electromagnetic-wave propagation, antennas, and microwave and millimeter-wave radar remote sensing. He is listed in *Who's Who in American Men and Women of Science*, *Who's Who in America*, and *Who's Who in Electromagnetics*.

Dr. Sarabandi is a member of the IEEE Geoscience and Remote Sensing Society (IEEE GRSS) Administrative Committee (AdCom), chairman of the Awards Committee of the IEEE GRSS, and a member of the IEEE Technical Activities Board Awards Committee. He is also a member of Commission F, International Scientific Radio Union (URSI), and the Electromagnetic Academy. He is the associate editor of the IEEE TRANSACTIONS ON ANTENNAS AND PROPAGATION and the IEEE SENSORS JOURNAL. He was the recipient of the Henry Russel Award presented by the Regent of The University of Michigan, the GAAC Distinguished Lecturer Award presented by the German Federal Ministry of Education, Science and Technology in 1999, and the 1996 Teaching Excellence Award presented by the Electrical Engineering and Computer Science Department, The University of Michigan at Ann Arbor.



Linda P. B. Katehi (S'81-M'84-SM'89-F'95) received the B.S.E.E. degree from the National Technical University of Athens, Athens, Greece, in 1977, and the M.S.E.E. and Ph.D. degrees from the University of California at Los Angeles, in 1981 and 1984, respectively.

In September 1984, she joined the faculty of the Electrical Engineering and Computer Science Department, The University of Michigan at Ann Arbor, as an Assistant Professor, and then became an Associate Professor in 1989 and Professor in

1994. She has served in many administrative positions, including Director of Graduate Programs, College of Engineering (1995-1996), Elected Member of the College Executive Committee (1996-1998), Associate Dean For Graduate Education (1998-1999), and Associate Dean for Academic Affairs (since September 1999). She is currently the Dean of the Schools of Engineering, Purdue University, West Lafayette, IN. She has authored or coauthored 410 papers published in refereed journals and symposia proceedings and she holds four U.S. patents. She has also generated 20 Ph.D. students.

Dr. Katehi is a member of the IEEE Antennas and Propagation Society (IEEE AP-S), the IEEE Microwave Theory and Techniques Society (IEEE MTT-S), Sigma Xi, Hybrid Microelectronics, and International Scientific Radio Union (URSI) Commission D. She was a member of the IEEE AP-S Administrative Committee (AdCom) (1992-1995). She was an associate editor for the IEEE TRANSACTIONS ON MICROWAVE THEORY AND TECHNIQUES and the IEEE TRANSACTIONS ON ANTENNAS AND PROPAGATION. She was the recipient of the 1984 IEEE AP-S W. P. King (Best Paper Award for a Young Engineer), the 1985 IEEE AP-S S. A. Schelkunoff Award (Best Paper Award), the 1987 National Science Foundation Presidential Young Investigator Award, the 1987 URSI Booker Award, the 1994 Humboldt Research Award, the 1994 University of Michigan Faculty Recognition Award, the 1996 IEEE MTT-S Microwave Prize, the 1997 International Microelectronics and Packaging Society (IMAPS) Best Paper Award, and the 2000 IEEE Third Millennium Medal.

Bandwidth Enhancement and Further Size Reduction of a Class of Miniaturized Slot Antennas

Nader Behdad, *Student Member, IEEE*, and Kamal Sarabandi, *Fellow, IEEE*

Abstract

In this paper new methods for further reducing the size and/or increasing the bandwidth of a class of miniaturized slot antennas are presented. In general miniaturized antennas show a small fractional bandwidth and poor radiation efficiency each of which can seriously limit their applications. In addition, impedance matching of electrically small antennas is difficult. Recently, a class of miniaturized slot antennas that shows high efficiency and is easy to match was introduced [4]-[5]. This paper examines techniques such as parasitic coupling and inductive loading to achieve higher bandwidth and further size reduction for this class of miniaturized slot antennas. A systematic procedure is developed to design parasitically coupled antennas at a designated frequency by extracting the coupling coefficient from a full-wave analysis. It is shown that, if the antenna structure is designed properly, the overall bandwidth can be increased by more than 100% with respect to a single resonant antenna. The behavior of miniaturized slot antennas once loaded with series inductive elements along the radiating section is also examined. The inductive loads are constructed by two balanced short circuited slot lines placed on opposite sides of the radiating slot. It is shown that the inductive loads can considerably reduce the antenna size at its resonance. Prototypes of double-antenna structure at 850 MHz and inductively loaded miniaturized antennas at around 1 GHz are designed and tested. Finally the application of both methods in a dual band miniaturized antenna is presented. In all cases measured and simulated results show excellent agreement.

Index Terms

Slot Antennas, Electrically Small Antennas, Parasitic Antennas, Multi-frequency Antennas.

Authors are with The Radiation Laboratory, Department of Electrical Engineering and Computer Science, The University of Michigan, Ann Arbor, MI, 48109-2122, USA.

I. INTRODUCTION

The current advancements in communication technology and significant growth in the wireless communication market and consumer demands, demonstrate the need for smaller, more reliable and power efficient, integrated wireless systems. Entire transceivers integrated on a single chip are envisioned for future wireless systems. This vision has the benefit of reducing costs and improving system reliability. Antennas are, of course, inherent parts of any wireless system and are considered to be the largest components of integrated wireless systems. Antenna miniaturization and integration is thus an important task towards achieving the optimal design for integrated wireless systems. The subject of antenna miniaturization is not new and has been extensively studied by various authors [1]-[3]. Early studies have shown that for a resonant antenna, as the size is decreased, its bandwidth (BW) and efficiency would also decrease [1]. This is a fundamental limitation which, in general, holds true independent of antenna architecture. However, research on the design of antenna topologies and architectures must be carried out to achieve maximum possible bandwidth and efficiency for a given antenna size. Impedance matching for small antennas is also challenging which often requires external matching networks. Therefore antenna topologies and structures which inherently allow for impedance matching are highly desirable. The fundamental limitation introduced by Chu [1] relates the radiation Q of a single resonance antenna with its bandwidth. However, whether such limitation can be directly extended to multi-resonance antenna structures or not is unclear. In fact, through a comparison with filter theory designing a relatively wide-band antenna may be possible using multi-pole (multi-resonance) high Q structures. In this paper we examine the applicability of multi-resonance antenna structures to enhance bandwidth.

Techniques for antenna miniaturization can be categorized into two basic groups including: 1) antenna miniaturization, using optimal antenna topology [4]-[5] and 2) Antenna miniaturization, using magneto-dielectric materials [6]-[7]. In pursuit of achieving antenna miniaturization while maintaining ease of impedance matching and attaining a relatively high efficiency a novel miniaturized slot antenna was recently presented [4]. Afterwards a similar architecture in the form of a folded antenna geometry was presented in order to increase the bandwidth of the previous miniaturized slot antenna [5]. Here we reexamine this topology [4] and propose modifications that can result in further size reduction and/or significant bandwidth enhancement without imposing

any significant constraint on impedance matching or antenna gain reduction. In order to improve the bandwidth of this antenna a dual resonance architecture is examined. Two similar miniaturized slot antennas (see Figure 1(a)) are considered in order to form a dual antenna structure (see Figure 1(b)) where one of the elements is fed by a microstrip transmission line and the other one is fed parasitically by the first antenna. It is shown that the bandwidth of this new double-antenna configuration is 2.7 times that of the individual constituent antennas. In other words, by slightly increasing the occupied area of a single miniaturized antenna, the bandwidth can be increased by a factor greater than two.

A resonant slot antenna, at its first mode of operation, can be modeled with a half-wavelength transmission line that is short circuited at both ends. It is shown that by using series inductive elements distributed along the antenna aperture, its size can be reduced considerably. In other words, the guided wavelength of the resonant slot line is shortened by increasing the inductance per unit length of the line achieved by loading the line with series distributed inductors. The size reduction is shown to depend on the number and values of the series inductors. The technique is first demonstrated using a standard resonant slot antenna (a magnetic dipole) and then incorporated in the miniaturized antenna topology to further reduce the resonant frequency without changing the area occupied by the antenna.

The aforementioned techniques for bandwidth enhancement and further size miniaturization can be used individually or in combination. In what follows, first the design of the miniaturized antenna with enhanced bandwidth and its simulation and measurement results are presented (section II). The concept of using distributed inductive loading for antenna miniaturization is then investigated and the simulation and measurement results are presented (section III). Finally the combined application of the techniques shown in sections II and III, is presented in section IV.

II. MINIATURIZED SLOT ANTENNA WITH ENHANCED BANDWIDTH

A. Design Procedure

In this section the design of coupled miniaturized slot antennas for bandwidth enhancement is studied. The configuration of the proposed antenna is shown in Figure 1(b) where two miniaturized slot antennas are arranged so that they are parasitically coupled. Each antenna occupies an area of about $0.15\lambda_0 \times 0.13\lambda_0$ and achieves miniaturization by the virtue of a special topology described in detail in [4]. However, it is shown that this antenna demonstrates a small

bandwidth (less than 1%). A close examination of the antenna topology reveals that the slot-line trace of the antenna only covers about half of the rectangular printed-circuit board (PCB) area. Therefore, it is possible to place another antenna, with the same geometry, in the remaining area without significantly increasing the overall PCB size. Placing two antennas in close proximity of each other creates strong coupling between the antennas, which if properly controlled can be employed to increase the total antenna bandwidth. Each antenna can be viewed as a resonator designed to resonate at a desired center frequency of $f_0 = 850\text{MHz}$. The resonant frequencies of the slot antennas are determined by the overall effective slot electrical length with the first resonance occurring at $l = \lambda_g/2$, where λ_g is the guided wavelength in the slot.

As shown in Figure 1(b), only one of the two antenna structures is fed by a microstrip line. The other antenna is parasitically fed through a capacitive coupling mostly at the elbow section. In reality, the coupling is a mixture of electric and magnetic couplings that counteract each other. At the elbow section, where the electric field is large and the electric current in the ground plane around each slot is small, the slots are very close to each other. Therefore, it is expected that the electric field coupling is the dominant coupling mechanism. It can easily be shown that the electric fields in the two antennas are in phase, or equivalently, the magnetic currents are in-phase and parallel to each other and the radiated far-field is enhanced. If the electric fields were out of phase, the radiation efficiency would have dropped significantly, rendering the combined antenna almost useless.

Ideally the return loss, S_{11} , of a well matched single antenna shows a null ($-\infty$ dB) at the resonant frequency. Similar to the design of a two-pole coupled resonator filter, the two coupled antennas are to be designed at the same resonance frequency $f_{r1} = f_{r2} = f_0$, where f_0 is the center frequency and f_{r1} and f_{r2} are the resonant frequencies of the two resonators. In this case the S_{11} spectral response of the coupled antenna will show two nulls, the separation of which is related to coupling coefficient between the two antennas. This coupling coefficient can easily be adjusted by varying the separation between the two antennas. The separation between the two antennas can be parameterized by two vertical and horizontal parameters d and s as shown in Figure 2. In order to relate d and s to the pole separation (S_{11} nulls), a coupling coefficient k_t can be defined as:

$$k_t = \frac{f_u^2 - f_l^2}{f_u^2 + f_l^2} \quad (1)$$

where f_u and f_l are the frequencies of the upper and lower nulls of return loss. Using this definition, a large separation between the nulls of S_{11} requires larger k_t and smaller separation requires smaller k_t . A full-wave electromagnetic simulation tool is used to extract k_t as a function of physical parameter d for a fixed s . Figure 2 shows the dependence of k_t to d for a fixed value of $s = 1mm$. By choosing the right value for the coupling coefficient, the nulls can be arranged such that the overall bandwidth of the antenna increases. Bandwidth maximization is accomplished by choosing a coupling coefficient so that S_{11} remains below -10 dB over the entire frequency band as the two nulls are separated. Here the resonant frequencies of both antennas are fixed at $f_{r1} = f_{r2} = 850MHz$, and k_t is used as the tuning parameter. However, it is also possible to change f_{r1} and f_{r2} slightly in order to achieve a higher degree of control for tuning the response. Section IV will demonstrate that k_t , f_{r1} , and f_{r2} can be used as design parameters to obtain a miniaturized dual band antenna. The input impedance of a microstrip-fed slot antenna, for a given antenna slot width, depends on the location of the microstrip feed relative to one end of the slot and varies from zero at the short circuited end to high resistance at the center. This characteristic of slot antennas can be used to easily match them to a wide range of desired input impedances. The optimum location of the feed line can be determined from the full-wave simulation. In the double antenna example the feed line consists of a 50Ω transmission line connected to an open-circuited 75Ω line crossing the slot. The 75Ω line is extended by $0.33\lambda_m$ beyond the strip-slot crossing to couple the maximum energy to the slot and also compensate for the imaginary part of the input impedance.

B. Fabrication and Measurement

The structures in Figure 1 were simulated using IE3D [9] which is a full wave simulation software based on Method of Moments (MoM) and generally assumes infinite ground plane and dielectric substrate. The unknowns in the MoM solution of this problem were the slot electric fields (magnetic currents) and the electric currents on the microstrip transmission line. Solving for the magnetic currents reduces the complexity and the time required for simulations but at the same time limits the capability of the software to calculate conductor losses associated with the electric currents flowing in the ground plane of the antenna. All antennas were fabricated on a Rogers RO4350B substrate with the thickness of $500\mu m$, dielectric constant of $\epsilon_r = 3.5$, and $\tan(\delta) = 0.003$ with a copper ground plane of $33.5 \times 23 cm^2$. The responses of the single-element

antenna as well as the double-antenna are presented in Figure 3. The single-element antenna shows a bandwidth of 8 MHz or nearly 0.9% whereas the bandwidth of the double-antenna is shown to be 21.6 MHz (2.54%) which indicates a factor of 2.7 increase in the bandwidth. By choosing a different substrate with different thickness and dielectric constant, it is possible to increase the overall bandwidth of both antennas. However, it is also expected that the bandwidth ratio of the double-antenna to the single antenna remains the same. The overall size of the double-antenna is $0.165\lambda_0 \times 0.157\lambda_0$ which shows a 25% size increase when compared to the size of a single element antenna ($0.133\lambda_0 \times 0.154\lambda_0$). Comparing this bandwidth enhancement method to that of [5] which uses a folded slot antenna to increase the bandwidth of a miniaturized slot antenna, the increase in size is smaller (25% versus 34%) while the increase in bandwidth is higher (2.7 vs. 2).

Radiation patterns of the antenna were measured at the center frequency and the gain of the antenna was measured at three different frequencies and are presented in Table I. Figure 4 shows the E- and H-Plane for both co-polarized and cross-polarized radiation patterns. The E- and H-Plane radiation patterns of this antenna are expected to be dual of those of a short electric dipole. Figure 4(b) shows the H-Plane radiation pattern which is very much like the E-Plane radiation pattern of an electric dipole antenna. Figure 4(a) however, does not show a uniform radiation pattern like the H-Plane radiation pattern of a short electric dipole. This can be attributed to the finiteness of the ground plane where some radiation comes from the electric currents on the antenna ground plane at the edges of the substrate. Since there is phase difference between the electric currents around the slot edge and those at the substrate edge, radiated fields from these currents interfere destructively causing the deeps in the E-Plane radiation pattern around $\theta = \pm 90^\circ$. The H-Plane pattern is expected to have deep nulls at these angles. Therefore, this effect is not significant for H-Plane pattern. Table I shows the radiation characteristics of the double- and single-antenna. It is shown that the gain-bandwidth product of the proposed double-antenna is significantly higher than that of the single antenna.

III. IMPROVED ANTENNA MINIATURIZATION USING DISTRIBUTED INDUCTIVE LOADING

A. Design Procedure

A slot antenna fed by a microstrip transmission line radiates as a magnetic dipole which is considered the dual of an electric dipole. This antenna at its first resonance has the length of $\lambda_g/2$,

where λ_g is the wavelength in the slot. The magnetic current distribution can be modelled by the field distribution over a $\lambda/2$ transmission line short circuited at both ends. A series inductor in this transmission line reduces its resonant length. For slot lines, insertion of series lumped elements is not possible. Besides, series lumped elements have a low Q which adversely affects antenna efficiency (gain). The wavelength in a transmission line (λ_g) can be made smaller, if the inductance per unit length of the line is increased. To realize a slot line with higher inductance per unit length, an array of distributed, short circuited, narrow slot-lines can be placed along the radiating segment of the slot antenna as shown in Figure 5(b). The impedance of a short circuited slot line is obtained by:

$$Z_S = jZ_{0s} \tan(\beta_g l) \quad (2)$$

where β_g is the propagation constant, Z_{0s} is the characteristic impedance, and l is the length of the short circuited slot-line. The characteristic impedance of a slot-line is inversely proportional to its width [8] therefore by using wider series slots, more inductance can be obtained for a fixed length of short circuited transmission line. The best location to put series inductors in a slot is near its end where the amplitude of magnetic current is small. Putting them at the center of the slot where the magnetic current is at its maximum strongly degrades the radiation efficiency. It can easily be seen that by increasing the number and value of inductors, the length of transmission line necessary to satisfy the short circuit conditions at both ends of the slot decreases.

The size reduction may also be interpreted by considering the electric current distribution in the conductor around the slot. There are two components of electric current in the ground plane of slot, one that circulates around the slot and one that is perpendicular to it. The latter is described by the continuity of the electric current and displacement current at the slot discontinuity. Putting a discontinuity (a slit) normal to the circulating current path forces the current to circle around the discontinuity. Hence the electric current traverses a longer path length than the radiating slot length which in turn lowers the resonant frequency. Figure 5(b) shows a slot antenna loaded with a number of narrow slits which act as an array of series inductors. These slits are designed to have a length smaller than $\lambda_g/4$ so that they behave as inductive elements. The slits carry a magnetic current whose direction is normal to that of the main radiator. Placing them only on one side of the radiating slot results in asymmetry in phase and amplitude of the current along

the slot which could create problems in matching and worsen cross polarization. In order to circumvent this problem, two series slits are placed on the opposite sides of the main slot. These slits carry magnetic currents with equal amplitudes and opposite directions. Since the lengths of these narrow slits are small compared to the wavelength and since they are closely spaced, the radiated fields from the opposite slits cancel each other. That is, the slits do not contribute to the radiated far-field.

Matching this slot antenna to the microstrip feed is no different than matching an ordinary slot antenna. As before, an off-center microstrip feed is used to match the input impedance. The optimum location and length of the microstrip line are found by trial and error, using full wave simulations. Here for both slot dipoles (with and without series inductors) the lengths of the extended microstrip lines are found to be $\lambda_m/4$ where λ_m is the wavelength in the microstrip transmission lines at their respective resonance frequencies. This shows that the imaginary parts of the input impedances in both cases are relatively small, and by choosing the right location for the feed line, the input impedances can be directly matched to a 50Ω line.

Figure 6 shows a miniaturized slot antenna configuration (similar topology as shown in [4]) loaded with series inductive slits to further reduce its resonant frequency. The antenna without the series inductors is already small and adding series inductive elements further reduces the resonant frequency or equivalently the electrical dimensions of the antenna. Instead of using identical inductive elements along the radiating slot, differently sized inductive slits are used to cover most of the available area on the PCB in order to maintain the area occupied by the antenna. The antenna is matched to a microstrip transmission line in a manner similar to the magnetic dipole described earlier. The feed line is a 75Ω open ended microstrip line connected to a 50Ω microstrip line. The reason for using a 75Ω line is its narrow width which allows for localized feeding. In this case the open circuited microstrip line lengths beyond the slot crossing are respectively $0.3\lambda_m$ and $0.26\lambda_m$ for both the miniaturized antenna and the loaded miniaturized antenna. This shows that the imaginary parts of the input impedances of both antennas are relatively small. In the next section the simulated and measured results for these antennas are presented.

B. Fabrication and Measurement

The magnetic dipoles with and without series inductors were simulated using IE3D and fabricated on a $500\mu\text{m}$ thick Rogers RO4350B substrate. Figure 7(a) shows the simulated and measured return losses for the slot antennas without and with inductive loading. This Figure shows the dipole resonant frequency and -10dB bandwidth of 2.2GHz , and 235 MHz (10.7%) respectively. The loaded dipole with the same length as that of the unloaded dipole has a resonance frequency of 1.24 GHz and a bandwidth of 63 MHz (5%). This result indicates a 44% reduction in the resonant frequency and a similar reduction in the bandwidth, as expected. The overall size can still be reduced by using longer short circuited slits, if they themselves could be designed in a compact fashion. The radiation patterns of the small slot antenna were measured in the anechoic chamber of the University of Michigan and are presented in Figure 8. It is seen that the cross polarization components in the far-field region in both E- and H-planes are negligible, thereby confirming the fact that the radiation from the magnetic currents in the inductive loadings with opposite directions cancel each other in the far-field region.

The miniaturized loaded and unloaded slot antennas were also fabricated using RO4350B substrate. Figure 7(b) shows the simulated and measured return losses of the loaded and unloaded miniaturized antennas. It is shown that, by inserting the series inductors, the resonant frequency of the antenna shifts down from 1116 MHz to 959 MHz (14% reduction). In this design, the overall PCB size is unchanged. Figure 9 shows the E- and H-Plane co- and cross-polarized radiation patterns of the loaded miniaturized antenna. The level of cross polarization is found to be negligible at broadside. The gains of the loaded and unloaded miniaturized slot antennas (antenna in Figure 6) were also measured in the anechoic chamber using a standard log-periodic reference antenna and were found to be 0.8 dB and 0.7 dB respectively. Comparing the gain of loaded and unloaded miniaturized slot antennas with each other, it can easily be seen that using series elements in the slot does not affect the gain significantly.

IV. DUAL BAND MINIATURIZED SLOT ANTENNA

In this section the techniques introduced in the previous sections are both used in the design of a dual band miniaturized slot antenna. The geometry of this antenna is shown in Figure 10. The resonant frequencies of the slot antennas (f_{r1} and f_{r2}) and the value of the coupling coefficient (k_t) can be used as design parameters to achieve the desired response. Increasing the vertical

displacement, d , and decreasing the horizontal separation, s , cause k_t to increase or equivalently result in a larger separation between the two frequency bands. Small changes in the resonance lengths of the slots result in slight changes in f_{r1} and f_{r2} which can be used as a means of fine-tuning. It should be noted, however, that resonant frequencies f_{r1} , and f_{r2} should be close to each other so that coupling takes place. The dual band behavior of this antenna can be explained by small modifications in the coupled resonator filter theory. Theoretically the separation between the two nulls can be very large, but it requires values for k_t that are prohibitively large and cannot easily be obtained using these types of coupled structures where both electric and magnetic couplings are present and add destructively. In addition to this problem, matching the antenna at the two bands becomes increasingly difficult. The parameter Δ_f is defined as a measure of separation between the two frequency bands:

$$\Delta_f = \frac{\Delta f}{f_0} = \frac{f_u - f_l}{f_0} \quad (3)$$

where f_0 is the center frequency. In practice by changing k_t , f_{r1} , and f_{r2} , values of Δ_f up to 10% can easily be obtained. This architecture is particularly useful for wireless applications that use two separate frequency bands (different bands for transmit and receive for example) that are close to each other but still cannot be covered with the available bandwidth of these types of miniaturized antennas.

In order to reduce the size of the antenna even more, series inductive elements are also used to reduce the resonance frequencies of each antenna. This way a higher level of miniaturization can be achieved for a given antenna size. Figure 11 shows the simulated and measured return loss of such a dual band antenna. The discrepancies between the simulated and measured results are due to the finiteness of the ground plane as described in [4]. The measured results indicate an $f_l = 761.5MHz$ and $f_u = 817.5MHz$ or equivalently a $\Delta_f = 7.1\%$. Matching this antenna to the microstrip transmission feed is similar to the matching techniques used in the previous sections, where an off center microstrip is used. The microstrip line is extended by 7 cm over the slot-strip transition to obtain a good match at both frequencies. The overall size of the structure is $5.73cm \times 5.94cm$ or equivalently $0.145\lambda_0 \times 0.15\lambda_0$ at the lowest frequency of operation. Radiation patterns of the antenna are measured and found to be similar to those of the single element antenna topology.

V. CONCLUSIONS

Two approaches are introduced for increasing the bandwidth and reducing the size of miniaturized slot antennas. Placing two similar slot antennas in close proximity of each other creates a coupled resonator structure, the response of which is a function of relative spacing between the two antennas. The coupled miniaturized antenna can be designed to have more than twice the bandwidth of a single antenna or to behave as a dual band antenna. It is shown that the bandwidth can be increased by a factor of 2.7 while increasing the size by only 25%. Excellent agreement between simulation and measured results are shown.

For a fixed resonant frequency, it is shown that adding series inductive elements to a slot antenna reduces its size. The size reduction is a function of number and values of the inserted inductive elements. It is demonstrated that using series inductive elements does not adversely affect impedance matching and antenna gain. This technique is also used in combination with other miniaturization techniques to further decrease the size of the radiating structure. The technique is applied to a straight as well as a miniaturized slot antenna and for a given antenna size, significant reduction in resonant frequencies are observed. Good agreement between simulated and measured results are shown.

Finally, both techniques are applied to the design of a miniaturized dual band antenna. Series slits (inductors) are used to reduce the resonant frequencies of each resonator. A large value of coupling coefficient is used to achieve a large separation between the two nulls in the S_{11} response of the parasitically coupled antenna. The values of k_t , f_{r1} , and f_{r2} are used as design parameters in order to obtain a miniaturized dual band slot antenna with relatively good simultaneous matching.

ACKNOWLEDGMENT

This work was supported in part by the Engineering Research Centers program of the National Science Foundation under NSF Award Number EEC-9986866 and by the US Army Research Office under the contract DAA-99-1-01971.

REFERENCES

- [1] L. J. Chu, "Physical limitations on omni-directional Antennas", J. Appl. Phys., vol. 19 pp. 1163-1175, Dec 1948.
- [2] H. A. Wheeler, "Fundamental Limitations of small antennas", Proc. IRE. Vol. 35. pp. 1479-1484, Dec, 1947.

[3] R. C. Hansen, "Fundamental limitations in antennas", Proc. IEEE, Vol. 69, pp. 170-182, Feb 1981.

[4] K. Sarabandi and R. Azadegan, "Design of an efficient miniaturized UHF planar antenna", Proc. IEEE Int. Antennas Propagat. & URSI Symp., Boston, Massachusetts, July 8-13, 2001.

[5] R. Azadegan and K. Sarabandi, "Miniaturized Folded-Slot: An Approach to increase the Bandwidth and Efficiency of Miniaturized Slot Antennas", Proc. IEEE Int. Antennas Propagat. & URSI Symp., San Antonio, Texas, June 16-21, 2002.

[6] K. Sarabandi and H. Mosallaie, "Antenna Miniaturization with Enhanced Bandwidth and Radiation Characteristics: A Novel Design utilizing Periodic Magneto-Dielectric ", Proc. IEEE Int. Antennas Propagat. & URSI Symp., San Antonio, Texas, June 16-21, 2002.

[7] T. Ozdemir, P. Frantzis, K. Sabet, L. Katehi, K. Sarabandi, and J. Harvey, Compact wireless antennas using a superstrate dielectric lens, Proc. IEEE Trans. Antennas Propagat. & URSI Symp., Salt Lake City, Utah, July 2000.

[8] J.J. Lee, "Slotline Impedance", IEEE Transactions on Microwave Theory and Techniques, Vol. 39, pp. 666-672, Apr, 1991.

[9] IE3D, Electromagnetic Simulation and Optimization Software, Zeland Software, Inc.

Type	Size	Bandwidth	Gain			
			f(MHz)	848	852	860
Double Slot	$0.165\lambda_0 \times 0.157\lambda_0$	2.4%	G(dB)	1.5	1.7	1.7
Single Slot	$0.133\lambda_0 \times 0.154\lambda_0$	0.9%	1.5dB			

TABLE I

PHYSICAL AND ELECTRICAL PARAMETERS OF SINGLE-ELEMENT AND COUPLED ANTENNAS SHOWN IN FIGURE 1.

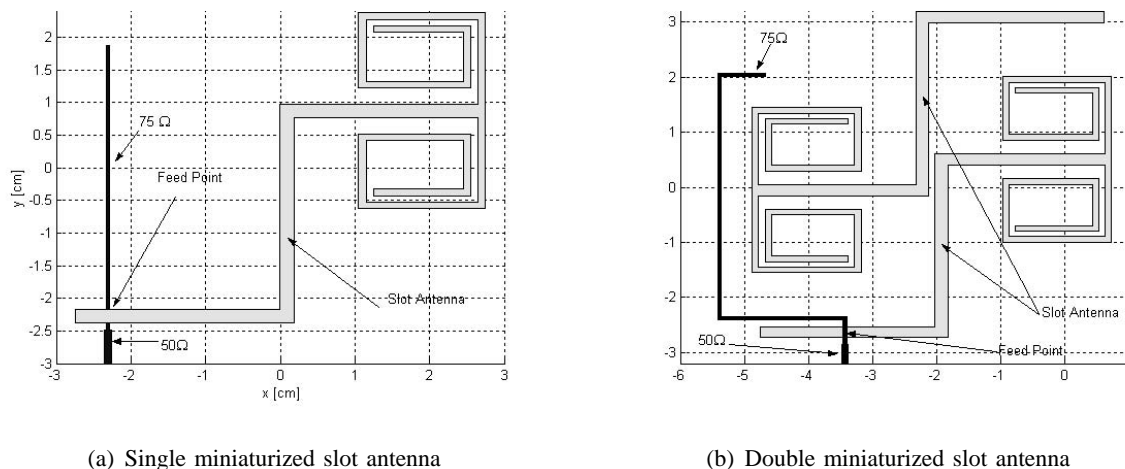


Fig. 1. The geometry of single and double miniaturized slot antennas

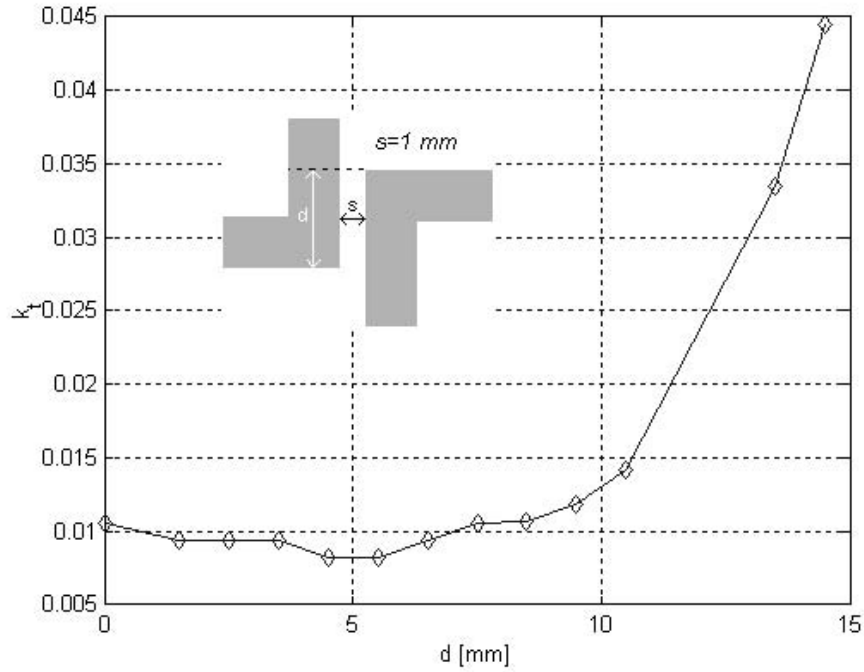


Fig. 2. Coupling coefficient k_t versus vertical displacement parameter d . k_t is derived from a number of full-wave simulations of the coupled antenna.

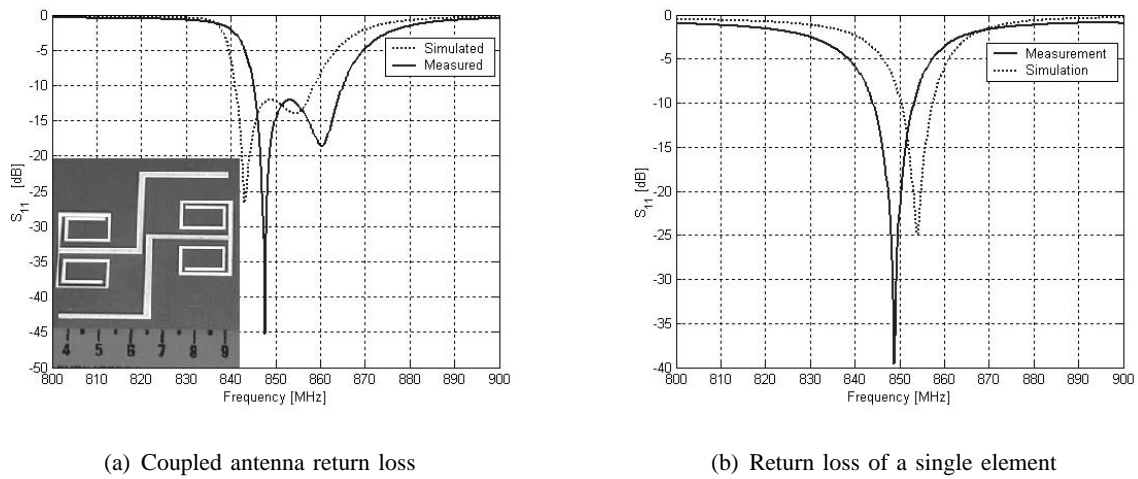


Fig. 3. Return losses of coupled antenna and one of the identical single elements that constitute it

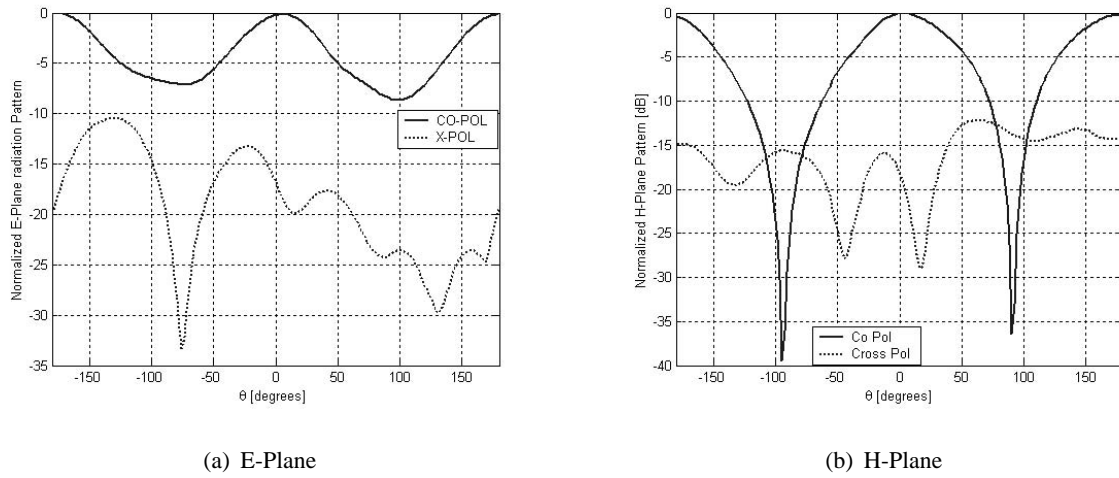


Fig. 4. Far field radiation patterns of the coupled double-element miniaturized antenna at 852 MHz

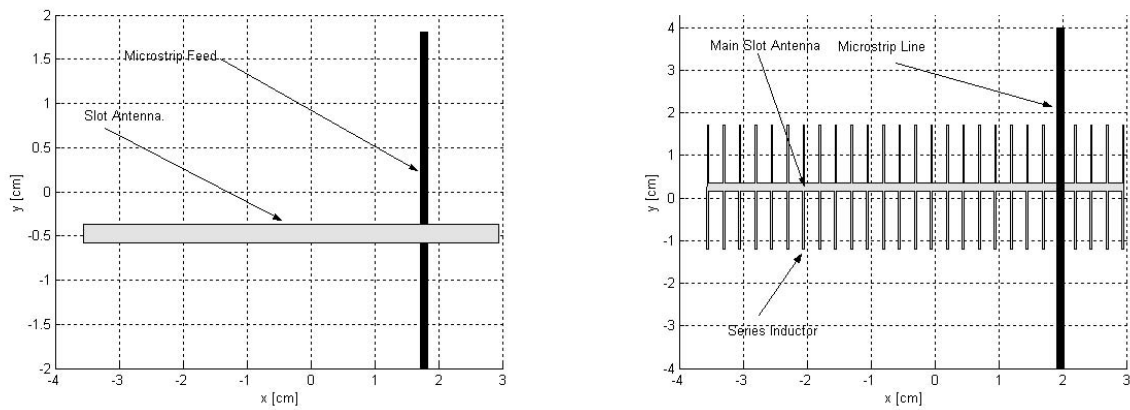


Fig. 5. Loaded and unloaded straight slot dipoles.

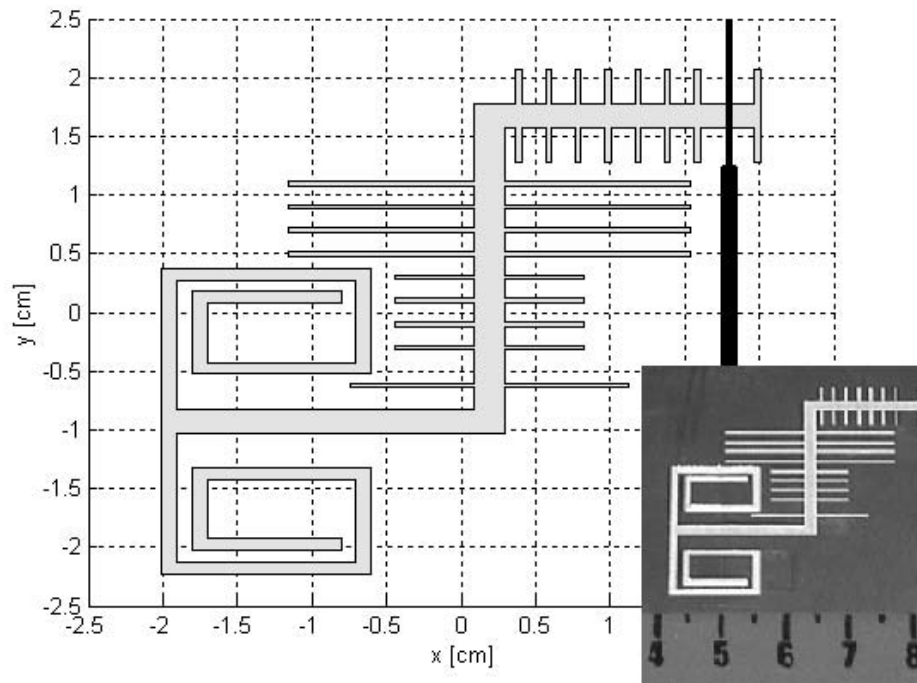
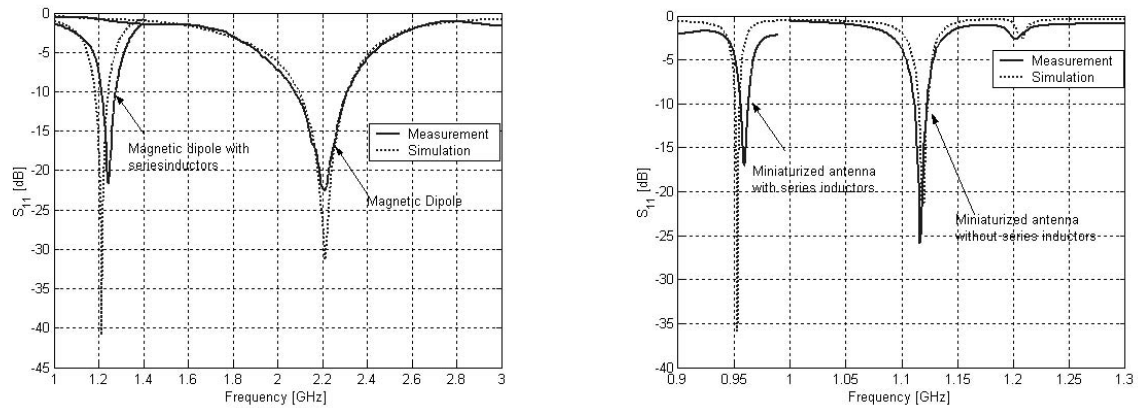


Fig. 6. Geometry of a miniaturized slot antenna loaded with series distributed inductors (slits).



(a) Return losses of straight loaded and unloaded slot dipoles

(b) Return losses of ordinary and loaded miniaturized slot antennas

Fig. 7. Simulated and measured return losses of the straight slot dipole and miniaturized slot antenna with and without inductive loading. (see Figures 5 and 6)

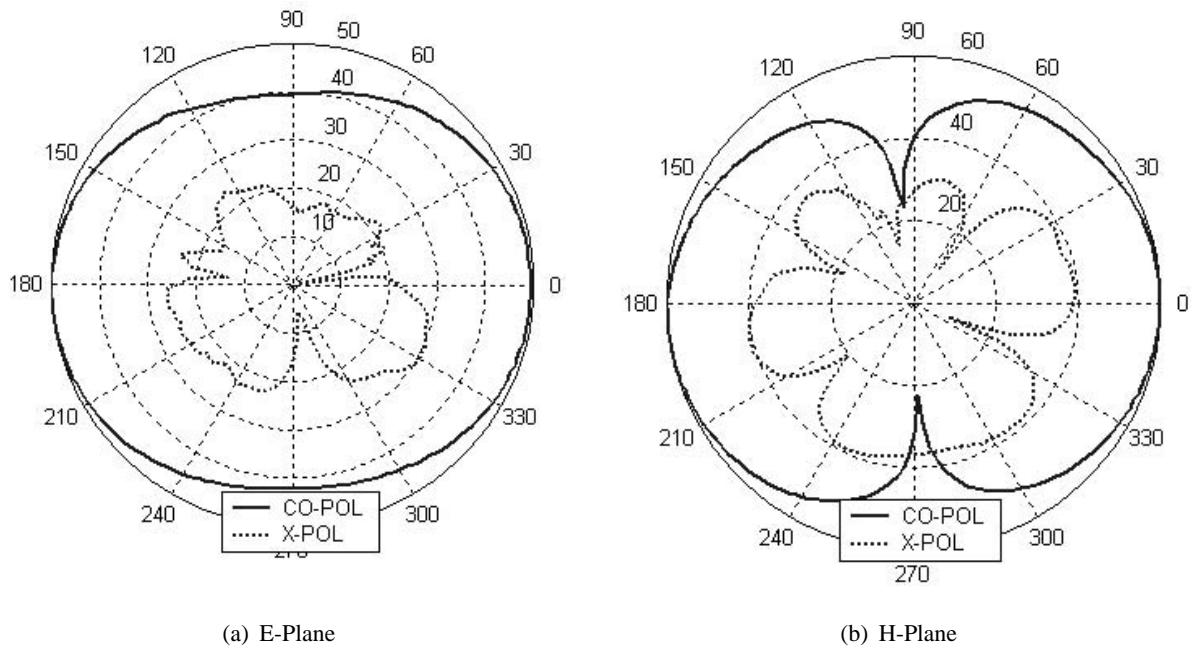


Fig. 8. Far field radiation patterns of loaded straight slot antenna shown in Figure 5(b)

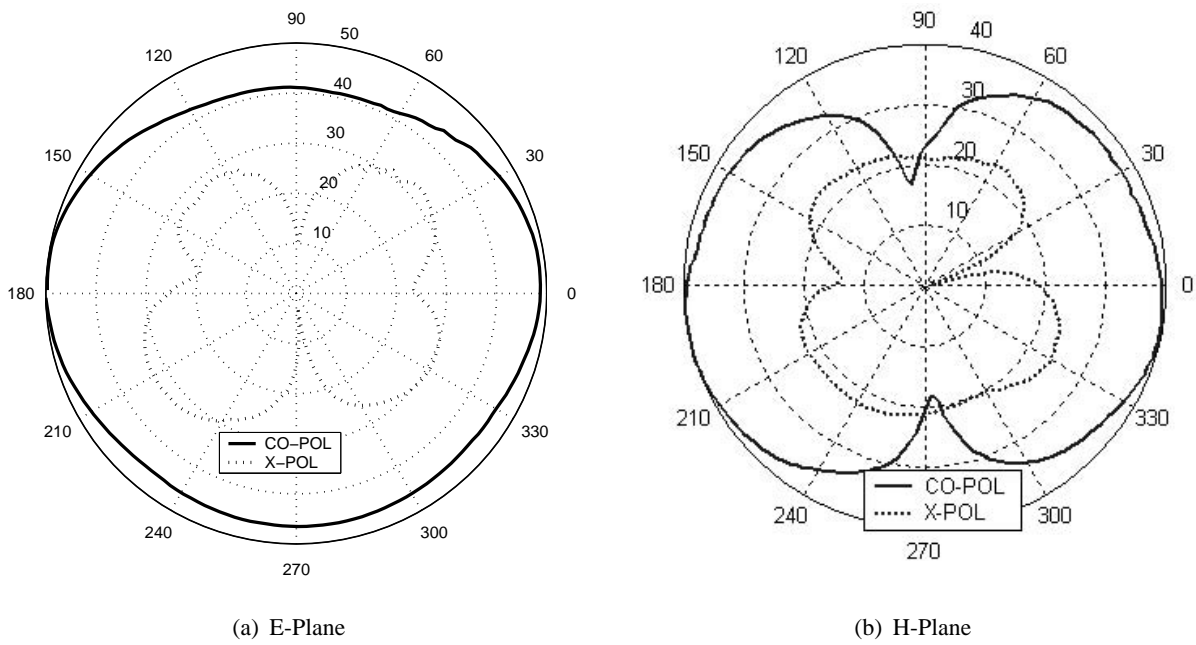


Fig. 9. Far field radiation patterns of loaded miniaturized slot antenna

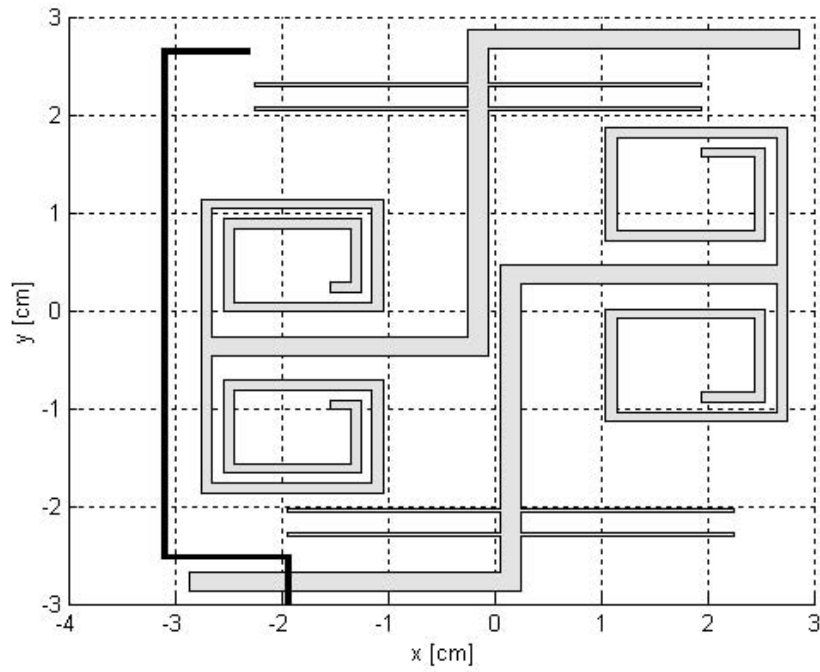


Fig. 10. Geometry of dual-band inductively loaded miniaturized slot antenna

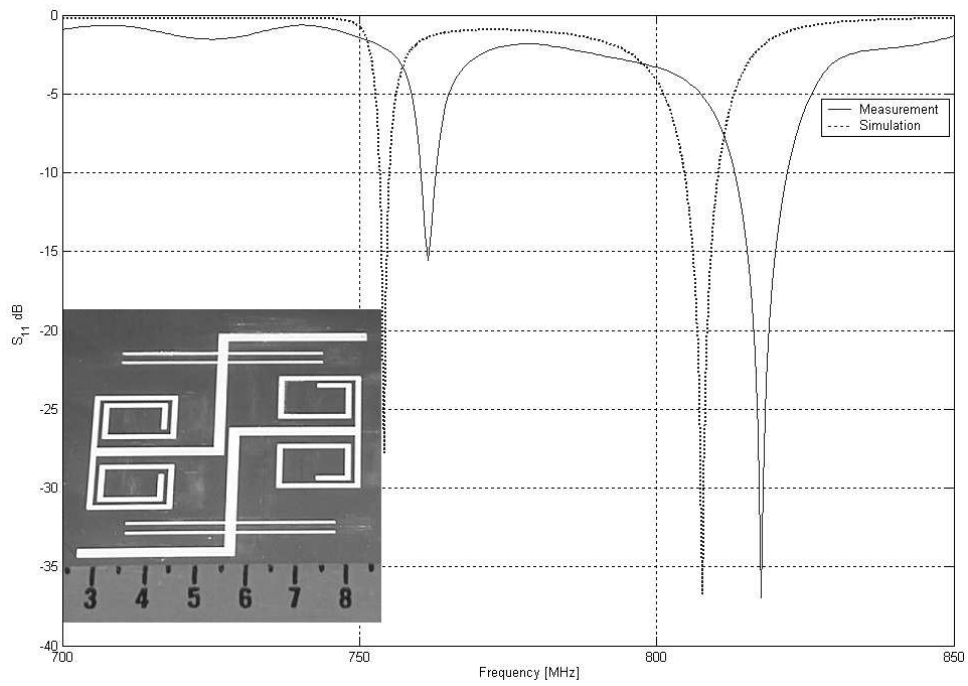


Fig. 11. Measured and simulated return loss of the miniaturized dual band slot antenna.

Miniaturized Slot Antennas with Enhanced Bandwidth

Nader Behdad^{*}, and Kamal Sarabandi

Radiation Laboratory,
Department of Electrical Engineering and Computer Science
University of Michigan, Ann Arbor, MI, 48109-2122
Tel: (734) 763-8162, Fax: (734) 647-2106
behdad@eecs.umich.edu, saraband@eecs.umich.edu

Introduction

With the current advancement in communication technology and tremendous growth in the wireless communication market and consumer demands, the need for smaller, more reliable and power efficient integrated wireless systems is more than ever felt. For future wireless devices, implementation of the entire transceivers on a single chip is being envisioned with the goal of reducing the cost and making them more affordable. Antennas are an inherent part of any wireless system and appear to be the largest components of any such system. Antenna miniaturization is then an important task towards achieving the integration and miniaturization of wireless communication systems. The subject of antenna miniaturization is not new and has been extensively studied by various authors [1-3]. Early studies have shown that for a single resonance antenna as the size is decreased its bandwidth (BW), if it can be matched, and efficiency decrease [1]. This is a fundamental limitation which in general holds true independent of antenna architecture. However, research on the design of antenna topologies and architectures must be carried out to achieve maximum possible bandwidth for given size and examine the applicability of the fundamental limitation on multi resonance antennas. Recently, there have been a number of studies on different approaches for antenna miniaturization while maintaining a relatively high bandwidth and efficiency. A novel miniaturized slot antenna was recently presented [4] and later a similar architecture was presented in the form of a folded antenna geometry in order to increase the bandwidth of the miniaturized slot antennas [5]. In this paper antenna bandwidth enhancement using a dual resonance architecture is examined. Basically the miniaturized slot antenna configuration similar to the one used in [4] is considered to form a dual antenna structure. In this new configuration one of the elements is fed by a micro-strip transmission line and the other one is fed parasitically by the first antenna. It is shown that the bandwidth of this new double-antenna configuration is twice the bandwidth of a single antenna that occupies the same space. In other words by keeping the same space as the single antenna the bandwidth is increased by a factor of two. In the following sections first the design steps will be studied and then the simulation and measurement results will be presented.

Double-Slot Antenna Design

In this section we will study the design of a double-slot miniaturized antenna using the configuration of a single slot antenna presented in [4]. This slot antenna [4], whose topology is shown in figure 1, occupies a small rectangular section of length a ($\approx 0.15\lambda_0$).

and width b ($\approx 0.13\lambda_0$), however shows a rather small bandwidth (less than 1%). A close examination of the antenna topology reveals that the antenna covers only half of the rectangular area, and therefore another antenna with the same geometry may be placed in the remaining half without significantly increasing the size. Placing two antennas in such proximity to each other allows for a parasitic coupling which can be taken advantage of to increase the total bandwidth of the antenna (Figure 2a). In this design the two antennas are tuned to resonate at f_0 by adjusting the overall slot length to an effective length of $\lambda_g/2$, where λ_g is the guided wavelength in the slot. This way, the structure acts like a coupled resonator the bandwidth of which is a factor of coupling strength between the two resonators. By considering this antenna as a two port network where the second port is in free space, its behavior can be explained using the coupled resonator filter theory. Here the two antennas are chosen to be identical and their resonant frequency (f_0) determines the center frequency of the operation. The frequency domain reflection coefficient (S_{11}) of this second order system has two distinct zeros with a separation proportional to the coupling coefficient. When these two zeros are close to each other, the pass-band ripple is small. Conversely as the separation is increased the pass-band ripple also increases and as a result the return loss, in the pass-band, deteriorates. Bandwidth maximization is accomplished by choosing a coupling coefficient so that S_{11} remains below -10 dB over the entire frequency band as the two zeros are separated. The coupling coefficient is controlled by changing the length of the overlap section and the separation between the two antennas (d and s in Figure 2b). The coupling is very strong in the middle section of both antennas (figure 2a) where the separation, s , is small. The other sections of the two slots don't couple significantly because of the large separation between them. For this antenna, as can be seen from Figure 4, the two zeros occur at 848MHz and 860 MHz and the pass-band ripple is about 0.6 dB, equivalent to a maximum S_{11} of -12dB at the center of the band.

One of the ways to match a slot antenna to the micro-strip transmission line is to use an off-center feed. The input resistance of a slot depends on the location of the micro-strip feed relative to the slot and varies from zero in the short circuited edge to a high resistance at the center [4]. Therefore the location of strip-slot crossing can be chosen such that best impedance match is achieved. Here, the feed is a narrow 75Ω micro-strip open circuited transmission line connected to a main 50Ω micro-strip line. The length of the open circuited micro-strip line can be chosen to compensate for the reactive part of the input impedance. Here the input impedance is not purely real therefore the 75Ω line is extended by $0.33\lambda_m$ (λ_m is the wavelength in micro-strip line) after the strip-slot crossing to compensate for the reactive part.

Simulation, Measurement, and Fabrication

The double-slot antenna was simulated using *IE3D* [6] and fabricated on the Rogers RO4350B substrate with the thickness of $500\mu m$, dielectric constant of 3.5 and $\tan\delta=0.003$ with a ground plane of $30.5\times 22.9\text{ cm}^2$. Figure 4 shows the measured and simulated return losses of the antenna where a very good agreement is observed. The discrepancy between the simulated and measured results is less than 0.46% and is mostly because of the finite size of the ground plane. According to measured results the antenna has a -10dB bandwidth of 21 MHz or 2.4% which is more than twice the bandwidth of a single element antenna. This bandwidth can also be further increased (or decreased) by changing the coupling value. Simulation results show that by reducing the overlap distance, one can expect a maximum bandwidth of about 25 MHz from this particular antenna. Figure 3 shows the simulated and measured return losses of a single element

used in the double-antenna which shows a bandwidth of 8 MHz or 0.9% and a center frequency of 849 MHz.

The radiation patterns of the antenna were measured in the anechoic chamber of the University of Michigan and the H-plane and E-plane radiation patterns are shown in Figures 5 and 6 respectively. As can be seen from these figures, the cross-polarization level is about -17dB at boresight. The gains of the double-slot and single-slot antennas were also measured in the anechoic chamber using a standard reference log-periodic antenna and are reported in Table I. The two slot antennas in the double-antenna are excited in-phase therefore their equivalent magnetic currents generate in-phase fields which will add up in the far field. Therefore the overall directivity of the double-slot miniaturized antenna is more than a single element. The current distribution, however, is not the same for different frequencies therefore slight changes in radiation pattern and directivity occurs over the bandwidth. The double-slot antenna is about 25% larger than the single antenna and features a bandwidth which is 2.3 times that of the single antenna. In comparison with [5] which uses a folded slot antenna geometry to increase the bandwidth, the increase in size is smaller (25% vs. 34%) and the increase in bandwidth is larger (2.3 vs. 2). If the size of the double antenna is reduced to the size of the single antenna a bandwidth increase of 100% can be achieved without increasing the size.

Table I. Comparison of different parameters between single and double slot antennas

Type	Size	Bandwidth	Gain			
			f (MHz)	848	852	860
Double slot	0.165 λ_0 x 0.157 λ_0	2.4%	G (dB)	1.5	1.7	1.7
			1.5 dB			
Single-Slot	0.133 λ_0 x 0.154 λ_0	0.9%				

Conclusions

A new approach to increase the bandwidth of miniaturized slot antennas using two resonant structures is presented. This is accomplished by placing two antennas in close proximity of each other without increasing the area occupied by the antenna substantially. It is shown that the bandwidth can be increased by a factor of 2.3 while increasing the area by only 25%. It is also possible to change the coupling to get a dual band antenna with the same geometry.

References

- [1] L. J. Chu, "Physical limitations on omni-directional Antennas" *J. Appl. Phys.*, vol. 19 pp. 1163-1175, Dec 1948.
- [2] H. A. Wheeler, "Fundamental Limitations of small antennas" *Proc. IRE*. Vol. 35. pp. 1479-1484, Dec, 1947.
- [3] R. C. Hansen, "Fundamental limitations in antennas", *Proc IEEE*, Vol. 69, pp. 170-182, Feb 1981.
- [4] K. Sarabandi and R. Azadegan, "Design of an efficient miniaturized UHF planar antenna", *Antennas and Propagation Society, 2001 IEEE International Symposium*, Vol. 4, 2001 pp:446-449.
- [5] R. Azadegan and K. Sarabandi, "Miniaturized Folded-Slot: An Approach to increase the Bandwidth and Efficiency of Miniaturized Slot Antennas", *Antennas and Propagation Society, 2002 IEEE International Symposium*, Vol. 4, 2002 pp:14-17.
- [6] IE3D *Electromagnetic Simulation and Optimization Software*, Zeland Software, Inc.

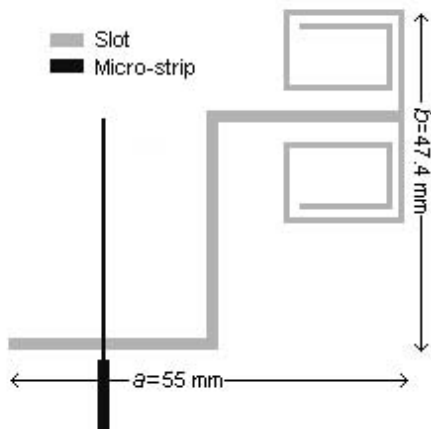


Figure 1. Geometry of the single miniaturized slot antenna and its feeding network.

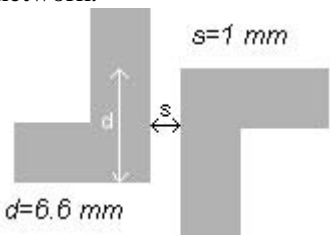


Figure 2b. Coupling area between the two antennas.

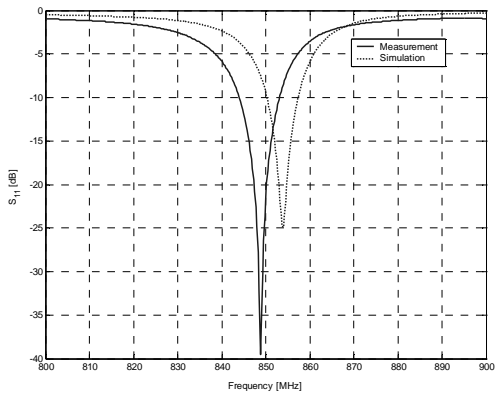


Figure 3. Simulated and measured return loss of single antenna.

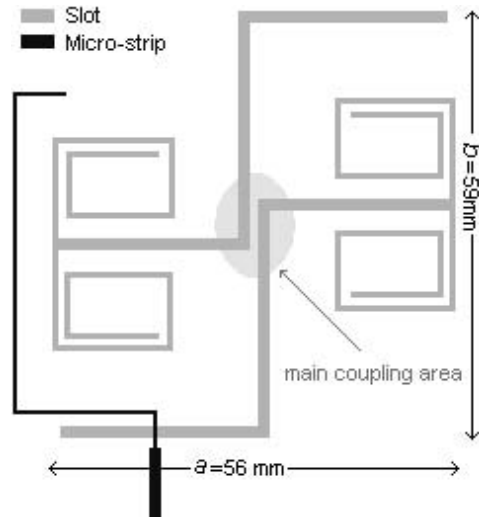
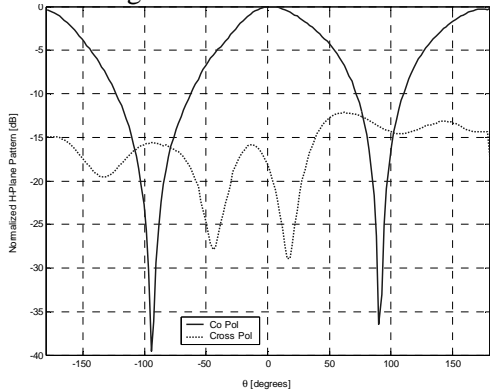


Figure 2a. Double-Slot antenna and its micro-strip feed network.

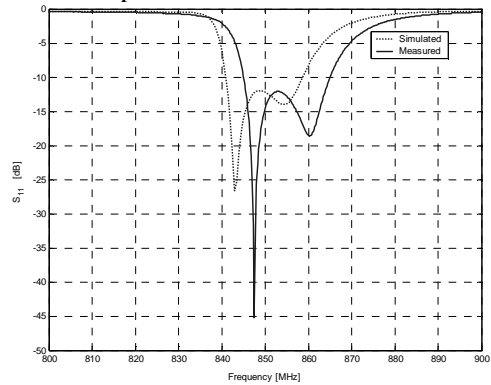


Figure 4. Simulated and measured return loss of the double antenna.

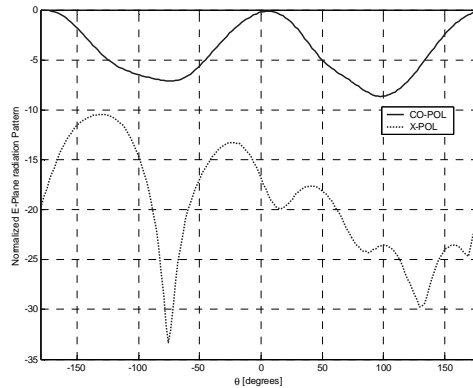


Figure 6. Double slot antenna, E-Plane pattern.

← Figure 5. Double slot antenna H-Plane pattern.

Slot Antenna Miniaturization Using Distributed Inductive Loading

Nader Behdad*, and Kamal Sarabandi

Radiation Laboratory, Department of EECS
University of Michigan, Ann Arbor, MI, 48109-2122
Tel: (734) 763-8162, Fax: (734) 647-2106
behdad@eecs.umich.edu, saraband@eecs.umich.edu

Introduction

Antenna miniaturization is a subject that has been around for a long time. The early studies in the subject resulted in a series of theoretical papers describing the fundamental limitations on small antennas [1]. As the size of an antenna structure is reduced, it is predicted that its bandwidth and efficiency are reduced as well. Despite these qualitative limitations, research must be carried out to achieve optimal antenna structures that can provide the highest bandwidth and efficiency for a given antenna space available. This has become an important research subject in recent years because of high demand for compact and power efficient mobile wireless devices. Techniques for antenna miniaturization can be categorized into three basic categories including 1) antenna miniaturization using optimal antenna topology, 2) Antenna miniaturization using magneto-dielectric materials, and 3) Antenna miniaturization using multi-resonance radiating structures. A procedure for designing efficient miniaturized slot antennas was proposed by Sarabandi [2] in which a special topology is used to achieve miniaturization. In this paper we reexamine this topology and propose a modification that can result in further size reduction without imposing any significant constraint on impedance matching or reduction in the antenna gain. A resonant slot antenna can be modeled with a half-wavelength transmission line short circuited at both ends. We will show that by using series inductive elements distributed along the antenna aperture, its size can be reduced. In other words, the guided wavelength of the resonant slot line is shortened by increasing the inductance per unit length of the line by loading the line with series distributed inductors. The size reduction is shown to depend on the number and value of the series inductors. The technique will first be applied to a standard resonance magnetic dipole as a means of comparison and then it will be applied to the miniaturized topology used in [2] to achieve a lower resonant frequency without changing the area occupied by the antenna. In what follows we will first study the design of both antennas and then present the simulation and measurement results for them.

Antenna Designs

A slot antenna fed by a micro-strip transmission line radiates as a magnetic dipole which is considered the dual of an electric dipole. It is a simple antenna to analyze and its characteristics are well-known. This antenna at its first resonance has the length of $\lambda_g/2$, where λ_g is the wavelength in the slot. The magnetic current distribution can be modeled by the current of a $\lambda/2$ transmission line short circuited at both ends. A series inductor in this transmission line reduces its length at resonance. For slot lines, insertion of series lumped elements is not possible. Besides, series lumped elements have a rather low Q which adversely affect the antenna efficiency (gain). To realize the effect of series inductors, a systematic array of distributed short circuited narrow slot-lines that are

placed along the radiating segment of the slot antenna. The reduction in size may also be interpreted noting that the electric current flows in the conductor around the slot and by putting a discontinuity (a series slot) normal to the current path, the current has to circle around the discontinuity which creates a longer effective length for the antenna. Figure 1 shows a slot antenna loaded with a number of narrow slits which act as series inductors. These slits are designed to have a length smaller than $\lambda_g/4$ in order to behave as inductive elements. They, however, carry a magnetic current whose direction is normal to that of the main radiator. Placing of only one slit at a given point along the radiating slot will cause significant asymmetry which can result in difficulties in antenna matching and generation of cross-polarization. In order to circumvent this problem, two series slits are placed on the opposite sides of the main slot. These slits now carry magnetic currents with equal amplitudes and opposite directions. Since the lengths of these narrow slits are small compared to the wavelength and they are closely spaced the radiated fields from the opposite slits cancel each other. That is, the slits will not contribute to the radiated field. Matching this slot antenna to the micro-strip feed is no different than ordinary slot antennas and standard slot antenna matching techniques can be used. Here an off-center micro-strip feed is used to match the input impedance. The micro-strip feed can then be grounded after the slot-strip transition or an open circuit quarter wavelength line can be used instead. Using an open circuited micro-strip line gives the flexibility to compensate for the reactive part of the input impedance by changing the line length. The best location and length of the micro-strip line are found by trial and error in the full wave simulations. Here for both slot dipoles (with and without series inductors) the lengths of the extended micro-strip lines were found to be $\lambda_m/4$ where λ_m is the wavelength in the micro-strip transmission line at their respective resonance frequencies. This shows that the imaginary parts of the input impedances in both cases are relatively small and by choosing the right location for the feed, the input impedances can be directly matched to the 50Ω transmission line feed.

Figure 5 shows a miniaturized slot antenna designed using the same procedure outlined in [2], however the radiating slot is modified by inserting a number of series inductive elements. This antenna without the series inductors is already miniaturized but adding series inductive elements further reduces the resonance frequency of the antenna. Instead of using identical inductive elements along the radiating slot, different size inductive slits are used to cover most of the available area on the printed circuit in order to not increase the antenna size. The antenna is matched to a micro-strip transmission line in a manner similar to the magnetic dipole described before. The only difference is that here the feed line is a 75Ω micro-strip connected to a 50Ω transmission line. The reason for using a 75Ω line is its narrow width which allows for localized and compact feeding. In this case the open circuited micro-strip line lengths beyond the slot crossing are respectively $0.3\lambda_m$ and $0.26\lambda_m$ for the miniaturized antenna and loaded miniaturized antenna. This shows that the imaginary parts of the input impedances of both antennas are relatively small. In the next section the simulation and measured results for these antennas are presented.

Simulation, Fabrication, and Measurement

The magnetic dipoles with and without series inductors were simulated using *IE3D* [3] and fabricated on a $500\ \mu\text{m}$ thick Rogers RO4350B substrate with $\epsilon_r=3.5$ and $\tan\delta=0.003$. Figure 2 shows the simulated and measured return losses for the magnetic dipoles. As can be seen the dipole has a resonance frequency of 2.22 GHz and a 10 dB bandwidth of 235 MHz or 10.7%. The loaded dipole with the same length as that of the unloaded dipole has a resonance frequency of 1.24 GHz and bandwidth of 63 MHz or 5%. This result indicates a 44% reduction in the resonant frequency and a reduction in

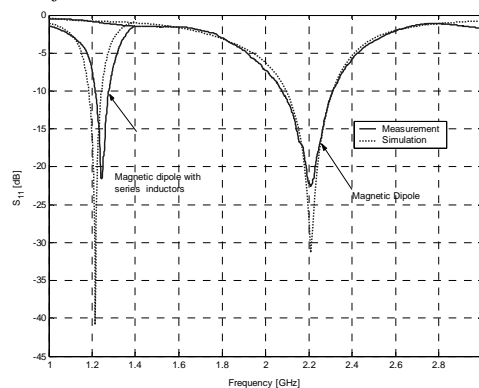
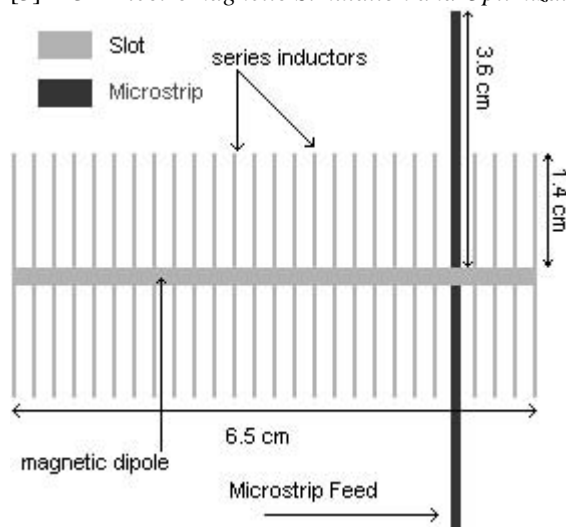
bandwidth as expected. The overall size can still be reduced by using longer short circuited transmission line loadings if they can be designed in a compact configuration. The radiation patterns of the small dipole antenna were measured in the anechoic chamber of the University of Michigan and are presented in Figures 3 and 4. It is shown that the cross polarization components in the far field in both planes are negligible therefore confirming the fact that the radiation from the magnetic currents in the inductive loadings with opposite directions cancel each other in the far field. The loaded and unloaded slot antennas based on the design given by [2] were also fabricated on the same RO4350B substrate. Figure 5 shows the schematic of a loaded miniaturized slot antenna (note that the inductive series slits are not identical). Figure 6 shows the simulated and measured return losses of the loaded and original miniaturized antennas. It is shown that the resonant frequency of the antenna shifts down from 1116 MHz down to 959 MHz (14% reduction) by inserting series inductors. In this design, the overall printed circuit size is unchanged. Figures 7 and 8 show the E-Plane and H-Plane radiation patterns of the loaded miniaturized antenna, respectively. The gains for these miniaturized antennas were measured in the anechoic chamber using a standard log-periodic reference antenna and were found to be 0.8 dB and 0.7 dB for the antennas with and without series inductors, respectively.

Conclusions

In this paper the effect of inserting an array of series inductors to a resonant slot antenna, on size, bandwidth, and gain of the antenna was investigated. The results show that the antenna size can be reduced efficiently without adverse effect on the impedance matching and antenna gain. However, as it is expected that the antenna bandwidth is reduced as a result of this miniaturization process. The technique was demonstrated using a standard and a miniaturized slot antenna and good agreement between simulations and measured results were obtained.

References

- [1] H. A. Wheeler, "Fundamental Limitations of small antennas" *Proc. IRE*. Vol. 35. pp. 1479-1484, Dec, 1947.
- [2] K. Sarabandi and R. Azadegan, "Design of an efficient miniaturized UHF planar antenna", *Antennas and Propagation Society, 2001 IEEE International Sym*, Vol. 4, 2001 pp:446-449.
- [3] *IE3D Electromagnetic Simulation and Optimization Software*, Zeland Software, Inc.



↑ Figure 2. Measured and simulated return losses of the magnetic dipole with and without series inductors.

← Figure 1. Magnetic dipole with series inductors.

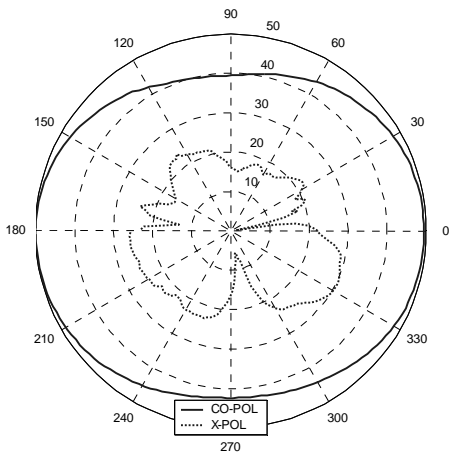


Figure 3. Far field E-Plane pattern of the small magnetic dipole

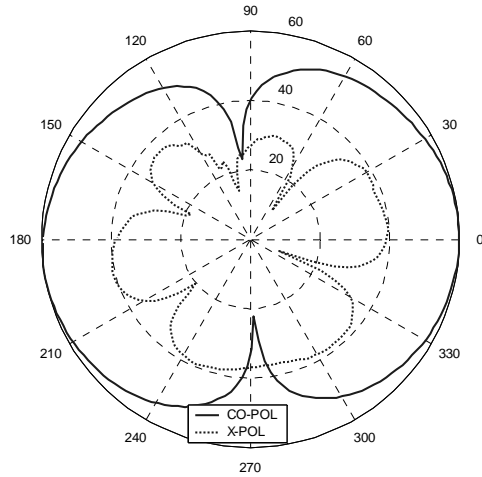
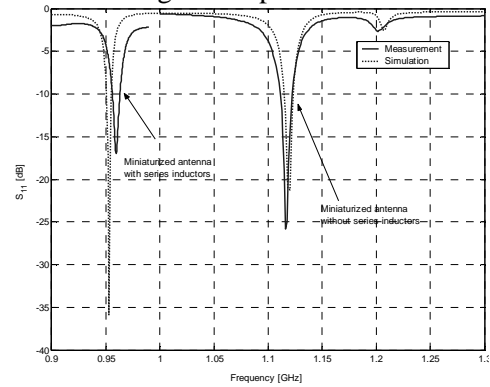
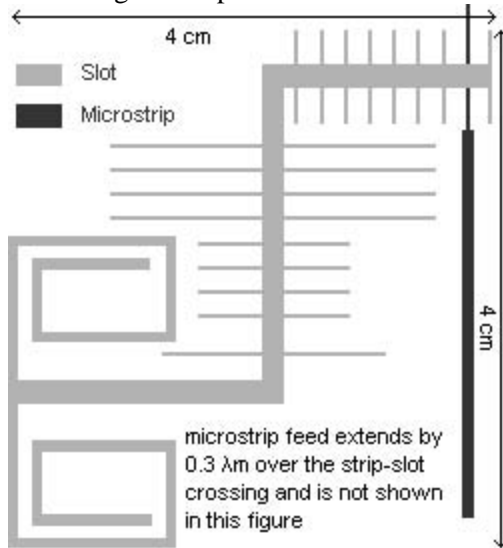


Figure 4. Far field H-Plane pattern of the small magnetic dipole



↑ Figure 6. Measured and Simulated return losses of the miniaturized antenna with and without series inductors

← Figure 5. Geometry of the loaded miniaturized slot antenna

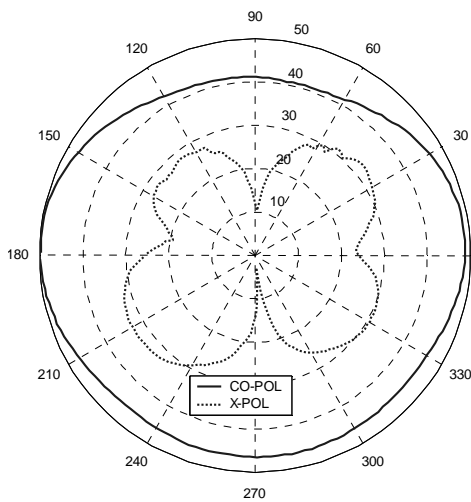


Figure 7. Far field pattern of the loaded miniaturized slot antenna (E-Plane)

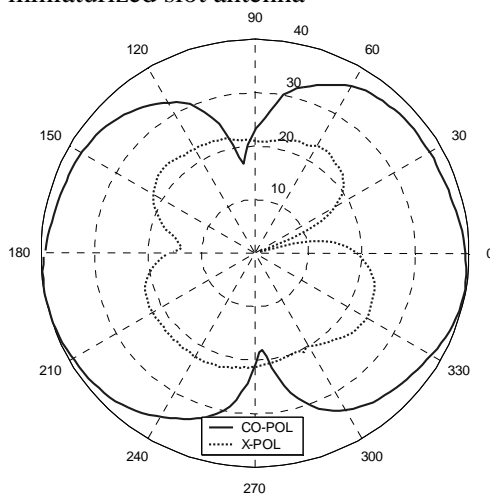


Figure 8. Far field pattern of the loaded miniaturized slot antenna (H-Plane).

A Compact Planar Folded-Dipole Antenna for Wireless Applications

Reza Azadegan, and Kamal Sarabandi

Radiation Laboratory,
Department of Electrical Engineering and Computer Science
The University of Michigan Ann Arbor, MI 48109-2122
Tel: (734) 936-1575, Fax: (734) 647-2106
E-mail: azadegan@eecs.umich.edu

INTRODUCTION

Antenna miniaturization for mobile wireless applications has recently drawn a lot of attention. This interest is, in part, owing to the ever-increasing demand for numerous applications on a single platform, which typically operate at different frequency bands, and therefore, require different antennas. In addition to the size of an antenna, power efficiency and cost are among other important issues that have to be considered in any antenna design for wireless applications. Recently, the authors have proposed a novel miniaturized topology to be used for designing miniaturized slot antennas [1]. This structure can provide very small antennas with rectangular dimensions as small as $(0.05\lambda_0 \times 0.05\lambda_0)$. Figure 1 depicts the layout of this design at 300 MHz. In order to increase the bandwidth of the proposed antenna, a new miniaturized design, namely, a miniaturized folded-slot structure was proposed [2]. The structure, shown in Figure 2, typically has a bandwidth twice as wide as that of the miniaturized slot antenna. In addition to their small size, the proposed structures are highly efficient as compared to a typical miniaturized antenna. Moreover, the input impedances of these antennas are matched to a 50Ω transmission line without introducing any loss in the feed network. The above figures of merit associated with the proposed miniaturized structures make a slot antenna a prudent choice for wireless applications. However, there is a concern with regard to the ground plane of the slot-lines and slot antennas, and how the size of slot ground plane can affect the radiation characteristics of the antenna. Note that in order for a slot antenna to be dual to its complementary dipole antenna through Babinet's Principle, the ground plane should be assumed infinite, which is not realizable except when magnetic current discretization is applied in Moment Method simulation [3]. Additionally, the size of the antenna's ground plane has been demonstrated to affect the radiation characteristics and the efficiency of the antenna [4]. In essence, [4] asserts that as the size of the ground plane decreases, the gain of proposed slot antenna reduces, and its radiation pattern and resonant frequency deviates from that of an ideal infinitesimal dipole. Despite these ramifications, the proposed slotted structures are still very suitable since in many mobile platforms, such as automotive and military vehicles, a large ground plane is readily available. For a system with multiple antennas, a ground plane can be shared among different antennas, and therefore, it does not increase the overall size of the system. This paper focuses on eliminating the need for a ground-plane when it is not readily available. To serve this purpose, a topology dual to the previously proposed *miniaturized folded-slot* is introduced, and will be referred to as a *miniaturized printed folded-dipole*. A prototype of this miniaturized printed antenna has been designed, fabricated, and tested. The radiation characteristic of the printed antenna is then compared with its dual structure.

MINIATURIZED PRINTED FOLDED-DIPOLE

In this paper, we propose a new miniaturized antenna structure which unlike slot antennas, does not need a ground plane. Figure 3 shows the layout of a typical printed folded-dipole topology.

As mentioned before, this structure is a dual to the folded-slot antenna of Figure 2. As illustrated in Figure 3, there are two main vertical arms at the center of the structure terminated by distributed capacitive loadings. Since the electric current gains its maximum on these two center arms, they contribute considerably to the radiation resistance of the structure. In addition to these two main arms, the radiation from the capacitive terminations cannot be overlooked. The radiation resistance of an infinitesimal dipole with a constant current distribution can be calculated analytically [5]. This quantity is multiplied by a factor of four in the case of an infinitesimal folded-dipole; that is:

$$R_a = 4 \times 80\pi^2 \left(\frac{\ell}{\lambda}\right)^2 \quad (1)$$

Using (1), the radiation resistance of a miniaturized folded-dipole antenna with the length of $0.055\lambda_0$, is calculated to be $R_a = 9.55\Omega$. Obviously, this value is only the contribution of the center arms radiating in free space, and the radiation from the loading coils is yet to be included. Furthermore, the effect of the dielectric substrate in increasing R_a has to be determined using a full-wave simulation [3]. Figure 4 shows the simulated input admittance of the miniaturized printed folded-dipole antenna of Figure 3 when fabricated on a $0.762mm$ thick RT Duroid 5880 substrate, with dielectric constant of $\epsilon_r = 2.2$, and loss tangent of $\tan \delta = 0.0009$. The simulated input impedance of this structure at resonance can be read from Figure 4 as $R_a = 42.7\Omega$. The difference between this value and the one obtained from (1) is owing to the radiation from the coiled terminations, as well as the effect of dielectric material to raise the input impedance level. This difference emphasizes the need for an accurate full-wave simulation to precisely predict the near field characteristics of a miniaturized antenna. For comparison, the simulated input impedance of the slot antenna, shown in Figure 2, is regenerated from [2] and illustrated in Figure 5. As shown in this figure, the folded slot has a resonance at $337.9MHz$ with a radiation resistance of about $5K\Omega$. Note that such a high impedance can only be matched to a 50Ω line by means of a proper matching network, whereas the printed folded dipole is already impedance matched. In the view of the Babinet principle, the input impedance of the two complementary structures could have been linked if the dielectric constant of the substrate had been set to $\epsilon_r=1$, (free space.) Although the Babinet principle calls for free space radiation, it provides the designer with a good intuition about the range of input impedances of the two antennas on a dielectric substrate. Invoking Booker's relation gives:

$$R_{dipole} = \frac{1}{\sqrt{\epsilon_r}} \left[\frac{\eta_0^2}{4} \times \frac{1}{\sqrt{\epsilon_r} R_{slot}} \right] = \frac{1}{\epsilon_r} \frac{\eta_0^2}{4} \frac{1}{R_{slot}} \quad (2)$$

Using (2) and substituting $R_{slot} = 5K\Omega$ obtained from simulation, the approximate value for the miniaturized printed folded-dipole antenna is found to be $R_{dipole} = 3.23\Omega$, which is very far from the simulated value of $R_a = 42.7\Omega$. The discrepancy comes is owing to the fact that the is not radiating in a homogeneous dielectric space where the Equation (2) holds. Thus, there is no choice other than using the full wave simulation for the antenna structure. Another advantage of the printed miniature topology is that its impedance is very close to 50Ω and no complicated matching network is needed.

Antenna Fabrication and Experiment

The printed dipole antenna requires a balance input to ensure a symmetric current distribution on both arms of the antenna. Both lumped element (RF Transformer chips) and distributed baluns can be used to transform the unbalanced coaxial feed into balanced coplanar strips (CPS), which are ultimately connected to the printed folded-dipole. Figure 6 shows a typical Marchand balun [6]. The layout of the antenna with a Marchand balun is illustrated in Figure 7. This antenna was fabricated, and its radiation characteristics were measured. This antenna can fit within a rectangular area of $0.060\lambda_0 \times 0.065\lambda_0$ at $336MHz$. The simulated and measured input return loss of this antenna are compared in Figure 8, where very good agreement is observed between the two. However, there is about 1% shift in the resonant frequency, which

Table I. Comparison between miniaturized slot and miniaturized folded slot antennas.

Antenna Type	Size	BW (%)		Gain (dBi)		Directivity (dB)
		sim	meas	Sim	meas	
Miniature slot[1]	$0.05\lambda_0 \times 0.05\lambda_0$	0.058	0.34	1.0	-3.0	1.9
Folded slot [2]	$0.067\lambda_0 \times 0.067\lambda_0$	0.12	0.93	1.0	-2.7	1.8
Printed dipole	$0.06\lambda_0 \times 0.065\lambda_0$	0.45	0.70	-7.0	-6.5	2.4

can be attributed to the numerical error and the finite size of the dielectric substrate. The measured radiation pattern of this antenna for E and H principle planes were plotted in Figures 9. It is seen that the E plane pattern of this structure is very similar to that of an infinitesimal dipole. In contrast, an asymmetric null appeared in the H plane pattern at $\theta = -90^\circ$, even though a constant pattern in the H plane had been expected. This asymmetry emerged because of the presence of the balun. The major portion of the observed cross-polarized radiation is believed to emanate from feeding cables rather than the antenna itself. The far-field gain of this antenna is measured to be -6.5 dBi, which is slightly higher than the value predicted by the simulation. Table I, shows a comparison between both simulated and measured bandwidth of the antenna proposed in this paper with two previously proposed miniaturized slot antennas [1]-[2]. Obviously, one can see a considerable difference between the efficiency and gain of slot antennas and the printed dipole introduced in this paper.

CONCLUSIONS

A new miniaturized printed antenna was presented as a dual structure to the miniature folded slot antenna. This antenna requires neither a ground plane, nor any matching network. Considering its size, this resonant antenna had a fairly wide bandwidth. It can be ascertained that miniaturized slot antennas exhibit superior efficiency compared to their printed duals, given that a large enough ground plane is readily available.

REFERENCES

- [1] R. Azadegan, K. Sarabandi, "Design of miniaturized slot antennas," *Antennas and Propagation Society, 2001 IEEE International Sym.*, Vol. 4, 2001 pp: 565–568.
- [2] R. Azadegan, and. K. Sarabandi, "Miniaturized folded-slot: an approach to increase the band width and efficiency of miniaturized slot antennas," in *Proc. IEEE Antennas Propagat.* vol.4, San Antonio, TX., June 2002, pp. 14-17.
- [3] IE3D Electromagnetic Simulation and Optimization Package, ver. 9.2, *Zeland Software, Inc*, 2002.
- [4] K. Sarabandi, R. Azadegan, "Design of an efficient miniaturized UHF planar antenna," *Antennas and Propagation Society, 2001 IEEE International Sym.*, Vol. 4, 2001 pp.: 446–449.
- [5] Balanis K. A., *Antenna Theory and Design*. 2nd ed. John Wiley, New York, 1997.
- [6] Pugilia K. V., "Application notes: Electromagnetic simulation of some common balun structures," *IEEE Microwave Mag.*, Sept. 2002, pp.56-61.

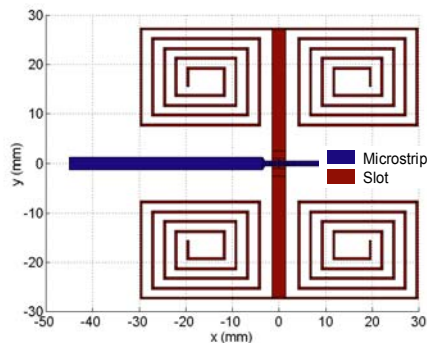


Fig. 1. Miniaturized slot antenna [1].

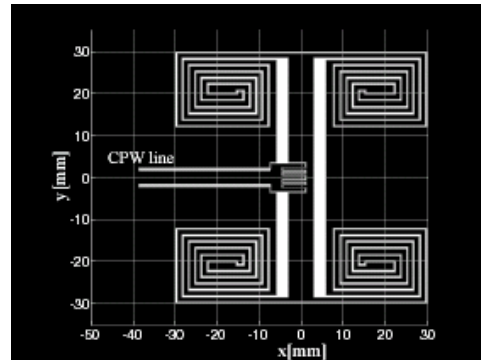


Fig. 2. Miniaturized folded slot antenna [2].

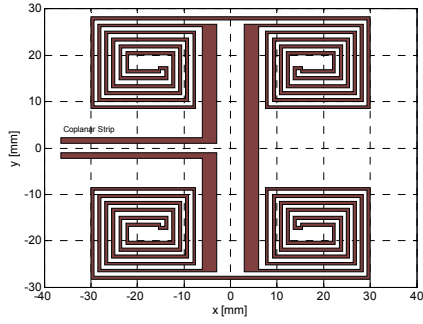


Figure 3. Topology of a miniaturized printed folded dipole to operate around 340 MHz

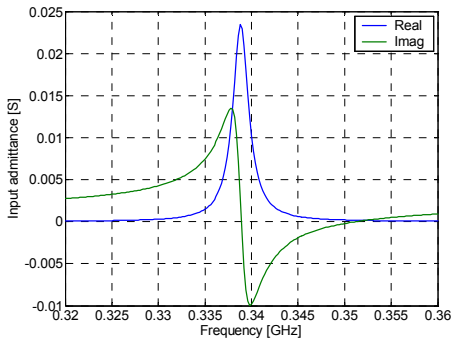


Figure 4. The input admittance of the antenna that is shown in Figure 3.

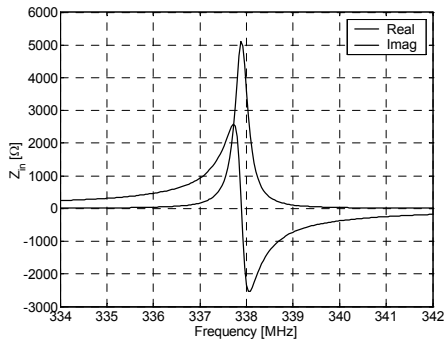


Figure 5. The input impedance of the miniaturized antenna of Fig. 2 [2].

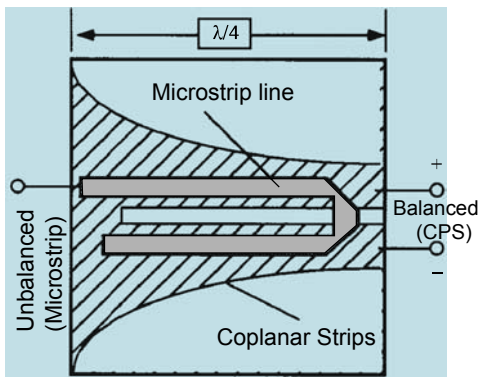


Figure 6. Marchand balun [6].

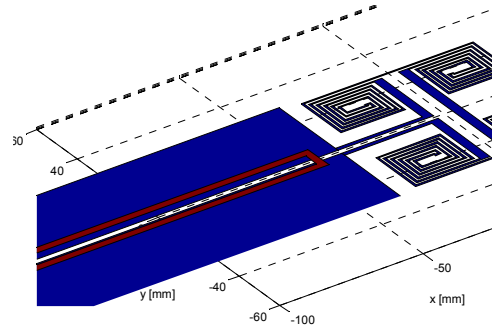


Figure 7. Layout of a miniaturized printed dipole antenna with a Marchand balun.

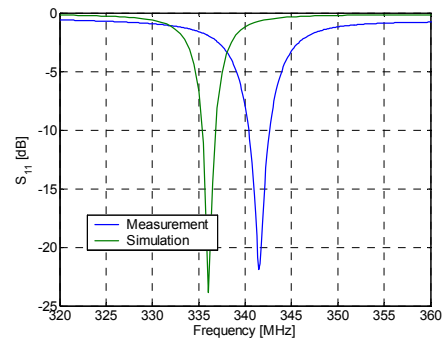


Figure 8. Printed folded-dipole return loss (measurement and simulation.)

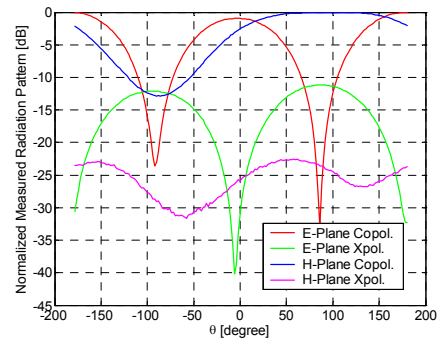


Figure 9. Measured radiation pattern of the printed antenna in principle planes.

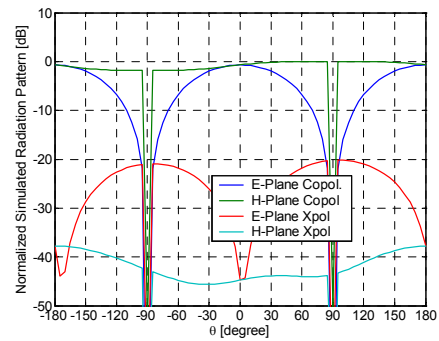


Figure 10. Simulated radiation pattern of the miniaturized printed dipole antenna.

Miniaturized Slot-line and Folded-Slot Band-pass Filters

Reza Azadegan, and Kamal Sarabandi

Radiation Laboratory, Department of Electrical Engineering and Computer Science,

The University of Michigan, Ann Arbor, MI 48109-2122.

Email: azadegan@eecs.umich.edu

Abstract —In this paper the concept of a new class of miniaturized filters using printed circuit technology is presented. The building block of the proposed filter is a miniaturized high-Q printed slot-line resonator, which allows for the realization of both standard coupled-line and cross-coupled quasi-elliptic filters. Each resonator occupies an area as small as $0.03\lambda_0 \times 0.06\lambda_0$ and can be shown to have a Q as high as 200 at 2.4 GHz. Analytical, and numerical methods are employed to outline a design procedure. An integral equation full-wave method is used to macro-model the coupling coefficient between two adjacent resonators as a function of their relative distance and orientation. Filter theory is used to design different filter types. The design procedure is validated by comparing the simulated S-parameters of a two-pole and a four-pole Chebyshev filter with those measured from prototypes operating, respectively at 515 MHz and 400 MHz.

I. INTRODUCTION

With the ever-increasing demand for mobile wireless devices, there is a significant interest in low-cost, power-efficient, and miniaturized active and passive RF components. Filters and multiplexers are common components of almost all wireless devices. Hence in recent years, interest in research into novel filter architectures, with an emphasis in filter miniaturization, has been renewed [1]-[3].

In what follows the application of a novel miniaturized slot-line resonator which shows a relatively high Q for the design of different filter types is considered. The basic architecture of these resonators is the basis for a class of miniaturized planar antennas considered for integration on a wireless chip [4]-[6]. For the antenna design, a specific topology was considered to enhance radiation from the antenna structure. However, for the application at hand the resonator topology is modified so that the radiation from different segments of the slot-line resonator would cancel each other in the far-field region and thereby a high-Q non-radiating resonator is achieved.

The ultimate goal here is to incorporate a high efficiency miniaturized on-chip antenna design with the proposed high performance slot-line miniaturized filter to achieve a superior RF front-end performance for mobile

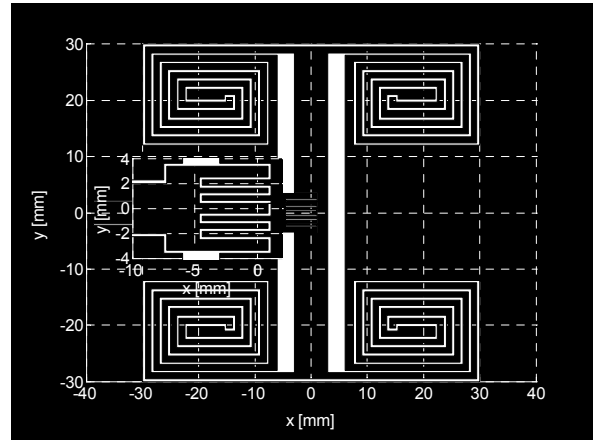


Fig. 1. Schematic of a miniaturized folded slot antenna fed by a capacitively coupled CPW line

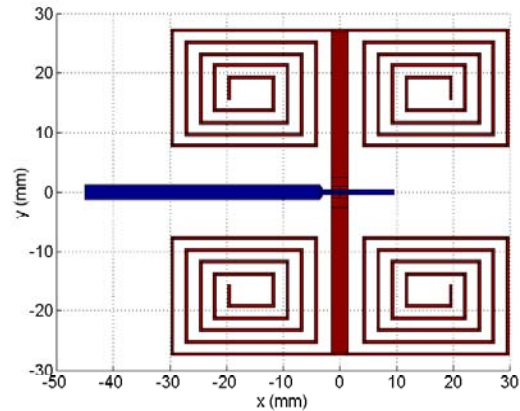


Fig. 2. Schematic of a miniaturized inductively loaded slot antenna fed by a microstrip-line.

wireless devices. The authors have proposed extremely miniaturized slot antenna structures for mobile wireless applications, namely, a miniaturized folded slot antenna [4], and an inductively loaded miniaturized slot antenna [5], which are shown in Figs. 1 and 2, respectively. The dimensions of these two antennas are as small as $0.067\lambda_0 \times 0.067\lambda_0$ and $0.05\lambda_0 \times 0.05\lambda_0$, respectively. These antennas were also shown to be perfectly matched without

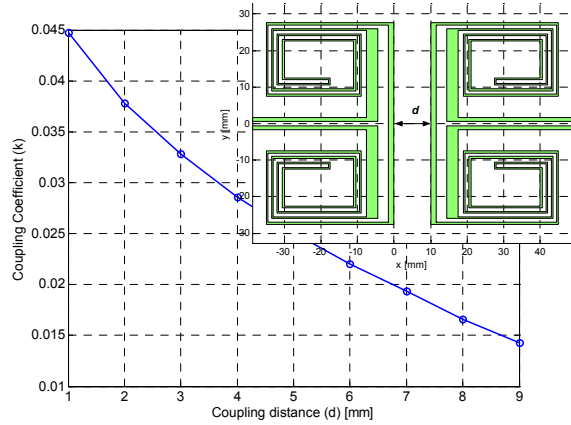


Fig. 3. Extracted coupling coefficient for the back-to-back miniaturized folded slot resonators configuration.

having used any resistive loading, and are therefore, highly efficient. The high efficiency of these antennas indicates that the proposed slotted structures are very good choices for designing low insertion-loss band-pass filters.

In this paper preliminary results related to the design procedure and performance evaluation of the proposed miniaturized filters are demonstrated.

II. DESIGN PROCEDURE

A band-pass filter may be characterized by a set of internally coupled resonators (not necessarily identical) all resonating at the same frequency, and an external quality factor denoting the input and output couplings. The couplings between resonator pairs and the input/output coupling are represented by k_{ij} , and Q_{ext} , respectively. The coupling coefficient between two resonator pairs is extracted from the full-wave simulation of the two-port structure [7], using the pole-splitting method [8]. In the pole splitting method, a relationship is established between the frequency separation of the poles, and the coupling coefficients. Given that f_u and f_l are the frequencies at which the S_{21} reaches its peak values, the coupling coefficients can be obtained from:

$$k = \frac{f_u^2 - f_l^2}{f_u^2 + f_l^2} \quad (1)$$

The external quality factor can be characterized using the full-wave simulation of the excited input or output resonators. The external coupling can be expressed in the form of:

$$Q_{ext} = \frac{f_0}{\delta f_{-3dB}}, \quad (2)$$

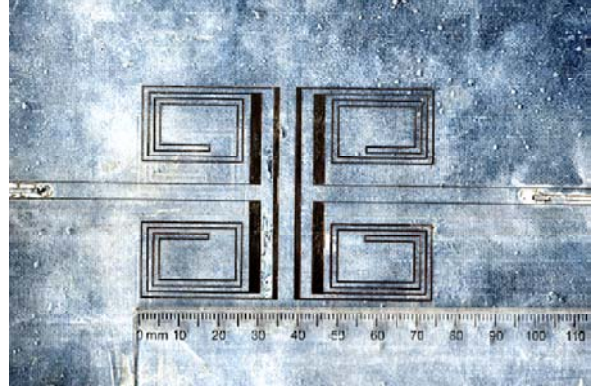


Fig. 4. Photograph of the two-pole filter at 515MHz.

where in the above f_0 and δf are the resonant frequency and the $-3dB$ bandwidth of the input and output resonators, respectively. The extracted external couplings obtained from the full-wave Method of Moment (MoM) simulation for slotted structures, however, are not very accurate since the size of the substrate and ground plane is assumed to be infinite, and also the slot ground plane is considered a perfect electric conductor. Thus, the external coupling needs to be fine-tuned experimentally.

III. MINIATURIZED FOLDED-SLOT BAND-PASS FILTER

Figure 3 shows the schematic of two coupled folded miniaturized resonators, which are inductively excited. The coupling coefficient of this structure is extracted from the full-wave simulation data and plotted in Fig. 3 as a function of resonators' distance (d). Since the two resonators are very compact, two different mechanisms contribute to the coupling between them, and in general both electric and magnetic coupling are present. In this configuration, however, the electric coupling is dominant. The external couplings of these resonators can be controlled by introducing an impedance step between a 50Ω CPW line and the folded miniaturized slot [1].

As the first example, a two-pole band-pass Chebyshev filter with the fractional bandwidth of $\Delta=2.5\%$ at the frequency of 515 MHz, and pass-band ripple of 0.15 with the return loss of less than $-15dB$ is considered. The required coupling coefficient and external quality factor of this filter is found to be $k=0.0317$, and $Q_{ext}=38.02$, respectively [9]. The coupling coefficient between the two resonators can be realized using the data provided in Fig.3, and the distance between the two resonators is found to be $d=4mm$. This filter was fabricated on a RT5880 Duroid [10] substrate with $\epsilon_r=2.2$, and $\tan(\delta) = 0.0009$. Fig. 4 shows the photograph of this filter.

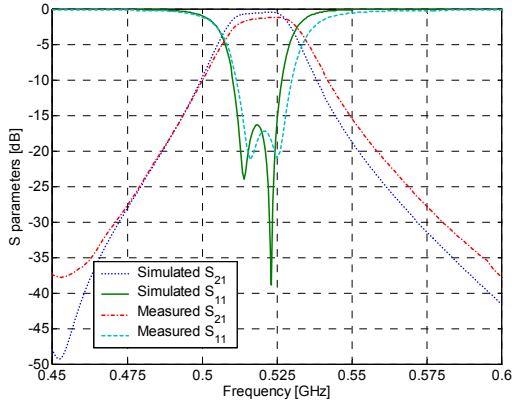


Fig. 5. Comparison between the simulated and measured frequency responses of the filter in Fig. 4.

The simulated and measured frequency responses of this filter have been compared in Fig. 5, where a very good agreement between the two is observed. This filter can be fit in a rectangular area of $0.09\lambda_0 \times 0.12\lambda_0$. The minimum insertion loss of this filter is measured to be 1.2dB. As mentioned earlier the MoM simulation used here cannot model the metallic loss of the structure and that is why there is a slight difference between the insertion loss predicted by the simulation and the measured one.

III. MINIATURIZED SLOT-LINE BAND-PASS FILTER

The next example entails a four-pole miniaturized band-pass filter design, with a bandwidth of $\Delta=3.0\%$ at about 390MHz. In this example, the inductively loaded miniature resonators [2] are employed. The size of each single resonator, used to design this filter, is $0.032\lambda_0 \times 0.058\lambda_0$ where λ_0 is the free space wavelength at the center frequency. The miniaturized resonator pairs, in this filter structure, are coupled in back-to-back and face-to-face configurations. Each of these configurations has been studied, and its corresponding coupling coefficients were extracted. Fig. 6(a) and 6(b) show the schematic of these two configurations, in addition to the extracted coupling coefficients. A slot incision is introduced in the face-to-face coupling configuration to reduce the coupling between the resonator pairs, without having to increase the separation between the pairs, and therefore, to achieve a more compact design. Fig. 7 depicts the photograph of this filter fabricated on a RT58850 Duroid substrate similar to the one used for in the previous example. The dimensions of this four-pole filter are as small as $0.058\lambda_0 \times 0.15\lambda_0 = 0.009\lambda_0^2$ at the center frequency. A comparison of the measured and simulated frequency responses of this filter is illustrated in Fig. 8, where a very

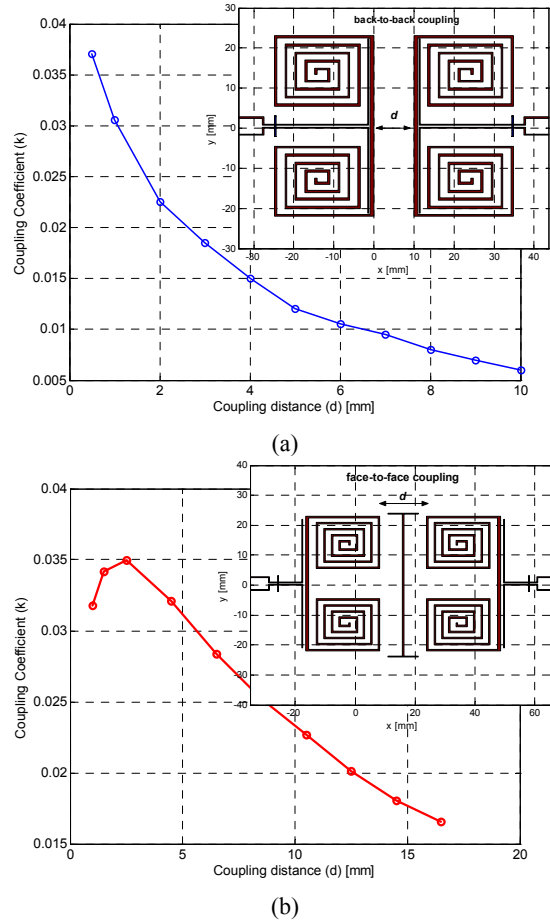


Fig. 6. Extracted coupling coefficients for two different coupling configurations: (a) back-to-back configuration; (b) face-to-face configuration with an incision.

good agreement is observed. In this example, an insertion loss of 3.7dB is achieved. Obviously, because of introducing an incision in the face-to-face coupling configuration, a zero associated with the mixed electric and magnetic couplings appears in one side of the rejection band. Note that the observed zero here is coming from a mechanism different than that for an elliptical filter, while in elliptical filters, the pass-band zeros are the results of the cancellation of multi-pass signals through different resonators.

V. CONCLUSION

In this paper, two novel miniaturized slot-line resonator structures were proposed. The slot-line and folded slot-line miniaturized resonators were shown to be excellent candidates to design low insertion-loss band-pass filters. Moreover, the size of these resonators can be varied depending on the magnitude of the inductive loading of the resonator with a moderate decrease in the resonators'

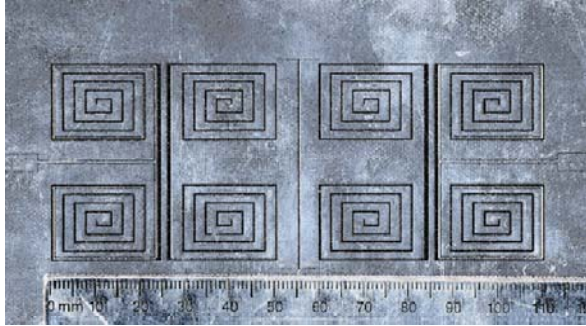


Fig. 7. Photograph of the four-pole miniaturized slot-line filter.

Q. Different types of coupling mechanisms, including electric, magnetic, and mixed coupling is feasible by proximity and only depending on the mutual orientation of the resonator pairs. A few of these coupling configurations were characterized and employed to design two prototype filters. One was a two-pole band-pass filter with a fractional bandwidth of $\Delta=2.5\%$ at 515MHz and an insertion loss of 1.2dB, which only occupies an area as small as $0.09\lambda_0 \times 0.12\lambda_0$. The other example is a four-pole band-pass filter with $\Delta=3.0\%$ at 400MHz, with an insertion loss of 3.7dB, and dimensions of $0.058\lambda_0 \times 0.15\lambda_0$.

REFERENCES

[1] M. Sagawa, K. Takahashi, and M. Makimoto, "Miniaturized hairpin resonator filters and their application to receiver front-end MIC's," *IEEE Trans. Microwave Theory and Tech.*, vol. 37, pp. 1991-1997, Dec. 1989.
 [2] H. T. Su, F. Huang, and M. J. Lancaster, "Highly miniature HTS microwave filters," *IEEE Trans. Appl. Superconduct.*, vol. 11, pp. 349-352, Mar. 2001.

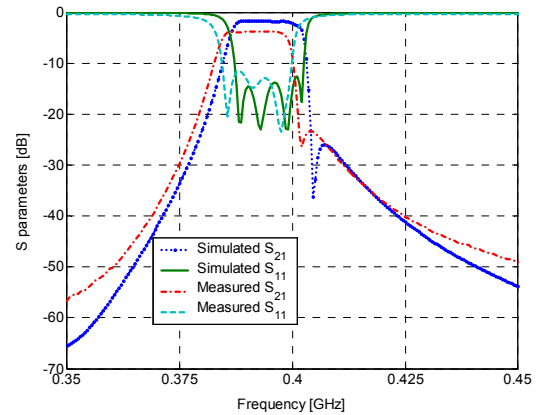


Fig. 8. Comparison between simulated and measured frequency responses of the filter shown in Fig. 7.

[3] T. Tsujiguchi, H. Matsumoto, and T. Nishikawa, "A miniaturized double-surface CPW band-pass filter improved spurious response," *IEEE Trans. Microwave Theory and Tech.*, vol. 49, pp. 879-885, May 2001.
 [4] R. Azadegan, and K. Sarabandi, "Miniaturized folded-slot: an approach to increase the band width and efficiency of miniaturized slot antennas," in *Proc. IEEE Antennas Propagat.* vol.4, San Antonio, TX., June 2002, pp. 14-17.
 [5] R. Azadegan, and K. Sarabandi, "Design of miniaturized slot antennas," in *Proc. IEEE Antennas Propagat.* vol.4, Boston, MA., July 2001, pp. 565-568.
 [6] K. Sarabandi, and R. Azadegan, "Design of an efficient miniaturized UHF planar antenna," in *Proc. IEEE Antennas Propagat.* vol.4, Boston, MA., July 2001, pp. 446-449.
 [7] IE3D Electromagnetic Simulation and Optimization Package, ver. 9.2, *Zeland Software, Inc*, 2002.
 [8] J-S. Hong and M. J. Lancaster, "Couplings of microstrip square open-loop resonators for cross-coupled planar microwave filters," *IEEE Trans. Microwave Theory and Tech.*, vol. 44, pp. 2099-2109, Dec. 1996.
 [9] G. L. Matthaei, L. Young, and E. M. T. Jones, *Microwave Filters, Impedance-Matching Networks and Coupling Structures*, New York: McGraw-Hill, 1964.
 [10] RT/duroid 5880, *Roger Corporation Microwave Material Division*.

Design of Reconfigurable Slot Antennas

Dimitrios Peroulis, *Student Member, IEEE*, Kamal Sarabandi, *Fellow, IEEE*, and Linda P.B. Katehi *Fellow, IEEE*

University of Michigan, Electrical Engineering and Computer Science Department, Radiation Laboratory, 1301 Beal Ave., Ann Arbor, MI 48109-2122 E-mail : saraband@eecs.umich.edu

Abstract

In this paper the design of a compact, efficient and electronically tunable antenna is presented. A single-fed resonant slot loaded with a series of PIN diode switches constitute the fundamental structure of the antenna. The antenna tuning is realized by changing its effective electrical length, which is controlled by the bias voltages of the solid state shunt switches along the slot antenna. Although the design is based on a resonant configuration, an effective bandwidth of 1.7:1 is obtained through this tuning without requiring a reconfigurable matching network. Four resonant frequencies from 540 to 890 MHz are selected in this bandwidth and very good matching is achieved for all resonant frequencies. Theoretical and experimental behavior of the antenna parameters is presented and it is demonstrated that the radiation pattern, efficiency and polarization state of the antenna remain essentially unaffected by the frequency tuning.

Keywords

Reconfigurable antenna, electronic tuning, compact design, resonant frequency, PIN diode switch, MEMS device.

I. INTRODUCTION

With ever-increasing demand for reliable wireless communications, the need for efficient use of electromagnetic spectrum is on the rise. In modern wireless systems spread spectrum signals are used to suppress the harmful effects of the interference from other users who share the same channel (bandwidth) in a multiple-access communication system and the self-interference due to multipath propagation. Also spread spectrum signals are used for securing the message in the presence of unintended listeners and alleviating the effects of communication jammers. One common feature of spread spectrum signals is their relatively high bandwidth. This is specifically true for frequency-hopped spread spectrum communications system. In a frequency-hopped spread spectrum system a relatively large number of contiguous frequency slots spread over a relatively wide bandwidth are used to transmit intervals of the information signal. The selection of the frequency slots for each signal interval is according to a pseudo-random pattern known to the receiver.

Signal propagation over large distances and in urban and forested environment can take place at UHF and lower frequencies. At these frequencies, the size of broadband and efficient antennas is considerable. Techniques used to make the antenna size small, usually renders narrow-band antennas. To make miniature size antennas compatible for a

frequency-hopped spread spectrum system, we may consider a reconfigurable narrow-band antenna that follows the pseudo-random pattern of the frequency-hopped modulation. In this paper the design aspects of compact, planar, and reconfigurable antennas are considered and the feasibility of such designs is demonstrated by constructing and testing a planar reconfigurable slot antenna operating at UHF.

Compared to broadband antennas, reconfigurable antennas offer the following advantages: 1) compact size, 2) similar radiation pattern and gain for all designed frequency bands, and 3) frequency selectivity useful for reducing the adverse effects of co-site interference and jamming.

In recent years, reconfigurable antennas have received significant attention for their applications in communications, electronic surveillance and countermeasures by adapting their properties to achieve selectivity in frequency, bandwidth, polarization and gain. In particular, preliminary studies have been carried out to demonstrate electronic tunability for different antenna structures [1-11]. It has been shown that the operating frequency or bandwidth of resonant antennas can be varied when a tuning mechanism is introduced. Several interesting approaches are presented by Sengupta [1], [2] and Guney [3]. In the literature, tuning is accomplished using varactor diodes [4], [5], or by the application of electrically [6] and magnetically tunable substrates [7], [8] with the use of barium strontium titanate (BST) and ferrite materials respectively.

Tuning of printed dipole or slot antenna have also been considered since they share the same advantages of portability, low profile and compatibility in integration with other monolithic microwave integrated circuits (MMICs). Kawasaki and Itoh [9] presented a 1λ slot tunable antenna loaded with reactive FET components. Although the radiation pattern properties were preserved in all resonant frequencies, the tuning range of the resulting antenna was very limited. Second-resonance cross slot antennas were also presented by Forman et. al. [10] in a mixer/phase detector system. A varactor diode was used in the microstrip feed line and the resonance could be electronically tuned over a 10% bandwidth. The bandwidth was increased to 45% when mechanical tuning was used by varying the feed line length. Dipole tunable antennas were proposed by Roscoe et. al [11] where printed dipoles in series with PIN diodes were studied. The dipole length was varied from

$\lambda/2$ to 1λ depending on whether the dipoles were off or on. The operating frequencies were selected from 5.2 to 5.8 GHz, while matching of only 4–5 dB was achieved.

The slot antenna proposed in this paper utilizes shunt switches that effectively change its electrical length over a very wide bandwidth. To demonstrate the technique a reconfigurable slot antenna capable of operating at four different resonant frequencies over a bandwidth of 1.7:1 is designed and tested. Measurements of the return loss indicate that excellent impedance match can be obtained for all selected resonant frequencies. No special matching network is used and the matching properties are solely determined by the placement of the switches. The loading effect of the PIN diodes in the antenna is also characterized by a full wave analysis and transmission line theory and comparisons between the real and ideal switches are also studied. Per design goals, it is demonstrated that the reconfigurable slot antenna has the same radiation pattern at all frequencies. Also, the measured radiation patterns agree with the theoretical ones. The polarization characteristics and the efficiency behavior of the antenna as a function of frequency are investigated using both theoretical and experimental data. Finally, some design guidelines are provided and possible design improvements are discussed.

The strict requirements of a constant input impedance, gain, radiation pattern and polarization can only be met, if both the passive structure and the tuning mechanism are carefully designed and effectively integrated into the final design. Therefore, these issues are discussed separately. Section II focuses on the passive antenna structure and its properties. The switching mechanism, its loading effect on the antenna and the final reconfigurable antenna are discussed in Section III. Finally, the measured results are presented in section IV.

II. PASSIVE ANTENNA DESIGN

The antenna size at UHF and lower becomes critical and therefore special consideration is required. A compact planar geometry is best suited since three-dimensional large and bulky structures are in general undesirable, especially for military applications. Furthermore, some miniaturization techniques have been applied to reduce the size. This section focuses on the passive slot antenna design issues emanating from the above principles.

First, the miniaturization capabilities provided by a high dielectric constant substrate

were investigated. Inasmuch as an accurate characterization of its effect is needed, a commercially available moment method code [12] was employed. First, simple slot antennas were simulated at 600 MHz and their resonant length was determined as a function of the substrate thickness and dielectric constant (Fig. 1). This analysis suggests that even at low frequencies where the substrate is very thin compared to the wavelength, a miniaturization factor of about 2:1 is possible, if a high dielectric constant substrate is employed. However, the standard commercially available substrates are electrically thin at UHF and below and therefore the 2:1 factor seems to be a limit difficult to exceed even for substrate permittivities as high as 10.

In an effort to further decrease the total area occupied by the antenna, the slot configuration was altered from its standard straight form to an S-shape. From the simulated equivalent magnetic current distribution on the straight and S-shape slots (Fig. 2), it is obvious that they both closely follow a sinusoidal pattern with the maximum current concentrated in the middle of the slot. Other more complicated geometrical shapes can also be used, but the S-shape slot does not contain any segment supporting opposing currents, which would considerably deteriorate the radiation efficiency. It should also be mentioned that, although the total area of the antenna is greatly reduced by this geometrical change, the resonant length remains almost unchanged. For example, a resonant length of 136 mm for a straight slot is slightly increased to 139 mm for S-slot at 600 MHz for a substrate with $\epsilon_r = 10.2$ and thickness of 2.54 mm.

The standard microstrip feed for the simple slot can also be used for the S-shape slot. Fig. 3a shows the slot antenna with its feed-line, while Fig. 3b presents the input impedance at the feeding point as a function of frequency. To achieve a good match to a 50Ω line, the microstrip feed line has to be moved close to one end of the slot antenna. This implies that the antenna input impedance is not very sensitive to small changes in the length of the longer segment (l_2 , see Fig. 3a). This property will greatly simplify the design of the tunable slot and its feeding network and will result in minimum complexity and maximum reliability for the final antenna. More details on this issue can be found in Section III. This property of the slot antenna makes it an attractive choice as a reconfigurable structure, since most other antennas (such as dipoles) would require a specially designed matching

network.

The resonant frequency of the above structure can be tuned by changing the electrical length of the slot. This may be readily accomplished by introducing a short circuit at a specific location. Then the slot will appear to be shorter and therefore the antenna will resonate at a higher frequency. Fig. 4 and 5 show these concepts. In Fig. 4 three different S-shape slots are presented along with their magnetic current distributions. The first slot (a) is the one previously presented in Fig. 2 and it resonates at 600 MHz with a resonant length of 139 mm. The second antenna (b) is 21 mm shorter and is found to resonate at 700 MHz. Finally, the third slot (c) is obtained by modifying (a). Basically antenna (a) is short circuited at 21 mm above its lower end. The simulated return losses for these three slots are shown in Fig. 5. It is also important to note that the microstrip feed-line remains unchanged in all three cases. That is, the distance between the top end of the slot and the feed line cross point remains constant and is equal to 3.2 mm. Fig. 5 shows that very good matching is achieved for both (b) and (c) slot antennas without the need for modifying the feeding network. In addition, the slot antennas (b) and (c) have almost identical resonant frequencies. The small difference in the resonant frequency comes from the fact that antenna (c) appears somewhat electrically longer than (b) due to the parasitic effects of the short circuit. Therefore, tunability is possible by introducing these short circuits with no special matching network.

III. MODELING AND DESIGN OF ACTIVE ANTENNAS

In the previous section we presented the basic principle of controlling the antenna resonant frequency. It was also shown that even when a perfect short circuit is used, the parasitic effects of the short can slightly affect the antenna performance and particularly the resonant frequency. The parasitic effects become worse when a switch with finite isolation is used. This section addresses the issues related to the design of a suitable solid state switch and on the characterization of its effects on the antenna performance. Finally, the complete reconfigurable antenna design is presented at the end of the section together with its theoretical performance.

A. Switch Design

To implement the electronic reconfigurability, the ideal shunt switches must be replaced with PIN diodes. PIN diode's reliability, compact size, high switching speed, small resistance and capacitance in the on and off state respectively make it most appropriate for the application at hand. The RF equivalent circuit of the diode is shown in Fig. 6 for both the on and off states. The reactive components C_p and L_p model the packaging effect, while the others come from the electric properties of the diode junction in the on and off positions [13]. Typical values are also given for the HSMP-3860 diode [14] used in this paper. The computed isolation (defined as $1/|S_{21}|^2$) for the circuit shown in Fig. 6a is given by [14]:

$$\alpha = 10 \log \left[\frac{\left(\frac{R_d Z_0}{R_d^2 + X_d^2} + 2 \right)^2 + \left(\frac{X_d Z_0}{R_d^2 + X_d^2} \right)^2}{4} \right] \quad (1)$$

where $Z_d = R_d + jX_d$ is the equivalent impedance of the diode and Z_0 is the characteristic impedance of the line. In the example considered here, the characteristic impedance of the line is approximately equal to 60Ω , which is calculated by the moment method code [12] for a slotline with width of 2 mm, a finite ground plane of 60 mm (on both sides of the slot) and a substrate permittivity $\epsilon_r = 10.2$ (RT/Duroid) [15]. The isolation computed in (1) is plotted in Fig. 7 as a function of frequency for the HSMP-3860 diode in the 60Ω slotline. Although more than 25 dB isolation is possible at low frequencies, it degrades to 17 dB at 600 MHz and only 11 dB at 1 GHz due to the diode parasitic elements. However, as will be shown, this attenuation is sufficient for a successful antenna tuning up to 900 MHz (see Section IV).

The switch bias network is presented in Fig. 8. An inductor of 470nH and three 10pF capacitors are used to improve the RF-DC signal isolation. These values were chosen based on the bias network RF equivalent circuit shown in Fig. 8b. The simulated performance for the on and off states is presented in Fig. 8c. The RF-DC isolation is better than 30 dB for both states and the return loss is less than -20 dB for the off state. Finally, the RF-RF isolation is comparable to the one shown in Fig. 7.

B. Switch loading on the Antenna

Although the switch isolation is important since it determines the frequency selectivity of the antenna, the switch loading on the antenna is equally important inasmuch as it affects its resonant frequency and input impedance. The loading effects must be taken into account for an accurate prediction of the antenna resonant frequency and input impedance, especially when more than one switch is used for multi-frequency operation.

A transmission line equivalent circuit that models the loading effect of one diode on the antenna is shown in Fig. 9. The transverse resonant technique [16] states that:

$$Z_R(z') + Z_L(z') = 0 \quad (2)$$

where $Z_R(z')$ and $Z_L(z')$ are the input impedances on the right and left of the reference point respectively. For the unloaded transmission line in Fig. 9a equation (2) simplifies to:

$$\tan(\beta l_L) + \tan(\beta l_R) = 0 \quad (3)$$

or

$$l_L + l_R = n \frac{\pi}{2}, \quad n = 1, 2, 3 \dots \quad (4)$$

which is the well known formula for these resonant antennas. Now it is important to see what happens in the simplest case of having one switch on the antenna. Fig. 9b shows the equivalent circuit of a transmission line loaded with one switch in the off position. Equation (2) becomes then:

$$[Z_0 \omega_R C - \cot(\beta l_{R2})] [\tan(\beta l_L) + \tan(\beta l_{R1})] = 1 + \tan(\beta l_L) \tan(\beta l_{R1}) \quad (5)$$

Equation (5) can of course be solved numerically and an iterative method can be employed for finding the unknown lengths until the desired resonant frequency (f_R) has been achieved. A similar procedure can be followed if more than one switch is used on the slot, but the process becomes a little more complicated if all resonant frequencies are to be specified. We also need to note that equation (5) does not include any packaging effects, but these can be readily incorporated in the model, resulting in more accurate modeling.

Only the loading effects when the switch is in its off state have been discussed up to now. Nevertheless, the small on-state resistance also affects the antenna performance and

particularly its input impedance. Full wave analysis was used to model these effects. For a first order approximation, the resistance was modeled as a thin film resistor on top of the slot and the packaging parasitic elements were neglected in this analysis. The parasitic elements effect in the on-state can be important especially at the highest frequencies (see Fig. 7). Fig. 10a shows the simulated geometry of an S-shape slot antenna loaded with a resistive film, which is fed by a microstrip line and the Fig. 10b shows the simulated return loss versus the switch on-state resistance for four different cases between 0 to 5.6Ω . In all four cases the position of the 50Ω feed-line was kept unchanged. It is obvious that the matching level deteriorates rapidly as the resistance value increases, and for resistance values above 1.5Ω the matching level becomes unacceptable.

However, this degradation can be avoided to some extent by elongating the upper end of the slot as the resistance is increased. Fig. 10c shows the improvement on antenna matching when the slot length was adjusted. It is found that, in all three cases, only a very small line segment length needs to be added in order to improve the input impedance of the antenna. Even for an extreme resistance value of 5.6Ω the required line segment length is less than 3% of the total slot length, resulting in only a small change in the resonant frequency. This method, maintaining a good impedance match will be utilized later (for the design of reconfigurable antenna) by placing additional switches (matching-switches) on the slot above the feed-line and synchronizing them together with the switches at the other end of the slot (frequency-switches). However, it should be noted that the matching switches will not represent perfect shorts and they will introduce an extra loading effect. Nonetheless, this effect is negligible and matching levels of better than -20 dB can be achieved, as will be seen next. Therefore, the matching properties of the reconfigurable antenna will solely depend on the position of an array of switches on the slot and no matching network will be necessary as frequency changes.

Having discussed the loading effects of the switches on the matching properties of the antenna, their effects on the radiation characteristics of the antenna need to be found as well. Ideally, the radiation efficiency should be that of the half-wavelength dipole, since the antenna behaves effectively as a $\lambda/2$ resonant slot at each of its operating frequencies. However, the resistance of the switches in on states will obviously dissipate power and

TABLE I

COMPUTED EFFICIENCY FOR SLOT ANTENNAS WITH A SINGLE SWITCH VERSUS ON-STATE RESISTANCE VALUE

R [Ω]	0	1.4	2.8	5.6
Efficiency [%]	71.8	55.6	45.6	33.9

deteriorate the antenna efficiency. The dissipated power obviously depends on the diode's on-resistance and on the number of the switches on the antenna. Table I shows the computed efficiency for the antennas previously discussed in Fig. 10. Dielectric loss has been included in all cases. This explains the non-ideal efficiency when $R = 0\Omega$.

The above antenna efficiency analysis shows that even for a small series resistance of $R = 1.4\Omega$ the antenna gain will be approximately 2.5 dB lower than that of an ideal half-wavelength dipole. This is an inherent drawback of using PIN diode switches. However, micro-electro-mechanical (MEMS) switches are becoming increasingly important and are now a viable alternative as they offer very low power consumption and they come even in smaller packages. [17], [18]. It has also been shown [20] that capacitive type MEMS switches exhibit very low ohmic losses and therefore can be used for maximized antenna efficiency. However, the required on-capacitance values renders them impractical for UHF frequencies. Hence metal-to-metal contact, which have no cut-off frequency must be considered [22].

C. Design Considerations of a Metal-to-Metal Contact MEMS Switch

In this section the specifics of a metal-to-metal contact MEMS switch are described. A slotline MEMS switch architecture similar to the one reported in [18] is especially designed for the application at hand (see Fig. 11). The switch was originally developed for ultra low actuation voltage (less than 10V) and low insertion loss. Furthermore, it is well suited for low power applications, since the reported DC power consumption is in the μW region.

The switch beam is made of electroplated Nickel (Ni) and is suspended approximately $d = 3\mu\text{m}$ on top of the bottom metal layer (circuit metal layer). This is the standard up-state of the switch. The beam is connected to the anchor points through thin meander lines that have been included for low actuation voltage performance [18]. The switch

actuation takes place when a DC voltage is applied between the switch beam and the DC actuation pads (see Fig. 11). If the electrostatic force associated with this DC voltage is sufficiently high, then the switch beam will bent downwards and will introduce a short circuit through a physical contact with the RF pads. On the other hand, any metal-to-metal contact between the switch beam and the DC actuation pads would be undesirable, since it would result in a very high DC current flow that would cause the metals to stick. Thus, a thin Silicon Nitride layer between the two metals has been deposited as a dielectric insulator to prevent any DC contact. This is the reason for not connecting the slotline ground planes and the DC actuation pads. In fact, the slotline ground planes are kept at the same DC voltage as the switch beam to prevent any DC current flow through the RF contact areas. The RF contact pads are about $1\mu\text{m}$ thicker than the circuit metal layer for a better contact in the down position. The fabrication process is rather complex and is not discussed here. Interested readers are referred to [18].

The RF equivalent circuits for the up and down states of this switch are shown in Fig. 12. These equivalent circuits are valid only for low frequencies (below 8 GHz) where the distributed nature of the switch can be ignored. For higher frequencies, however, the small transmission line sections between the three movable beams and the air-bridges have to be taken into account because they will considerably affect the switch performance.

In the up-state the switch presents a very small parasitic capacitance in series with a small inductance. For a first-pass design the up-state capacitance can be approximated using the quasi-static formula of the parallel plate capacitor. A more accurate model can be obtained with a full wave simulator to account for the fringing field effects [19]. IE3D is used in this particular case and an up-state capacitance of $C_{UP} = 50\text{fF}$ was calculated for a distance $d = 3\mu\text{m}$. Since the RF pads are $1\mu\text{m}$ thicker than the circuit metal layer, the effective gap for the up-state capacitor in the areas of the RF pads is $2\mu\text{m}$. These calculations show that the up-state capacitance is an order of magnitude lower than that of the PIN diode considered in the previous section . The series inductance can be also modeled using full wave simulations [19], [21]. The simulated inductance value for this structure is 1pH . It is obvious that the up-state equivalent components have negligible values at UHF or lower and therefore they will not affect the performance of the antenna.

Modeling of the down-state equivalent circuit components appears to be more difficult, due to the uncertainty of the resistance R_p . This resistance includes the ohmic loss of the metal beam and the contact resistance in the RF pad areas. The ohmic loss is usually small for this type of switches and is in the order of 0.1Ω [19]. However, the contact resistance, which will be the dominant factor, is difficult to predict and it can be more accurately extracted from S-parameter measurements. In general, contact resistances depend on the dimensions of the contact area, the conductivity of the metal used for the switch beam and the contact pads as well as the value of the actuation force. More details can be found in [23] where it is shown that large actuation forces result in low resistance values. This implies that the actuation voltage for this switch should be higher than the minimum value presented in [18].

The development of this switch and the resulting reconfigurable antenna is the subject of further investigation and therefore estimated values for the components of the equivalent circuits will be used here to assess the performance of the reconfigurable antenna with this type of MEMS switches. Nevertheless, based on the previous discussion, the effects of using a MEMS switch instead of a PIN diode are easily recognizable. The fact that the values of the up-state equivalent circuit components are negligible, will greatly simplify the design since the non-active switches will not affect the antenna resonance frequency. In other words, the loading effect of a non-active switch will be negligible. However, this would not necessarily hold in a higher frequency design. For example, for a Ka-band or even an X-band antenna should still have to consider the effects of the up-state components, as well as the previously mentioned distributed effects.

The loading effects in the down state will also be less severe. First, the power consumption of the active antenna will be considerably lower with MEMS switches, as discussed before. Second, since the inductance L_{pm} is three orders of magnitude lower than the PIN parasitic inductance, the switch isolation will be nearly constant with respect to frequency. Therefore, a design at a higher frequency can be easily realized without having the limitation of a poor switch performance. Third, if a low RF contact resistance is realized, the efficiency of the antenna will be greatly improved. Full wave simulations were performed with the switch shown in Fig. 11 assuming a contact resistance of 0.5Ω . The calculated

TABLE II
THEORETICALLY CALCULATED RESONANT FREQUENCIES USING FULL WAVE ANALYSIS AND
TRANSMISSION LINE MODEL

f_R [MHz] (TLN) ^a	f_R [MHz] (MM) ^b	Switch Configuration
542	561	1 = ON 2,3,4 = OFF
596	627	1,4 = ON 2,3 = OFF
688	711	1,3 = ON 2,4 = OFF
1002	950	2 = ON 1,3,4 = OFF

^aTransmission Line Model

^bMoment Method

efficiency for the antenna of Fig. 10 is 62.2% which is considerably higher than the one obtained with the PIN diode implementation.

On the other hand, the switching speed of electrostatically actuated switches is in the order of a few μsec , while the PIN diode speed is in the nsec region. Nonetheless, this speed is still rather acceptable in many applications in the wireless communication market.

D. Final Reconfigurable Antenna Design and Properties

Based on the design principles discussed previously, a reconfigurable slot (shown in Fig. 13a) design is presented here. Four switches are used in order to tune the antenna over a range of 540 to 950 MHz. Both full wave analysis and the transmission line model were used in the design process. In this design three frequency-switches and a single matching-switch are used. Table II summarizes the calculated resonant frequencies and the conditions of all four switches for each resonant frequency. The transmission line model has the advantage of allowing fast and accurate (as will be proven later) computation of the resonant frequencies and can easily incorporate all the diode parasitics. However, the full wave analysis is essential when an accurate prediction of the antenna input impedance is needed. In the moment method code, the diodes were simulated as metal-insulator-metal (MIM) capacitors and as thin film resistors in the off and on states respectively and as a

TABLE III
CALCULATED POLARIZATION FOR THE RECONFIGURABLE ANTENNA

f_R [MHz]	561	627	711	950
Angle ($^\circ$)	60	70	60	40

result the packaging parasitics were ignored. This explains the 5% differences observed in the computed resonances between the two models. Fig. 13b shows the calculated return loss where a matching level of better than -20 dB has been achieved for all the operating frequencies.

Since at every operating frequency the antenna radiates as a $\lambda/2$ slot, the radiation pattern remains unchanged when the frequency is shifted. The E and H-planes of a typical calculated pattern are shown in Fig. 13c. The same holds for the antenna directivity. However the efficiency and the gain will be reduced compared to a half-wavelength dipole due to the resistive losses caused by the diodes. Fig. 13d shows the calculated gain using the moment method analysis [12]. The gain is approximately -1 dB for the lowest frequencies and increases to 1 dB for the highest one. Similar results hold for the antenna efficiency.

The reference angle of 0° represents the boresight radiation angle. Although the S-shape pattern considerably reduces the antenna occupied area, it has the inherent drawback that the polarization does not remain constant as the frequency is changed. The antenna polarization (always linear) is determined by the orientation of a segment of the slot (middle segment), where most radiated field is emanated from. However, as Table III shows, the polarization does not change considerably (variation of about 30°). Therefore, if the orientation of the receiving antenna does follow that of the transmitter as the frequency is changed, a maximum polarization mismatch of 25% will be incurred. The orientation of linear polarization reported in Table III is with respect to the x-axis (see Fig. 13a).

IV. MEASUREMENTS AND DISCUSSION

The reconfigurable antenna designed in the previous section was fabricated on a 100 mil thick RT/Duroid substrate ($\epsilon_r = 10.2$). The size of the ground plane was 5×5 in².

TABLE IV

MEASURED RESONANT FREQUENCIES AND THE NECESSARY BIAS VOLTAGES FOR THE SWITCHES

f_R [MHz]	Bias Voltage [V]			
	S1	S2	S3	S4
537	-20	-20	-20	1.1
603	1.1	-20	-20	1.1
684	0	1.1	-20	1.1
887	0	1.1	1.1	0.2

The first task was to measure the resonances and an HP8753D vector network analyzer was used for the S-parameter measurements. The biasing voltage for the switches was provided by a DC voltage source. After calibrating the network analyzer the antenna return loss was measured when different combinations of the switches were activated. The measured data are presented in Fig. 14, where a return loss of better than -13 dB is observed at all resonances. The measured resonances are shown in Table IV together with the necessary biasing conditions. Satisfactory agreement between theoretical, Table II, and experimental, Table IV, data is observed. In addition, the transmission line model gives slightly better results — except the highest frequency — mainly because the parasitic reactive elements have been included in this model and not in the moment method technique. However, this is not true for the highest resonant frequency where an error of 13% exist between the transmission line model and the measurement. This discrepancy can be attributed to the fact that the properties of the diodes, and particularly the element values of its equivalent circuit, cannot be assumed constant up to 1 GHz.

A reverse voltage of -20 dB was applied to maintain the switches in off position and by doing so a better matching level was achieved. This is an important issue particularly when the antenna is used as the transmitter. Since the structure is a resonant structure strong electric fields are established that can turn the diodes on and off at the RF frequency and ruin the small signal design. This effect was clearly observed at the lowest resonance with an input power of 0 dBm. In this case an improvement of about 5 dB was achieved

by changing 0V bias to -20V . With -20V bias we ensured that the diode remains in the presence of RF signal.

One more interesting effect was observed for the highest resonance. We noticed that better matching level would occur, if not only S3 but also S2 was forward biased. This is due to the relatively low isolation that each diode provides at these relatively high frequencies (see Fig. 7). Therefore biasing S2, results in higher isolation and reduces the effect of leaked magnetic current in the area after the switch. The improvement in the return loss was approximately 10 dB compared to leaving S2 unbiased for this frequency.

Next, far field patterns were measured in the University of Michigan's anechoic chamber. The E and H-plane were measured as well as the corresponding cross-polarization for each operating frequency. An RF signal and a DC voltage source were used with the reconfigurable antenna and a dipole with adjustable length was employed as the receiver's antenna. The dipole length was appropriately adjusted for each operating frequency of the transmitting antenna until maximum received power was recorded. In order to find the E-plane, the transmitting antenna was rotated until the electric field was vertically polarized. Then the transmitter, placed on a turn table, was azimuthally rotated for measuring E-plane cuts. The cross-polarized pattern was measured by rotating the receiver antenna by 90° . H-plane pattern measurements were conducted in a similar manner.

Although for slot antennas printed on a substrate it is expected that the radiated power be higher in the half-space that include the dielectric substrate, no appreciable difference was observed experimentally. This is easily explained since in this case the dielectric thickness is about $\lambda/200$ at 600 MHz and the size of the ground plane is small (approximately $\lambda/3$) at the same frequency. Therefore the antenna is almost bi-directional and equivalent to a dipole in free space.

The measured data are presented in Fig. 15 for each resonant frequency. In these plots 0° denote the direction normal to the ground plane. These measurements show that the H-plane closely follows the expected sinusoidal pattern. However, some slight asymmetries near $\pm 90^\circ$ exist for almost all frequencies. These discrepancies originate primarily from two sources. First, parasitic radiation from the cables and the feeding network and second, radiation from the edges of the dielectric. These sources of radiation also affected the E-

TABLE V
MEASURED POLARIZATION FOR THE RECONFIGURABLE ANTENNA

f_R [MHz]	537	603	684	887
Angle ($^\circ$)	57	70	55	33

plane pattern measurements and they caused a difference of 3–4 dB between the minimum and maximum measured value. (see Fig. 15). Despite these discrepancies, it is clear that the far-field pattern remains unchanged versus the frequency tuning.

Gain measurements are accomplished using the comparison method [24]. A log-periodic antenna with 6 dBi gain at 600 MHz was used as a reference antenna for these measurements. The second resonance at 593 MHz was chosen as the operating frequency of the reconfigurable antenna, so that to make direct comparisons with the reference antenna possible. To measure the gain, the power received by the receiver dipole at 593 MHz was recorded when both the reference and the reconfigurable antennas were used in the transmitting mode inside the anechoic chamber under the same conditions. The measured gain was found -1.1 dBi, which corresponds to an efficiency of 47%. These results closely resemble the calculated data. It should also be pointed out that the gain of the slot antenna is reduced not only from the forward-biased diode resistance, but also from the small ground plane size. However, a comparison between the measured and calculated data reveals that the dominant degrading factor in gain is the dissipated power on the diodes rather the ground plane size.

Finally, the antenna polarization was measured and the method previously described for the pattern measurement was employed. The measured polarization orientation at each frequency is provided in Table V. As discussed before, although the polarization does not remain absolutely constant as the frequency is changed, the variation range is small and comparable to the theoretical data (see table III).

V. CONCLUSIONS

A novel method for designing affordable, compact, reconfigurable antennas is proposed in this paper. This method relies on changing the effective length of a resonant slot antenna

by controlling combinations of electronic RF switches. Theoretical results for important antenna parameters were validated experimentally. Important issues involved in the design of such antennas and guidelines were also discussed. Based on the proposed method, a compact planar reconfigurable slot antenna was designed, fabricated and measured and a tuning range of 1.7:1 in the operating frequency was demonstrated. An important feature of this design, backed by theory and experiments, is that radiation characteristics of this antenna remain essentially unaffected by the frequency tuning. The design procedure is general enough that allows wider tuning ranges to be achieved and can be used in many commercial and military applications.

ACKNOWLEDGMENTS

This work was supported by the US Army Research Office under Contact DAAD19-99-1-0197.

REFERENCES

- [1] D. L. Sengupta, *Resonant Frequency of a Tunable Rectangular Patch Antenna*, Electronics Letters, 1984, Vol. 20 pp. 614-5.
- [2] D. L. Sengupta, *Transmission Line Model Analysis of Rectangular Patch Antennas*, Electromagnetics, 1984, Vol. 4, pp. 355-376.
- [3] K. Guney, *Resonant Frequency of a Tunable Rectangular Microstrip Patch Antenna*, Microwave and Optical Technology Letters 1984, Vol. 7, pp. 581-5.
- [4] N. Fayyaz, S. Safavi-Naeini, E. Shin, N. Hodjat, *A Novel Electronically Tunable Rectangular Patch Antenna with One Octave Bandwidth*, Proceedings of IEEE Canadian Conference on Electrical and Computer Engineering, 1998, Vol. 1, pp. 25-8.
- [5] S. H. Al-Charchafchi, M. Frances, *Electronically Tunable Microstrip Patch Antennas*, IEEE Antennas and Propagation Symposium Digest, 1998, Vol. 1, pp. 304-7.
- [6] K. A. Jose, V. K. Varadan V. V. Varadan, *Experimental Investigations on Electronically Tunable Microstrip Antennas*, Microwave and Optical Technology Letters, 1999, Vol. 20, pp. 166-9.
- [7] P. J. Rainville, F. J. Harackewiez, *Magnetic Tuning of a Microstrip Patch Antenna Fabricated on a Ferrite Film*, IEEE Microwave and Guided Wave Letters, 1992, Vol. 2 pp. 483-5.
- [8] R. K. Misra, S. S. Pattnaik, N. Das, *Tuning of Microstrip Antenna on Ferrite Substrate*, IEEE Transactions on Antennas and Propagation, 1993, Vol. 41, pp. 230-3.
- [9] S. Kawasaki, T. Itoh, *A Slot Antenna with Electronically Tunable Length*, IEEE Antennas and Propagation Symposium Digest, 1991, Vol. 1, pp. 130-3.
- [10] M. A. Forman, Z. B. Popovic, *A Tunable Second-Resonance Cross-Slot Antenna*, IEEE Antennas and Propagation Symposium Digest, 1997, Vol. 1, pp. 18-21.

- [11] D. J. Roscoe, L. Shafai, A. Ittipiboon, M. Cuhaci, R. Douville, *Tunable Dipole Antennas*, IEEE Antennas and Propagation Symposium Digest, 1972, Vol. 2, pp. 672-5.
- [12] Zeland's IE3D, Release 7, 2000.
- [13] Hewlett Packard, *Linear Models for Active Diode Surface Mount Packages*, Application Note 1124.
- [14] Hewlett Packard, *Applications of PIN diodes*, Application Note 922.
- [15] Rogers Microwave Products.
- [16] C. Balanis, *Advanced Engineering Electromagnetics*, John Willey & Sons, Chapter 8.
- [17] C. Goldsmith, J. Randall, S. Eshelman, T. H. Lin, D. Denniston, S. Chen, B. Norvell, *Characteristics of Micromachined Switches at Microwave Frequencies*, IEEE Microwave Theory and Techniques Symposium Digest, 1996, Vol. 2 pp. 1141-4.
- [18] S. Pacheco, L. P.B. Katehi, C. T. Nguyen *Design of Low Actuation Voltage RF MEMS Switch*, IEEE Microwave Theory and Techniques Symposium Digest, 2000, Vol. 1 pp. 165-170.
- [19] J. B. Muldavin, G. M. Rebeiz, *High-Isolation CPW MEMS Shunt Switches-Part 1: Modeling*, IEEE Transactions on Microwave Theory and Techniques, 2000, Vol. 48 pp. 1045-1052.
- [20] J. B. Muldavin, G. M. Rebeiz, *High-Isolation CPW MEMS Shunt Switches-Part 2: Design*, IEEE Transactions on Microwave Theory and Techniques, 2000, Vol. 48 pp. 1053-1056.
- [21] D. Peroulis, S. Pacheco, K. Sarabandi, L. P. B. Katehi, *MEMS Devices for High Isolation Switching and Tunable Filtering*, IEEE Transactions on Microwave Theory and Techniques, 2000, Vol. 2 pp. 1217-1220.
- [22] J. J. Yao, M. F. Chang, *A Surface Micromachined Miniature Switch for Telecommunications Applications with Signal Frequencies from DC up to 4 GHz*, Proceedings of the International Solid-State Sensors and Actuators Conference - TRANSDUCERS 1995. Vol.2. pp. 25-9.
- [23] D. Hyman, M. Mehregany *Contact Physics of Gold Microcontacts for MEMS Switches*, IEEE Transactions on Components and Packaging Technology, 1999, Vol. 22, pp. 357-364
- [24] W. L. Stutzman, G. A. Thiele, *Antenna Theory and Design*, John Willey & Sons, Second Edition, Chapter 9.

LIST OF FIGURES

1	Resonant length at 600 MHz for straight slot antenna (in free-space wavelength) as a function of substrate thickness and dielectric constant.	22
2	Computed magnetic current distribution on (a) straight and (b) S-shape first-resonant slot antenna.	23
3	(a) S-slot antenna with microstrip feed-line and (b) the real and imaginary parts of the input impedance as a function of frequency.	24
4	Current distribution for (a) 600 MHz S-slot, (b) 700 MHz S-slot, and (c) 600 MHz S-slot with a short-circuit 21 mm above its bottom edge.	25
5	Simulated results for the return loss of the antennas presented in Fig. 4.	26
6	(a) PIN diode connected as a shunt switch in a transmission line. (b) RF equivalent circuit for PIN diode including packaging effects.	27
7	Isolation from a shunt diode used as a switch placed in a 60Ω line.	28
8	(a) Layout of switch biasing network. (b) RF equivalent circuit. (c) On and Off-state simulated RF performance	29
9	RF equivalent circuits for determining the resonant frequency of (a) unloaded and (b) loaded with a single switch slot antenna.	30
10	(a) Slot antenna with resistive load representing actuated switch (units are in mm). (b) Return loss for different values of switch resistance. (c) Improved return loss with minor adjustments (< 4 mm) in the slot length above the feeding point.	31
11	Slotline MEMS switch (dimensions are in μm)	32
12	RF equivalent circuit for the MEMS switch in the (a) up and (b) down states	32
13	(a) Reconfigurable slot antenna (units are in mm) (b) Simulated return loss for the four resonant frequencies. (c) Typical radiation pattern. (d) Simulated gain the four resonant frequencies.	33
14	Measured resonant frequencies of the reconfigurable antenna.	34
15	Measured radiation patterns for the four resonant frequencies	35

LIST OF TABLES

I	Computed efficiency for slot antennas with a single switch versus on-state resistance value	10
II	Theoretically calculated resonant frequencies using full wave analysis and transmission line model	13
III	Calculated polarization for the reconfigurable antenna	14
IV	Measured resonant frequencies and the necessary bias voltages for the switches	15
V	Measured polarization for the reconfigurable antenna	17

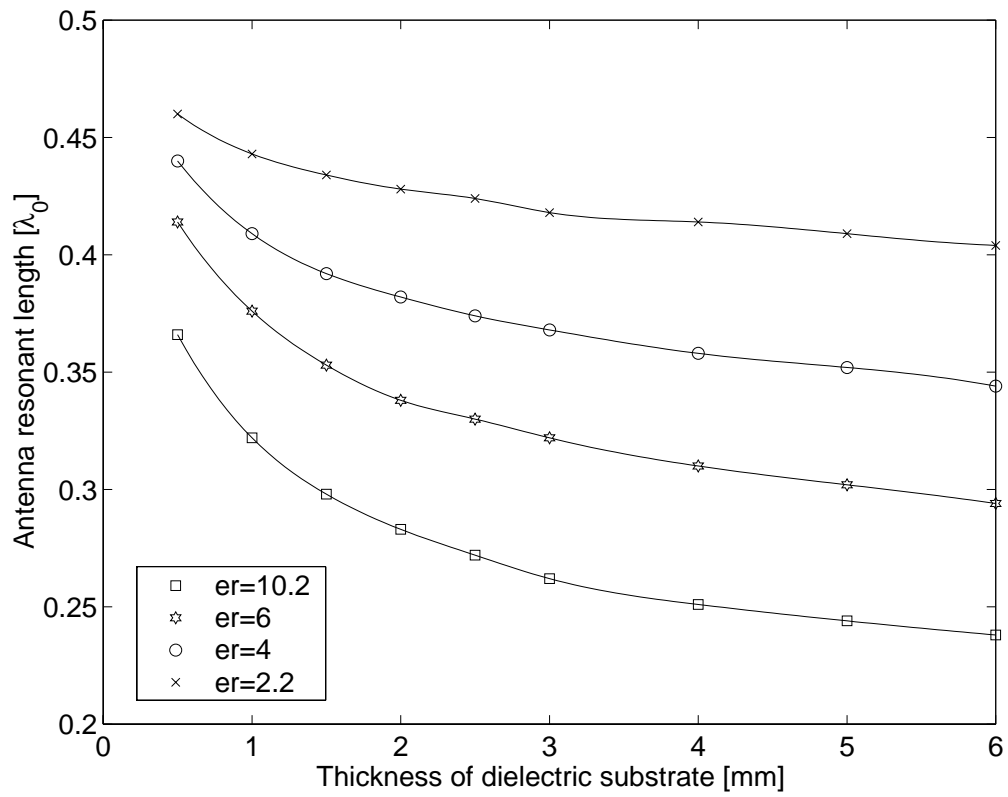


Fig. 1. Resonant length at 600 MHz for straight slot antenna (in free-space wavelength) as a function of substrate thickness and dielectric constant.

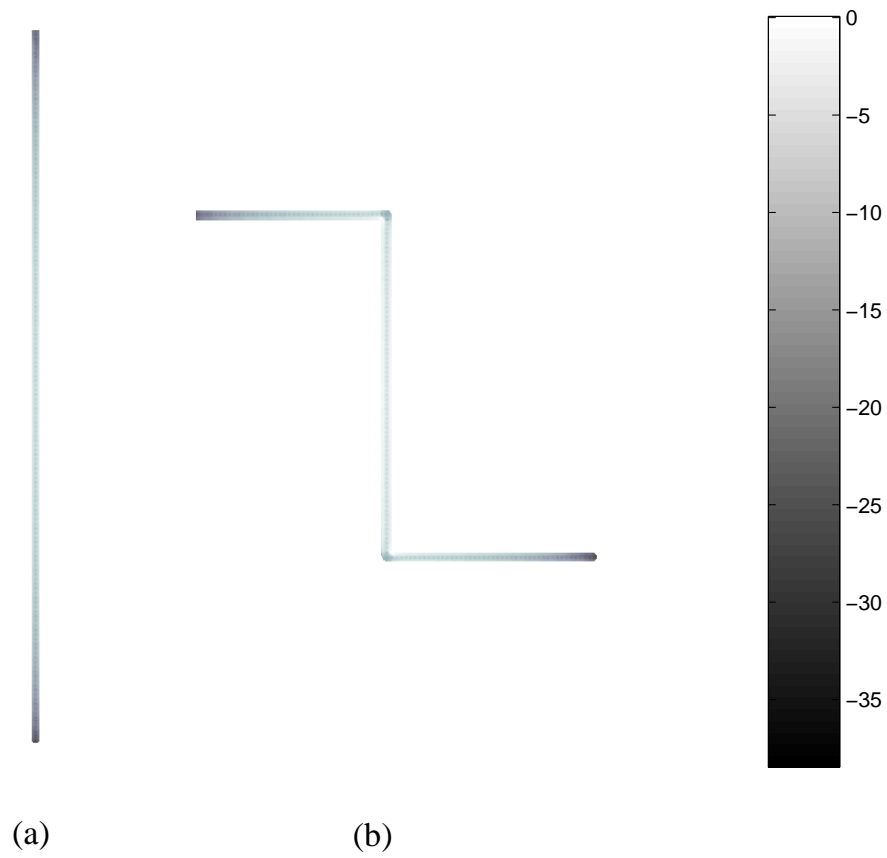
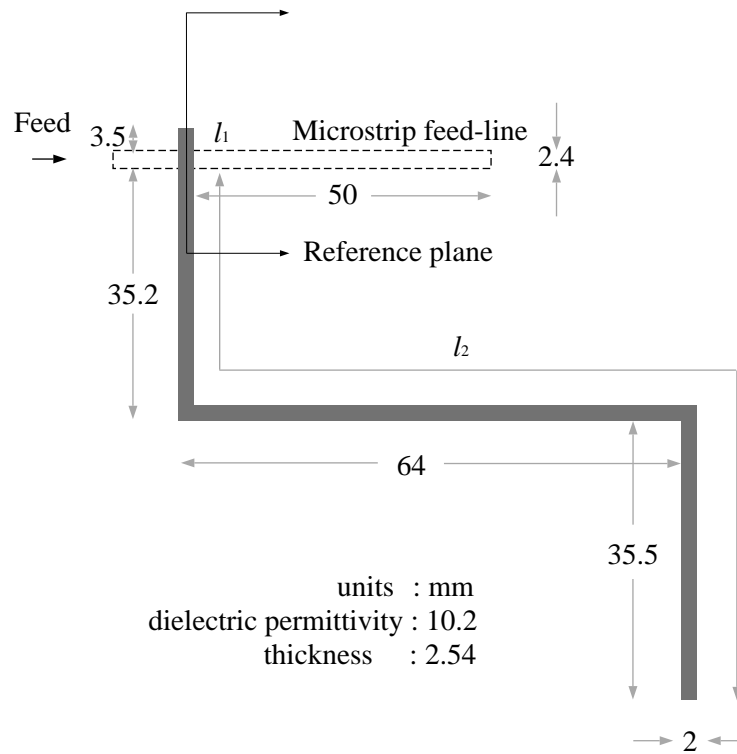
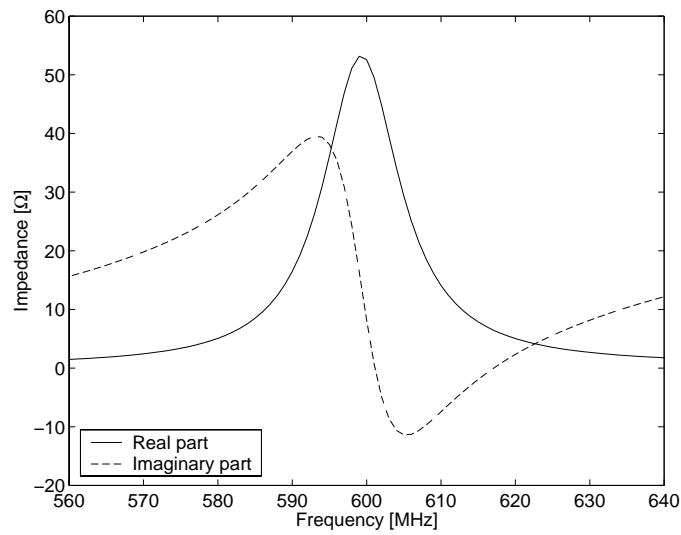


Fig. 2. Computed magnetic current distribution on (a) straight and (b) S-shape first-resonant slot antenna.



(a)



(b)

Fig. 3. (a) S-slot antenna with microstrip feed-line and (b) the real and imaginary parts of the input impedance as a function of frequency.

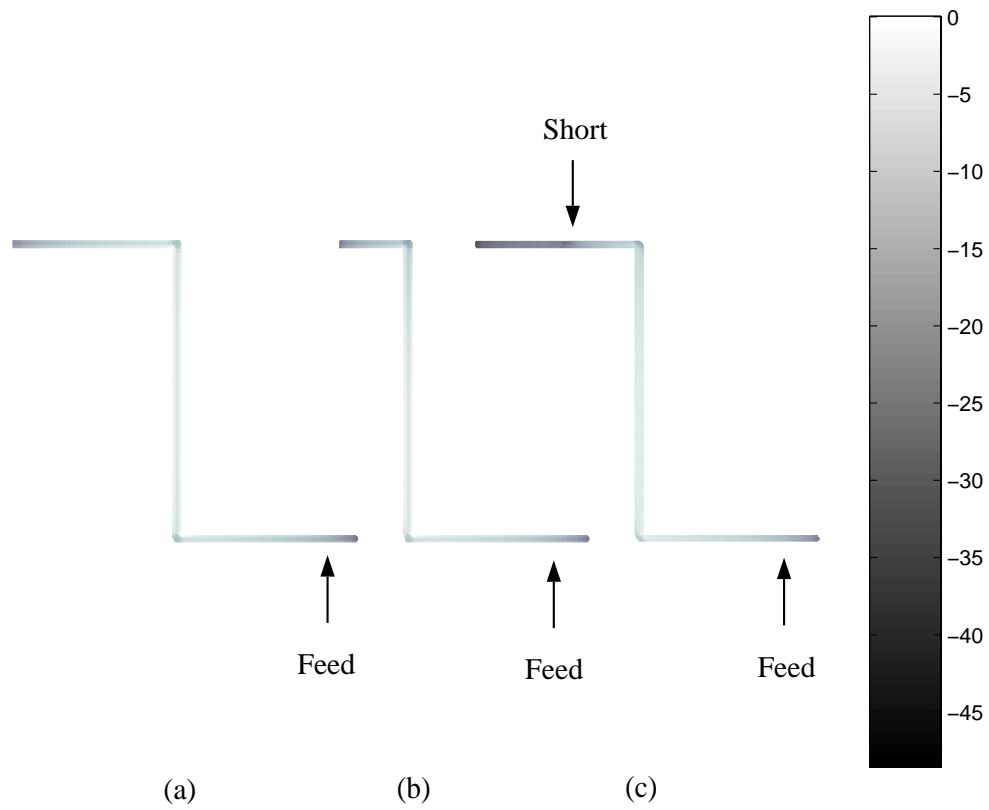


Fig. 4. Current distribution for (a) 600 MHz S-slot, (b) 700 MHz S-slot, and (c) 600 MHz S-slot with a short-circuit 21 mm above its bottom edge.

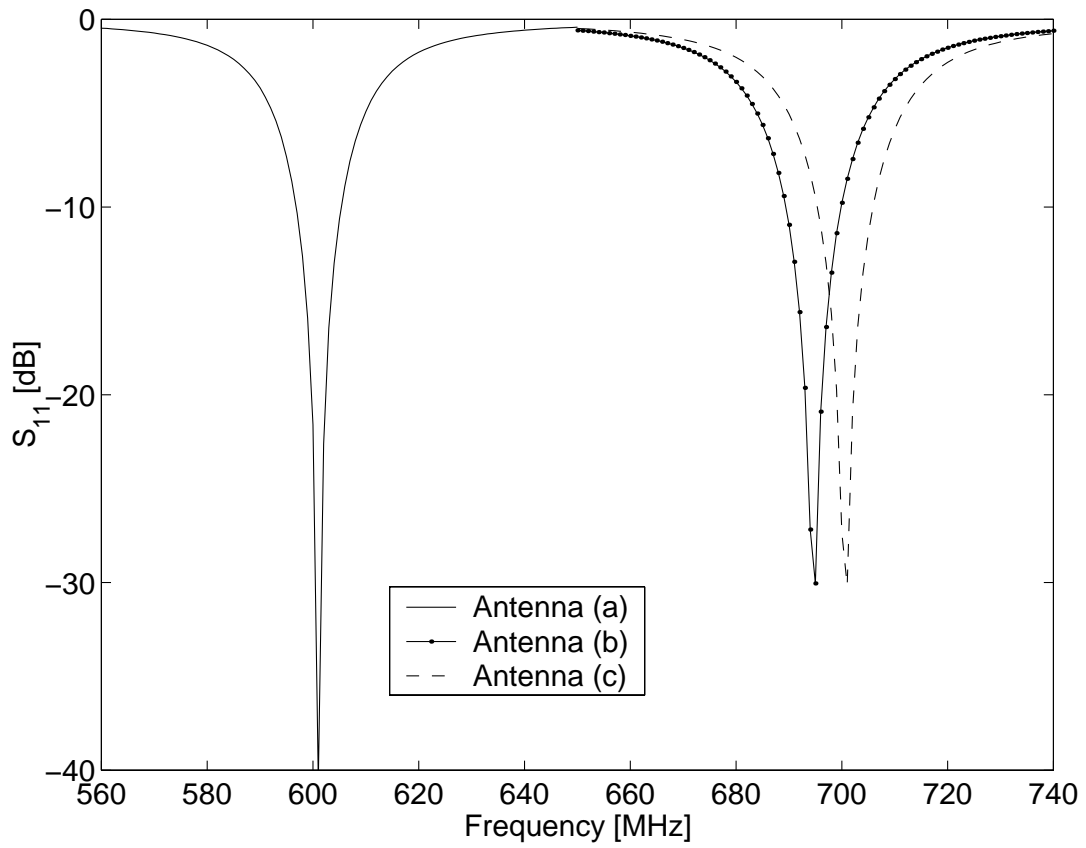
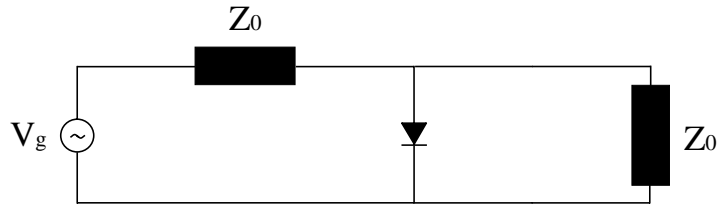
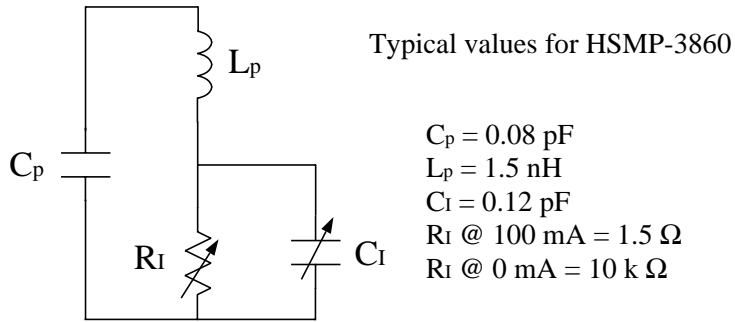


Fig. 5. Simulated results for the return loss of the antennas presented in Fig. 4.



(a)



(b)

Fig. 6. (a) PIN diode connected as a shunt switch in a transmission line. (b) RF equivalent circuit for PIN diode including packaging effects.

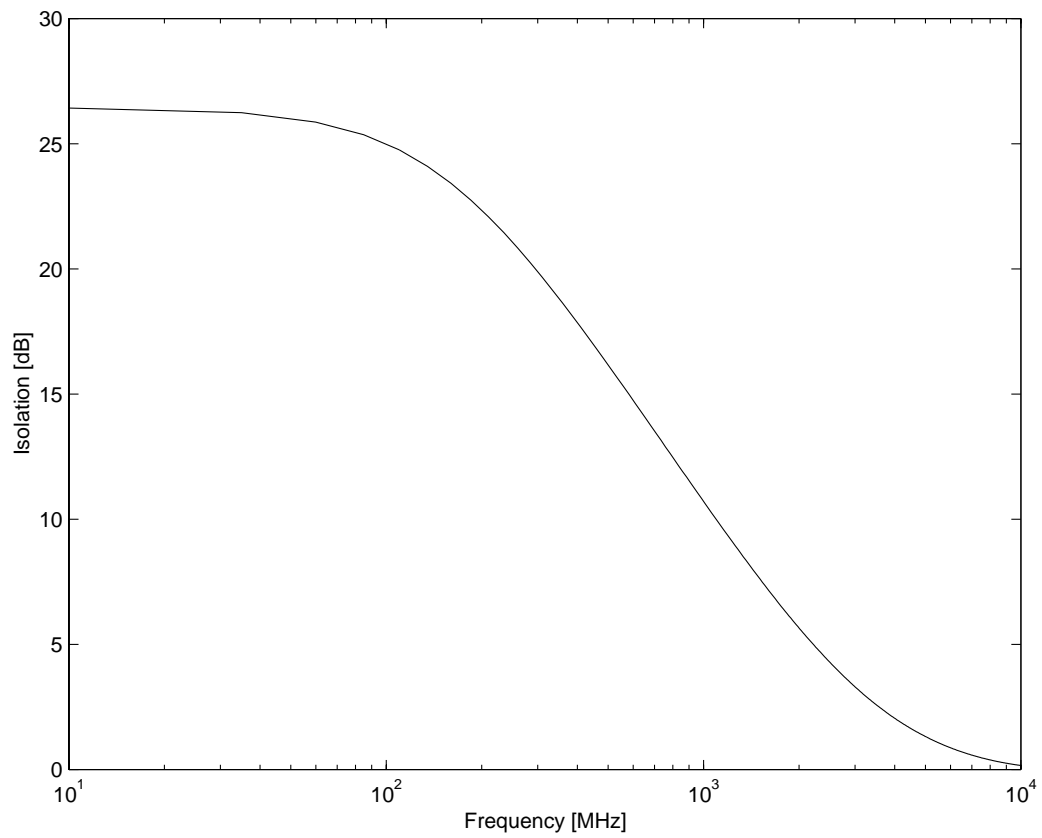
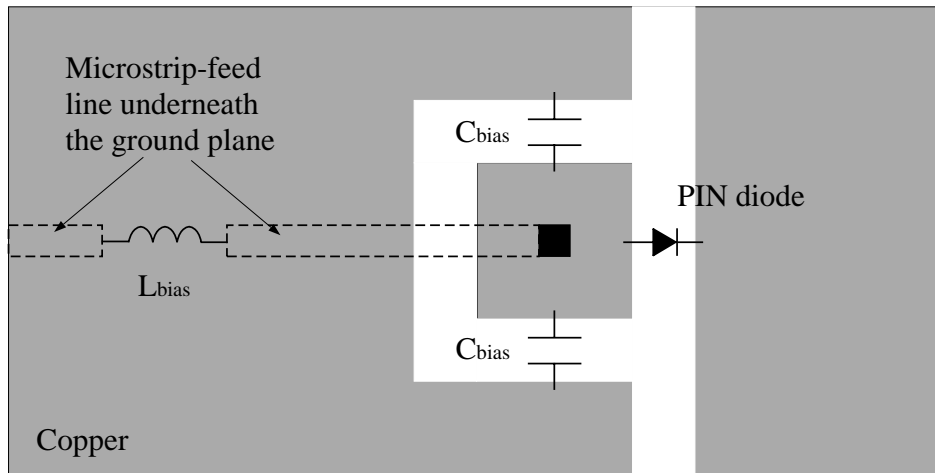
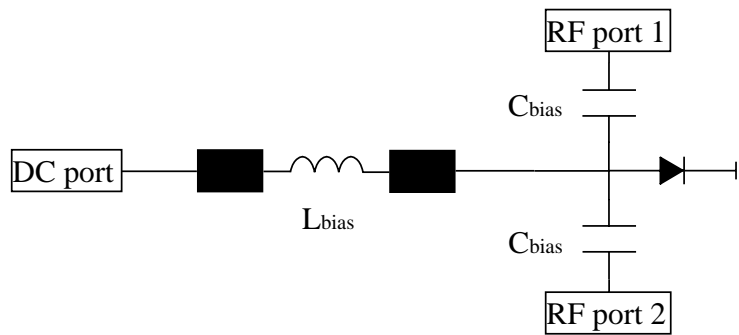


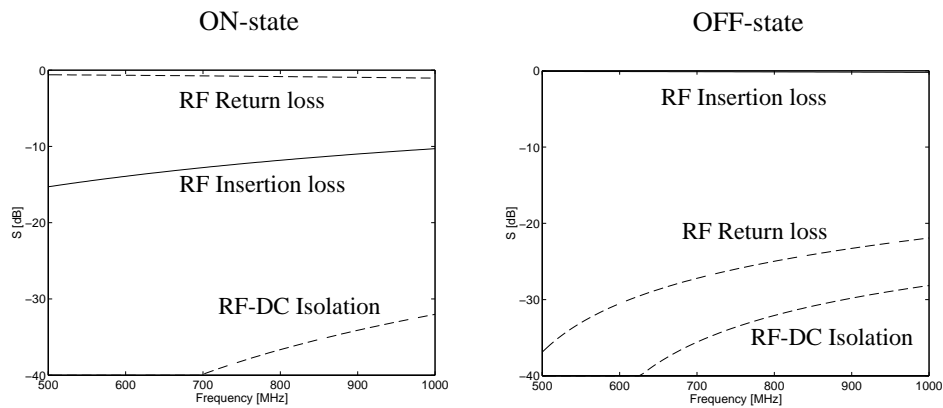
Fig. 7. Isolation from a shunt diode used as a switch placed in a 60Ω line.



(a)



(b)



(c)

Fig. 8. (a) Layout of switch biasing network. (b) RF equivalent circuit. (c) On and Off-state simulated RF performance

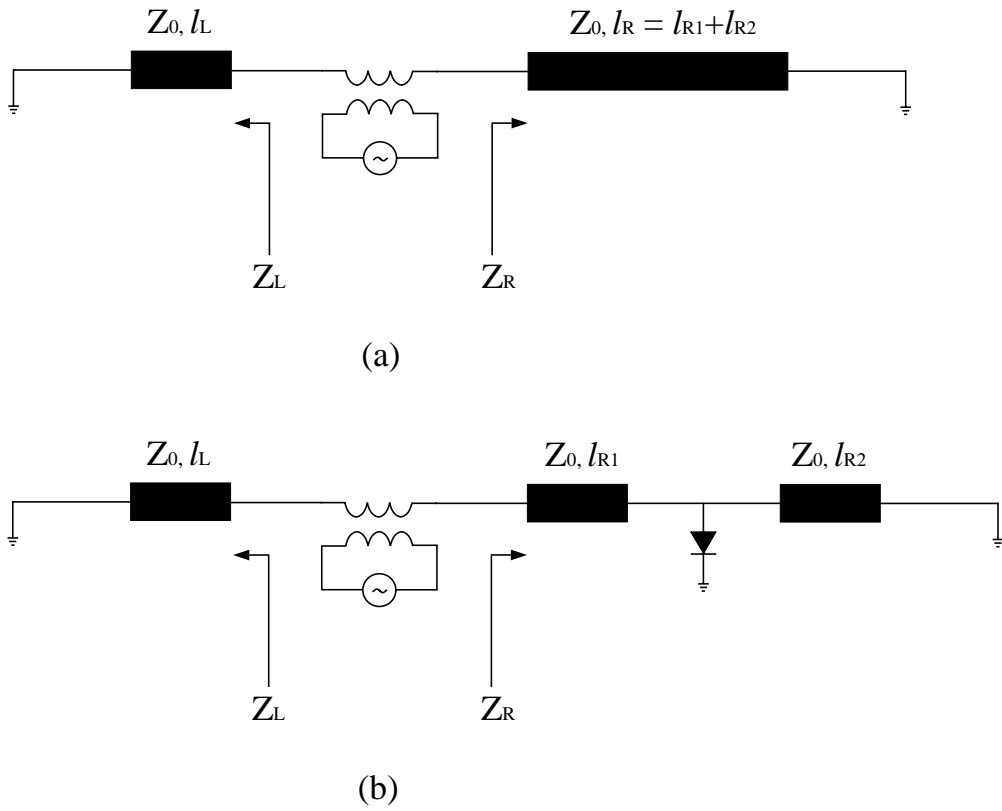


Fig. 9. RF equivalent circuits for determining the resonant frequency of (a) unloaded and (b) loaded with a single switch slot antenna.

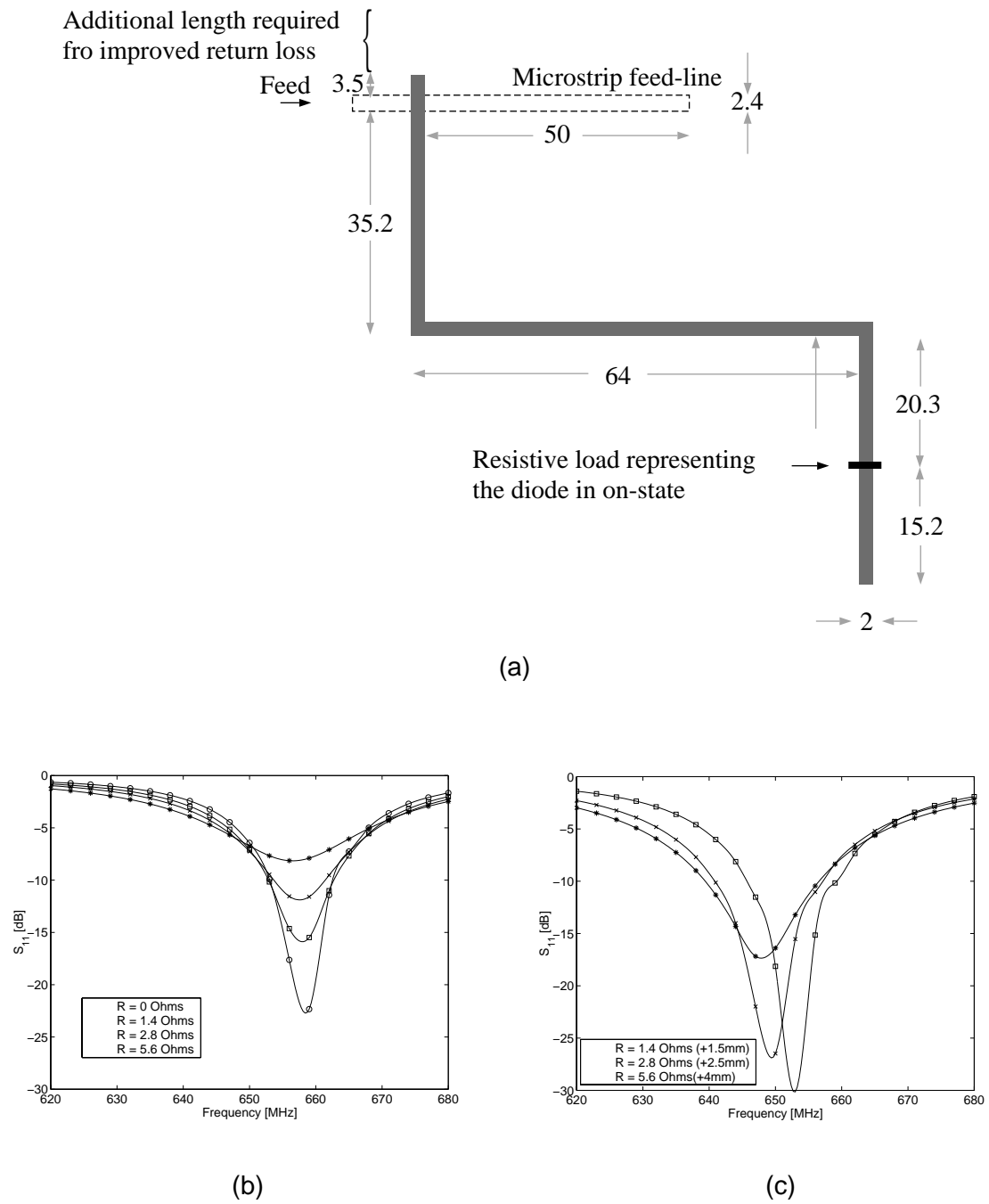


Fig. 10. (a) Slot antenna with resistive load representing actuated switch (units are in mm). (b) Return loss for different values of switch resistance. (c) Improved return loss with minor adjustments (< 4 mm) in the slot length above the feeding point.

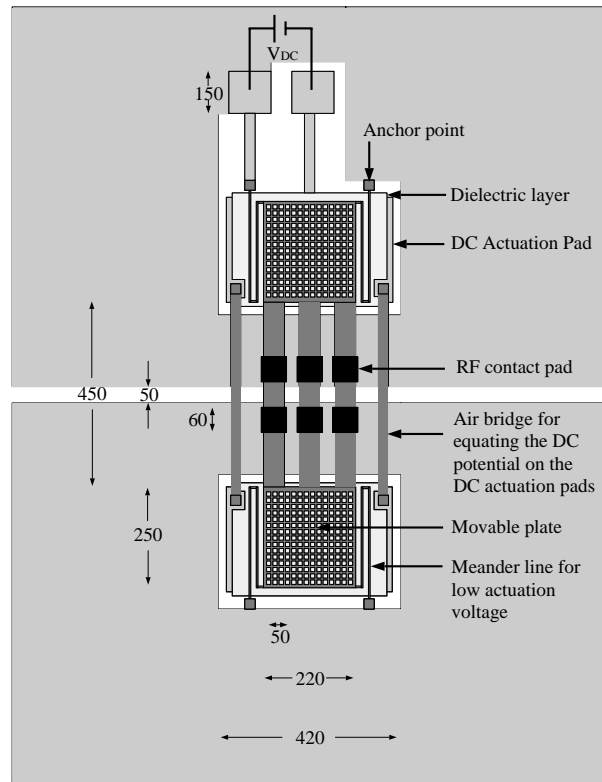
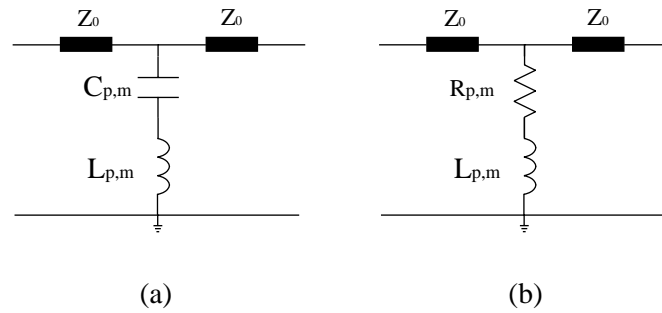


Fig. 11. Slotline MEMS switch (dimensions are in μm)



Estimated values

$$\begin{aligned}
 C_{p,m} &= 50 \text{ fF} \\
 L_{p,m} &= 1 \text{ pH} \\
 R_{p,m} &= 0.5 \sim 1.5 \ \Omega
 \end{aligned}$$

Fig. 12. RF equivalent circuit for the MEMS switch in the (a) up and (b) down states

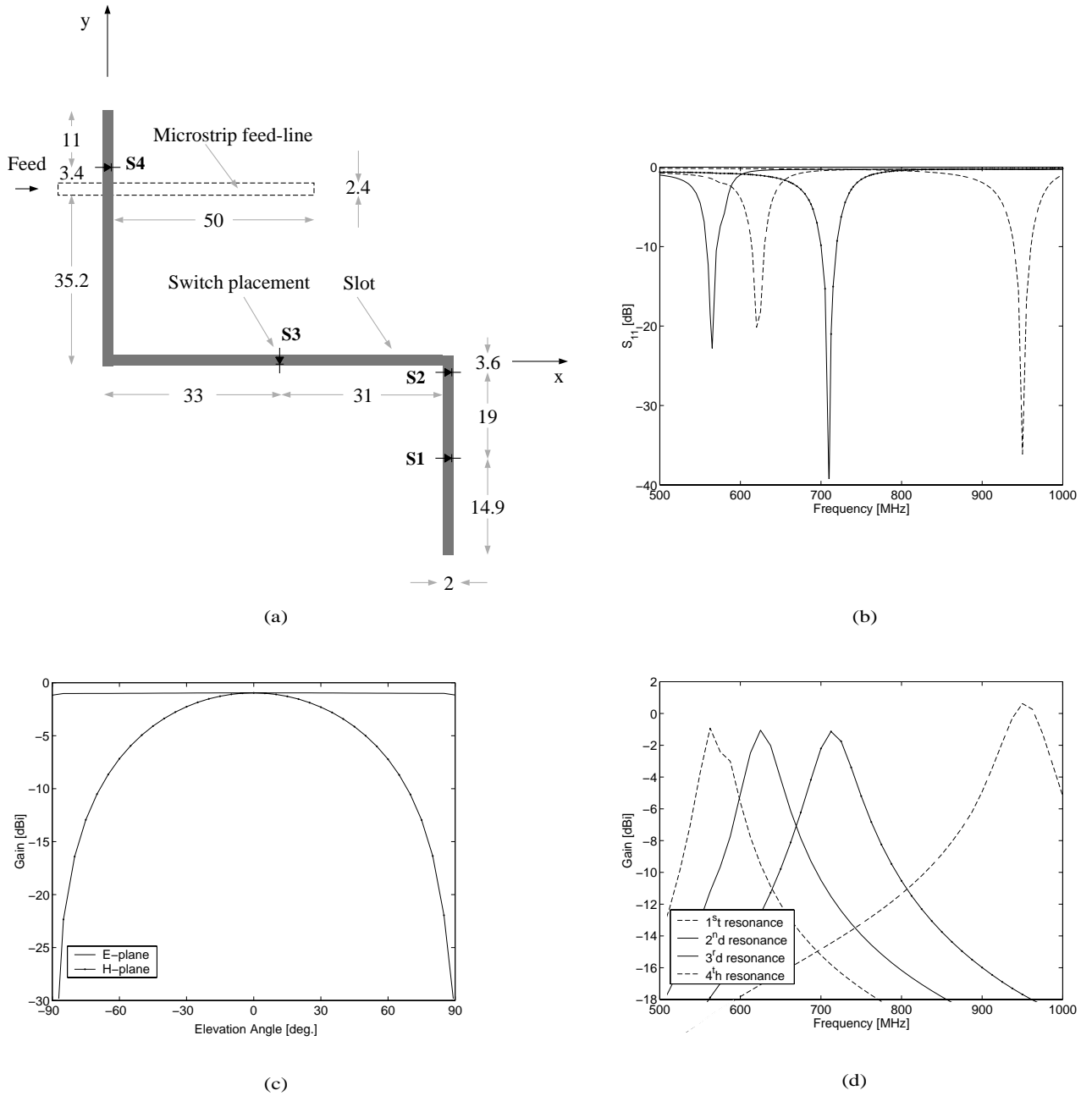


Fig. 13. (a) Reconfigurable slot antenna (units are in mm) (b) Simulated return loss for the four resonant frequencies. (c) Typical radiation pattern. (d) Simulated gain the four resonant frequencies.

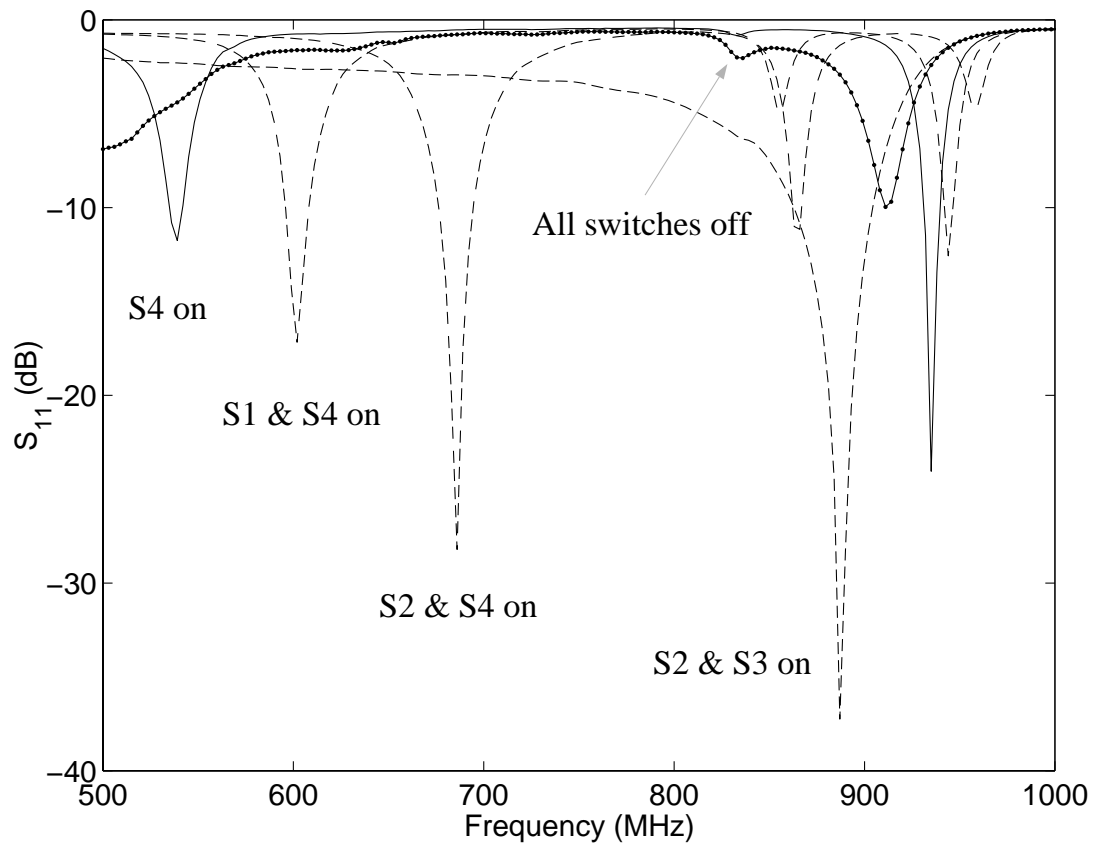
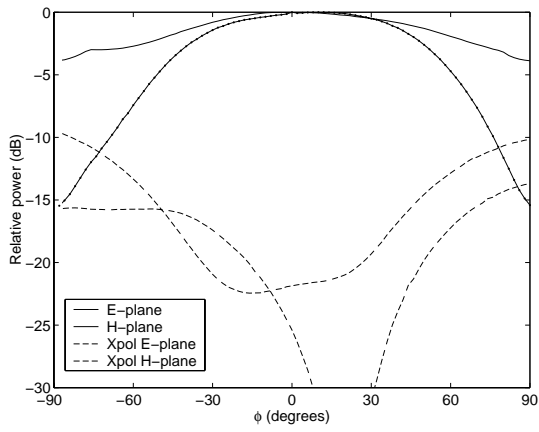
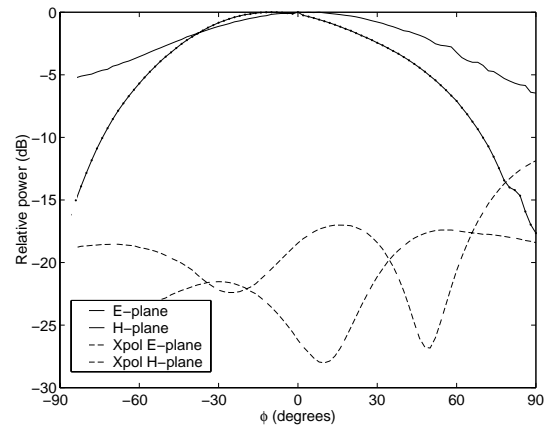


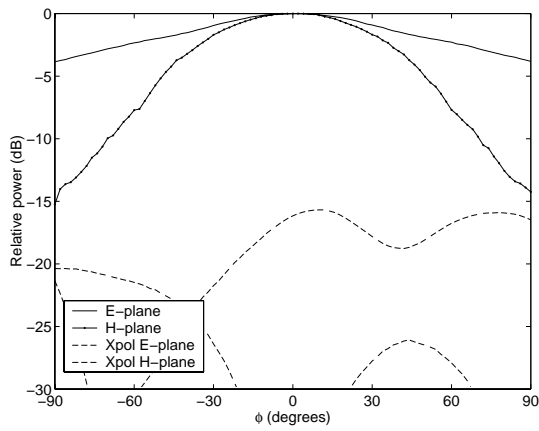
Fig. 14. Measured resonant frequencies of the reconfigurable antenna.



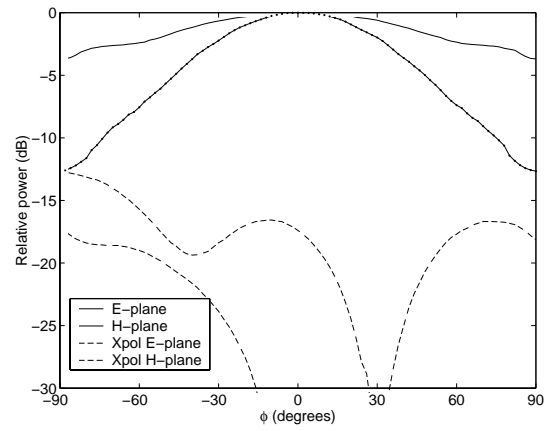
(a) $f = 537$ MHz



(b) $f = 603$ MHz



(c) $f = 684$ MHz



(d) $f = 887$ MHz

Fig. 15. Measured radiation patterns for the four resonant frequencies